University of Liège
Structural Dynamics Research Group
Aerospace and Mechanical Engineering Department

Theoretical and Experimental Modal Analysis of Nonlinear Vibrating Structures using Nonlinear Normal Modes

PhD Thesis Dissertation

by

Maxime PEETERS
Ingénieur Civil Electro-Mécanicien (Aérospatiale)

November 2010

Author's Coordinates

Maxime PEETERS, Ir.
Structural Dynamics Research Group
Aerospace and Mechanical Engineering Department
University of Liège

Chemin des chevreuils, 1
4000 Liège
Belgium

Office phone: +32 (0)4 366 4854
Email: m.peeters@ulg.ac.be

Members of the Examination Committee

Gaëtan KERSCHEN (President of the committee)
Professor - University of Liège
Email: G.Kerschen@ulg.ac.be

Jean-Claude GOLINVAL (Supervisor)
Professor - University of Liège
Email: JC.Golinval@ulg.ac.be

Alex CARRELLA
Professor - University of Bristol (UK)

Ludovic NOELS
Professor - University of Liège

Fabrice THOUVEREZ
Professor - Ecole Centrale de Lyon (France)

Cyril TOUZE
Professor - Ecole Nationale Supérieure de Techniques Avancées (France)

David WAGG
Professor - University of Bristol (UK)

Abstract

Theoretical and experimental modal analysis, i.e., the computation of vibration modes from a mathematical model and from experimental data, respectively, is quite sophisticated and advanced in linear structural dynamics. However, nonlinearity is a frequent occurrence in real-world engineering structures, and the existing linear methodologies fail dramatically in the presence of nonlinear dynamical phenomena. Therefore, the present thesis focuses on the development of a practical nonlinear analog of modal analysis for properly accounting for nonlinearity in mechanical systems.

The concept of nonlinear normal mode (NNM) provides solid mathematical and theoretical foundations for a rigorous, yet understandable by the practicing engineer, analysis of nonlinear dynamical behaviors. In this context, a useful framework for nonlinear modal analysis of vibrating structures, which includes the computation of NNMs from finite element models and their identification from experimental data, is proposed in this dissertation. In view of the still limited use of NNMs in structural dynamics, special attention is devoted to progress toward a practical tool that has the potential to deal with large-scale, real-world structures.

Targeting an effective and exact computation of NNMs, even in strongly nonlinear regimes of motion, one original contribution of this work is to resort to numerical methods. An algorithm combining a shooting procedure and the so-called pseudo-arclength continuation method is developed. On the other hand, a nonlinear extension of phase resonance testing (also known as force appropriation) is introduced for the experimental identification of NNMs, which is another innovative aspect of the doctoral thesis. In particular, the phase lag quadrature criterion, which is used for linear experimental modal analysis, is generalized in the presence of nonlinear dynamical behavior.

Academic examples are first considered to illustrate, in a simple manner, that the proposed methods form an effective and adequate framework for nonlinear modal analysis. Furthermore, more realistic structures, including a full-scale aircraft, are studied to demonstrate the potential applicability of the approach to large-scale, real-life applications.

Acknowledgments

This doctoral dissertation is the result of several years of research at the University of Liège and would be unachievable without the involvement of a number of people.

First of all, I would like to express my gratitude to my advisors Professors Jean-Claude Golinval and Gaëtan Kerschen for their precious help, guidance and support during the course of this research. I appreciated their advice and their confidence in me. Thank you also for the meticulous reading of the thesis draft.

I am pleased to acknowledge my current and former colleagues I had the pleasure to meet at the Structural Dynamics Research Group *and more generally in the* Aerospace and Mechanical Engineering Department*. I am especially thankful to Fabien Poncelet and Régis Viguié who created a friendly working atmosphere, and with whom I had a lot of helpful discussions.*

During my stay at Ecole Centrale de Marseille *and at* Laboratoire de Mécanique et d'Acoustique (CNRS-LMA)*, I had the opportunity to interact with several researchers and faculty members. I would like to thank Professor Bruno Cochelin and Doctor Sergio Bellizzi for hosting my visit. In addition, I am grateful to Doctors Pascal Lubrina and Cyrille Stéphan for their warm welcome at the* French Aerospace Laboratory, ONERA*, and for providing a finite element model of a full-scale aircraft.*

I would like to acknowledge Professors Alex Carrella, Ludovic Noels, Fabrice Thouverez, David Wagg and Doctor Cyril Touzé for accepting to participate in the examination committee of this doctoral thesis.

Many thanks also go to my parents, my sister and my family-in-law for the constant encouragements provided throughout the course of my research.

Finally and foremost, my thoughts go to Marie who has always supported me in the choices I have made. I would like to thank you for always being there for me.

Contents

List of Acronyms

CWT	Continuous wavelet transform
DOF	Degree of freedom
EMA	Experimental modal analysis
FEP	Frequency-energy plot
FRF	Frequency response function
LNM	Linear normal mode
MAC	Modal assurance criterion
MIF	Mode indicator function
MSE	Mean square error
NNM	Nonlinear normal mode
ODE	Ordinary differential equation
PSD	Power spectral density
RFS	Restoring force surface
TMA	Theoretical modal analysis

Introduction

The concept of a normal mode is central in the theory of linear vibrating systems. Besides their obvious physical interpretation, the linear normal modes (LNMs) have interesting mathematical properties. They can be used to decouple the governing equations of motion; i.e., a linear system vibrates as if it were made of independent oscillators governed by the eigensolutions. Two important properties that directly result from this decoupling are:

1. *Invariance*: if the motion is initiated on one specific LNM, the remaining LNMs remain quiescent for all time.
2. *Modal superposition*: free and forced oscillations can conveniently be expressed as linear combinations of individual LNM motions.

The framework of LNMs lays down the foundations of the so-called modal analysis, which refers to the analysis of the dynamics of a vibrating structure in terms of its modal parameters, namely the mode shapes, natural frequencies and damping ratios. These modal parameters can be determined either from mathematical models (direct approach or theoretical modal analysis, TMA) or from experimental data (inverse approach or experimental modal analysis, EMA). For linear systems, TMA is performed merely by solving an eigenvalue problem. Alternatively, modal testing and EMA have been developed over the past 40-50 years, and numerous techniques are available nowadays [38].

These two ways of performing modal analysis are extensively used for finite element model updating and validation [41]. In addition, LNMs are relevant dynamical features that can be exploited for various purposes including model reduction (e.g., substructuring techniques [29]), damage detection and structural health monitoring [34].

Clearly, though, linearity is an idealization, an exception to the rule; nonlinearity is a frequent occurrence in real-life engineering applications [64] and can drastically alter their behavior. For instance, in an aircraft, besides nonlinear fluid-structure interaction, typical nonlinearities include backlash and friction in control surfaces and joints, hardening nonlinearities in engine-to-pylon connections, saturation effects in hydraulic actuators, plus any underlying distributed nonlinearity in the structure [15]. Furthermore, the next generations of aircraft are using materials such as glass-fiber or carbon-fiber composites to a greater extent for structural weight reduction. These materials entail new challenges for

performance prediction, because they exhibit a structural behavior deviating significantly from linearity. Their increased use also creates more interfaces between different materials, which are further sources of nonlinear behavior. Satellites are other examples of aerospace applications where nonlinearity may considerably impact the dynamic behavior [22, 98].

Any attempt to apply traditional linear analysis to nonlinear systems results, at best, in suboptimal design. Thus, there is a need for efficient, analytically rigorous, broadly applicable analysis techniques for nonlinear structural dynamics. In this context, nonlinear normal modes (NNMs) offer a solid theoretical and mathematical tool for interpreting a wide class of nonlinear dynamical phenomena, yet they have a clear and simple conceptual relation to the LNMs, with which practicing structural engineers are familiar. Other appealing features of the NNMs are that they are capable of handling strong structural nonlinearity and that they have the potential to address the individualistic nature of nonlinear systems.

Nonlinear Normal Modes: A Brief Historical Perspective and Current State-of-the-Art

The most straightforward definition of an NNM is a *vibration in unison* of the system (i.e., a synchronous oscillation). NNMs were pioneered in the 1960s thanks to Rosenberg's seminal work [121–123]. They were further studied in the 1970s by Rand [115–117] and Manevitch and Mikhlin [83]. They were regarded as a theoretical curiosity until the beginning of the 1990s when they were given a new impetus through the efforts of Vakakis et al. [25, 65, 146, 148, 149, 154] and Shaw and Pierre [127–130]. Since then, a large body of literature has addressed, with notable success, the qualitative and quantitative analysis of nonlinear phenomena using NNMs (see, e.g., [1, 13, 33, 44, 55, 62, 67, 68, 72, 76, 86, 88, 90, 97, 102, 114, 132, 135, 142, 161, 166, 167]). For a few typical applications and comprehensive reviews, the reader can refer to [92, 112, 149, 154].

However, most structural engineers still view NNMs as a concept that is foreign to them, and they do not yet consider NNMs as a useful concept for analyzing nonlinear structural dynamics. There are several reasons supporting this statement:

1. Nonlinear systems can exhibit extremely complex behaviors which linear systems cannot. These phenomena include jumps, bifurcations, saturation, subharmonic, superharmonic and internal resonances, resonance captures, limit cycles, modal interactions and chaos.

2. NNMs have two important limitations compared to their linear counterpart. First and foremost, the principle of superposition, which is the cornerstone of linear theory, does not apply to nonlinear systems. Second, the lack of orthogonality relations

satisfied by the NNMs complicates their exploitation as bases for order reduction of the nonlinear dynamics.

3. The vast majority of the NNM literature deals with low-order lumped-mass models (systems with typically a few degrees of freedom - DOFs) or focuses on specific resonances of distributed parameter systems.

4. Most existing constructive techniques for computing NNMs are based on asymptotic approaches and rely on fairly involved mathematical developments.

Motivation

The objective of the present doctoral thesis is to progress toward a practical modal analysis of nonlinear vibrating structures using the concept of NNMs. According to the complementary routes to modal analysis, the aim is therefore twofold, as illustrated in Figure 1. First, TMA consists in computing the NNMs from a mathematical model of the structure. Second, EMA targets the identification of NNMs from experimental data of the structure. This doctoral dissertation focuses on the development of an adequate framework for proposing a nonlinear analog of these two approaches for modal analysis.

In this context, because NNMs have not yet been applied to large-scale engineering structures with multiple components and strong nonlinearities, several key aspects that might drive their development and exploitation for nonlinear modal analysis are highlighted throughout the manuscript:

1. There have been very few attempts to compute NNMs using numerical methods [9, 19, 56, 72, 109, 133, 162]. Interestingly, algorithms for the continuation of periodic solutions are really quite sophisticated and advanced (see, e.g., [35, 93, 126]), yet they have not been fully exploited for the computation of nonlinear modes. We support that these numerical algorithms pave the way for an effective and practical computation of NNMs of complex (and possibly strongly) nonlinear structures.

2. Phase resonance testing, also known as force appropriation, is commonly used for linear EMA, particularly in the aerospace industry (e.g., for ground vibration testing of aircrafts [30] and modal survey of satellites [31, 32]). We show that this approach can lay down the foundations for a rigorous experimental identification of NNMs.

3. Time-frequency analysis is a versatile tool for analyzing nonstationary signals; i.e., signals whose spectral contents vary with time. It has been successfully exploited in structural dynamics, e.g., for linear and nonlinear system identification [7, 42, 136]. Unlike the Fourier transform, a method such as the wavelet transform models the time evolution of the dominant frequency components of a signal. Because

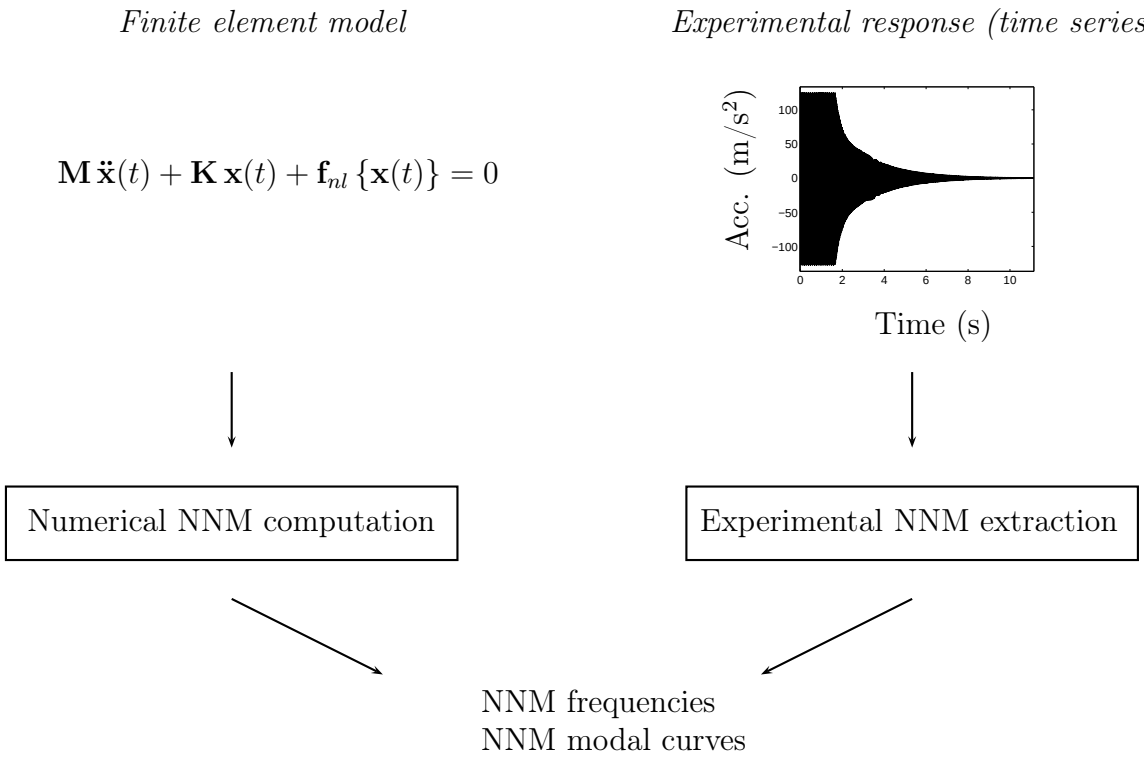

Figure 1: Theoretical and experimental nonlinear modal analysis.

this method can deal adequately with the frequency-energy dependence inherent to nonlinear oscillations, we believe that it is the ideal companion to the NNMs.

4. An appropriate graphical depiction of the NNMs is key to their exploitation. In this study, we show that the representation of NNMs in a frequency-energy plot is particularly convenient. It facilitates the interpretation of the dynamics and clarifies the bifurcations that connect, generate or eliminate the different NNM branches.

The parallel development of EMA and TMA in this manuscript leads to an overall methodology (see Figure 1) that could be exploited for model identification and updating of nonlinear systems. For instance, one specific application that could ultimately benefit from the proposed advancements is aircraft ground vibration testing (GVT) [48, 106]. GVTs are performed on aircraft prototypes before their first flight and provide critical data for flutter analysis. Identification of an accurate model during GVTs could allow the effects of nonlinearity on flutter to be explored by calculation prior to the flight test programme. Such an improvement would increase the aeroelastic prediction capabilities.

Outline of the Thesis

Chapter 1 focuses on the framework and relevance of NNMs in structural dynamics. The definition of NNMs and their fundamental properties are described and illustrated with several examples. Different analytical and numerical methods for computing NNMs are briefly reviewed. The potential applications of NNMs in structural dynamics, especially for modal analysis, are also discussed.

Chapter 2 deals with TMA. An efficient computational technique for calculating the NNMs of structures discretized by the finite element method is developed. The procedure is based on the numerical continuation of periodic solutions of nonlinear conservative systems. To this end, the proposed algorithm is a combination of shooting and pseudo-arclength continuation methods. A detailed description of these numerical techniques is given, and special attention is devoted to the reduction of the computational burden. The algorithm is demonstrated using a nonlinear 2DOF system.

In Chapter 3, the numerical computation of NNMs is addressed using structural systems of increasing complexity. An essentially nonlinear system is first considered. Next, a simplified discrete model of a nonlinear bladed disk assembly is investigated. As a final application, the finite element model of a full-scale aircraft possessing softening nonlinearities is studied. This is achieved to support that the proposed algorithm holds promise for an effective and practical NNM computation tool that can deal with large-scale, real-world structures.

Chapter 4 is concerned with EMA. A modal testing methodology in the presence of nonlinear dynamic behavior is introduced by targeting the identification of NNMs from experimental data. The methodology relies on a nonlinear extension of phase resonance testing in order to isolate a single NNM during the experiments. To this end, the phase lag quadrature criterion is generalized to nonlinear structures. Thanks to the invariance principle, the NNM is identified from the resulting free decay response with the help of time-frequency analysis. The methodology is illustrated using two numerical examples, namely a 2DOF system and a nonlinear cantilever beam.

Chapter 5 is dedicated to the experimental demonstration of the proposed methodology for NNM identification. An experimental set-up composed of a cantilever beam with geometrical nonlinearity is considered, and the performance of the procedure is assessed by extracting its first two NNMs.

Finally, conclusions regarding the completed research and the associated contributions to the field of nonlinear modal analysis are drawn. A discussion of the ways in which this research may be extended is also given.

Chapter 1

Nonlinear Normal Modes: A Useful Framework in Structural Dynamics

Abstract

The concept of nonlinear normal modes (NNMs) is discussed in the present chapter. Because there is virtually no application of NNMs to large-scale engineering structures, this chapter is an attempt to highlight several features that might drive their development in the future. Another objective of this chapter is to describe, in simple terms, and to illustrate the fundamental properties of NNMs. This is achieved to convince the structural dynamicist not necessarily acquainted with them that they are a useful framework for the analysis of nonlinear vibrating structures.

1.1 Nonlinear Normal Modes: What Are They ?

The free response of discrete undamped mechanical systems is considered, assuming that continuous systems have been spatially discretized using, e.g., the finite element method. The equations of motion are

$$\mathbf{M}\,\ddot{\mathbf{x}}(t) + \mathbf{K}\,\mathbf{x}(t) + \mathbf{f}_{nl}\left\{\mathbf{x}(t)\right\} = 0 \tag{1.1}$$

where $\mathbf{M}$ is the mass matrix; $\mathbf{K}$ is the stiffness matrix; $\mathbf{x}$ and $\ddot{\mathbf{x}}$ are the displacement and acceleration vectors, respectively; $\mathbf{f}_{nl}$ is the nonlinear restoring force vector, including stiffness terms only.

To illustrate the different concepts, a two-degree-of-freedom (2DOF) system with a cubic stiffness is chosen. The system is depicted in Figure 1.1, and its motion is governed by the equations

$$\begin{aligned} \ddot{x}_1 + (2x_1 - x_2) + 0.5\,x_1^3 &= 0 \\ \ddot{x}_2 + (2x_2 - x_1) &= 0 \end{aligned} \tag{1.2}$$

For comparison purposes, the underlying linear system

$$\begin{aligned} \ddot{x}_1 + (2x_1 - x_2) &= 0 \\ \ddot{x}_2 + (2x_2 - x_1) &= 0 \end{aligned} \tag{1.3}$$

is also considered in this study. The time series corresponding to in-phase and out-of-phase normal mode motions of the linear system (1.3) are depicted in Figure 1.2. Motion in the configuration space (i.e., in the plane of the displacements $x_1(t)$ and $x_2(t)$) is given in Figure 1.3. Obviously, linear normal mode (LNM) motions correspond to straight lines in this plane.

1.1.1 Definition of a Nonlinear Normal Mode

There exist two main definitions of nonlinear normal modes (NNMs) in the literature, due to Rosenberg [121–123] and Shaw and Pierre [127–130]. There have been additional definitions, which include a complex-valued invariant manifold formulation [94, 96] and group theoretic definitions [154], but they are not described herein.

Historically, Lyapunov and Poincaré contributions served as the cornerstone of the NNM development. For n-DOF conservative systems with no internal resonances, Lyapunov showed that there exist at least n different families of periodic solutions around the stable equilibrium point of the system [81]. At low energy, the periodic solutions of each family are in the neighborhood of a LNM of the linearized system. These n families define n NNMs that can be regarded as nonlinear extensions of the n LNMs of the underlying linear system. Poincaré and Poincaré-Dulac theorems are fundamental for establishing the theory of normal form, which was later exploited for NNM computation [55, 142].

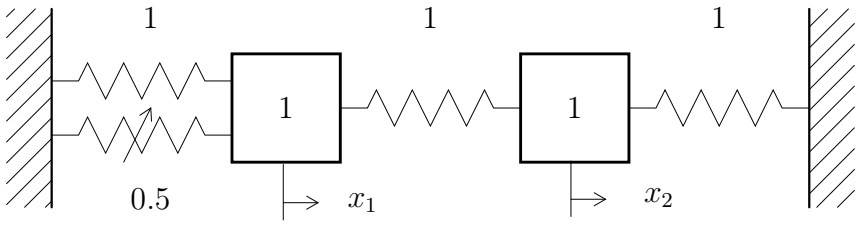

Figure 1.1: Schematic representation of the 2DOF system example.

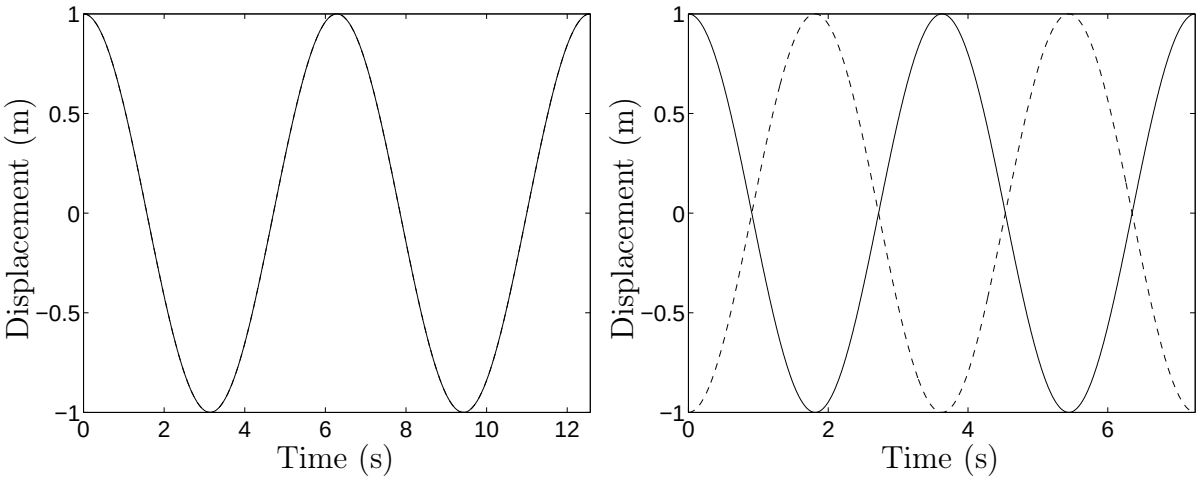

Figure 1.2: Time series of LNM motions of system (1.3) (——: $x_1(t)$; − − −: $x_2(t)$). Left plot: in-phase LNM ($[x_1(0)\ x_2(0)\ \dot{x}_1(0)\ \dot{x}_2(0)] = [1\ 1\ 0\ 0]$); right plot: out-of-phase LNM ($[x_1(0)\ x_2(0)\ \dot{x}_1(0)\ \dot{x}_2(0)] = [1\ -1\ 0\ 0]$).

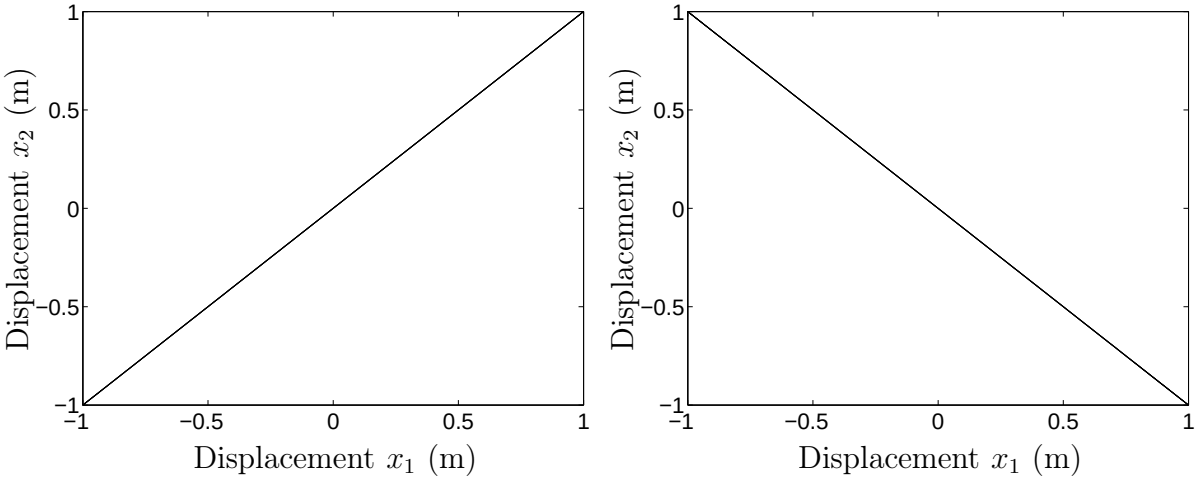

Figure 1.3: LNM motions of system (1.3) in the configuration space. Left plot: in-phase LNM; right plot: out-of-phase LNM.

Rosenberg's Definition

During the normal mode motion of a linear conservative system, each system component moves with the same frequency and with a fixed ratio amongst the displacements of the components. Targeting a straightforward nonlinear extension of the LNM concept, Rosenberg defined an NNM as a *vibration in unison* of the system (i.e., a synchronous periodic oscillation). This definition requires that all material points of the system reach their extreme values and pass through zero simultaneously and allows all displacements to be expressed in terms of a single reference displacement.

For illustration, the time series and the configuration space of in-phase and out-of-phase NNM motions during the free response of system (1.2) are depicted in Figures 1.4 and 1.5, respectively. The modal lines of this nonlinear system are curves, resulting from the nonlinear relationship between the coordinates during the periodic motion. These curved NNMs, termed nonsimilar NNMs by Rosenberg, are generic in nonlinear systems, and their existence certainly complicates the concept of orthogonality between modes [69, 70]. A particular feature of these NNMs is that their shape depends on the total energy present in the system. When special spatial symmetries exist, the NNMs may degenerate into (energy-invariant) straight modal lines, as in the linear case [25]. According to Rosenberg's terminology, these modes are referred to as similar NNMs.

The Invariant Manifold Approach

Shaw and Pierre proposed a generalization of Rosenberg's definition that provides a direct and elegant extension of the NNM concept to damped systems. Based on geometric arguments and inspired by the center manifold technique [51], they defined an NNM as a two-dimensional invariant manifold in phase space. Such a manifold is invariant under the flow (i.e., orbits that start out in the manifold remain in it for all time), which extends the invariance property of LNMs to nonlinear systems. In order to parameterize the manifold, a single pair of state variables (i.e., both the displacement and the velocity) are chosen as master coordinates, the remaining variables being functionally related to the chosen pair. Therefore, the system behaves like a nonlinear single-DOF system on the manifold.

Geometrically, LNMs are represented by planes in phase space, and NNMs are two-dimensional surfaces that are tangent to them at the equilibrium point. For illustration, the manifolds corresponding to in-phase and out-of-phase NNMs of system (1.2) are given in Figure 1.6.

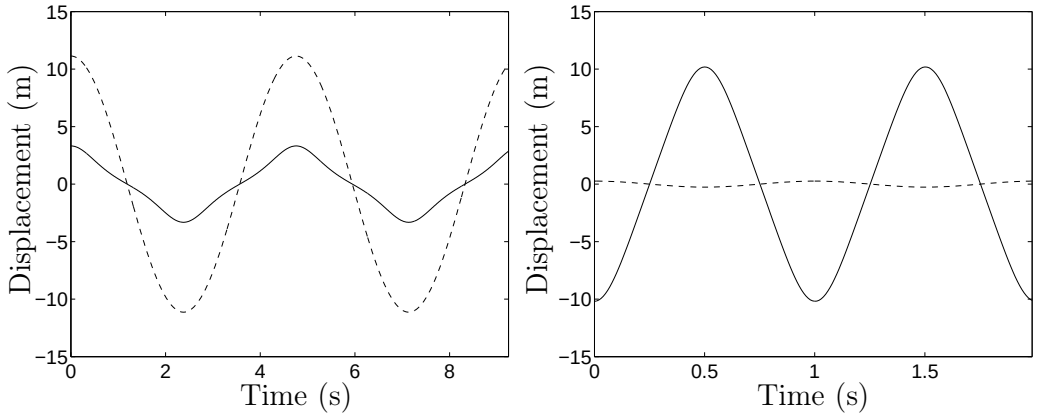

Figure 1.4: Time series of NNM motions of system (1.2) (——: $x_1(t)$; − − −: $x_2(t)$). Left plot: in-phase NNM ($[x_1(0)\ x_2(0)\ \dot{x}_1(0)\ \dot{x}_2(0)] = [3.319\ 11.134\ 0\ 0]$); right plot: out-of-phase NNM ($[x_1(0)\ x_2(0)\ \dot{x}_1(0)\ \dot{x}_2(0)] = [-10.188\ 0.262\ 0\ 0]$).

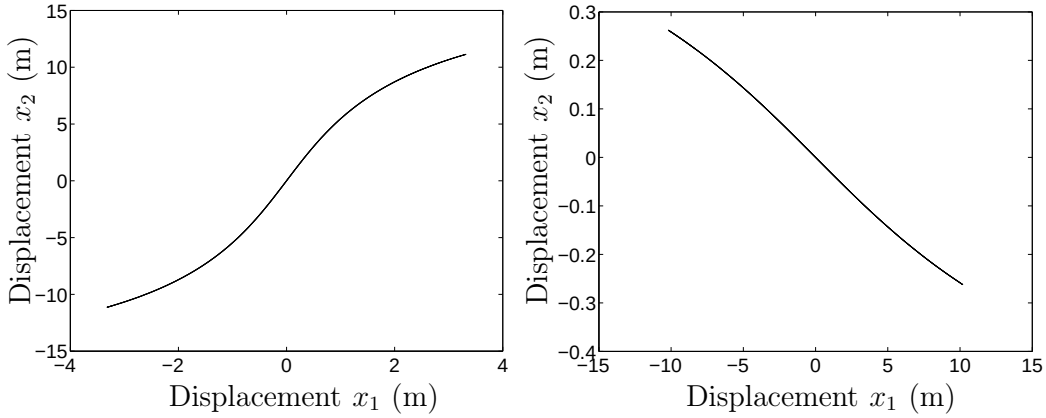

Figure 1.5: NNM motions of system (1.2) in the configuration space. Left plot: in-phase NNM; right plot: out-of-phase NNM.

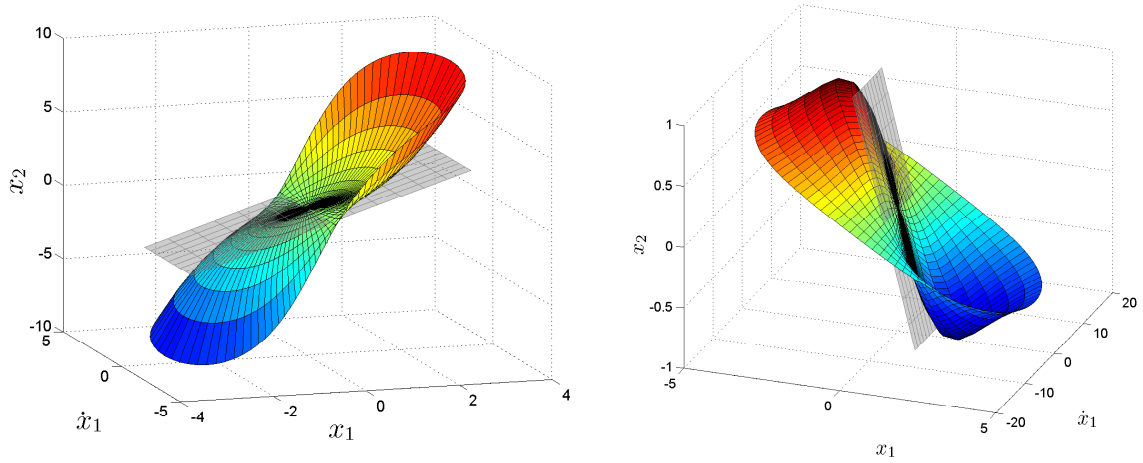

Figure 1.6: Two-dimensional invariant manifolds of system (1.2) with the corresponding LNMs. Left plot: in-phase LNM and NNM; right plot: out-of-phase LNM and NNM.

The Approach Followed in this Study

At first glance, Rosenberg's definition may appear restrictive in two cases:

1. This definition, as such, cannot be easily extended to nonconservative systems.
2. In the presence of internal resonances (i.e., when two or more NNMs interact), some coordinates may have a dominant frequency component different than that of the other coordinates (e.g., some coordinates may vibrate faster than others). In this case, the system no longer vibrates in unison. This is illustrated in Figure 1.7 for an internally resonant NNM (3:1 internal resonance) of system (1.2).

However, these two limitations can be circumvented. Firstly, as shown in Section 1.3.2 and experimentally observed in Chapter 5, the damped dynamics can often be interpreted based on the topological structure and bifurcations of the NNMs of the underlying undamped system [62, 72, 153]. We also note that, due to the lack of knowledge of damping mechanisms, engineering design in industry is often based on the conservative system, and this even for linear vibrating structures. Secondly, realizing that the motion is still periodic in the presence of internal resonances, Rosenberg's definition of an NNM can be extended to *a (non-necessarily synchronous) periodic motion of the conservative system* (1.1). This extended definition is particularly attractive when targeting a numerical computation of the NNMs. As evidenced in Chapter 2, it enables the nonlinear modes to be effectively computed using algorithms for the continuation of periodic solutions, which are really quite sophisticated and advanced. This NNM definition is considered throughout the present dissertation.

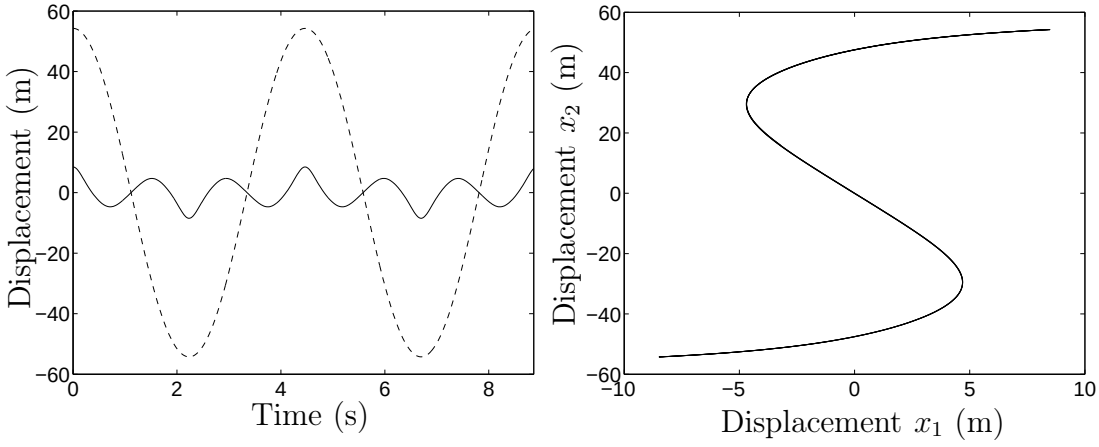

Figure 1.7: Internally resonant NNM of system (1.2) (3:1 internal resonance; $[x_1(0)\ x_2(0)\ \dot{x}_1(0)\ \dot{x}_2(0)] = [8.476\ 54.263\ 0\ 0]$). Left plot: time series (——: $x_1(t)$; − − −: $x_2(t)$); right plot: configuration space.

1.1.2 Fundamental Properties

NNMs have intrinsic properties that are fundamentally different from those of LNMs. They are reviewed and illustrated in what follows.

Frequency-Energy Dependence

One typical dynamical feature of nonlinear systems is the frequency-energy dependence of their oscillations. One important consequence is that the frequency response functions (FRFs) of nonlinear systems are no longer invariant. For illustration, the FRFs of system

$$\begin{aligned} \ddot{x}_1 + (0.02\dot{x}_1 - 0.01\dot{x}_2) + (2x_1 - x_2) + 0.5\,x_1^3 &= F\cos\omega t \\ \ddot{x}_2 + (0.02\dot{x}_2 - 0.01\dot{x}_1) + (2x_2 - x_1) &= 0 \end{aligned} \tag{1.4}$$

are depicted in Figures 1.8 and 1.9 for external excitation F varying between 0.002 N and 0.2 N.

The modal curves and frequencies of oscillation of NNMs also depend on the total energy in the system. In contrast to linear theory, this energy dependence prevents the direct separation of space and time in the governing equations of motion, which complicates the analytical calculation of the NNMs.

Returning to the undamped system (1.2), Figure 1.10 shows the time series, the configuration space, the power spectral density (PSD) and two-dimensional projections of the phase space of three in-phase NNM motions of increasing energies. The NNM motion at low energy resembles that of the in-phase LNM of the underlying linear system (1.3). The modal curve is a straight line, there is one main harmonic component in the system response, and the motion in phase space is a circle. For the motion at moderate energy, the NNM motion is now a curve, and the presence of two harmonic components can be detected. A clear departure from the LNM (harmonic) motion is observed. At high energy, this is even more enhanced. For instance, the motion in phase space is a strongly deformed ellipse. When moving from the low- to the high-energy NNM, the period of the motion decreases from 6.28 s to 4.755 s. This is due to the hardening characteristic of the cubic spring. Another noticeable characteristic of the NNMs is that the modes at higher energies are not the geometric continuation of those at lower energies. For illustration, Figure 1.11 superposes the three in-phase NNM motions in the configuration space.

To further illustrate the frequency-energy dependence of the NNMs, the harmonic balance method can be applied to system (1.2). This approximate method expresses the periodic motion of a system by means of a finite Fourier series [95]. For simplicity, a series with a single harmonic component is considered

$$x_1(t) = A\cos\omega t, \quad x_2(t) = B\cos\omega t \tag{1.5}$$

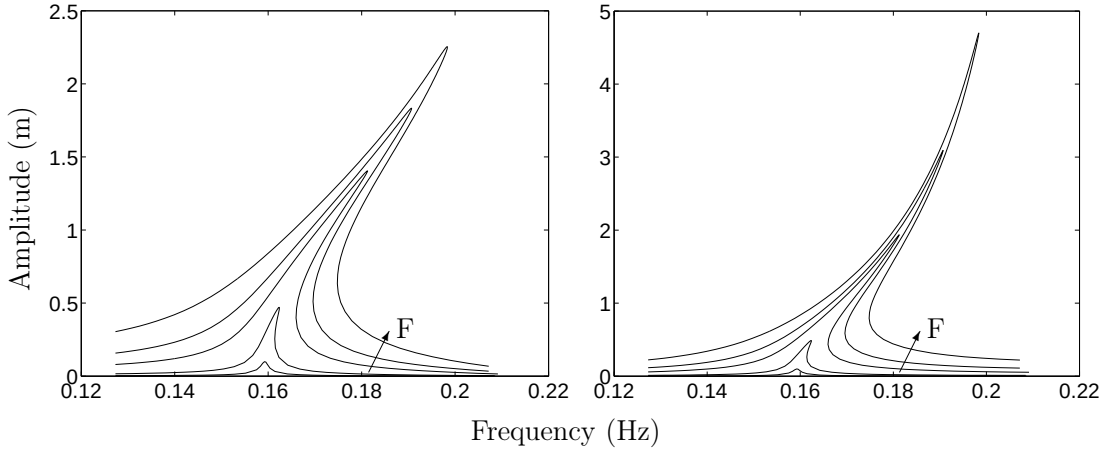

Figure 1.8: Nonlinear frequency response functions of system (1.4) close to the first resonant frequency (5 different forcing amplitudes F: 0.002N, 0.01N, 0.05N, 0.1N, 0.2N). Left plot: x_1; right plot: x_2.

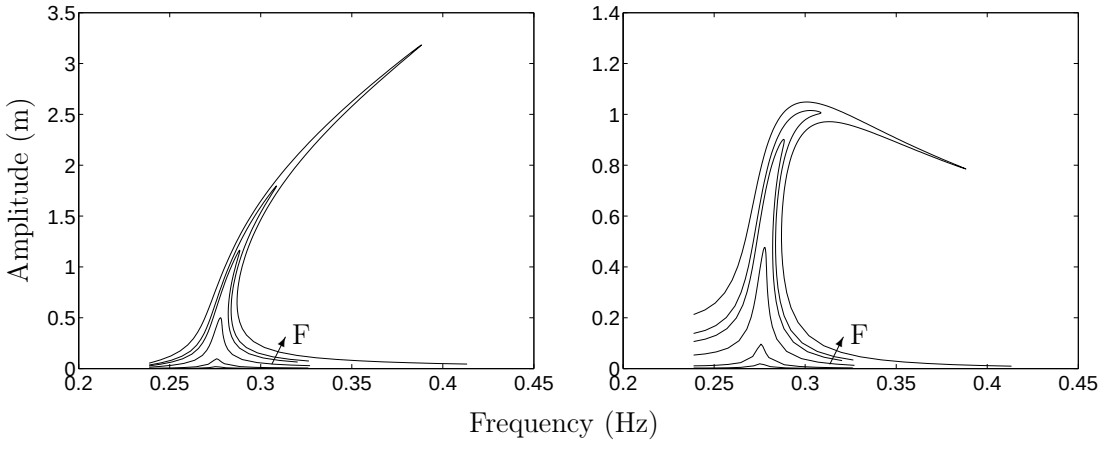

Figure 1.9: Nonlinear frequency response functions of system (1.4) close to the second resonant frequency (5 different forcing amplitudes F: 0.002N, 0.01N, 0.05N, 0.1N, 0.2N). Left plot: x_1; right plot: x_2.

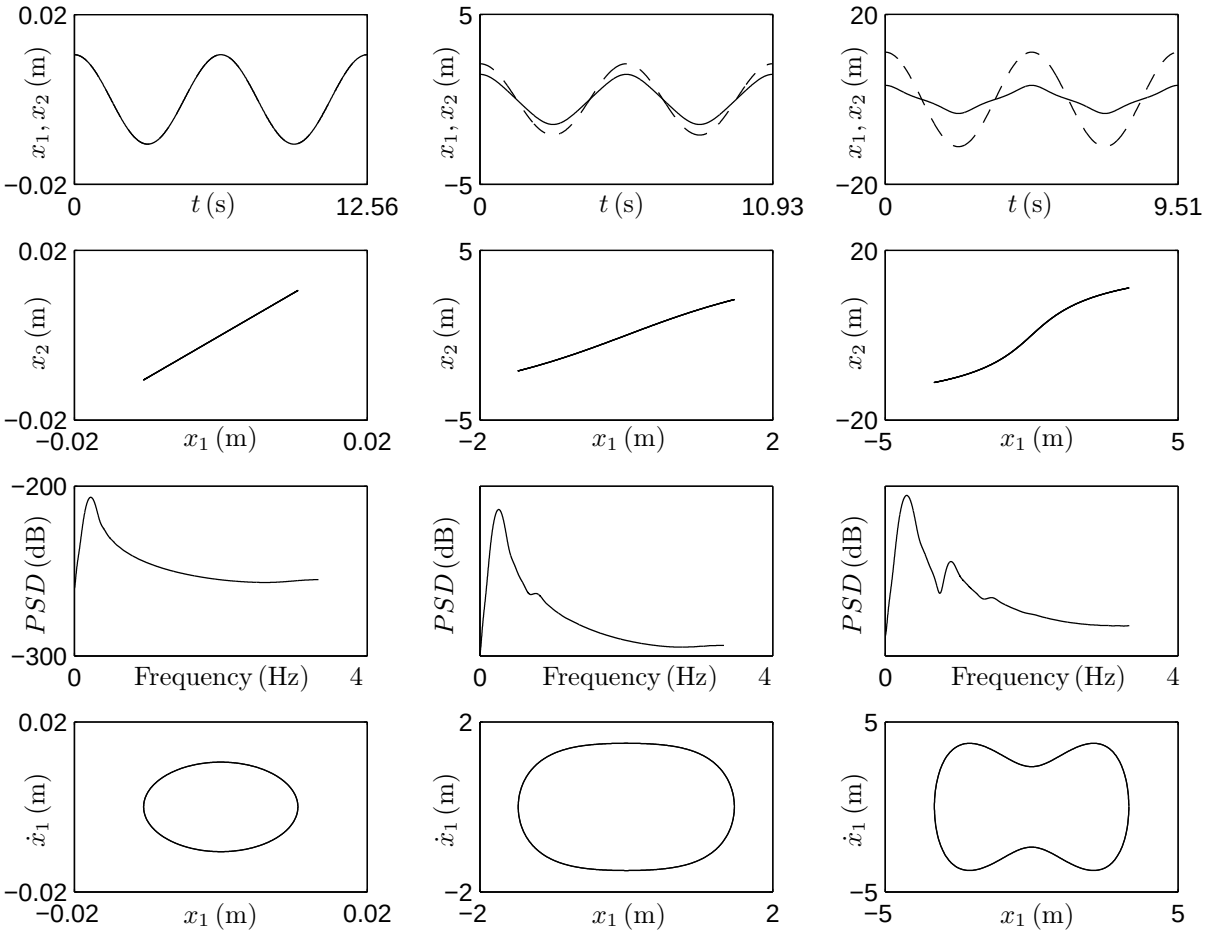

Figure 1.10: Frequency-energy dependence of NNMs. From left to right: low- ($[x_1(0)\ x_2(0)\ \dot{x}_1(0)\ \dot{x}_2(0)] = [0.105\ 0.105\ 0\ 0]$), moderate- ($[x_1(0)\ x_2(0)\ \dot{x}_1(0)\ \dot{x}_2(0)] = [1.476\ 2.100\ 0\ 0]$) and high- ($[x_1(0)\ x_2(0)\ \dot{x}_1(0)\ \dot{x}_2(0)] = [3.319\ 11.134\ 0\ 0]$) energy in-phase NNM motions of system (1.2). From top to bottom: time series (——: $x_1(t)$; $- - -$: $x_2(t)$); configuration space; power spectral density of $x_1(t)$; two-dimensional projections of the phase space.

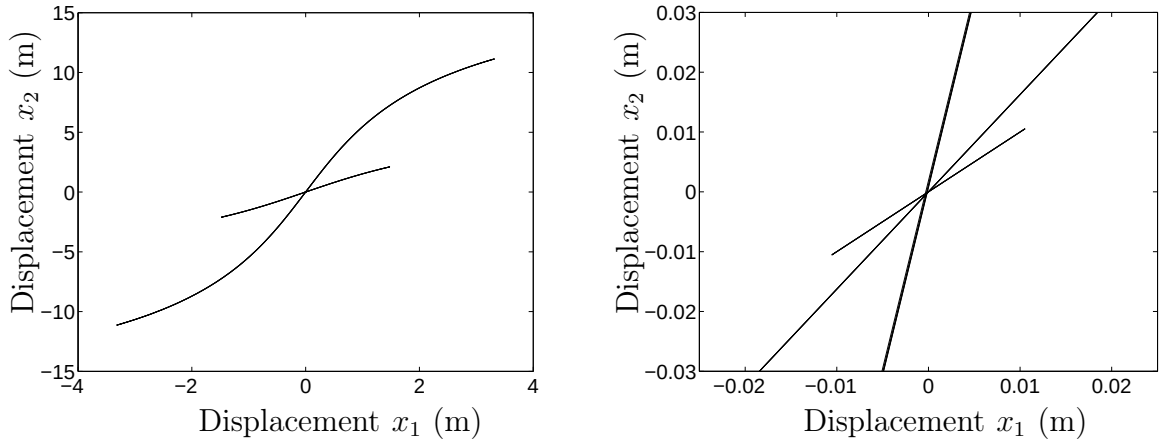

Figure 1.11: Superposition of low-, moderate- and high-energy NNM motions of system (1.2) in the configuration space. The right plot is a close-up near the origin of the left plot.

This *ansatz* is plugged into the equations of motion (1.2). Expanding $\cos^3 \omega t$ in terms of $\cos \omega t$ and $\cos 3\omega t$, and balancing all the coefficients of the $\cos \omega t$ terms yields

$$\begin{aligned} -A\omega^2 + (2A - B) + 0.5\,\frac{3A^3}{4} &= 0 \\ -B\omega^2 + (2B - A) &= 0 \end{aligned} \tag{1.6}$$

Analytic approximate expressions for coefficients A and B are then readily obtained

$$A = \pm\sqrt{\frac{8(\omega^2 - 3)(\omega^2 - 1)}{3(\omega^2 - 2)}} \tag{1.7}$$

$$B = \frac{A}{2 - \omega^2} \tag{1.8}$$

The square root exists in the two frequency intervals

$$\omega_1 \in [1, \sqrt{2}[\quad \text{and} \quad \omega_2 \in [\sqrt{3}, +\infty[\tag{1.9}$$

noting that $\omega = 1\,\text{rad/s}$ and $\omega = \sqrt{3}\,\text{rad/s}$ are the two natural frequencies of the underlying linear system (1.3). In the first (second) frequency interval, B has the same (opposite) sign as A; an in-phase (out-of-phase) NNM motion is observed for initial conditions $[x_1(0)\ x_2(0)\ \dot{x}_1(0)\ \dot{x}_2(0)] = [A\ B\ 0\ 0]$.

The (conserved) total energy during the free response of system (1.2) is

$$\begin{aligned} \text{Total Energy} &= \text{Kinetic Energy} + \text{Potential Energy} \\ &= \frac{A^2}{2} + \frac{(B - A)^2}{2} + \frac{B^2}{2} + 0.5\,\frac{A^4}{4} \end{aligned} \tag{1.10}$$

which, according to Equations (1.7) and (1.8), demonstrates the frequency-energy dependence of NNM motions.

An appropriate graphical depiction of the NNMs is key to their exploitation. The usual representation in the literature is to plot the motion amplitude at a particular DOF as a function of frequency. Due to the frequency-energy dependence, we believe that the representation of NNMs in a *frequency-energy plot* (FEP) is particularly convenient [62, 72]. An NNM motion is represented by a point in the FEP, which is drawn at a frequency corresponding to the minimal period of the periodic motion and at an energy equal to the conserved total energy during the motion. A branch, represented by a solid line, is a family of NNM motions possessing the same qualitative features (e.g., the in-phase NNM motions of a 2DOF system).

As a point of comparison, the FEP of the underlying linear system (1.3) is shown in Figure 1.12. Because the natural frequencies do not depend on energy, this FEP comprises two horizontal lines at the two resonant frequencies of the system. The LNM motions represented in the configuration space are inset and are obviously unaltered by the energy level.

The FEP of the nonlinear system (1.2) was computed using the method proposed in Chapter 2 and is shown in Figure 1.13. The modal curves (i.e., the NNM motions in the configuration space) are inset. The backbone of the plot is formed by two branches, which represent in-phase ($S11+$) and out-of-phase ($S11-$) synchronous NNMs. These fundamental NNMs are the direct nonlinear extension of the corresponding LNMs. The letter S refers to symmetric periodic solutions for which the displacements and velocities of the system at half period are equal but with an opposite sign to those at time $t = 0$. As shown in the next section, unsymmetric periodic solutions may also be encountered and are denoted by a letter U. The indices in the notations are used to mention that the two masses vibrate with the same dominant frequency. The FEP clearly shows that the nonlinear modal parameters have a strong dependence on the total energy in the system:

1. The frequency of both the in-phase and out-of-phase NNMs increases with the energy level, which reveals the hardening characteristic of the system.

2. The modal curves change for increasing energies. The in-phase NNM tends to localize to the second DOF (i.e., it resembles a vertical curve), whereas the out-of-phase NNM localizes to the first DOF (i.e., it resembles an horizontal curve). This localization property is a key feature of nonlinear systems. It is discussed extensively in [154] and exploited for vibration mitigation in [62, 72, 73, 150].

The comparison between Figures 1.12 and 1.13 also reveals that NNMs have a clear and simple conceptual relation to the LNMs.

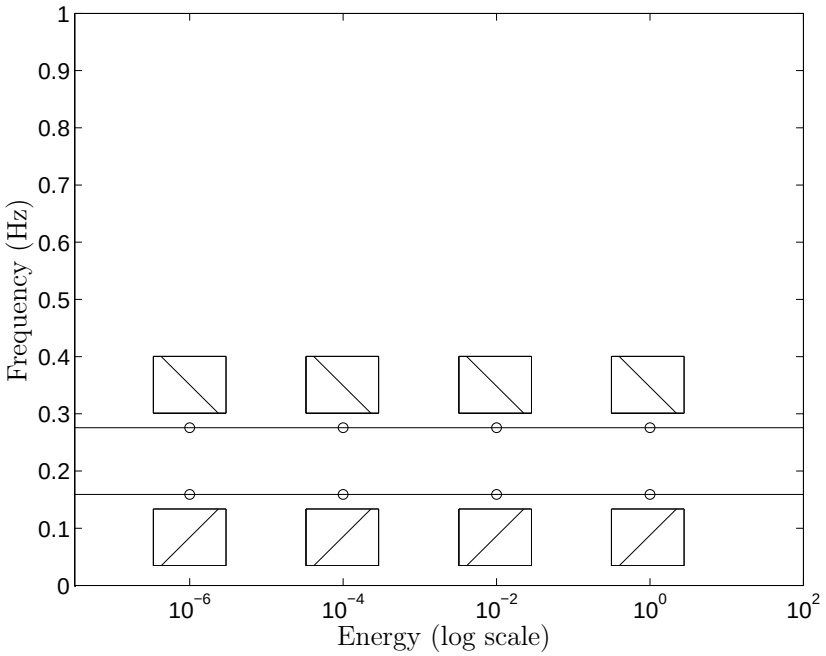

Figure 1.12: Frequency-energy plot of system (1.3). LNM motions depicted in the configuration space are inset.

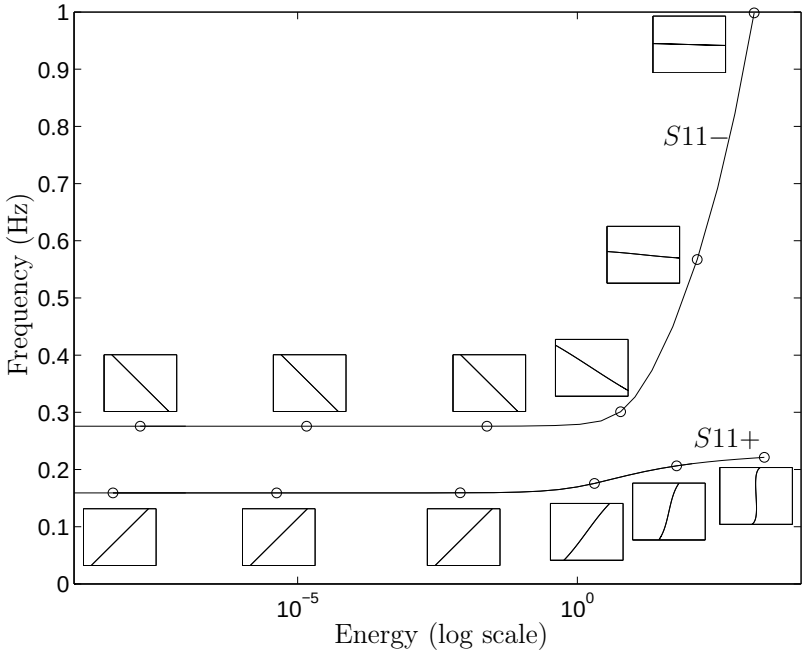

Figure 1.13: Frequency-energy plot of system (1.2). NNM motions depicted in the configuration space are inset. The horizontal and vertical axes in these plots are the displacements of the first and second DOFs, respectively; the aspect ratio is set so that increments on the horizontal and vertical axes are equal in size to indicate whether or not the motion is localized to a particular DOF.

Modal Interactions — Internally Resonant Nonlinear Normal Modes

Another salient feature of nonlinear systems is that NNMs may interact during a general motion of the system. Nonlinear modal interactions have been studied extensively in the literature (see, e.g., the monograph [92]). A case of particular interest is when the linear natural frequencies are commensurate or nearly commensurate [16, 57, 66, 70]. An energy exchange between the different modes involved may therefore be observed during the internal resonance. For instance, exciting a high-frequency mode may produce a large-amplitude response in a low-frequency mode. Vibration absorbers exploiting these energy transfers have been studied in [99].

Internally resonant NNMs, as opposed to fundamental NNMs, have no counterpart in linear systems and are generated through bifurcations. Considering system (1.2) and according to the discussion in the previous section, the FEP in Figure 1.13 does not seem to feature internally resonant NNMs. However, when carrying out the NNM computation at higher energy levels, Figure 1.14 shows that another branch of periodic solutions, termed a tongue, emanates from the backbone branch $S11+$. On this tongue, denoted $S31$, there is a 3:1 internal resonance between the in-phase and out-of-phase NNMs.

Surprisingly, the ratio of the linear natural frequencies of system (1.2) is $\sqrt{3}$. Due to energy dependence, a 3:1 ratio between the two frequencies can still be realized, because the frequency of the in-phase NNM increases less rapidly than that of the out-of-phase NNM. This clearly shows that *NNMs can be internally resonant without necessarily having commensurate linear natural frequencies*, a feature that is rarely discussed in the literature [78, 79]. This also underlines that important nonlinear phenomena can be missed when resorting to perturbation techniques, which are limited to small-amplitude motions.

To better illustrate the resonance mechanism, the branch $S11-$ is represented in the FEP of Figure 1.15 at the third of its frequency. This is relevant, because a periodic solution of period T is also periodic with period $3T$, and the resulting branch is therefore denoted $S33-$. It turns out that a smooth transition from $S11+$ to $S33-$ occurs on tongue $S31$. This transition is also depicted in Figure 1.16 where the evolution of the configuration space and of the Fourier coefficients is shown for several points on $S31$ or in its vicinity. Starting from NNM (a), an in-phase motion characterized by two perceptible harmonic components is observed. From (a) to (d), the relative importance of the third harmonics grows, as clearly confirmed by the motion in the configuration space. Moving from (d) to (e) corresponds to a drastic qualitative change in the dynamics. Firstly, the first harmonics has completely disappeared for both oscillators. Secondly, the signs of the coefficients of the third harmonics are opposite. Overall, this means that an out-of-phase motion with a three times as large frequency is realized. Eventually, through a 3:1 internal resonance, the motion ends up on $S33-$ or, equivalently, on $S11-$. From (f) to (h), the relative importance of the third harmonics diminishes, and a motion qualitatively similar to that at (a) is observed. However, the configuration space of NNM (h) reveals the presence of a fifth harmonics, which is a precursor to the gradual development of tongue $S51$.

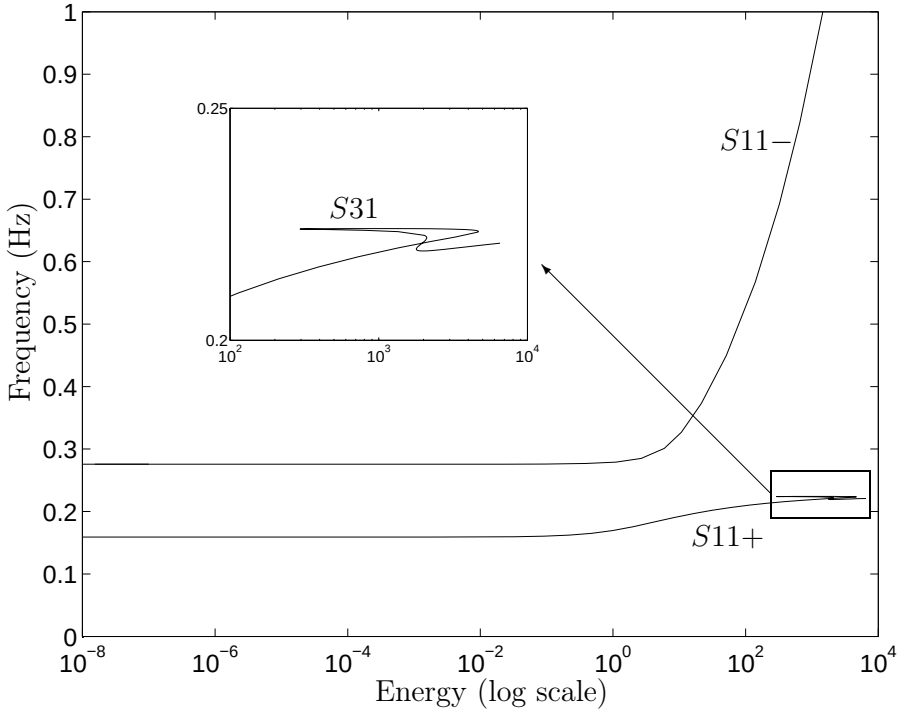

Figure 1.14: Frequency-energy plot of system (1.2) featuring a 3:1 internal resonance between the in-phase and out-of-phase NNMs.

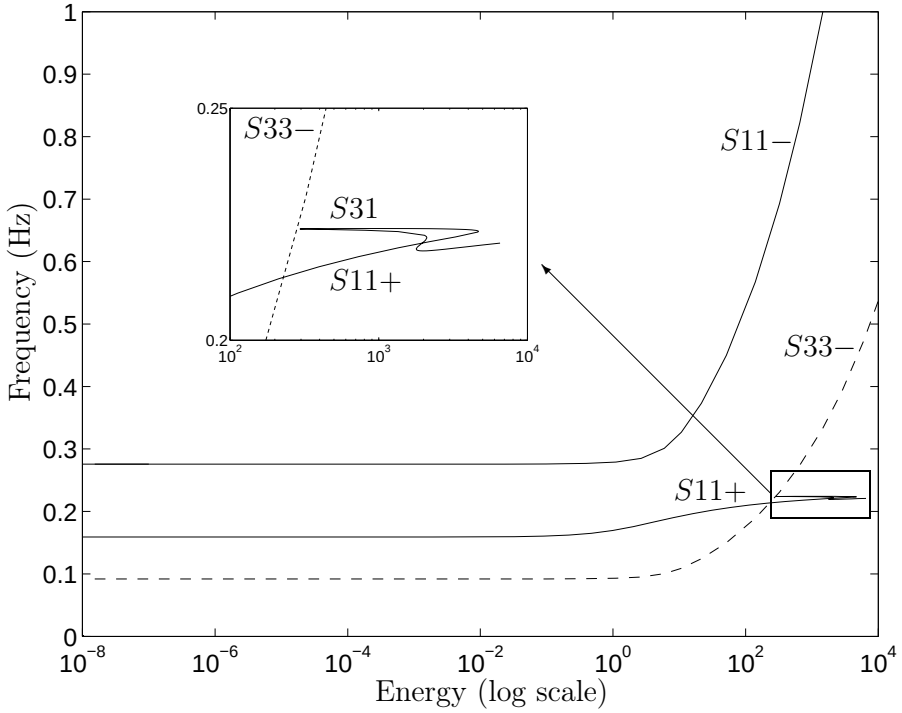

Figure 1.15: Frequency-energy plot of system (1.2). − − −: $S33-$, that is $S11-$ represented at the third of its dominant frequency.

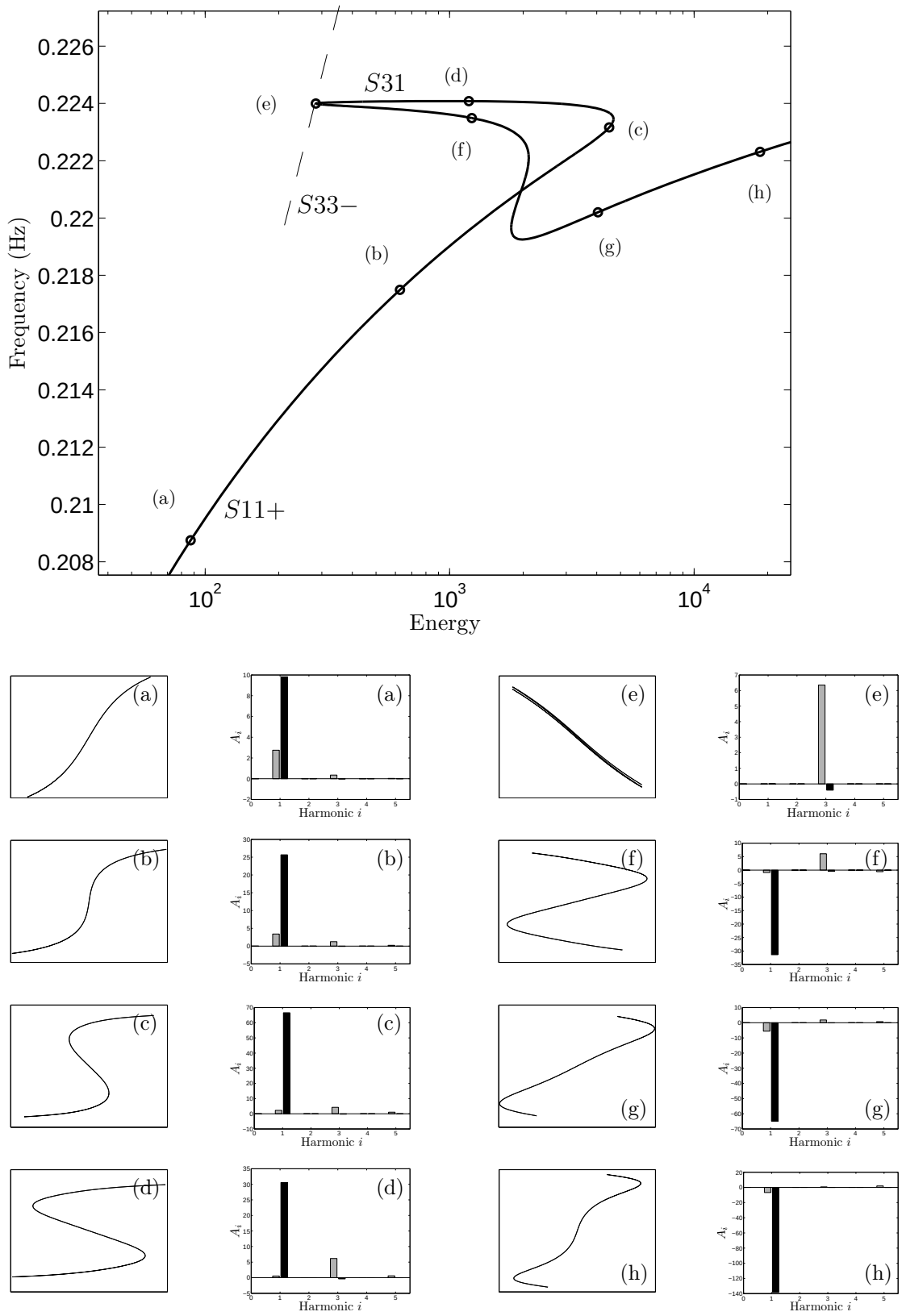

Figure 1.16: Internally resonant NNMs (3:1 resonance) of system (1.2). Top plot: close-up of the tongue $S31$ in the frequency-energy plot. Bottom plots: configuration space (horizontal axis: x_1; vertical axis: x_2) and Fourier coefficients of a series containing cosine terms only (grey: x_1; black: x_2).

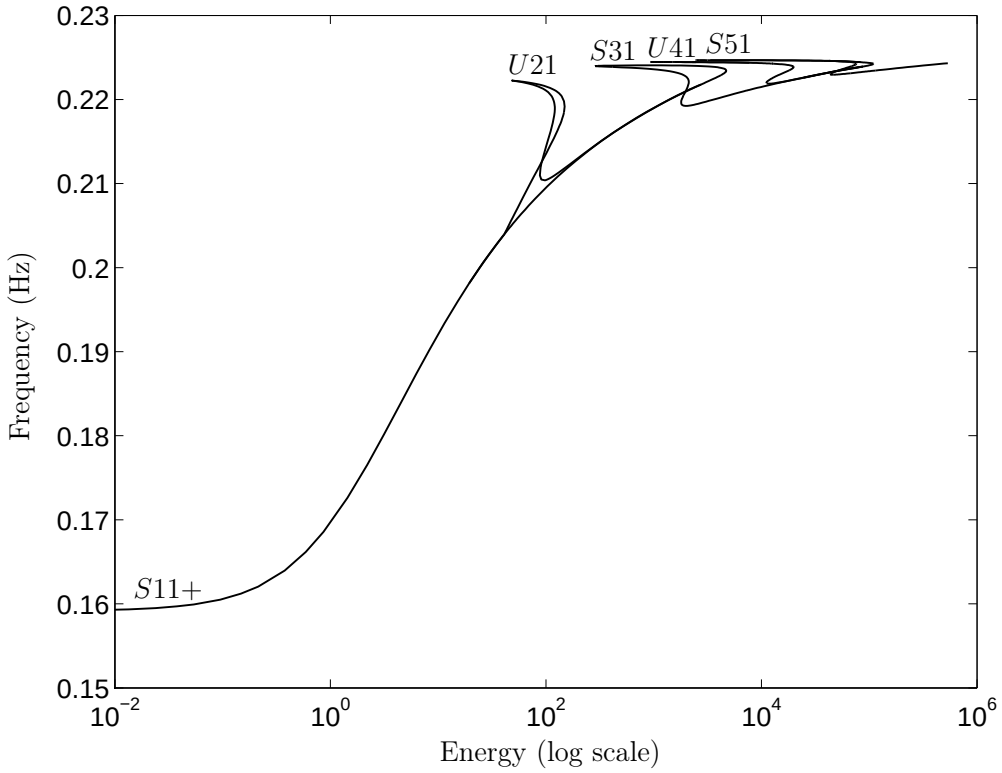

Figure 1.17: Close-up of $S11+$ of system (1.2) at higher energy levels.

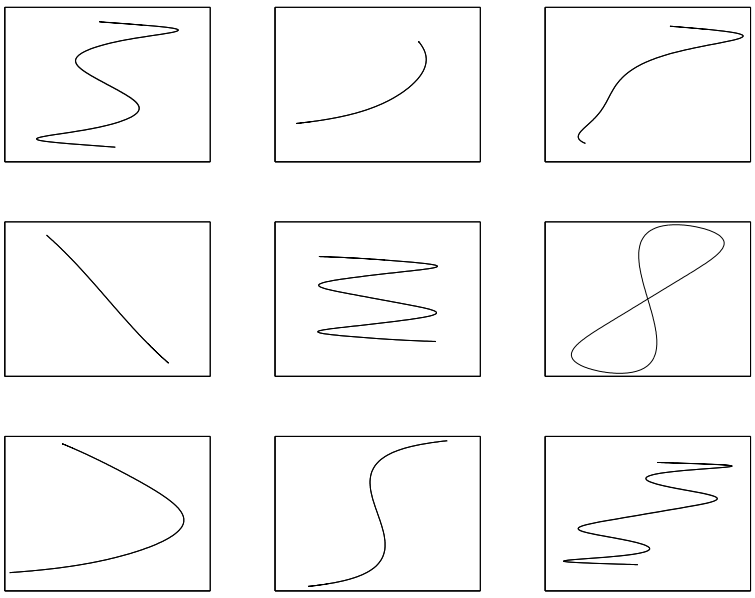

Figure 1.18: A few representative NNMs of system (1.2) in the configuration space (horizontal axis: x_1; vertical axis: x_2).

This indicates that other resonance scenarios exist in this seemingly simple system. The frequency of the out-of-phase NNM motions on $S11-$ steadily increases for increasing energies, whereas the NNM motions on $S11+$ have their frequency asymptotically approaching a value close to $\sqrt{3}\,\mathrm{rad/s}$. Following this reasoning, we expect the existence of a countable infinity of internal resonance cases (e.g., 2:1, 4:1, 5:1, etc.). To confirm this conjecture, additional tongues have been computed numerically and are represented in Figure 1.17. These tongues emanate from $S11+$ and coalesce into $S11-$ following a mechanism similar to that described above (Figure 1.16). To illustrate the rich dynamics, a few representative NNMs of system (1.2) are depicted in Figure 1.18. Such a complex dynamics was first observed in [72] for a system with an essential nonlinearity. It is interesting that this can also be reproduced for more generic nonlinear systems.

Mode Bifurcations and Stability

A third fundamental property of NNMs is that their number may exceed the number of DOFs of the system. Due to mode bifurcations, not all NNMs can be regarded as nonlinear continuation of normal modes of linear systems [154, 156, 157]. Internally resonant NNMs are one example. Another possible example corresponds to the NNM bifurcations of the system

$$\begin{aligned} \ddot{x}_1 + x_1 + x_1^3 + K(x_1 - x_2)^3 &= 0 \\ \ddot{x}_2 + x_2 + x_2^3 + K(x_2 - x_1)^3 &= 0 \end{aligned} \tag{1.11}$$

for variations of the coupling spring K [25]. This system possesses similar NNMs that obey to the relation $x_2(t) = cx_1(t)$. Eliminating x_2 from Equations (1.11) yields

$$\begin{aligned} \ddot{x}_1 + x_1 + \left[1 + K(1-c)^3\right] x_1^3 &= 0 \\ \ddot{x}_1 + x_1 - \frac{1}{c}\left[K(1-c)^3 + c^3\right] x_1^3 &= 0 \end{aligned} \tag{1.12}$$

Because both equations must lead to the same solution, it follows

$$K(1+c)(c-1)^3 = c(1-c^2), \quad c \neq 0 \tag{1.13}$$

Equation (1.13) means that system (1.11) always possesses two modes characterized by $c = \pm 1$ that are direct extension of the LNMs. However, this system can possess two additional similar NNMs that cannot be captured using linearization procedures. At $K = 0.25$, these NNMs bifurcate from the out-of-phase mode, as shown in Figure 1.19.

Another important characteristic of NNMs is that they can be stable or unstable, which is in contrast to linear theory where all modes are neutrally stable. In this context, instability means that small perturbations of the initial conditions that generate the NNM motion lead to the elimination of the mode oscillation. Therefore, unstable NNMs are not physically realizable. The NNM stability analysis can be performed numerically or analytically. In Figure 1.20, stability is computed numerically through the eigenvalues of

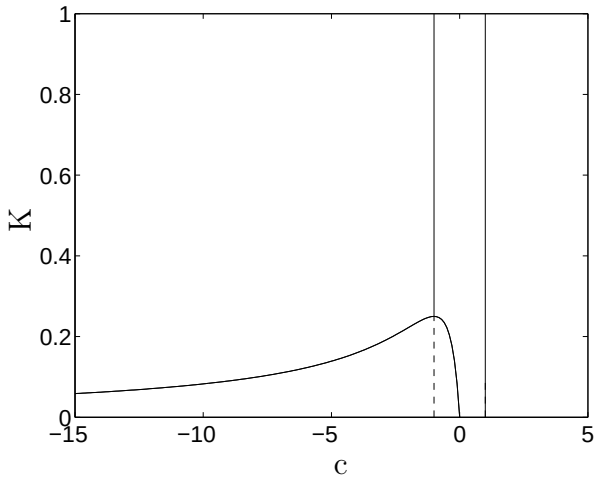

Figure 1.19: NNM bifurcations of system (1.11) [25] (——: stable NNMs; − − −: unstable NNMs).

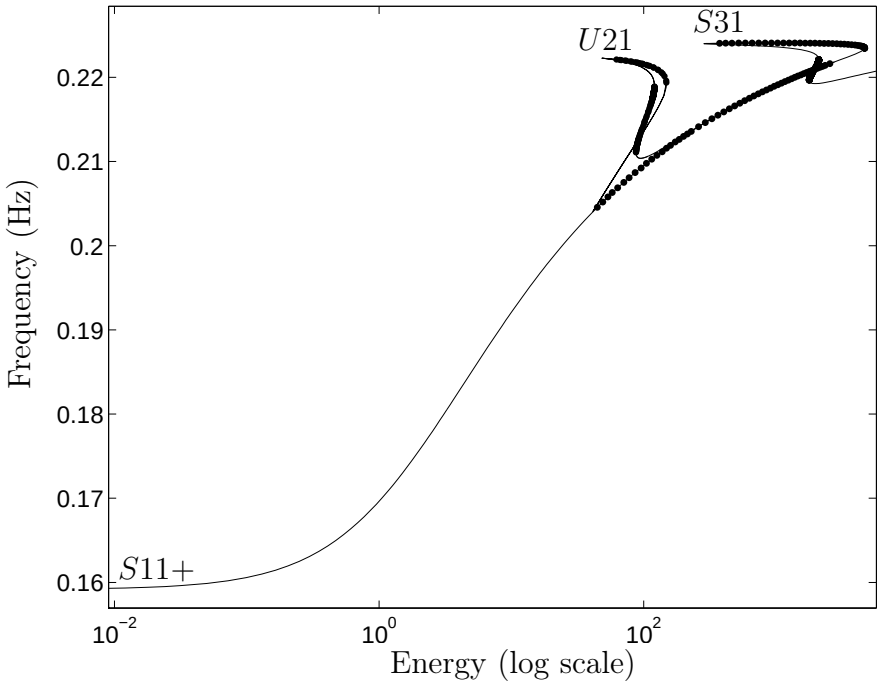

Figure 1.20: Close-up of $S11+$ of system (1.2) with stability results (——: stable NNMs; • • •: unstable NNMs).

the monodromy matrix. In other studies, analytical results are obtained through Floquet theory after adding small perturbations to the periodic solutions. For a detailed stability analysis of the NNMs, the reader can refer to [25, 65, 103, 118, 154].

Bifurcations and stability are interrelated concepts, because a change in stability occurs through a bifurcation. For instance, the bifurcation in system (1.11) generates a pair of stable/unstable NNMs (Figure 1.19). Returning to system (1.2), another illustration of NNM stability is shown in the FEP of Figure 1.20. When the tongue $U21$ bifurcates from $S11+$, the NNMs on this latter branch lose stability. A detailed description of this tongue and the related dynamical mechanisms (e.g., symmetry-breaking bifurcation) is beyond the scope of this work. This figure also shows that stability can be lost when a turning point is encountered.

1.2 Nonlinear Normal Modes: How to Compute Them ?

Different methods for computing NNMs of discrete and continuous systems are briefly described in this section. They are classified in two categories, according to whether the computation relies on analytical or numerical methods. This discussion is by no means a comprehensive overview of the past and current approaches and focuses on the free response of nonlinear vibrating systems. There is no attempt to summarize the methods dealing with the forced response case.

1.2.1 Analytical Techniques

Rosenberg was the first to develop constructive techniques for computing NNMs of discrete conservative oscillators. Rand obtained explicit approximate expressions for modal curves in 2DOF systems by applying a perturbation method to a modal equation [115]. Manevitch and Mikhlin reduced the problem of computing nonsimilar NNMs to a set of singular boundary value problems, which were then solved using power series expansions [83] (see below). The book by Vakakis et al. [154] summarizes the developments until the 1990s.

The early 1990s witnessed a resurgence of interest in the NNMs with the works of Vakakis [25, 65, 146, 148] and Shaw and Pierre [127–130]. Simple discrete systems were first studied [127, 129, 148], but the generalization to continuous systems [65, 130] soon followed. For continuous systems, two main approaches exist in the literature. The first approach is to study directly the original partial differential equations [65, 130]. An alternative method is to discretize the governing nonlinear partial differential equations into an infinite set of ordinary differential equations that is truncated to a finite number of equations [128]. The two alternatives are compared in [17] using the invariant manifold approach.

An Energy-Based Formulation

This formulation relies on Rosenberg's work [123] and expresses an NNM as a modal curve in the configuration space. It was further developed by Manevitch and Mikhlin for discrete conservative oscillators [83] and exploited in a few other studies [148, 154]. To illustrate the method, it is applied to system (1.2)

$$\begin{aligned} \ddot{x}_1 + (2x_1 - x_2) + 0.5\,x_1^3 &= 0 \\ \ddot{x}_2 + (2x_2 - x_1) &= 0 \end{aligned} \tag{1.14}$$

When the system vibrates along an NNM, the displacement x_2 is linked to x_1 through the expression of the modal curve $\hat{x}_2$

$$x_2 = \hat{x}_2(x_1) \tag{1.15}$$

The objective of the method is to eliminate the time derivatives from the equations of motion (1.14). To compute the second time derivative of x_2, relation (1.15) is differentiated twice using the chain rule

$$\ddot{x}_2 = \hat{x}_2''\dot{x}_1^2 + \hat{x}_2'\ddot{x}_1 \tag{1.16}$$

where prime denotes differentiation with respect to x_1. This expression involves the second time derivative of x_1, which is readily obtained from the equations of motion

$$\ddot{x}_1 = -2x_1 + \hat{x}_2 - 0.5x_1^3 \tag{1.17}$$

It then remains to compute the first time derivative of x_1 appearing in Equation (1.16). To this end, a first integral of motion expressing explicitly the conservation of energy during the motion is written by multiplying Equation (1.17) by $\dot{x}_1$ and integrating

$$\dot{x}_1^2 = 2\int_0^{\dot{x}_1} \dot{x}_1\,\mathrm{d}\dot{x}_1 = -2\int_{X_1}^{x_1} \left[2u - \hat{x}_2(u) + 0.5u^3\right]\,\mathrm{d}u \tag{1.18}$$

where X_1 is the maximum amplitude attained by x_1; i.e., when $\dot{x}_1 = 0$. The derivatives are substituted into the second of Equations (1.14), which yields the equation governing the modal curve:

$$\hat{x}_2''\left\{-2\int_{X_1}^{x_1}\left[2u - \hat{x}_2(u) + 0.5u^3\right]\,\mathrm{d}u\right\} + \hat{x}_2'\left[-2x_1 + \hat{x}_2 - 0.5x_1^3\right] + (2\hat{x}_2 - x_1) = 0 \tag{1.19}$$

Because the coefficient of the highest derivative vanishes when $x_1 = X_1$, this functional equation is singular at the maximum equipotential surface. It must therefore be supplemented by a boundary condition

$$\left\{\hat{x}_2'\left[-2x_1 + \hat{x}_2 - 0.5x_1^3\right] + (2\hat{x}_2 - x_1)\right\}_{x_1 = X_1} = 0 \tag{1.20}$$

which expresses that the nonlinear mode intersects orthogonally the maximum equipotential surface in the configuration space. Equation (1.19) does not depend on the time variable, and its solution is amenable to a power series expansion:

$$\hat{x}_2(x_1) = \hat{x}_2^{(0)}(x_1) + \epsilon\hat{x}_2^{(1)}(x_1) + \epsilon^2\hat{x}_2^{(2)}(x_1) + O(\epsilon^3) \tag{1.21}$$

This formulation was extended to undamped continuous systems in [65]. The displacement of any point of the system is expressed in terms of a single reference displacement $x_0(t) = x(s_0, t)$ by the functional relation

$$x(s,t) = X\left[s, x_0(t)\right] \tag{1.22}$$

where s is the spatial coordinate, and X is a modal function characterizing the considered NNM. Then, an integral equation expressing the conservation of energy during the motion is used in conjunction with Equation (1.22) to eliminate the time derivatives from the equations of motion. Eventually, the equation governing the modal function X is obtained and is solved using power series.

In the presence of internal resonances, the folding of the NNMs in the configuration space may result in multivalued relationship among the various coordinates (see Figure 1.7). This has been nicely addressed in [66] by considering NNMs in an appropriately defined modal space.

The Invariant Manifold Approach

The invariant manifold approach [127–130] is similar in spirit to the energy-based formulation. The difference with the previous approach is that a pair of state variables (i.e., both the displacement and the velocity) are chosen as master coordinates, the remaining variables being functionally related to the chosen pair:

$$x(s,t) = X_1\left[s, x_0(t), \dot{x}_0(t)\right] \quad \text{and} \quad \dot{x}(s,t) = X_2\left[s, x_0(t), \dot{x}_0(t)\right] \tag{1.23}$$

These relations define a two-dimensional invariant manifold in phase space. By taking the time derivative of these constraint equations and using the chain rule differentiation, the explicit time dependence from the equations of motion can be eliminated. Eventually, this yields a set of partial differential equations governing the modal functions X_1 and X_2. These equations are as difficult to solve as the original problem, but the solution can be approximated using power series. In summary, this is a six-step procedure:

1. Choose master coordinates $x_0(t), \dot{x}_0(t)$;
2. Express slaved coordinates as $X_1\left[s, x_0(t), \dot{x}_0(t)\right]$, $X_2\left[s, x_0(t), \dot{x}_0(t)\right]$;
3. Use the invariant manifold technique to eliminate time dependence;
4. Approximate a local solution using polynomial expansion of X_1 and X_2 in terms of $x_0(t)$ and $\dot{x}_0(t)$;
5. Substitute expansions into time-independent partial differential equations governing the geometry of the manifold, and solve polynomial expansion of X_1 and X_2;

6. Replace the slaved coordinates with their expansions, thus eliminating them from the system.

For systems with internal resonances, a multi-mode invariant manifold is considered in [16] to account for the influence of several modes. For instance, when two modes are resonant, the master coordinates comprise two pairs of state variables, and the resulting invariant manifold is four-dimensional. The invariant manifold approach was also reformulated using a complex framework [96], which was then extended to systems with internal resonances [94].

The Multiple Scales Method

One perturbation method that has received considerable attention for NNM computation is the method of multiple scales [44, 69, 70, 80, 85, 96, 162]. Governing partial differential equations can be attacked directly (i.e., without spatial discretization) with this method. The first step is to introduce a small nondimensional parameter ϵ to indicate the smallness of the nonlinear terms. The solution is then sought in the form of an asymptotic expansion [95].

The underlying idea of the multiple scales method is to consider expansions in terms of multiple independent time scales, instead of a single independent variable t

$$x(s,t) = \epsilon x_1(s, T_0, T_1, T_2, ...) + \epsilon^2 x_2(s, T_0, T_1, T_2, ...) + ... \quad \text{with } T_i = \epsilon^i t \tag{1.24}$$

where T_0 is a time scale characterizing the fast motion of the system (i.e., the motion occurring at the dominant frequency of the NNM). Because the generic motion of a nonlinear system is not harmonic, other time scales are necessary to describe the motion; these are the slow time scales $T_1, T_2, ...$ An increasingly accurate approximation is therefore obtained as additional time scales enter in the analysis. The approximating functions $x_i(s, T_0, T_1, T_2, ...)$ are then determined after integration of linear differential equations for each order of ϵ, and imposition of solvability conditions, which correspond to the elimination of secular terms.

Other Approaches

The method of normal forms was first employed by Lamarque and Jézéquel [55] and Nayfeh [91] using a complex formulation. A real normal theory for NNM computation was then proposed in [144, 145] for conservative systems and in [142] for nonconservative systems. The philosophy of the method is to seek a nonlinear change of coordinates[1] that brings the equations of motion into the simplest possible form, termed the normal form

[1] To recover the linear results at small-amplitude motions, the applied coordinate transformations must be near-identity. As a result, the method can only be used in the neighborhood of an equilibrium point.

[51]. In other words, the objective of the method is to eliminate as many as possible of the nonlinear terms from the governing equations, which is similar in spirit to the decoupling of the equations of motion provided by the LNMs of a linear system. However, a complete decoupling of the equations is generally not possible for nonlinear systems, and only the invariance property can be enforced. Eventually, the computed normal form dictates the dynamics of the system on the invariant manifold.

Another technique that assumes that the NNM motion is periodic in time and approximates it by means of a finite Fourier series is the harmonic balance method; e.g.,

$$x(s,t) = \sum_{n=0}^{N} \phi_1^n(s) \cos n\omega t + \sum_{n=0}^{N} \phi_2^n(s) \sin n\omega t \tag{1.25}$$

By substituting this relation into the governing equations of motion and 'balancing the harmonics', the nonlinear modes can be computed by solving nonlinear boundary value problems for the ϕ^n [14, 20, 28, 53, 77, 101, 108, 139, 140]. Because analytical solutions are available in a limited number of cases (mostly when a single harmonic component is considered; see Section 1.1.2), numerical methods are often used to solve the resulting equations. The harmonic balance method can therefore be viewed as a semi-analytical technique.

A method similar in spirit to the harmonic balance method and to the Galerkin-based approach in [109] was introduced in [12, 13]. The most distinctive feature of this formulation is that the modal vector and the corresponding frequency depend on the amplitude but also on the total phase variable. The dynamics is defined by a differential equation, governing the total phase motion, from which the period of the oscillations is deduced. Moreover, complex nonlinear modes of nonconservative systems are calculated based on a generalized Fourier series in [71].

1.2.2 Numerical Techniques

Most existing constructive techniques for computing NNMs are based on asymptotic approaches. Despite that robust algorithms for the computation of isolated periodic orbits [59] and for the continuation of a family of orbits [35, 93, 126] have been developed, it is somewhat surprising that there have been very few attempts to compute NNMs using numerical methods [9, 19, 56, 72, 109, 133, 162].

One of the first approaches was proposed by Slater in [133]. Based on Rosenberg's definition, the procedure integrates directly the governing equations of motion over one period using numerical algorithms (e.g, Runge-Kutta and Newmark). It comprises two steps:

1. An isolated periodic solution corresponding to a specific energy level is computed by modifying iteratively the initial conditions governing the free response of the system. This is carried out using optimization algorithms that minimize a periodicity

condition (i.e., a cost function representing the lack of periodicity of the current iterate).

2. Low-energy modal curves and the corresponding periods of oscillation are first computed, taking the normal modes and natural frequencies of the underlying linear system as initial guesses. The energy is then gradually increased with the previously computed NNM as an initial guess for the next NNM.

This step-wise type of continuation of periodic solutions is called sequential continuation [93]. Similarly, shooting algorithms coupled with sequential continuation were considered in Lee et al. [61, 72] and Bajaj et al. [162, 163] to numerically solve the nonlinear boundary value problem that defines a family of NNM motions.

A more sophisticated continuation method is the so-called asymptotic-numerical method [27]. It is a semi-analytical technique that is based on a power series expansion of the unknowns parameterized by a control parameter. It is utilized to follow the NNM branches in conjunction with the harmonic balance method in [108] or with finite difference methods in [8, 9]. Another well-established method used for instance in the AUTO software is the pseudo-arclength continuation. It is the approach implemented for the NNM calculation in Chapter 2.

Based on the invariant manifold approach, Pesheck et al. [109, 111] developed a meaningful numerical extension of it. In the original formulation, the master variables are the position and velocity in Cartesian coordinates, and the solution is sought using a polynomial expansion. In the proposed Galerkin-based approach, an alternative set of coordinates is defined (i.e., the amplitude and phase of the considered mode), and the polynomial approach is replaced by a Galerkin method. Eventually, a set of nonlinear algebraic equations is obtained and solved using local optimization algorithms.

Finally, we note that computer implementation of both the multiple scales and the invariant manifold approach have been carried out in [85, 134] and applied to finite element models of planar frames and beams.

1.2.3 Assessment of the Different Methodologies

Analytical methodologies have the advantage that NNMs can be constructed symbolically, which is certainly useful for gaining insight into the dynamics and for performing parametric studies. Among other things, they clearly highlight the frequency-energy dependence of NNMs. The fundamental drawbacks of these techniques is that (i) they are quite analytically involved and require a careful treatment in the presence of internal resonances; (ii) the resultant dynamics are only accurate for small-amplitude motions; and (iii) the upper bound for these motions is not known a priori.

The energy-based formulation is an elegant approach, but, because it is based on symmetry

arguments, it requires that the nonlinearities be of odd order. It is also a priori limited to undamped systems. The invariant manifold approach does not present these limitations. However, though its basic definition allows for large-amplitude motions, the constructive technique, which relies on power series expansions, is limited to small motions. Regarding perturbation analysis (e.g., the multiple scales method), it can now be performed using symbolic manipulation programs, but their application to nonlinear systems with more than a few DOFs remains involved. Different analytical methods have been compared in [91, 163], and the results obtained were consistent. In [91], the author reports that the method of multiple scales is the simplest and involves the least algebra. Finally, we note that the harmonic balance method yields solutions which are generally valid over a much larger domain compared to the aforementioned methodologies. However, because analytic expressions of the resulting equations are available only in a limited number of cases, it should be regarded more as a numerical technique.

Analytical approaches may become inaccurate in the moderate to strongly nonlinear range of motion and are limited to systems with low dimensionality. Their utility for real-world structures is therefore questionable. In this context, numerical methods have certainly the potential to 'push the envelope' and to make nonlinear modal analysis more accessible to the practicing structural engineer. The key advantage of these methods is that they lend themselves fairly easily to strongly nonlinear systems with large-amplitude motions, which is nicely evidenced in [110, 111]. In addition, most of them provide an *exact* solution to the NNM calculation. Their fundamental drawback is that they rely on extensive numerical simulations and are still computationally intensive.

The Galerkin-based invariant manifold approach is one of the most effective techniques for building reduced-order models of nonlinear vibrating systems. It is truly versatile and can be applied to a large variety of nonlinear dynamic systems, including nonconservative, gyroscopic and piecewise-linear systems, with an accuracy controlled over the chosen amplitude range. One possible limitation is that the interpretation of the NNMs is complicated when multi-mode invariant manifolds, which are higher-dimensional surfaces, are computed.

On the contrary, a particularly appealing feature of the continuation of periodic solutions is that the resulting NNMs have a clear conceptual relation to the LNMs, with which practicing structural engineers are familiar (see Section 1.1.2). As discussed in Section 1.3.2, this makes it a promising technique for developing a practical nonlinear analog of modal analysis, which is well-established for linear systems. In this framework, the implementation of sequential continuation techniques is truly straightforward, and the calculations can be performed with limited user interaction. They represent the ideal starting point for the dynamicist not necessarily acquainted with the numerical calculation of the NNMs. However, their computational efficiency is limited, and they are likely to fail when a turning point or a bifurcation is encountered. Effective alternatives are those based on more sophisticated continuation techniques (e.g., the asymptotic-numerical method and the pseudo-arclength continuation). One limitation of the continuation of periodic solutions is that it is not clear how they can be extended to nonconservative systems.

Nevertheless, as shown in Section 1.3.2, the damped dynamics can be interpreted based on the topological structure and bifurcations of the NNMs of the underlying undamped system.

1.3 Nonlinear Normal Modes: Why Are They Useful ?

The objective of this section is to describe several applications where NNMs represent a useful framework for the structural dynamicist. Specifically, we highlight how useful the NNMs are for modal analysis and system identification and how they may be exploited in conjunction with time-frequency analysis in order to extend the existing linear methodologies [38]. Nonlinear model reduction and the study of localization phenomena are also discussed.

1.3.1 'Linear' Modal Analysis

Modal analysis and testing of linear mechanical structures have been developed over the past 40-50 years, and the techniques available today are mature and advanced [38]. While the common practice is to assume linear behavior, nonlinearity is a frequent occurrence in engineering applications and can drastically alter their behavior. In the presence of nonlinear phenomena, the structural dynamicist should therefore ask the question: *can I still use the linear modes ?* Obviously, the answer depends on the type of the nonlinearity and on the excitation level.

In this context, we believe that the computation of the NNMs and their representation in a FEP is a robust and accurate tool to decide whether or not the linear framework is still applicable. It can be used to determine which modes (and to what extent) are sensitive to the nonlinearity. Going back to Figure 1.13, it is clear that, until an energy of 10^{-1}, the mode shapes and natural frequencies are unaffected by the nonlinearity and can safely be used. Beyond this critical energy level, both the in-phase and out-of-phase modes show a significant departure from the LNMs and become dependent on the total energy in the system.

As another example, the FEP of system

$$\begin{aligned} \ddot{x}_1 + (2x_1 - x_2) &= 0 \\ \ddot{x}_2 + (2x_2 - x_1 - x_3) + 0.5\,x_2^3 &= 0 \\ \ddot{x}_3 + (2x_3 - x_2) &= 0 \end{aligned} \tag{1.26}$$

is depicted in Figure 1.21. The linear modal parameters remain unchanged until approximately an energy of 10^{-1}. Another interesting finding is that the nonlinearity has no influence whatsoever either on the frequency or on the mode shape of the second mode.

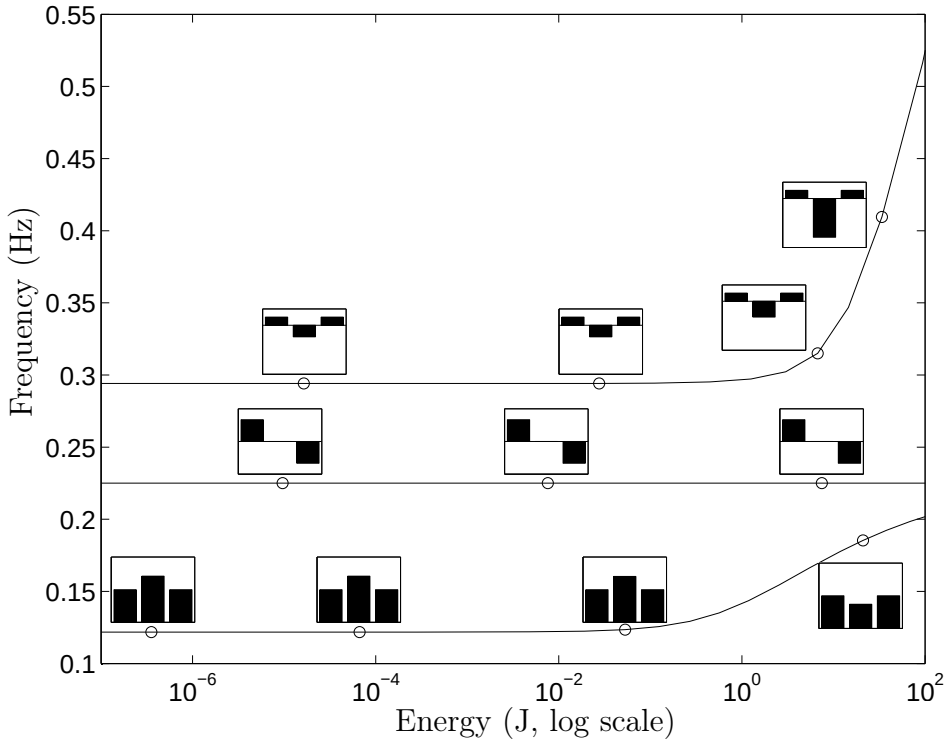

Figure 1.21: Frequency-energy plot of system (1.26). NNMs represented by bar graphs are inset; they are given in terms of the initial displacements that realize the periodic motion (with zero initial velocities assumed).

1.3.2 Nonlinear Modal Analysis

When it is certain that the system is excited in the nonlinear range, the linear framework should be abandoned in favor of nonlinear modal analysis. Any attempt to apply traditional linear analysis in this context results, at best, in a suboptimal design.

Considering again system (1.2) as a first example, its FEP in Figure 1.13 greatly helps to understand how the modal curves deform under the action of the nonlinearity. The in-phase NNM tends to localize to the second DOF, whereas the out-of-phase NNM localizes to the first DOF. Regarding the corresponding frequency of oscillation, both modes are characterized by a hardening behavior due to the presence of the cubic spring.

As a second example, a planar cantilever beam discretized by 20 finite elements and with a cubic spring at the free end is now considered (see Table 1.1 for the geometrical and mechanical properties). This models a real nonlinear beam that was used as a benchmark for nonlinear system identification during the European action COST F3 [141]. This structure is studied in detail in Chapters 4 and 5 where a more accurate modeling is considered. The first two modes are plotted in the FEPs of Figures 1.22 and 1.23, respectively. Considering the same energy level, the first modal shape seems somewhat more affected by the nonlinearity compared to the second modal shape. Their frequencies of os-

Length (m)	Width (m)	Thickness (m)	Young's modulus (N/m^2)	Density (kg/m^3)	Nonlinear coeff. (N/m^3)
0.7	0.014	0.014	2.05×10^{11}	7800	6×10^9

Table 1.1: Geometrical and mechanical properties of the planar cantilever beam.

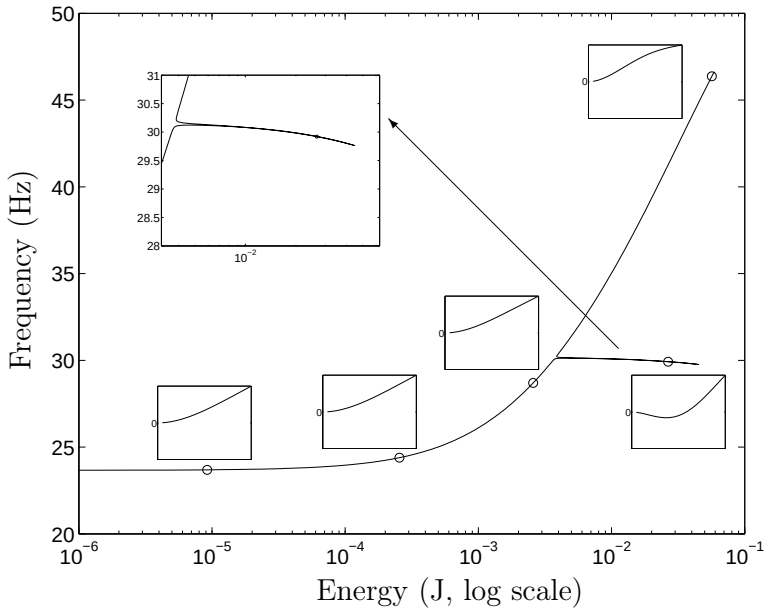

Figure 1.22: Frequency-energy plot of the cantilever beam; close-up of the first NNM.

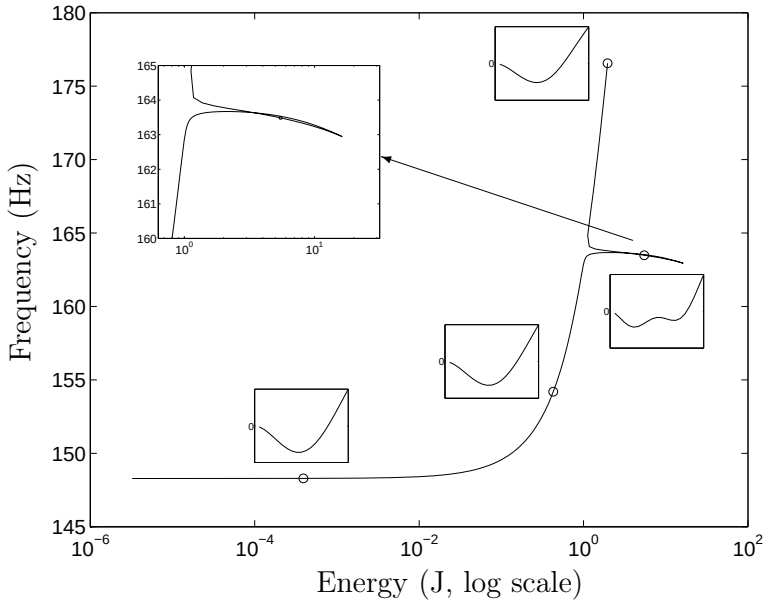

Figure 1.23: Frequency-energy plot of the cantilever beam; close-up of the second NNM.

cillation undergo a strong increase with increasing energy levels. The FEPs also highlight the presence of two tongues, revealing the existence of internal resonances. The tongue in Figure 1.22 corresponds to a 5:1 internal resonance between the first and second NNMs of the beam. When the energy gradually increases along the tongue, a smooth transition from the first mode to the second mode occurs following a dynamical mechanism similar to that described in Section 1.1.2. Similarly, a 5:1 internal resonance between the second and fourth modes is observed in Figure 1.23. These internal resonances occur despite that the linear natural frequencies are not commensurate, as also discussed in Section 1.1.2.

These two examples demonstrate that such a nonlinear modal analysis is an important tool for thoroughly understanding the system's vibratory response in the nonlinear regime. Clearly, this cannot be achieved using linearization procedures. However, because the general motion of a nonlinear system cannot be expressed as a superposition of individual NNM motions and because the modes in all these figures are computed based on the underlying undamped system, the practical utility of the nonlinear modal analysis might appear, at first, questionable.

A first motivation to compute and exploit the NNMs is that forced resonances in nonlinear systems occur in their neighborhoods. The knowledge of the NNMs can therefore provide valuable insight into the structure of the resonances, a feature of considerable engineering importance [154]. For illustration, the forced response of the damped 2DOF system (1.4) is considered. In Figures 1.24 and 1.25, the NNM backbone of the FEP of Figure 1.13 is superposed to the nonlinear frequency response functions of Figure 1.8 and 1.9. It can be observed that the NNMs of the underlying conservative system trace the locus of the forced frequency response peaks for both the in-phase and out-of-phase modes. Furthermore, Figure 1.26 compares the forced response of the system close to the first resonance (for $F = 0.1$, see the square in Figure 1.24) to the NNM motion of the corresponding point of the backbone. An excellent agreement is obtained between the two types of motion.

A second motivation is that the damped dynamics closely follows the NNMs of the underlying undamped system. To demonstrate this, a time-frequency analysis method, the continuous wavelet transform (CWT) [82], is used. In contrast to the Fourier transform, which assumes signal stationarity, the CWT involves a windowing technique with variable-sized regions. Small time intervals are considered for high-frequency components, whereas the size of the interval is increased for lower-frequency components. The CWT can therefore track the temporal evolution of the instantaneous frequencies, which makes it an effective tool for analyzing nonlinear signals. The usual representation of the transform is to plot its modulus as a function of time and frequency in a three-dimensional or contour plot. To use the CWT in conjunction with the FEP, a different representation is proposed herein. The CWT is represented in a FEP by substituting the instantaneous energy in the system for time.

The free response of the damped 2DOF system

$$\begin{aligned} \ddot{x}_1 + 0.03\dot{x}_1 + (2x_1 - x_2) + 0.5\,x_1^3 &= 0 \\ \ddot{x}_2 + 0.01\dot{x}_2 + (2x_2 - x_1) &= 0 \end{aligned} \tag{1.27}$$

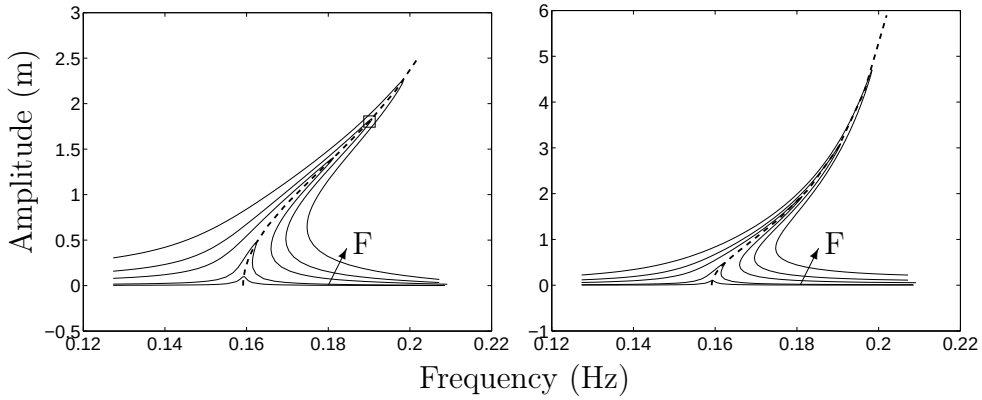

Figure 1.24: Nonlinear frequency response functions of system (1.4) close to the first resonant frequency (5 different forcing amplitudes F: 0.002N, 0.01N, 0.05N, 0.1N, 0.2N). The dashed line is the in-phase NNM backbone $S11+$ of the underlying conservative system (1.2). Left plot: x_1; right plot: x_2.

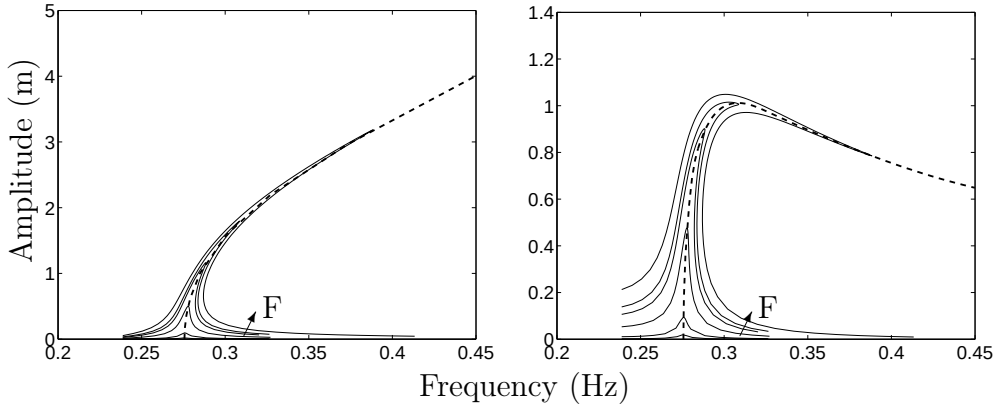

Figure 1.25: Nonlinear frequency response functions of system (1.4) close to the second resonant frequency (5 different forcing amplitudes F: 0.002N, 0.01N, 0.05N, 0.1N, 0.2N). The dashed line is the out-of-phase NNM backbone $S11-$ of the underlying conservative system (1.2). Left plot: x_1; right plot: x_2.

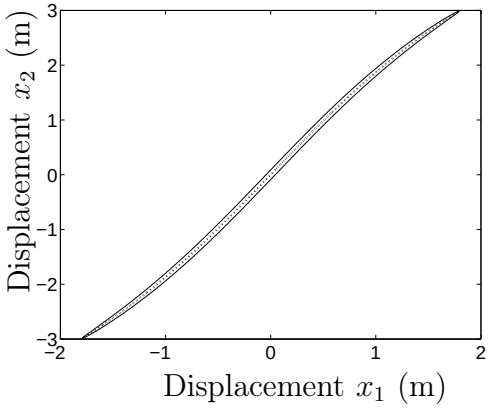

Figure 1.26: Forced response of system (1.4) and NNM motion of the underlying conservative system (1.2) in the configuration space. ——: forced response close to the first resonance ($F = 0.1$); - - -: in-phase NNM motion corresponding to the same frequency.

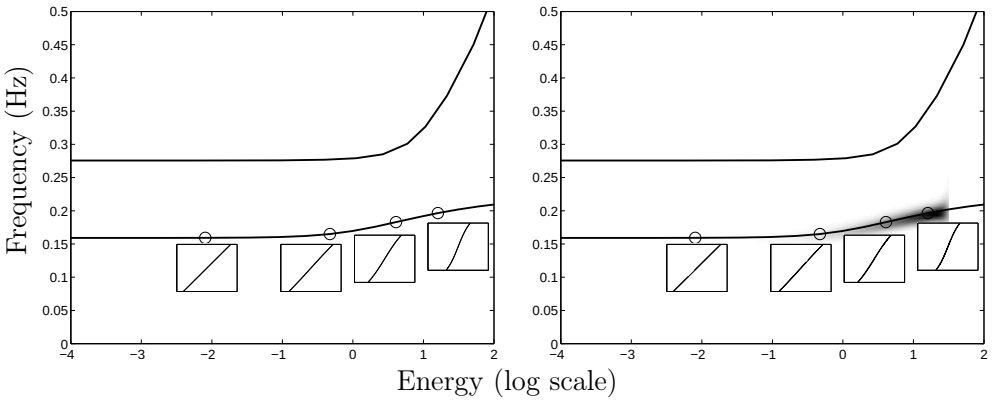

Figure 1.27: Frequency-energy plot of system (1.2). Left plot: theoretical FEP; right plot: experimental FEP for an excitation of the in-phase NNM ($[x_1(0)\ x_2(0)\ \dot{x}_1(0)\ \dot{x}_2(0)] = [2.500\ 5.895\ 0\ 0]$).

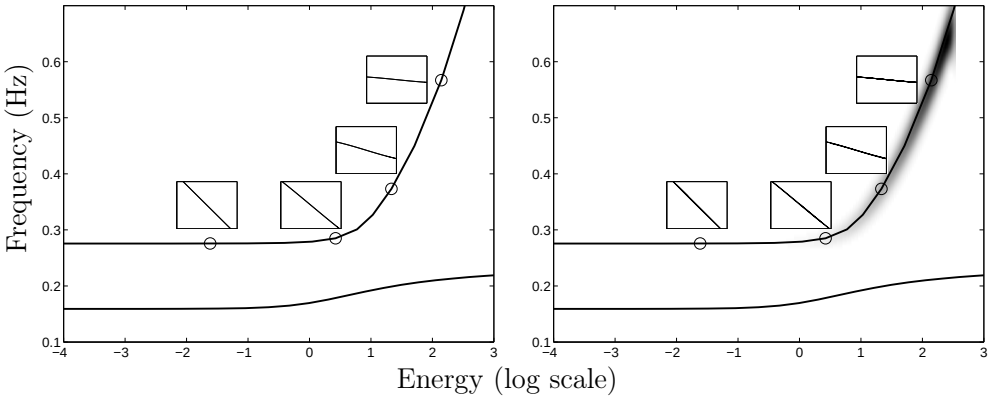

Figure 1.28: Frequency-energy plot of system (1.2). Left plot: theoretical plot; right plot: experimental plot for an excitation of the out-of-phase NNM ($[x_1(0)\ x_2(0)\ \dot{x}_1(0)\ \dot{x}_2(0)] = [-6.842\ 0.389\ 0\ 0]$).

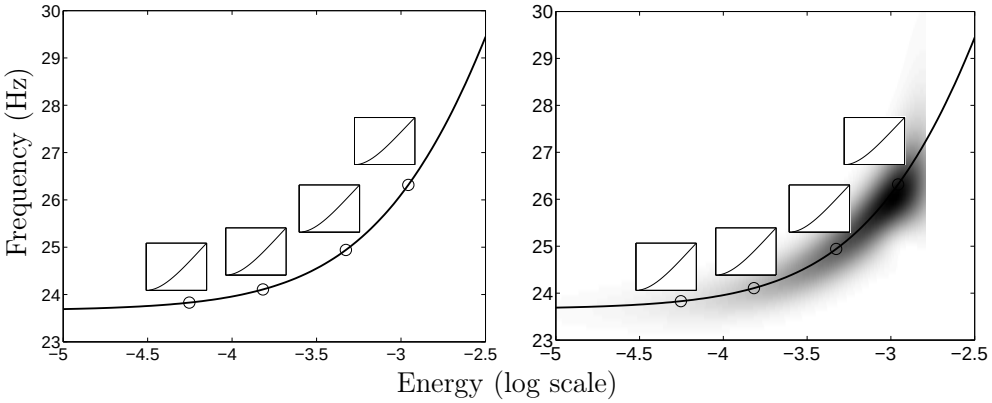

Figure 1.29: Frequency-energy plot of the planar cantilever beam. Left plot: theoretical plot; right plot: experimental plot for an excitation of the first mode.

is depicted in Figures 1.27 and 1.28 for an excitation of the in-phase and out-of-phase NNMs, respectively. The left plot is the theoretical FEP, that is the FEP of NNMs computed from the equations of motion of the underlying undamped system (1.2). The right plot is the 'experimental' FEP, calculated directly from the time series of the damped system (1.27): (i) the backbone is provided by the CWT, and (ii) the modal curves are obtained by representing the time series in the configuration space for one oscillation around a specific energy level. For comparison, the theoretical backbone is represented by a solid line in the experimental FEP. A perfect agreement is obtained between the two FEPs, which shows that the undamped NNMs are attractors for the damped trajectories. In the present case, the modal damping ratios are 1% and 0.6%, but we note that this result holds for higher damping ratios.

Figure 1.29 displays the free response of the planar cantilever beam excited at its first mode (with a damping matrix equal to the mass matrix, $\mathbf{C} = \mathbf{M}$). It shows that similar conclusions can also be reached for more complex systems.

Even if a possible criticism of the proposed approach is that it defines an NNM as a periodic solution of the underlying undamped system, these two examples support that they still give a very accurate picture of the damped dynamics. These results also show that the CWT is the ideal companion to the NNMs. We believe that the combined use of the FEP and the CWT represents a suitable framework for developing a new nonlinear system identification method, which could be viewed as a practical nonlinear analog of experimental modal analysis. This is addressed in Chapter 4 which deals with experimental identification of NNMs.

1.3.3 Reduced-Order Modeling

In a recent series of works [57, 109, 111, 142–144], it was shown that NNMs can provide effective bases for constructing reduced-order models of the dynamics of discrete and continuous nonlinear oscillators.

Specifically, Touzé et al. performed a comparative study of reduced-order models of large-amplitude vibrations of shell structures of different configurations using either LNMs or NNMs [143]. They showed that one or two NNMs were sufficient for accurately capturing the shell dynamics, and even the bifurcation structure of the dynamics that resulted from the nonlinear interaction of two shell modes in internal resonance. By contrast, multiple linear modes were necessary to achieve the same accuracy. For illustration, a specific application taken from [143] is shown in Figure 1.30. It depicts the frequency response curve of the nondimensionalized amplitude of the transverse displacement of a hyperbolic paraboloid panel under harmonic excitation. The harmonic excitation is applied at the center of the panel, and its frequency is in the vicinity of the first eigenfrequency. Comparing the reference (exact) computational solution to reduced-order models obtained using the leading NNM and LNM, respectively, the accuracy of the NNM-based model and its superiority over the LNM-based model are established. In this example, 15 LNMs were

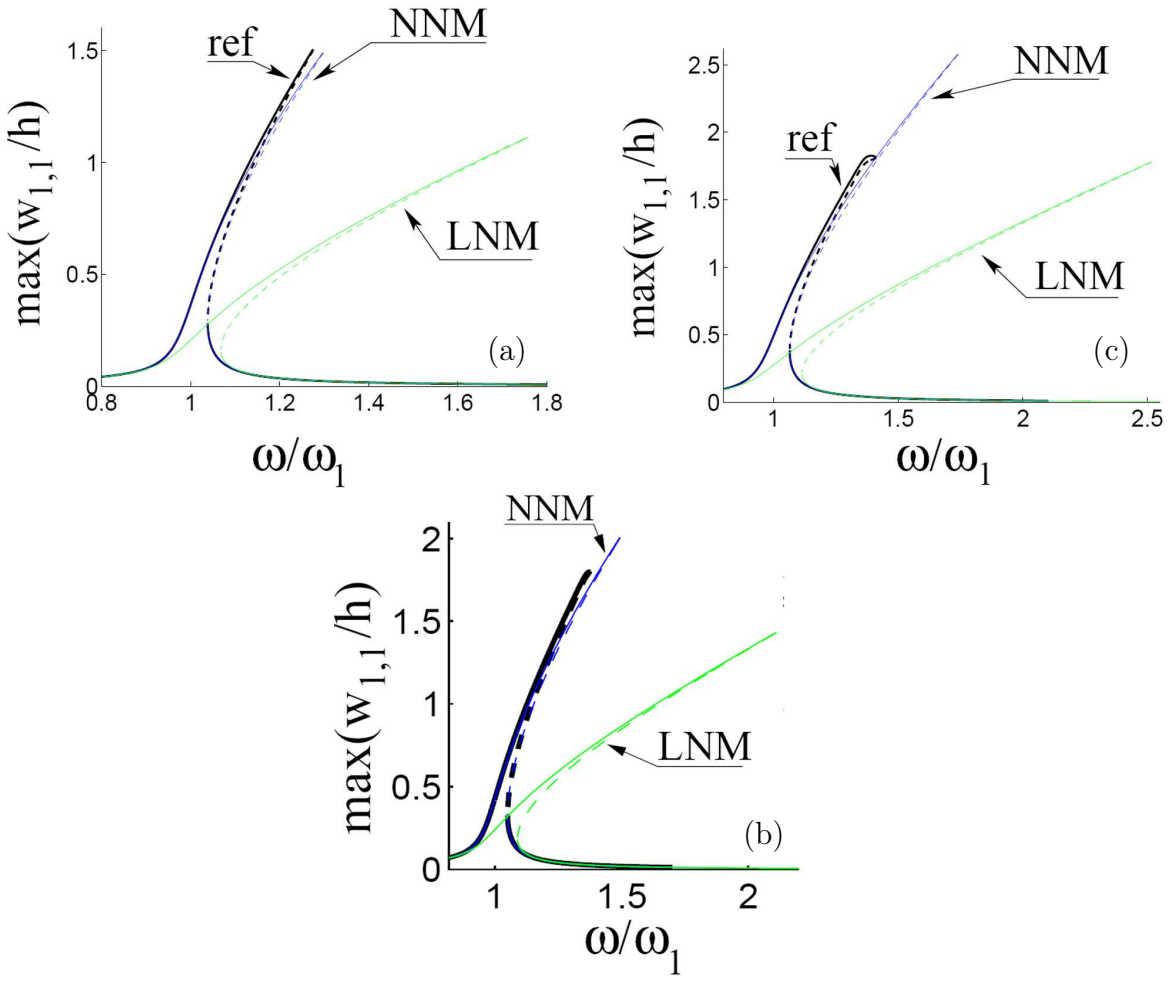

Figure 1.30: Frequency response curve of an hyperbolic paraboloid panel: reference (exact) computational solution compared to reduced-order models based on the leading LNM and NNM for varying forcing amplitudes. (a) 2.84N; (b) 4.37N and (c) 6.66N. Taken from Touzé et al. [143].

required to obtain results of similar accuracy.

These results demonstrate that NNMs hold promise for low-order reduction of structural models with many DOFs (e.g., finite element computational models). It is the application which has received the most attention so far in the literature. The reader can refer for instance to [5, 6, 21, 68, 76, 110, 112, 132, 135, 142, 143] and references therein for further detail. Even though NNMs do not possess orthogonality properties (as do the LNMs), the resulting models are still expected to be much more accurate compared to their linear counterpart (especially for systems with strong or even nonlinearizable nonlinearities). The reason for the enhanced accuracy of NNM-based reduced models lies in their invariance property and in the fact that they represent exact solutions of the free and forced nonlinear dynamics of the oscillators considered (i.e., oscillations in the neighborhoods of structural resonances can be captured by either a single NNM or a small set of NNMs when internal resonances occur).

1.3.4 Localization Phenomena

Localization and motion confinement are observed when vibrational energy tends to be confined to one particular area of a structure. They have first been observed for periodic linear structures presenting a structural irregularity (e.g., mistuned bladed disks [24]). Nonlinear localization has been studied extensively by Vakakis and co-workers (see, e.g., [11, 151, 154, 155, 164]). One of its distinctive features is that it can occur in periodic structures even in the absence of structural disorder.

Although the energy is shared between the two oscillators at low-energy, the NNMs of system (1.2) localize to either DOF for increasing energies. As evidenced in Figure 1.13, the in-phase NNM tends to localize to the second DOF, whereas the out-of-phase NNM localizes to the first DOF. Clearly, this localization property is to be attributed to the frequency-energy dependence of nonlinear oscillations.

The fact that some NNMs spatially confine vibrational energy can find applications in vibration mitigation of mechanical systems. For instance, the nonlinear energy pumping phenomenon directly exploits this property in order to transfer irreversibly vibrational energy from a primary structure to a nonlinear vibration absorber (see, e.g., [62, 72, 73, 150, 153]). Some authors are also exploiting mode localization for the design of microelectromechanical systems (MEMS) [33].

1.4 Concluding Remarks

Robust and accurate modeling of nonlinearity in realistic vibrating structures is one of the greatest challenges in structural engineering. In this context, NNMs certainly represent a useful framework for the dynamicist. They have a clear conceptual relation to the LNMs,

yet they can highlight nonlinear phenomena that are unexpected (and unexplainable) from a linear viewpoint.

In this chapter, the two main definitions, the fundamental properties and different analytical and numerical methods for computing NNMs were reviewed and illustrated with numerical examples. We have also highlighted that even seemingly simple nonlinear systems can exhibit very complicated dynamics. The 2DOF system investigated herein is characterized by an intricate NNM structure with (presumably) a countable infinity of internal resonances and strong motion localization in either oscillators. One interesting finding is that the internal resonances occur without necessarily having commensurate linear natural frequencies. This is rarely discussed in the literature and is a consequence of the frequency-energy dependence of the NNMs.

Because there is very little work that addresses the application of NNMs to real-word structures, we have identified several aspects that might drive their development in the future:

- Numerical algorithms for the continuation of periodic solutions provide a very accurate computation of the NNMs of strongly nonlinear systems. Despite their computational burden, they certainly pave the way for an effective and practical computation of the nonlinear modes. They are described and discussed in more details in Chapter 2 of this document.
- The wavelet transform is a versatile time-frequency analysis method that can track the temporal evolution of the frequency of oscillation of NNMs.
- A frequency-energy plot is a suitable tool to represent the NNMs and to interpret the dynamics of nonlinear systems.

Using the combination of these three tools, we can relate the damped dynamics to the different branches of periodic solutions in the frequency-energy plot. These tools should help to extend experimental modal analysis, which is well-established for linear systems, to a practical nonlinear analog based on force appropriation. This is attempted in Chapter 4 where an experimental methodology is proposed for NNM identification.

One of the most limiting features of NNMs is that the general motion of a nonlinear system cannot be expressed as a superposition of individual NNMs. Even if there is no reason to believe that this limitation will be resolved soon, this chapter has shown that NNMs still provide a valuable tool for understanding (and possibly exploiting) the effects of structural nonlinearities on the dynamics.

Chapter 2

Practical Computation of Nonlinear Normal Modes using Numerical Continuation Techniques

Abstract

One reason of the still limited use of nonlinear normal modes (NNMs) in structural dynamics is that their computation is often regarded as impractical. However, when resorting to numerical algorithms, we show that the NNM computation is possible with limited implementation effort, which leads to a practical method for determining the NNMs of nonlinear mechanical systems. The proposed algorithm relies on two main techniques, namely a shooting procedure and a method for the continuation of NNM motions. In addition, sensitivity analysis is used, thereby resulting in a computationally efficient procedure. The algorithm is demonstrated using a nonlinear 2DOF system.

2.1 Introduction

As evidenced in Chapter 1, nonlinear normal modes (NNMs) offer a meaningful framework for developing modal analysis of nonlinear structures. However, most structural engineers still view NNMs as a concept that is foreign to them, and they do not yet consider these nonlinear modes as a practical nonlinear analog of the linear normal modes (LNMs). One reason supporting this statement is that most existing constructive techniques for computing NNMs are based on asymptotic approaches and rely on fairly involved mathematical developments.

In this context, algorithms for the numerical continuation of periodic solutions are really quite sophisticated and advanced (see, e.g., [35, 60, 93, 126], and the AUTO and MATCONT software). These algorithms have been extensively used for computing the forced response and limit cycles of nonlinear dynamical systems [50, 100, 120, 137, 142, 143]. Doedel and co-workers used them for the computation of periodic orbits during the free response of conservative systems [36, 89].

Interestingly, there have been very few attempts to compute the periodic solutions of conservative mechanical structures (i.e., NNM motions) using numerical continuation techniques. As reported in Chapter 1, one of the first approaches was proposed by Slater in [133] who combined a shooting method with sequential continuation to solve the nonlinear boundary value problem that defines a family of NNM motions. Similar approaches were considered in Lee et al. [72] and Bajaj et al. [162]. A more sophisticated continuation method is the so-called asymptotic-numerical method. It is a semi-analytical technique that is based on a power series expansion of the unknowns parameterized by a control parameter. It is utilized in [9] to follow the NNM branches in conjunction with finite difference methods, following a framework similar to that of [89].

In the present chapter, a shooting procedure is combined with the pseudo-arclength continuation method for the computation of NNM motions. We show that the NNM computation is possible with limited implementation effort, which holds promise for a practical and accurate method for determining the NNMs of nonlinear vibrating structures.

This chapter is organized as follows. In the next section, the computational framework is briefly reviewed. In Section 2.3, the proposed algorithm for NNM computation is presented. Its theoretical background is first introduced, and the numerical implementation is then described. Improvements are also presented for the reduction of the computational burden. The algorithm is then demonstrated using a nonlinear 2DOF system.

2.2 Computational Framework

In the present study, an NNM motion is defined as a *(non-necessarily synchronous) periodic motion* of the conservative structural system. The free response of discrete undamped

mechanical systems with n DOFs is considered, assuming that continuous systems (e.g., beams, shells or plates) have been spatially discretized using the finite element method. The general equations of motion are

$$\mathbf{M}\,\ddot{\mathbf{x}}(t) + \mathbf{K}\,\mathbf{x}(t) + \mathbf{f}_{nl}\left\{\mathbf{x}(t)\right\} = 0 \tag{2.1}$$

where $\mathbf{M}$ is the mass matrix; $\mathbf{K}$ is the stiffness matrix; $\mathbf{x}$ and $\ddot{\mathbf{x}}$ are the displacement and acceleration vectors, respectively; $\mathbf{f}_{nl}$ is the nonlinear restoring force vector, including stiffness terms only, assumed to be regular. In principle, systems with nonsmooth nonlinearities can be studied with the proposed method, but they require special treatment [74].

As briefly discussed in Chapter 1, NNM motions can be symmetric or unsymmetric. The letter S refers to symmetric periodic solutions for which the displacements and velocities of the system at half period are equal but with an opposite sign to those at time $t = 0$. Unsymmetric periodic solutions can be also encountered and are denoted by a letter U. For illustration, the time series and modal curves corresponding to different NNM motions of 2DOF system (1.2) studied in Chapter 1 are represented in Figures 2.1 and 2.2. Figure 2.1 shows a fundamental NNM motion on the backbone $S11+$. Three internally resonant NNM motions, namely a motion on $S31$ and two different motions on $U21$, are illustrated in Figure 2.2. The difference between symmetric and unsymmetric NNM motions is evident in this plot. It can also be observed that an NNM motion may take the form of an open or a closed curve in the configuration space. Closed orbits imply phase differences between the two oscillators of the system; i.e., their velocities do not vanish at the same time instant. Interestingly, there exist two different tongues of 2:1 internal resonance in this system, depending on whether the NNM motion is an open or closed orbit in the configuration space. These properties of NNM motions can be exploited for their computation as discussed in Section 2.3.3.

2.3 Numerical Computation of NNMs

The numerical method proposed here for NNM computation relies on two main techniques, namely a shooting technique and the pseudo-arclength continuation method.

2.3.1 Shooting Method

The equations of motion of system (2.1) can be recast into state space form[1]

$$\dot{\mathbf{z}} = \mathbf{g}(\mathbf{z}) \tag{2.2}$$

[1]The equations of motion are rewritten as first-order differential equations for convenience only. The numerical computation is performed by directly integrating the second-order equations (2.1) (see Section 2.3.3).

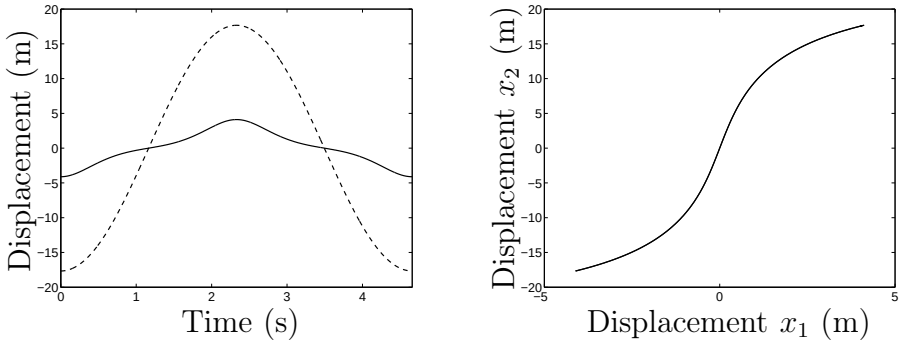

Figure 2.1: Fundamental NNM motion on $S11+$ (Frequency=0.213 Hz; energy=$10^{2.33}$ J). Left: time series (——: $x_1(t)$; $- - -$: $x_2(t)$). Right: modal curve in the configuration space.

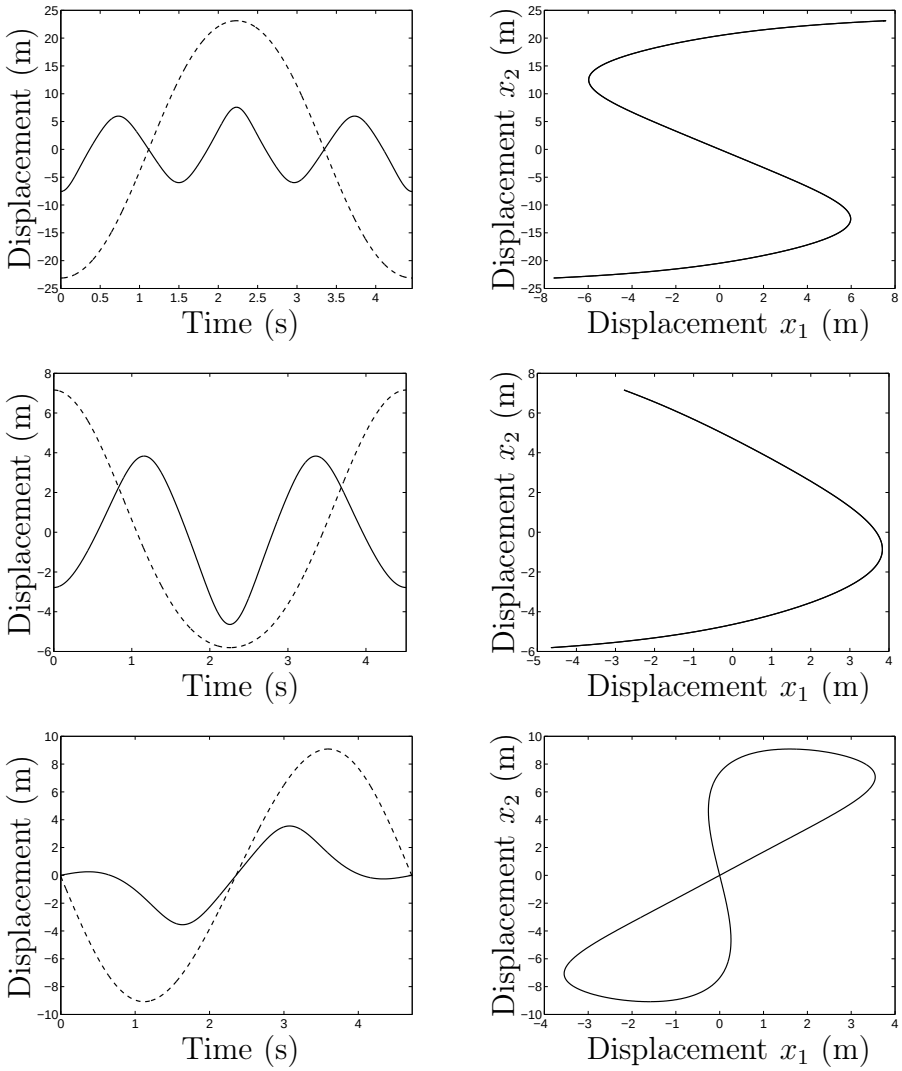

Figure 2.2: Internally resonant NNMs. From top to bottom: $S31$, open and closed $U21$ NNM motions. Left: time series (——: $x_1(t)$; $- - -$: $x_2(t)$). Right: modal curve in the configuration space.

where $\mathbf{z} = [\mathbf{x}^* \quad \dot{\mathbf{x}}^*]^*$ is the $2n$-dimensional state vector, and star denotes the transpose operation, and

$$\mathbf{g}(\mathbf{z}) = \begin{pmatrix} \dot{\mathbf{x}} \\ -\mathbf{M}^{-1}\left[\mathbf{K}\mathbf{x} + \mathbf{f}_{nl}(\mathbf{x})\right] \end{pmatrix} \tag{2.3}$$

is the vector field. It is assumed that the mass matrix is invertible. The solution of this dynamical system for initial conditions $\mathbf{z}(0) = \mathbf{z}_0 = [\mathbf{x}_0^* \quad \dot{\mathbf{x}}_0^*]^*$ is written as $\mathbf{z}(t) = \mathbf{z}\left(t, \mathbf{z}_0\right)$ in order to exhibit the dependence on the initial conditions, $\mathbf{z}\left(0, \mathbf{z}_0\right) = \mathbf{z}_0$. A solution $\mathbf{z}_p(t, \mathbf{z}_{p0})$ is a periodic solution of the autonomous system (2.2) if $\mathbf{z}_p(t, \mathbf{z}_{p0}) = \mathbf{z}_p(t+T, \mathbf{z}_{p0})$, where T is the minimal period.

The NNM computation is carried out by finding the periodic solutions of the governing nonlinear equations of motion (2.2). In this context, the *shooting method* is probably the most popular numerical technique [60, 93, 105, 126]. It solves numerically the two-point boundary-value problem defined by the periodicity condition

$$\mathbf{H}(\mathbf{z}_{p0}, T) \equiv \mathbf{z}_p(T, \mathbf{z}_{p0}) - \mathbf{z}_{p0} = \mathbf{0} \tag{2.4}$$

$\mathbf{H}(\mathbf{z}_0, T) = \mathbf{z}(T, \mathbf{z}_0) - \mathbf{z}_0$ is called the *shooting function* and represents the difference between the initial conditions and the system response at time T. Unlike forced motion, the period T of the free response is not known a priori.

The shooting method consists in finding, in an iterative way, the initial conditions $\mathbf{z}_{p0}$ and the period T inducing a periodic motion. To this end, the method relies on direct numerical time integration and on the Newton-Raphson algorithm.

Starting from some assumed initial conditions $\mathbf{z}_{p0}^{(0)}$, the motion $\mathbf{z}_p^{(0)}(t, \mathbf{z}_{p0}^{(0)})$ at the assumed period $T^{(0)}$ can be obtained by numerical time integration methods (e.g., Runge-Kutta or Newmark schemes). In general, the initial guess $(\mathbf{z}_{p0}^{(0)}, T^{(0)})$ does not satisfy the periodicity condition (2.4). This is illustrated in Figure 2.3 for a Duffing oscillator

$$\ddot{x} + x + 0.5x^3 = 0 \tag{2.5}$$

Two pairs of initial conditions, $[x(0) \ \dot{x}(0)] = 0.9 \times [4.9009 \ 0]$ and $[x(0) \ \dot{x}(0)] = 1.1 \times [4.9009 \ 0]$, are two approximations to the actual solution, $[x(0) \ \dot{x}(0)] = [4.9009 \ 0]$, for the current period $T = 2.0215\,\mathrm{s}$. The former (latter) approximation yields a motion with a too large (small) period.

A Newton-Raphson iteration scheme is therefore to be used to correct an initial guess and to converge to the actual solution. The corrections $\Delta\mathbf{z}_{p0}^{(0)}$ and $\Delta T^{(0)}$ are found by expanding the nonlinear function

$$\mathbf{H}\left(\mathbf{z}_{p0}^{(0)} + \Delta\mathbf{z}_{p0}^{(0)}, T^{(0)} + \Delta T^{(0)}\right) = 0 \tag{2.6}$$

in Taylor series

$$\mathbf{H}\left(\mathbf{z}_{p0}^{(0)}, T^{(0)}\right) + \left.\frac{\partial \mathbf{H}}{\partial \mathbf{z}_{p0}}\right|_{(\mathbf{z}_{p0}^{(0)}, T^{(0)})} \Delta\mathbf{z}_{p0}^{(0)} + \left.\frac{\partial \mathbf{H}}{\partial T}\right|_{(\mathbf{z}_{p0}^{(0)}, T^{(0)})} \Delta T^{(0)} + \text{H.O.T.} = 0 \tag{2.7}$$

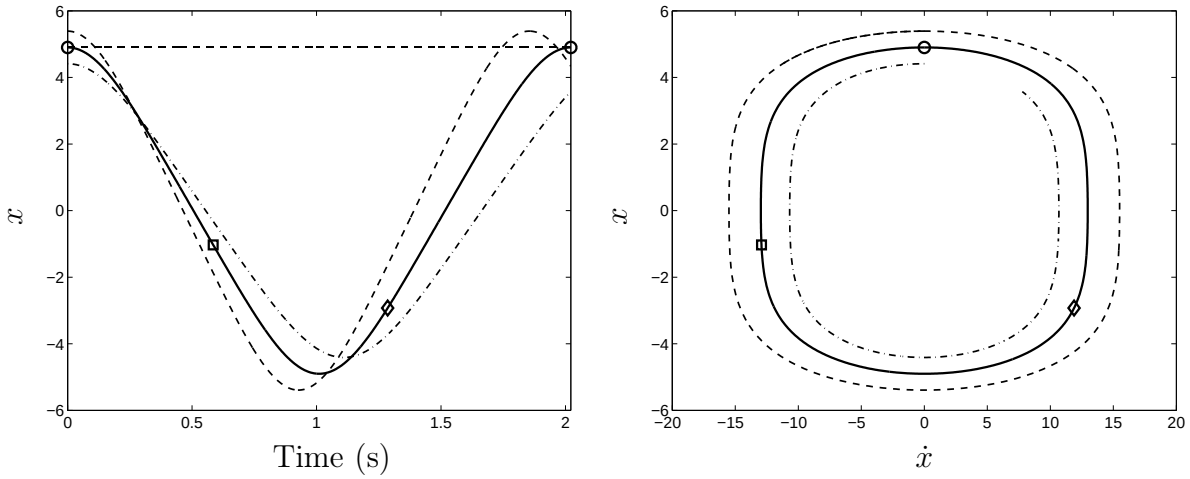

Figure 2.3: Solutions of the Duffing oscillator for different initial conditions. Left plot: time series; right plot: phase space. —— : periodic solution for $[x(0)\ \dot{x}(0)] = [4.9009\ 0]$ and $T = 2.0215$s; $- - -$: solution for $[x(0)\ \dot{x}(0)] = 1.1 \times [4.9009\ 0]$; $- \cdot - \cdot -$: solution for $[x(0)\ \dot{x}(0)] = 0.9 \times [4.9009\ 0]$. Markers represent different initial conditions of the periodic solution; ∘: $[x\ \dot{x}] = [4.9009\ 0]$; □: $[x\ \dot{x}] = [-1.0313\ -12.9188]$; ♢: $[x\ \dot{x}] = [-2.9259\ 11.8894]$.

and neglecting higher-order terms (H.O.T.).

The initial conditions $\mathbf{z}_{p0}$ and the period T characterizing the periodic solution are computed through the iterative procedure

$$\mathbf{z}_{p0}^{(k+1)} = \mathbf{z}_{p0}^{(k)} + \Delta\mathbf{z}_{p0}^{(k)} \text{ and } T^{(k+1)} = T^{(k)} + \Delta T^{(k)} \tag{2.8}$$

where the corrections are determined by solving the linearized equations

$$\left.\frac{\partial \mathbf{H}}{\partial \mathbf{z}_{p0}}\right|_{(\mathbf{z}_{p0}^{(k)}, T^{(k)})} \Delta\mathbf{z}_{p0}^{(k)} + \left.\frac{\partial \mathbf{H}}{\partial T}\right|_{(\mathbf{z}_{p0}^{(k)}, T^{(k)})} \Delta T^{(k)} = -\mathbf{H}\left(\mathbf{z}_{p0}^{(k)}, T^{(k)}\right) \tag{2.9}$$

k is the shooting iteration index. Convergence is achieved when $\mathbf{H}(\mathbf{z}_{p0}, T) \approx 0$ to the desired accuracy. In the neighborhood of the solution, the convergence is fast (i.e., quadratic convergence for an exact evaluation of the Jacobian matrix). However, it should be kept in mind that the Newton-Raphson method is a local algorithm; the convergence is guaranteed only when the initial guess is sufficiently close to the solution.

Sensitivity Analysis

Each shooting iteration involves the time integration of the equations of motion to evaluate the current shooting residue $\mathbf{H}\left(\mathbf{z}_{p0}^{(k)}, T^{(k)}\right) = \mathbf{z}_p^{(k)}(T^{(k)}, \mathbf{z}_{p0}^{(k)}) - \mathbf{z}_{p0}^{(k)}$. As evidenced by Equation (2.9), the shooting method also requires the evaluation of the partial derivatives of $\mathbf{H}(\mathbf{z}_0, T) = \mathbf{z}\left(T, \mathbf{z}_0\right) - \mathbf{z}_0$.

The $2n \times 1$ vector $\partial \mathbf{H}/\partial T$ is directly given by

$$\begin{aligned} \frac{\partial \mathbf{H}}{\partial T}(\mathbf{z}_0, T) &= \left.\frac{\partial \mathbf{z}(t, \mathbf{z}_0)}{\partial t}\right|_{t=T} \\ &= \mathbf{g}(\mathbf{z}(T, \mathbf{z}_0)) \end{aligned} \tag{2.10}$$

The $2n \times 2n$ Jacobian matrix $\partial \mathbf{H}/\partial \mathbf{z}_0$ is provided by

$$\frac{\partial \mathbf{H}}{\partial \mathbf{z}_0}(\mathbf{z}_0, T) = \left.\frac{\partial \mathbf{z}(t, \mathbf{z}_0)}{\partial \mathbf{z}_0}\right|_{t=T} - \mathbf{I} \tag{2.11}$$

where $\mathbf{I}$ is the $2n \times 2n$ identity matrix. There are basically two means of computing the Jacobian matrix $\partial \mathbf{z}(t, \mathbf{z}_0)/\partial \mathbf{z}_0$.

1. This matrix represents the variation of the solution $\mathbf{z}(t, \mathbf{z}_0)$ at time t when the initial conditions $\mathbf{z}_0$ are perturbed. It can therefore be evaluated through a classical finite-difference analysis by perturbing successively each of the $2n$ initial conditions and integrating the governing *nonlinear* equations of motion [93]. This approximate procedure therefore relies on extensive numerical simulations.

2. Targeting a reduction of the computational cost, a significant improvement is to use sensitivity analysis. This alternative computation is obtained by differentiating the equations of motion (2.2) with respect to the initial conditions $\mathbf{z}_0$

$$\frac{\partial}{\partial \mathbf{z}_0}\left[\dot{\mathbf{z}}(t, \mathbf{z}_0)\right] = \frac{\partial}{\partial \mathbf{z}_0}\left[\mathbf{g}(\mathbf{z}(t, \mathbf{z}_0))\right] \tag{2.12}$$

   It follows

$$\frac{d}{dt}\left[\frac{\partial \mathbf{z}(t, \mathbf{z}_0)}{\partial \mathbf{z}_0}\right] = \left.\frac{\partial \mathbf{g}(\mathbf{z})}{\partial \mathbf{z}}\right|_{\mathbf{z}(t,\mathbf{z}_0)} \left[\frac{\partial \mathbf{z}(t, \mathbf{z}_0)}{\partial \mathbf{z}_0}\right] \tag{2.13}$$

   with

$$\frac{\partial \mathbf{z}(0, \mathbf{z}_0)}{\partial \mathbf{z}_0} = \mathbf{I} \tag{2.14}$$

   since $\mathbf{z}(0, \mathbf{z}_0) = \mathbf{z}_0$. Hence, the matrix $\partial \mathbf{z}(t, \mathbf{z}_0)/\partial \mathbf{z}_0$ at $t = T$ can be obtained by numerically integrating over T the initial-value problem defined by the *linear* ordinary differential equations (ODEs) (2.13) with the initial conditions (2.14).

In addition to the integration of the current solution $\mathbf{z}(t, \mathbf{x}_0)$ of (2.2), these two methods for computing $\partial \mathbf{z}(t, \mathbf{z}_0)/\partial \mathbf{z}_0$ require $2n$ numerical integrations of $2n$-dimensional dynamical systems, which may be computationally intensive for large systems. However, equations (2.13) are linear ODEs and their numerical integration is thus far less expensive. As discussed in Section 2.3.3, the numerical cost can be further reduced if the solution of sensitivity equations (2.13) is computed together with the solution of the nonlinear equations of motion in a single simulation [18]. This reduction of the computational burden is significant for large-scale finite element models. In addition, sensitivity analysis

provides an exact evaluation of the Jacobian matrix. Convergence troubles (i.e., slow convergence or even no convergence) of the shooting procedure resulting from inaccurate computation of a finite-difference method are then avoided. Hence, sensitivity analysis is particularly attractive from a computational viewpoint. We note that a finite-difference procedure is nevertheless required when $\mathbf{g}$ is nondifferentiable, i.e., when the nonlinearities are nonsmooth [87, 93].

Phase Condition

In the present case, the phase of the periodic solutions is not fixed. If $\mathbf{z}(t)$ is a solution of the autonomous system (2.2), then $\mathbf{z}(t + \Delta t)$ is geometrically the same solution in phase space for any Δt. The initial conditions $\mathbf{z}_{p0}$ can be arbitrarily chosen anywhere on the periodic solution. This is illustrated in Figure 2.3 for the Duffing oscillator (2.5) where different initial conditions corresponding to the same periodic solution are shown. Hence, an additional condition has to be specified in order to remove the arbitrariness of the initial conditions. Mathematically, the system (2.9) of $2n$ equations with $2n + 1$ unknowns needs a supplementary equation, termed the *phase condition*.

Different phase conditions have been proposed in the literature [93, 126]. For instance, the simplest one consists in setting one component of the initial conditions vector to zero, as in [9]. This is illustrated in Figure 2.3 where the depicted periodic solution of the Duffing oscillator is characterized by a zero initial velocity. A phase condition particularly suitable for NNM computation is utilized in the present study and is discussed in Section 2.3.3.

In summary, the NNM computation is carried out by solving the augmented two-point boundary-value problem defined by

$$\mathbf{F}(\mathbf{z}_{p0}, T) \equiv \left\{ \begin{array}{rcl} \mathbf{H}(\mathbf{z}_{p0}, T) & = & 0 \\ h(\mathbf{z}_{p0}) & = & 0 \end{array} \right. \tag{2.15}$$

where $h(\mathbf{z}_{p0}) = 0$ is the phase condition.

Stability Analysis

As discussed in Chapter 1, an important characteristic of NNMs is that they can be stable or unstable. Instability means that small perturbations of the initial conditions that generate the NNM motion lead to the elimination of the mode oscillation. Nonetheless, the unstable NNMs can be computed using the shooting procedure.

The stability analysis can be performed numerically when an NNM motion has been computed by the shooting algorithm. The *monodromy matrix* Φ_T of a periodic orbit $\mathbf{z}_p\left(t, \mathbf{z}_{p0}\right)$ of period T is defined by its $2n \times 2n$ Jacobian matrix evaluated at $t = T$

$$\Phi_T(\mathbf{z}_{p0}) = \left. \frac{\partial \mathbf{z}_p\left(t, \mathbf{z}_{p0}\right)}{\partial \mathbf{z}_{p0}} \right|_{t=T} \tag{2.16}$$

Perturbing the initial conditions with the vector $\Delta\mathbf{z}_0$ and expanding the perturbed solution $\mathbf{z}(T, \mathbf{z}_{p0} + \Delta\mathbf{z}_0)$ in Taylor series yields

$$\Delta\mathbf{z}(T) = \Phi_T(\mathbf{z}_{p0})\Delta\mathbf{z}_0 + \mathcal{O}(\|\Delta\mathbf{z}_0\|^2) \tag{2.17}$$

where $\Delta\mathbf{z}(T) = \mathbf{z}(T, \mathbf{z}_{p0} + \Delta\mathbf{z}_0) - \mathbf{z}_p(T, \mathbf{z}_{p0})$.

Equations (2.17) shows that the monodromy matrix provides the first-order variation of the periodic solution after one period. After m periods, one obtains

$$\Delta\mathbf{z}(mT) = [\Phi_T(\mathbf{z}_{p0})]^m \Delta\mathbf{z}_0 + \mathcal{O}(\|\Delta\mathbf{z}_0\|^2) \tag{2.18}$$

The linear stability of the periodic solution calculated by the shooting algorithm is studied by computing the eigenvalues of its monodromy matrix Φ_T, which is a by-product of the procedure. The $2n$ eigenvalues, termed *Floquet multipliers*, provide the exponential variations of the perturbations along the eigendirections of the monodromy matrix. If a Floquet multiplier has a magnitude larger than one, then the periodic solution is unstable; otherwise, it is stable in the linear sense.

2.3.2 Continuation of Periodic Solutions

As stated in Chapter 1, the conservative system (2.2) comprises at least n different families of periodic orbits (i.e., NNMs), which can be regarded as nonlinear extensions of the LNMs of the underlying linear system. Due to the frequency-energy dependence, the modal parameters of an NNM vary with the total energy. An NNM family, governed by Equations (2.15), therefore traces a curve, termed an NNM branch, in the $(2n+1)$-dimensional space of initial conditions and period $(\mathbf{z}_{p0}, T)$. In addition, there may also exist additional NNMs (i.e., bifurcating NNMs) that are essentially nonlinear with no linear counterparts.

In this study, the NNMs are determined using methods for the *numerical continuation* of periodic motions (also called *path-following methods*) [4, 93, 126]. Starting from the corresponding LNM at low energy, the computation is carried out by finding successive points $(\mathbf{z}_{p0}, T)$ of the NNM branch. The space $(\mathbf{z}_{p0}, T)$ is termed the continuation space.

Different methods for numerical continuation have been proposed in the literature. The so-called pseudo-arclength continuation method is used herein.

Sequential Continuation

The simplest and most intuitive continuation technique is the *sequential continuation* method. This procedure is first explained due to its straightforward implementation. Moreover, it provides the fundamental concepts of continuation methods.

The sequential continuation of the periodic solutions governed by (2.15) is carried out in three steps:

1. A periodic solution $(\mathbf{z}_{p0,(1)}, T_{(1)})$ at sufficiently low energy (i.e., in the neighborhood of one LNM) is first computed using the shooting method. The period and initial conditions of the selected LNM are chosen as an initial guess.
2. The period is incremented, $T_{(j+1)} = T_{(j)} + \Delta T$.
3. From the current solution $(\mathbf{z}_{p0,(j)}, T_{(j)})$, the next solution $(\mathbf{z}_{p0,(j+1)}, T_{(j+1)})$ is determined by solving (2.15) using the shooting method with the period fixed:

$$\mathbf{z}_{p0,(j+1)}^{(k+1)} = \mathbf{z}_{p0,(j+1)}^{(k)} + \Delta\mathbf{z}_{p0,(j+1)}^{(k)} \tag{2.19}$$

where

$$\left.\frac{\partial \mathbf{F}}{\partial \mathbf{z}_{p0}}\right|_{(\mathbf{z}_{p0,(j+1)}^{(k)}, T_{(j+1)})} \Delta\mathbf{z}_{p0,(j+1)}^{(k)} = -\mathbf{F}(\mathbf{z}_{p0,(j+1)}^{(k)}, T_{(j+1)}) \tag{2.20}$$

The initial conditions of the previous periodic solution are used as a prediction $\mathbf{z}_{p0,(j+1)}^{(0)} = \mathbf{z}_{p0,(j)}$. Superscript k is the iteration index of the shooting procedure, whereas subscript j is the index along the NNM branch.

Eventually, one complete NNM branch is computed.

Pseudo-Arclength Continuation

The sequential continuation method parameterizes an NNM branch using the period T. It has two main drawbacks:

1. Because the convergence of the Newton-Raphson procedure depends critically on the closeness of the initial guess to the actual solution, the sequential continuation requires fairly small increments ΔT.
2. Because the value of the period is fixed during the Newton-Raphson corrections, it is unable as such to deal with turning points. This is illustrated in Figure 2.4 where no solution exists for a period larger than the period at the turning point.

For better performance, a continuation algorithm uses a better prediction than the last computed solution. In addition, corrections of the period are also considered during the shooting process. The pseudo-arclength continuation method relies on these two improvements in order to optimize the path following of the branch.

Starting from a known solution $(\mathbf{z}_{p0,(j)}, T_{(j)})$, the next periodic solution $(\mathbf{z}_{p0,(j+1)}, T_{(j+1)})$ on the branch is computed using a *predictor step* and a *corrector step*.

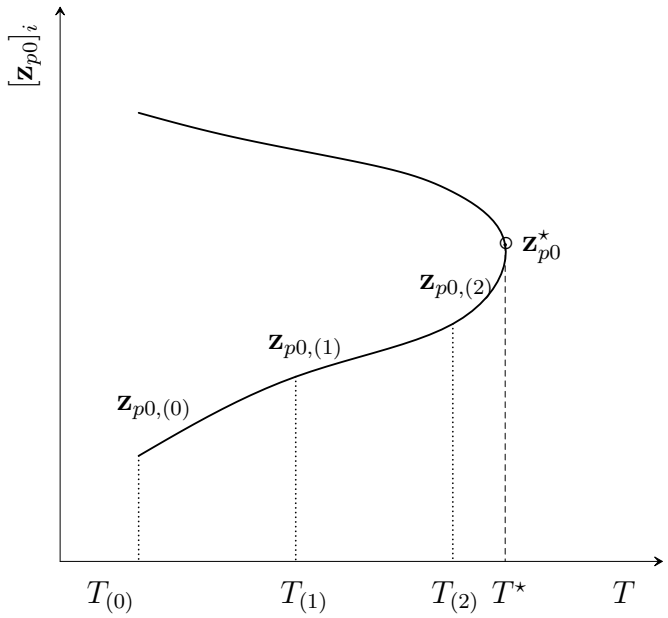

Figure 2.4: Turning point $(T^*, \mathbf{z}^\star_{p0})$ in the continuation space. Failure of the sequential continuation for $T \geq T^\star$.

Predictor step

At step j, a prediction $(\tilde{\mathbf{z}}_{p0,(j+1)}, \tilde{T}_{(j+1)})$ of the next solution $(\mathbf{z}_{p0,(j+1)}, T_{(j+1)})$ is generated along the tangent vector to the branch at the current point $\mathbf{z}_{p0,(j)}$

$$\begin{bmatrix} \tilde{\mathbf{z}}_{p0,(j+1)} \\ \tilde{T}_{(j+1)} \end{bmatrix} = \begin{bmatrix} \mathbf{z}_{p0,(j)} \\ T_{(j)} \end{bmatrix} + s_{(j)} \begin{bmatrix} \mathbf{p}_{z,(j)} \\ p_{T,(j)} \end{bmatrix} \tag{2.21}$$

where $s_{(j)}$ is the predictor stepsize. The tangent vector $\mathbf{p}_{(j)} = [\mathbf{p}^*_{z,(j)}\ p_{T,(j)}]^*$ to the branch defined by (2.15) is solution of the system

$$\begin{bmatrix} \frac{\partial \mathbf{H}}{\partial \mathbf{z}_{p0}}\Big|_{(\mathbf{z}_{p0,(j)}, T_{(j)})} & \frac{\partial \mathbf{H}}{\partial T}\Big|_{(\mathbf{z}_{p0,(j)}, T_{(j)})} \\ \frac{\partial h}{\partial \mathbf{z}_{p0}}^*\Big|_{(\mathbf{z}_{p0,(j)})} & 0 \end{bmatrix} \begin{bmatrix} \mathbf{p}_{z,(j)} \\ p_{T,(j)} \end{bmatrix} = \begin{bmatrix} \mathbf{0} \\ 0 \end{bmatrix} \tag{2.22}$$

with the condition $\left\|\mathbf{p}_{(j)}\right\| = 1$. The star denotes the transpose operator. This normalization can be taken into account by fixing one component of the tangent vector and solving the resulting overdetermined system using the Moore-Penrose matrix inverse; the tangent vector is then normalized to 1. For illustration, the predictor step is shown schematically in Figure 2.5.

Corrector step

The prediction is corrected by a shooting procedure in order to solve (2.15) in which the variations of the initial conditions and the period are forced to be orthogonal to the

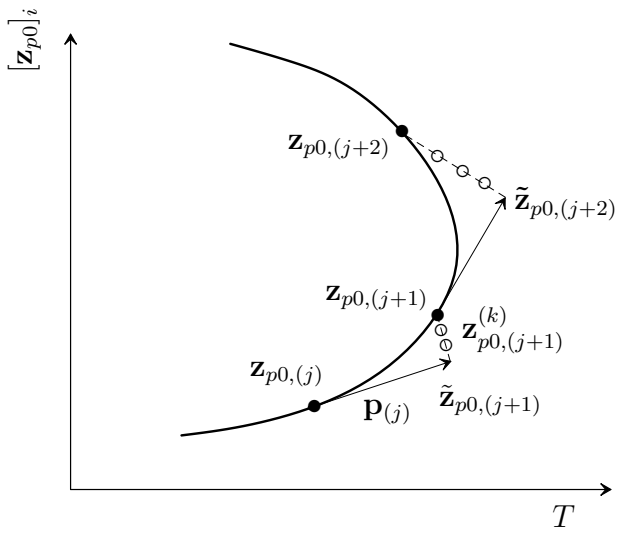

Figure 2.5: Pseudo-arclength continuation method: branch (——) with a turning point; predictor step (→) tangent to the branch; corrector steps (∘ ∘ ∘) perpendicular to the predictor step.

predictor step. At iteration k, the corrections

$$\begin{aligned} \mathbf{z}^{(k+1)}_{p0,(j+1)} &= \mathbf{z}^{(k)}_{p0,(j+1)} + \Delta\mathbf{z}^{(k)}_{p0,(j+1)} \\ T^{(k+1)}_{(j+1)} &= T^{(k)}_{(j+1)} + \Delta T^{(k)}_{(j+1)} \end{aligned} \tag{2.23}$$

are computed by solving the overdetermined linear system using the Moore-Penrose matrix inverse

$$\begin{bmatrix} \frac{\partial \mathbf{H}}{\partial \mathbf{z}_{p0}}\Big|_{(\mathbf{z}^{(k)}_{p0,(j+1)}, T^{(k)}_{(j+1)})} & \frac{\partial \mathbf{H}}{\partial T}\Big|_{(\mathbf{z}^{(k)}_{p0,(j+1)}, T^{(k)}_{(j+1)})} \\ \frac{\partial h}{\partial \mathbf{z}_{p0}}^{*}\Big|_{(\mathbf{z}^{(k)}_{p0,(j+1)})} & 0 \\ \mathbf{p}^{*}_{z,(j)} & p_{T,(j)} \end{bmatrix} \begin{bmatrix} \Delta\mathbf{z}^{(k)}_{p0,(j+1)} \\ \Delta T^{(k)}_{(j+1)} \end{bmatrix} = \begin{bmatrix} -\mathbf{H}(\mathbf{z}^{(k)}_{p0,(j+1)}, T^{(k)}_{(j+1)}) \\ -h(\mathbf{z}^{(k)}_{p0,(j+1)}) \\ 0 \end{bmatrix} \tag{2.24}$$

where the prediction is used as initial guess, i.e, $\mathbf{z}^{(0)}_{p0,(j+1)} = \tilde{\mathbf{z}}_{p0,(j+1)}$ and $T^{(0)}_{(j+1)} = \tilde{T}_{(j+1)}$.

The last equation in (2.24) corresponds to the orthogonality condition for the corrector step. We note that the partial derivatives in (2.24) are evaluated numerically, as explained previously.

This iterative process is carried out until convergence is achieved. The convergence test is based on the relative error of the periodicity condition:

$$\frac{\|\mathbf{H}(\mathbf{z}_{p0}, T)\|}{\|\mathbf{z}_{p0}\|} = \frac{\|\mathbf{z}_p(T, \mathbf{z}_{p0}) - \mathbf{z}_{p0}\|}{\|\mathbf{z}_{p0}\|} < \epsilon \tag{2.25}$$

where ϵ is the prescribed relative precision.

For illustration, the corrector step is shown schematically in Figure 2.5.

2.3.3 An Integrated Approach for NNM Computation

Basic Algorithm

The algorithm proposed for the computation of NNM motions is a combination of shooting and pseudo-arclength continuation methods, as summarized in Figure 2.6. Starting from the LNM motion at low energy, there are two steps within the algorithm:

1. The predictor step is *global* and goes from one NNM motion at a specific energy level to another NNM motion at a somewhat different energy level. For an efficient and robust NNM continuation, the stepsize $s_{(j)}$ is to be carefully controlled. A small stepsize leads to a small number of corrector iterations, but it requires a large number of continuation steps to follow an NNM branch. For a large stepsize, the number of corrector iterations is high, and the convergence is slow. The Newton-Raphson procedure may even break down if the prediction is not close enough to the actual solution. Continuation may therefore be computationally intensive in both cases. The stepsize has to be adjusted, possibly in an automatic and flexible manner. Various adaptive stepsize control procedures are discussed in [4, 126].

2. The corrector step is *local* and iteratively refines, using a shooting technique, the prediction to obtain the actual solution at a specific energy level. The size of the corrections during the corrector step is determined by the solutions of the overdetermined system (2.24).

This algorithm is applied to the Duffing oscillator (2.5) in Figure 2.7. The phase condition used in this example consists in enforcing the initial velocity $\dot{x}_{p0}$ to be zero. The continuation space is therefore composed of the initial displacement x_{p0} and the period T. The initial guess used to start the procedure is obtained at low energy where the system responds practically as the underlying linear system, which has an eigenfrequency of 1 rad/s (i.e., a period of $T = 6.28\,\mathrm{s}$).

Step Control

Unlike sequential continuation, the evolution path of this predictor-corrector method is parameterized by the distance $s_{(j)}$ along the tangent predictor, also referred to as arclength continuation parameter in the literature. As mentioned previously, the stepsize has to be carefully controlled for a robust and efficient NNM computation.

The stepsize control used herein relies on the evaluation of the convergence quality by the number of iterations of the corrector step. The stepsize is controlled so that the corrector step requires on average the desirable number of iterations $N^\star$. At each step, the stepsize is updated according to the ratio between the desirable number N^* and the previous

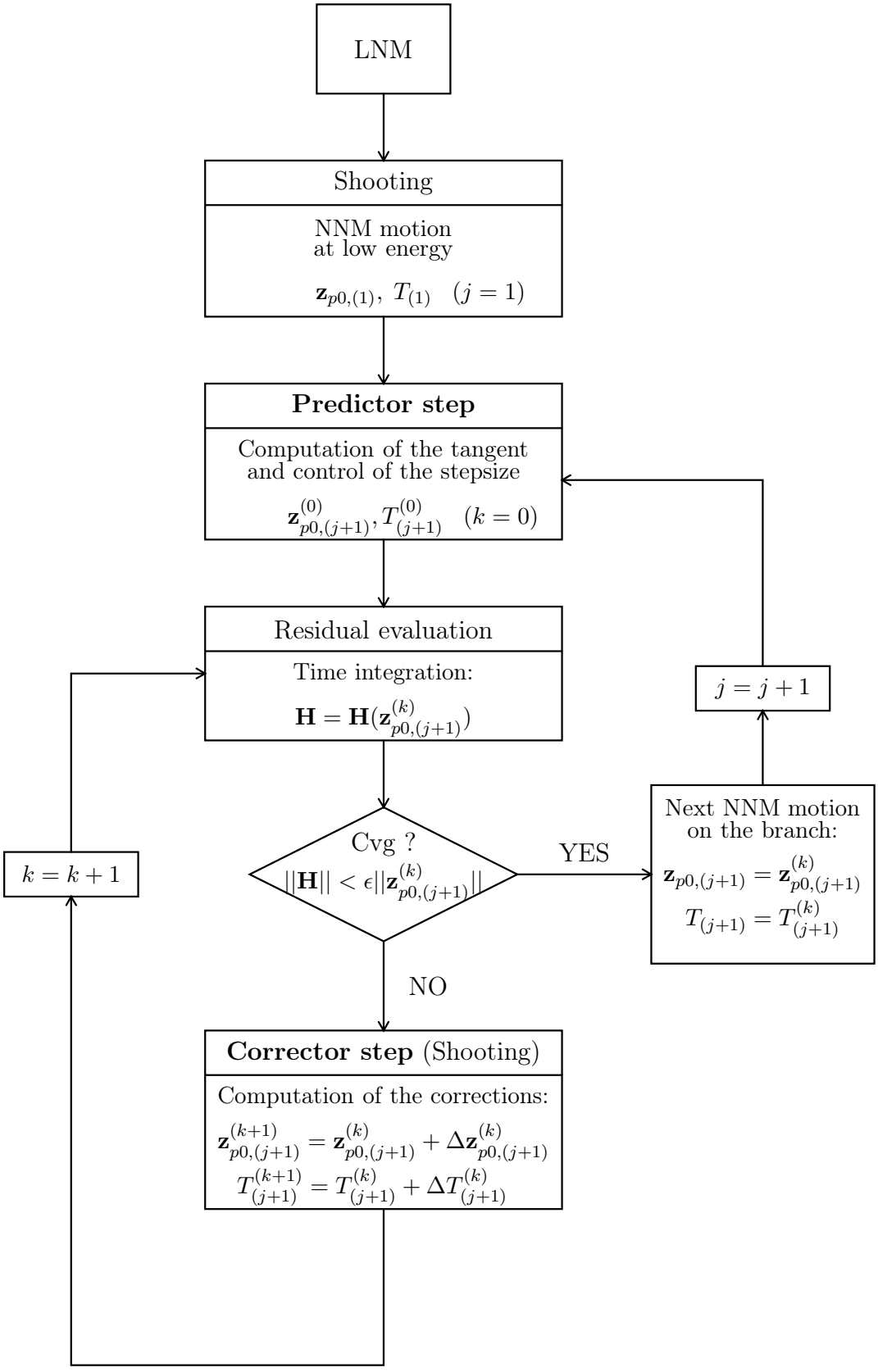

Figure 2.6: Algorithm for NNM computation.

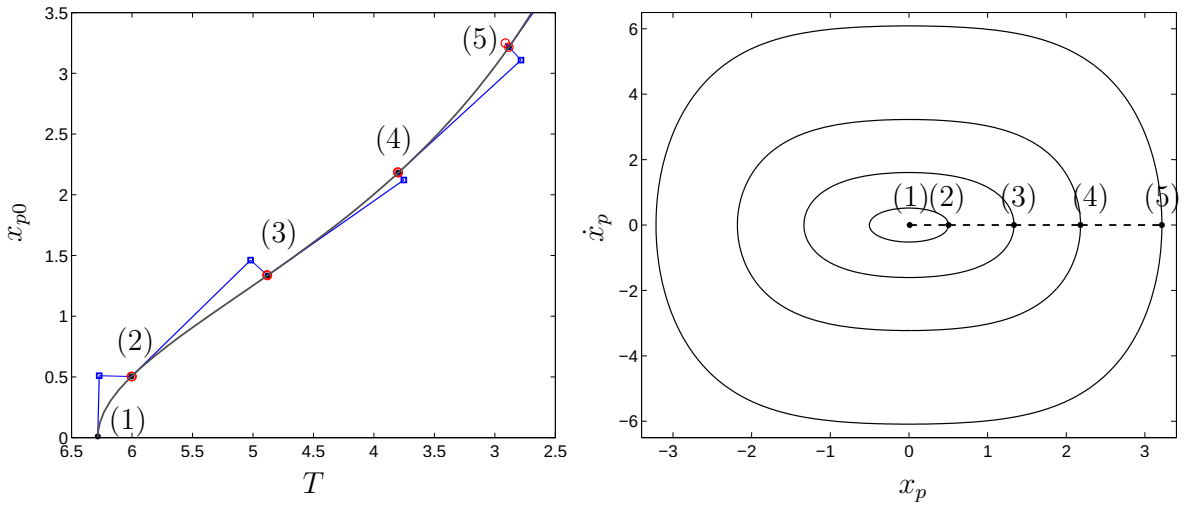

Figure 2.7: Continuation of periodic solutions for the Duffing oscillator (Phase condition: the initial velocity $\dot{x}_{p0} = 0$; initial guess point: $[x_{p0}\ \dot{x}_{p0}] = [0.01\ 0]$ and $T = 2\pi\ s$). Left plot: initial displacement x_{p0} as function of the period of motion (continuation space); exact branch (——) and computed points (•); predictor steps (□) and corrector steps (○). Right plot: family of periodic motions in the phase space; corresponding path following (− − −) and related periodic solutions (——).

number $N_{(j-1)}$ of iterations:

$$s_{(j)} = \left(\frac{N^*}{N_{(j-1)}}\right) s_{(j-1)} \tag{2.26}$$

In practice, the ratio $r = N^*/N_{(j-1)}$ is often bounded to make the adaptation stepsize more robust and to prevent the continuation from jumping between different branches[2]. The stepsize can also be bounded ($s_{(j)} < s_{max}$) to obtain enough discretized points on the branch during the continuation. In case of no convergence (i.e., when the residue increases or when the process requires more correction iterations than the prescribed maximum N_{max}), the stepsize is halved until convergence is achieved.

As a final remark, we note that the sign of the stepsize is chosen in order to follow the branch in the same direction, i.e.,

$$\left[s_{(j)}\mathbf{p}_{(j)}\right]^* \left[s_{(j-1)}\mathbf{p}_{(j-1)}\right] > 0 \tag{2.27}$$

According to the previous predictor step and the current tangent vector, the sign of $s_{(j)}$ is therefore given by

$$\text{sign}\left(s_{(j)}\right) = \text{sign}\left(s_{(j-1)}\mathbf{p}^*_{(j)}\mathbf{p}_{(j-1)}\right) \tag{2.28}$$

[2]Another possibility to avoid branch jumping phenomena is to limit the angle between consecutive predictor steps.

Numerical Time Integration

A widely-used method for solving first-order differential equations such as (2.2) is the Runge-Kutta scheme. In structural dynamics where second-order systems (2.1) are encountered, Newmark's family of methods is probably the most widespread technique for numerically integrating linear and nonlinear large-scale stiff mechanical systems [46]. The governing equations of motion (2.1) are directly solved without transforming them into first-order differential equations. This preserves the banded nature of the system of equations (typically resulting from finite element discretization), and the number of equations is not doubled. Newmark's time integration method is thereby a computationally more efficient approach. It is considered here for numerical time integration required during the shooting procedure. Newmark's scheme is detailed in Appendix A.

Similarly, the philosophy of sensitivity analysis (see Section 2.3.1) is directly applied to the second-order differential equations. The Jacobian matrix of the shooting procedure

$$\frac{\partial \mathbf{z}(t,\mathbf{z}_0)}{\partial \mathbf{z}_0} = \begin{pmatrix} \frac{\partial \mathbf{x}(t,\mathbf{z}_0)}{\partial \mathbf{z}_0} \\ \frac{\partial \dot{\mathbf{x}}(t,\mathbf{z}_0)}{\partial \mathbf{z}_0} \end{pmatrix}$$

is then obtained by integrating the following sensitivity equations

$$\mathbf{M}\,\frac{d^2}{dt^2}\left[\frac{\partial \mathbf{x}(t,\mathbf{z}_0)}{\partial \mathbf{z}_0}\right] + \mathbf{K}\left[\frac{\partial \mathbf{x}(t,\mathbf{z}_0)}{\partial \mathbf{z}_0}\right] + \left.\frac{\partial \mathbf{f}_{nl}\left\{\mathbf{x}\right\}}{\partial \mathbf{x}}\right|_{\mathbf{x}(t,\mathbf{z}_0)}\left[\frac{\partial \mathbf{x}(t,\mathbf{z}_0)}{\partial \mathbf{z}_0}\right] = 0 \tag{2.29}$$

resulting from the differentiation of the equations of motion (2.1) with respect to the initial conditions.

Besides the integration of the original equations of motion, Newmark's method is then reused for solving these sensitivity equations. This is combined in a single global time simulation. At each time step, the numerical integration of the current motion involves an iterative process (Newton-Raphson procedure using iteration matrix defined in Appendix A) since the equations (2.1) are nonlinear. At the end of the time step, the sensitivity equations (2.29), that are linear, are then solved in one single iteration using the same iteration matrix as for the original problem. Sensitivity analysis therefore requires only one additional iteration to compute the required Jacobian matrix. As mentioned previously, the impact on the overall computational cost of the algorithm turns out to be much smaller compared to a finite-difference method based on repeated time simulations [18].

The precision of the integration scheme, which is chosen by the end-user, directly influences the accuracy of the NNM computation. In fact, the computed solution can be regarded as an *exact* solution if the time step used to integrate the equations is sufficiently low. This is practically the only approximation in the proposed algorithm.

Reduction of the Computational Burden

As discussed in Chapter 1, a seemingly simple system such as system (1.2) can exhibit complicated NNM motions. This 2DOF system possesses branches of fundamental NNM motions, termed backbone branches, which are the nonlinear extension of the LNM motions. These branches coexist with a countable infinity of branches of internally resonant NNMs, referred to as tongues, with no counterpart in linear theory. In view of the infinite number of tongues and their sensitivity to small perturbations with increasing orders of internal resonance, an extensive computation of the tongues is certainly debatable. Although interesting, this discussion is beyond the scope of the present work.

The algorithm described so far may become computationally intensive when dealing with large-scale systems (i.e., systems with many DOFs). Because a practical and computationally tractable calculation of the NNM motions is targeted, two properties of some NNM families can be exploited to speed up the computation:

1. All symmetric NNM branches *Snm* (see, e.g., Figure 2.1 and the top plot in Figure 2.2) obey the symmetry condition

$$\mathbf{z}_p\left(\frac{T}{2}, \mathbf{z}_{p0}\right) + \mathbf{z}_{p0} = 0 \tag{2.30}$$

   For these branches, the shooting procedure can be performed over the half period $T/2$ by searching the initial conditions and the period T that solve this modified periodicity condition. Because the time integrations represent the main computational cost of the algorithm, this modified periodicity condition reduces the overall computational burden by a factor close to 2.

2. For branches of NNMs represented by an open loop in the configuration space (see, e.g., the first two NNM motions in Figure 2.2), a suitable phase condition is to set all the velocities to zero. The initial velocities are eliminated from the unknowns of the linear systems to solve at each Newton-Raphson iteration. These systems have therefore $2n + 1$ equations with $n + 1$ unknowns $\mathbf{x}_{p0}$ and T.

One advantage is that these modifications can be very naturally integrated in the basic algorithm in Figure 2.6.

In summary, two variants of the basic algorithm described in the previous section have been developed:

1. The *general strategy* consists in (i) carrying out the shooting over the period T and (ii) setting only one velocity to zero. This strategy can compute all possible NNM motions.

2. The *practical strategy* exploits the modified periodicity and phase conditions. The fundamental NNM motions of nonlinear structures often obey these conditions (e.g., the fundamental NNMs of nonlinear systems with odd nonlinearities are necessarily symmetric, because the loss of symmetry requires the so-called symmetry-breaking bifurcation).

Targeting a reduction of the computational burden, but without lack of generality, an approach that integrates the two variants is used. Starting from the LNMs, the fundamental NNM motions are first computed using the practical strategy; a subset of tongues can also be computed using this methodology. We note that the application of this strategy should often suffice for most engineering structures.

When a detailed analysis of the unsymmetric NNMs and those represented by a closed curve in the configuration space is required, the general strategy can then be utilized for computing these NNMs.

NNM Representation

So far, the NNMs have been considered as branches in the continuation space $(\mathbf{z}_{p0}, T)$. As explained in Section 1.1.2, an appropriate graphical depiction of the NNMs is to represent them in a frequency-energy plot (FEP). This FEP can be computed in a straightforward manner: (i) the conserved total energy is computed from the initial conditions realizing the NNM motion; and (ii) the frequency of the NNM motion is calculated directly from the period.

Numerical Implementation

The algorithm has been implemented in the MATLAB environment in combination with a graphical user interface, which makes the NNM computation more user-friendly.

2.4 Numerical Example

In what follows, the proposed algorithm for NNM computation is demonstrated using the nonlinear 2DOF system represented in Figure 1.1. Since the NNMs of this system have already been discussed in detail in Chapter 1, the computational aspects are principally investigated here.

The governing equations of motion of the system are

$$\begin{aligned} \ddot{x}_1 + (2x_1 - x_2) + 0.5\,x_1^3 &= 0 \\ \ddot{x}_2 + (2x_2 - x_1) &= 0 \end{aligned} \tag{2.31}$$

The two LNMs of the underlying linear system are in-phase and out-of-phase modes for which the two DOFs vibrate with the same amplitude. The natural eigenfrequencies are $f_1 = 1/2\pi \simeq 0.159$ Hz and $f_2 = \sqrt{3}/2\pi \simeq 0.276$ Hz.

The integrated approach described in Section 2.3.3 is applied to this system. The NNMs are then computed in a fairly automatic manner.

Starting from the corresponding LNMs at low energy, the computation of the fundamental NNMs is first performed using the modified phase and periodicity conditions. The in-phase NNM backbone $S11+$ is depicted in Figure 2.8(a), whereas the out-of-phase NNM backbone $S11-$ is given in Figure 2.9. The computed points are represented by circles. Though a large energy range is investigated, these figures show that the continuation method discretizes the two branches using very few points. Large stepsizes are therefore employed, and only a few seconds are required to compute each branch for 100 integration time steps per half period using a 2GHz processor. This is an important feature when targeting a computationally tractable calculation of the NNMs. The two backbones are depicted together in the FEP of Figure 1.13. The family of computed in-phase NNM motions is also represented in a three-dimensional projection of the phase space in Figure 2.8(b) and in the configuration space in Figure 2.8(c).

The NNM continuation can now be carried out at higher energy levels. The obtained FEP for the in-phase mode is depicted in Figure 2.10. It can be observed that a recurrent series of tongues, corresponding to internally resonant NNMs (i.e., $S31$, $S51$, $S71$, etc.), continue the backbone branch $S11+$ through turning points (fold bifurcations). Due to these turning points, smaller stepsizes are necessary, which renders the tongue calculation computationally more demanding. By contrast, at higher energy on $S11-$, the 1:1 out-of-phase motion persists, and $S11-$ extends to infinity. The complete FEP calculated using the practical strategy is shown in Figure 2.11.

We now move to the general strategy for the computation of unsymmetric NNMs and NNMs represented by a closed curve in the configuration space. These NNMs are generally generated through bifurcations (e.g., symmetry-breaking bifurcations for unsymmetrical NNMs). Because the tangent is not uniquely defined at the bifurcation point, they require a branching strategy to be effectively computed [126]. In this study, a perturbation technique is used to carry out branch switching, once the bifurcation point is located using the Floquet multipliers. The resulting FEP is displayed in Figure 1.17 and shows two unsymmetrical tongues ($U21$ and $U41$).

NNM stability is also provided by the proposed algorithm. Because the monodromy matrix is computed during the numerical procedure, its eigenvalues, the Floquet multipliers, are obtained as a by-product. The stability of the fundamental in-phase and internally resonant NNMs is presented in Figure 2.12. Clearly, the bifurcation points, which include fold and symmetry-breaking bifurcations, are characterized by a change of stability. The evolution of the Floquet multipliers along $S31$ is shown in the complex plane in Figure 2.13. This figure shows the mechanism of loss of stability; a pair of Floquet multipliers

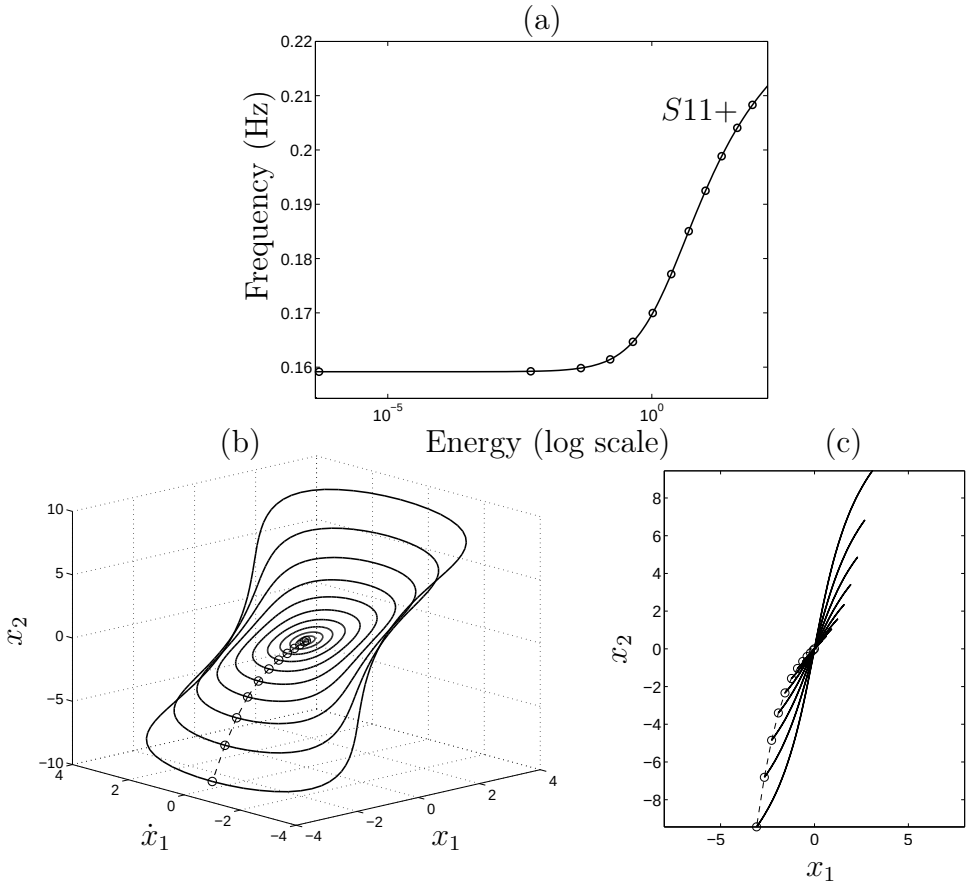

Figure 2.8: In-phase NNM motions on $S11+$ for the 2DOF system (2.31). (a) Frequency-energy plot; the computed points with $N^\star = 4$ are represented by $\circ$. (b) NNM periodic motions represented in a three-dimensional projection of the phase space. (c) NNM modal curves in the configuration space.

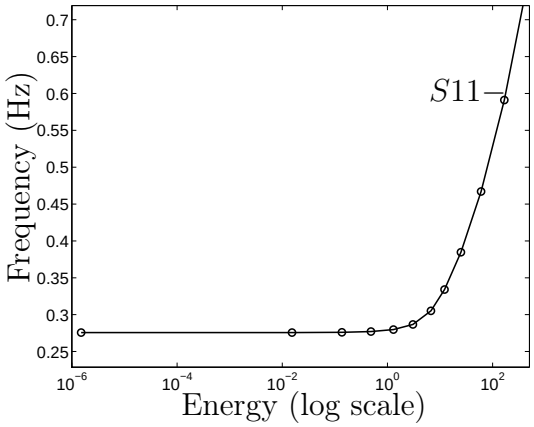

Figure 2.9: Frequency-energy plot gathering out-of-phase NNM motions on $S11-$ for the 2DOF system (2.31). The computed points with $N^\star = 4$ are represented by $\circ$.

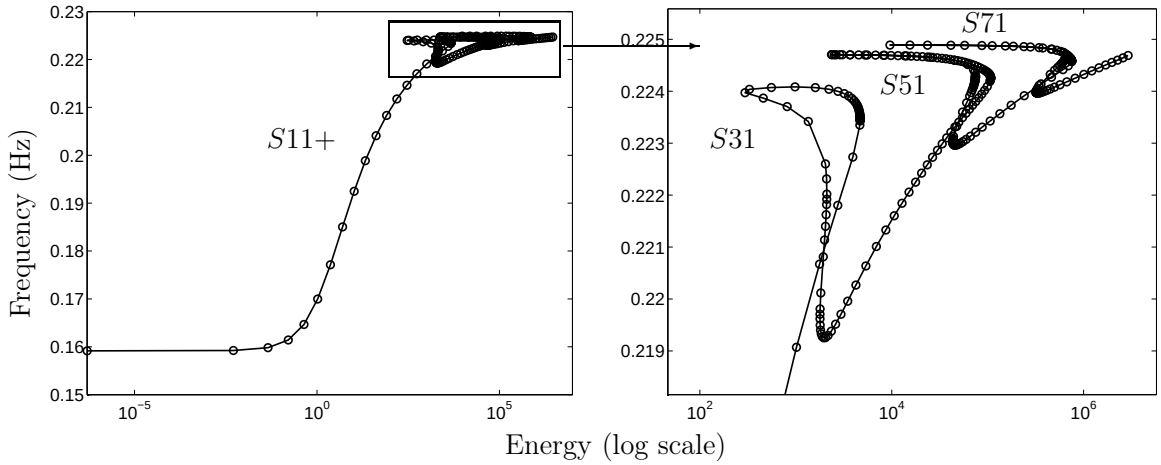

Figure 2.10: Frequency-energy plot at high energy for the 2DOF system (2.31). Left plot: in-phase NNM backbone $S11+$ and tongues (internally resonant NNMs). Right plot: close-up of the recurrent series of tongues ($S31$, $S51$ and $S71$) at high energy. The computed points are represented by $\circ$.

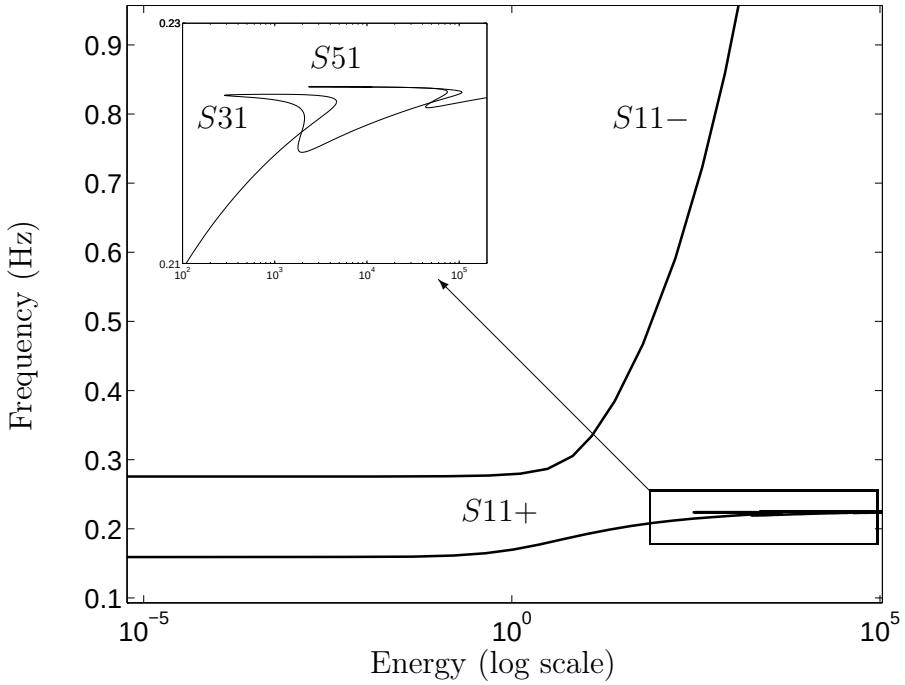

Figure 2.11: Frequency-energy plot of the 2DOF system (2.31).

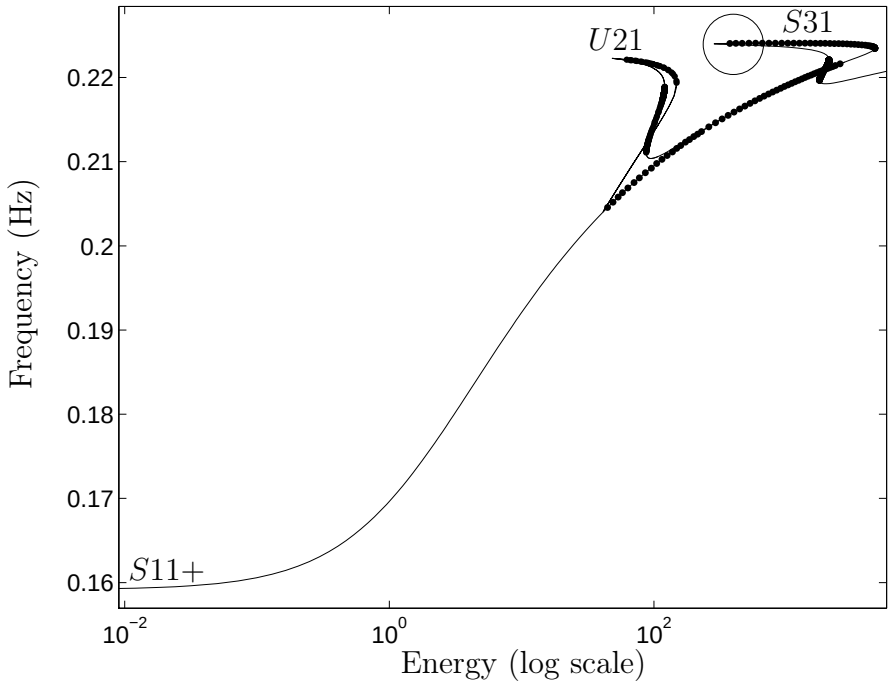

Figure 2.12: Close-up of $S11+$ for the 2DOF system (2.31) with stability results (——: stable NNM motions; • • • : unstable NNM motions).

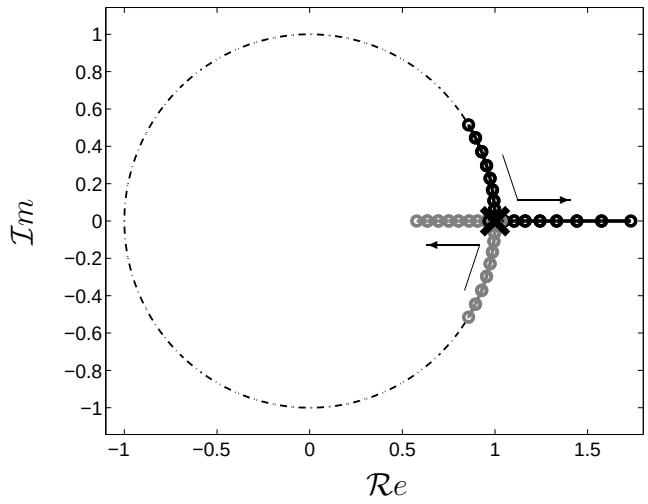

Figure 2.13: Evolution of the Floquet multipliers in the complex plane corresponding to the circled area in Figure 2.12. One Floquet multiplier is shown in black, another one in grey. The other two, which stay at +1, are represented by crosses.

leaves the unit circle through 1.

This example illustrates the efficiency of the algorithm for NNM computation, even for higher energy where the dynamics of this seemingly simple system becomes complicated, with the presence of several internal resonances.

2.5 Concluding Remarks

In this chapter, a numerical method for the computation of NNMs of nonlinear vibrating structures was introduced. The approach targets the computation of the NNMs of undamped mechanical structures discretized by finite elements and relies on the numerical continuation of periodic solutions. To this end, the proposed algorithm combines shooting and pseudo-arclength continuation methods. This computational framework allows to relax the assumption of small-amplitude motions of most existing techniques based on asymptotic approaches. The NNMs are then obtained accurately, even in strongly nonlinear regimes, and in a fairly automatic manner. The algorithm was illustrated using a 2DOF system.

This method represents a first step toward an effective and practical NNM computation with limited implementation effort. Through this numerical technique, nonlinear modal analysis of more complex structural models, compared to low-dimensional (i.e., with a few DOFs) and weakly nonlinear systems typically studied in the literature, is possible. In this context, the next chapter deals with an essentially nonlinear system, a discrete model of a nonlinear bladed disk and a finite element model of a full-scale aircraft. One limitation of this approach is that it relies on extensive numerical simulations which may be computationally intensive for large-scale finite element models.

Chapter 3

Numerical Applications of Nonlinear Normal Mode Computation

Abstract

The objective of the present chapter is to compute, using the numerical algorithm described in Chapter 2, the nonlinear normal modes (NNMs) of mechanical systems of increasing complexity, namely an essentially nonlinear 2DOF system, a discrete model of a bladed disk assembly and a finite element model of a full-scale aircraft. This is achieved to demonstrate the ability of the proposed method for NNM computation. Furthermore, the presence of complicated NNM motions, including internal resonances and strong motion localization, is discussed.

3.1 Introduction

This chapter is dedicated to the exploitation of the numerical method, proposed in Chapter 2, to compute the nonlinear normal modes (NNMs) of nonlinear vibrating structures. To this end, theoretical modal analysis of different mechanical systems is carried out. In addition to demonstrating the efficiency of the NNM computation, this chapter illustrates several nonlinear phenomena such as complex modal interactions and mode localization.

To highlight the capabilities of the computational method, three distinct systems are studied successively. First, an essentially nonlinear 2DOF system is briefly considered. Unlike perturbation techniques, this example shows that the numerical procedure is not limited to weakly nonlinear regimes, and can thereby deal with essentially nonlinear systems. Next, the NNM computation of more complex structures, in terms of number of DOFs, is addressed. To this end, the study of a discrete model of a nonlinear bladed disk assembly is carried out. Finally, a finite element model of a real-life aircraft with softening nonlinearities is examined.

3.2 Essentially Nonlinear 2DOF System

The method described in the previous chapter can accurately compute the NNMs in strongly nonlinear regimes of motion. For illustration, a 2DOF system with an essential nonlinearity is considered. The system is depicted in Figure 3.1, and its motion is governed by the equations

$$\begin{aligned} m_1\,\ddot{x}_1 + k_1\,x_1 + k_{nl_1}\,x_1^3 + k_{nl_2}(x_1 - x_2)^3 &= 0 \\ m_2\,\ddot{x}_2 + k_{nl_2}(x_2 - x_1)^3 &= 0 \end{aligned} \tag{3.1}$$

with $m_1 = k_1 = k_{nl_2} = 1$, $k_{nl_1} = 0.5$ and $m_2 = 0.05$.

In the context of vibration mitigation, the dynamics of such systems have been extensively studied by Vakakis and co-workers [45, 62, 72, 152] using the NNM concept. The motivation for using an essential nonlinearity is that the nonlinear attachment possesses no preferential resonant frequency; it can therefore interact with a single-DOF structure in a frequency-independent fashion or with virtually any mode of a multi-DOF structure.

Thanks to the proposed algorithm, system (3.1) has been successfully examined in recent works [159, 160], dealing with the design of nonlinear vibration absorbers. As for the 2DOF system in Chapter 1, a rich and complicated dynamics has been highlighted. Its complete description is nevertheless beyond the scope of the present section. The frequency-energy plot (FEP) of Figure 3.2 represents the computed NNM branches of system (3.1), which include the in-phase mode $S11+$, the out-of-phase mode $S11-$, and several internal resonances ($S13$, $S31$, $S15$, $S17$, $S19$). For clarity, stability is not indicated in this plot. A particular characteristic of this system is that $S11+$ is not bounded in frequency unlike the previous 2DOF system studied in Chapters 1 and 2.

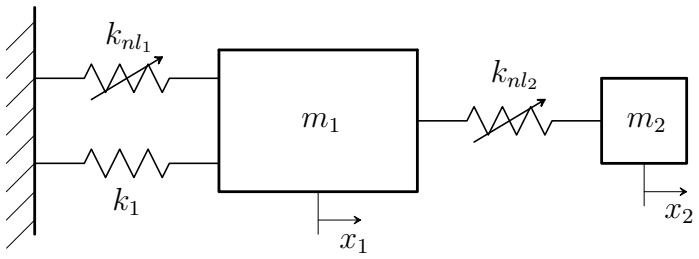

Figure 3.1: 2DOF system with an essential nonlinearity.

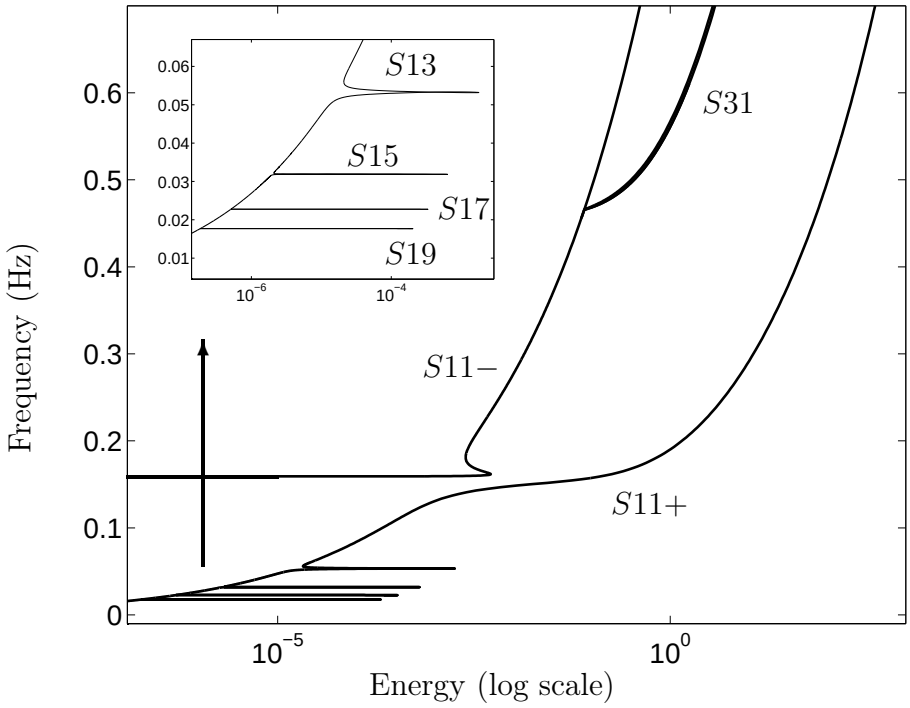

Figure 3.2: FEP for the 2DOF system with an essential nonlinearity.

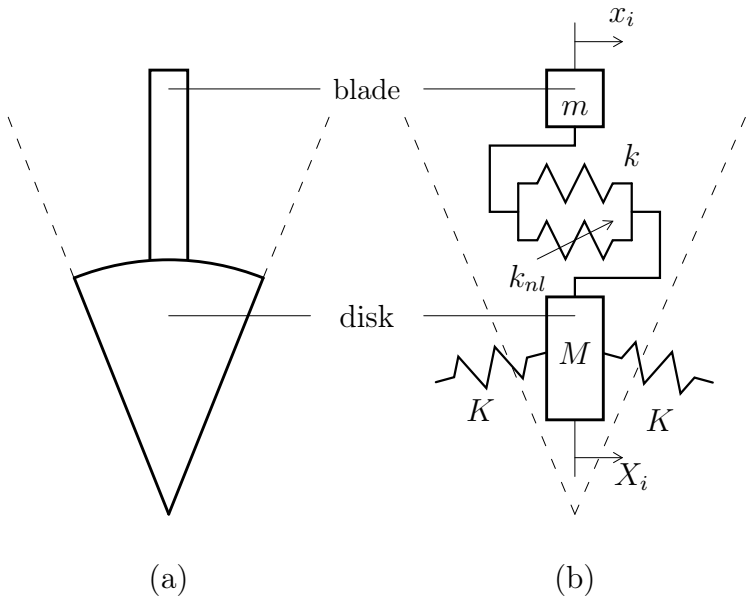

Figure 3.3: One sector of the nonlinear bladed disk assembly. (a) Continuous structure; (b) discrete model.

3.3 Nonlinear Bladed Disk

The NNMs of a more complex system consisting of a nonlinear periodic structure with cyclic symmetry are now investigated. To this end, the modal shapes and frequencies of oscillation of the different NNM branches are computed using the proposed numerical algorithm.

The system considered here is a simplified mathematical model of a bladed disk assembly. This model, though simplified, allows investigating interesting and complex dynamic phenomena related to the presence of nonlinearity. The lumped parameter model admits a single DOF for each blade and includes a similarly simplified representation of the flexible disk. The bladed disk is composed of 30 sectors assembled with cyclic periodicity; a single sector is represented in Figure 3.3. Each sector is modeled using disk (M) and blade (m) lumped masses, coupled by linear (k) and cubic (k_{nl}) springs. The nonlinear springs can, for instance, be representative of geometrically nonlinear effects in slender blades. The disk masses are connected together by linear springs K. The equations of motion of this 60-DOF system are

$$\begin{aligned} m\,\ddot{x}_i + k(x_i - X_i) + k_{nl}(x_i - X_i)^3 &= 0 \\ M\,\ddot{X}_i + K(X_i - X_{i+1}) + K(X_i - X_{i-1}) + k(X_i - x_i) + k_{nl}(X_i - x_i)^3 &= 0 \end{aligned} \tag{3.2}$$

for $i = 1, \ldots, 30$, where $X_{31} = X_1$, $X_0 = X_{30}$ (conditions of cyclic periodicity). X_i and x_i are the displacements of the disk and blade masses of the ith sector, respectively. The

values $M = 1$, $m = 0.3$, $K = 1$, $k = 1$, $k_{nl} = 0.1$ are used herein.

3.3.1 Modal Analysis of the Underlying Linear System

Before studying the NNMs of the nonlinear bladed disk assembly, the natural frequencies and mode shapes of the underlying linear system are first discussed. All bladed assemblies with circumferential symmetry exhibit *single* and *double* modes [37]:

- Double modes represent the majority. They have the same natural frequency and similar mode shapes. In fact, no unique mode shapes can be specified for these modes. Rather, it is sufficient to specify two suitably orthogonal shapes and to note that, when vibrating freely at that natural frequency, the structure can assume any form given by a linear combination of the two specified shapes. Further, at the corresponding natural frequency, the assembly can vibrate in any combination of $\cos n\theta$ and $\sin n\theta$ circumferential distributions of displacement around the assembly; i.e., in a shape of the form $\cos n\theta + \phi$. The mode shape is characterized by n *nodal diameters* since the displacement is constrained to be zero along n-equally spaced diametral lines. The mode shapes of a mode pair have mutually orthogonal nodal diameters.
- Single modes correspond to motion with all the blades undergoing, either in-phase (0 nodal diameter) or out-of-phase (N/2 nodal diameters) motion.

The natural frequencies of the underlying linear bladed assembly are listed in Table 3.1, where the modes are denoted by the integer pair (n,p), which corresponds to the number of nodal circles n and nodal diameters p for the considered mode. In the model (3.2), the nodal circle parameter n can only take the values $n = 0$ or $n = 1$, according to whether the blade and disk masses undergo in-phase or out-of-phase motion, respectively. One observes the existence of 28 pairs of double modes and 4 single modes. Figure 3.4 depicts four representative linear normal modes (LNMs) of the bladed assembly, namely mode (0,15) and one mode of the mode pairs (0,1), (1,5) and (1,14).

3.3.2 Nonlinear Modal Analysis

Using the previously described algorithm, NNM branches are computed by starting from the corresponding LNMs at low energy and gradually increasing the total energy in the system. The computed backbone branches are represented in Figure 3.5 and form the skeleton of the FEP. As we shall see, other NNM branches bifurcate from and coalesce into these backbone branches.

The first noticeable feature in Figure 3.5 is the frequency-energy dependence of the NNMs. The oscillation frequency of the modes with 1 nodal circle is strongly affected by the

Mode	Nodal circles	Nodal diameters	Freq. (rad/s)	Mode	Nodal circles	Nodal diameters	Freq. (rad/s)
1	0	0	0.000	31	1	0	2.082
2,3	0	1	0.183	32,33	1	1	2.084
4,5	0	2	0.363	34,35	1	2	2.092
6,7	0	3	0.536	36,37	1	3	2.104
8,9	0	4	0.700	38,39	1	4	2.123
10,11	0	5	0.850	40,41	1	5	2.147
12,13	0	6	0.985	42,43	1	6	2.178
14,15	0	7	1.103	44,45	1	7	2.215
16,17	0	8	1.202	46,47	1	8	2.258
18,19	0	9	1.282	48,49	1	9	2.304
20,21	0	10	1.346	50,51	1	10	2.350
22,23	0	11	1.394	52,53	1	11	2.394
24,25	0	12	1.428	54,55	1	12	2.431
26,27	0	13	1.452	56,57	1	13	2.460
28,29	0	14	1.465	58,59	1	14	2.478
30	0	15	1.470	60	1	15	2.485

Table 3.1: Natural frequencies of the underlying linear bladed disk assembly.

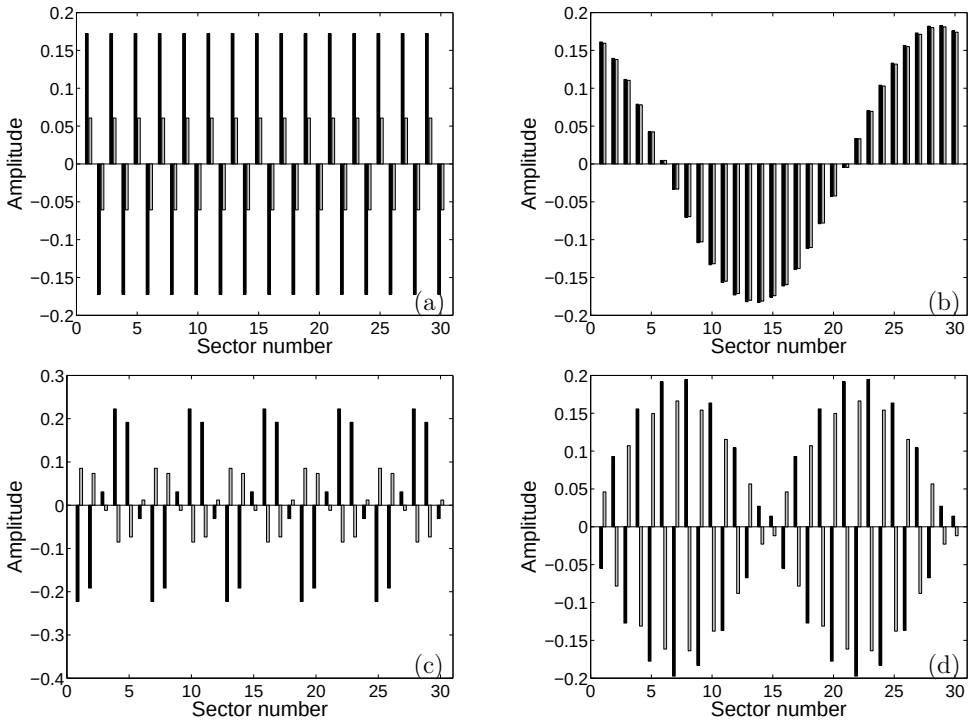

Figure 3.4: Representative LNMs of the bladed assembly; the blade and disk masses are shown in black and grey, respectively. (a) Mode (0,15) and one mode of the mode pair (b) (0,1); (c) (1,5) and (d) (1,14).

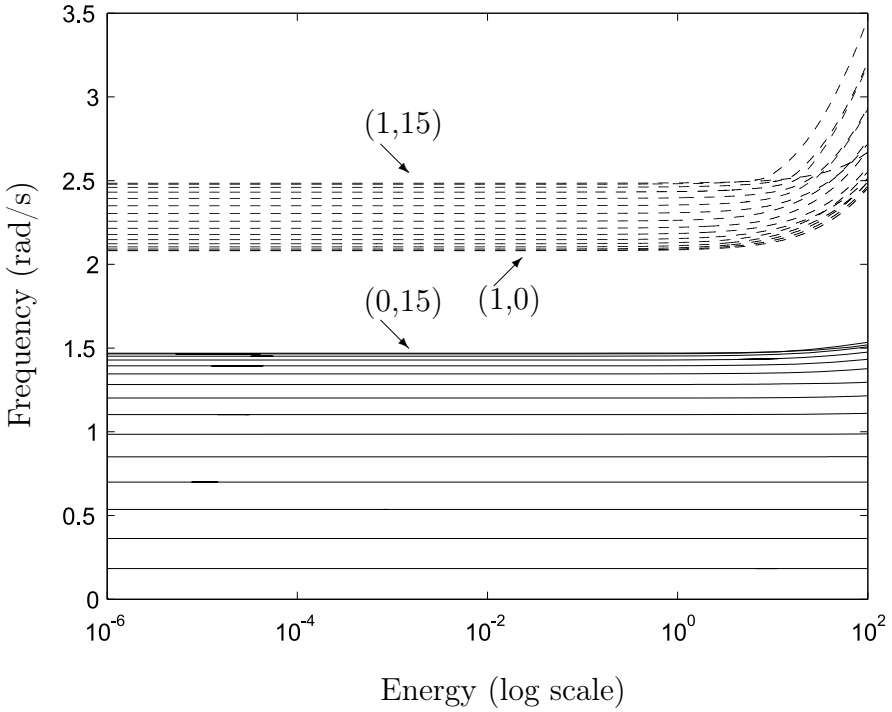

Figure 3.5: FEP of NNMs of the bladed disk assembly. Solid lines: NNM with 0 nodal circle; dashed lines: NNM with 1 nodal circle.

nonlinearities in the system. For these modes, the blade and disk masses vibrate in an out-of-phase fashion, which enhances nonlinear effects. On the other hand, the oscillation frequency of the modes with 0 nodal circle is much less affected. This is because the blade and disk masses vibrate in an in-phase fashion for these modes.

Similar and Nonsimilar NNMs

In addition to the dependence of their oscillation frequency, the NNMs may also have their modal shapes vary with the total energy in the system. As mentioned in Chapter 1, according to Rosenberg's terminology, a similar NNM corresponds to an (energy-independent) straight modal line in the configuration space and occurs in systems presenting certain spatial symmetries. A nonsimilar NNM corresponds to a curve in the configuration space, the shape of which varies with the total energy. Due to its symmetry properties, the system possesses both similar and nonsimilar NNMs. Two examples of similar NNMs in the bladed disk are the nonlinear extension of the LNMs with 0 nodal diameters, namely modes (0,0) and (1,0). Mode (0,0) is a rigid-body mode, which is obviously unaffected by nonlinearity. The FEP of mode (1,0) in Figure 3.6 clearly depicts that, while the NNM frequency is altered by the nonlinearities in the system, the modal shape remains unchanged.

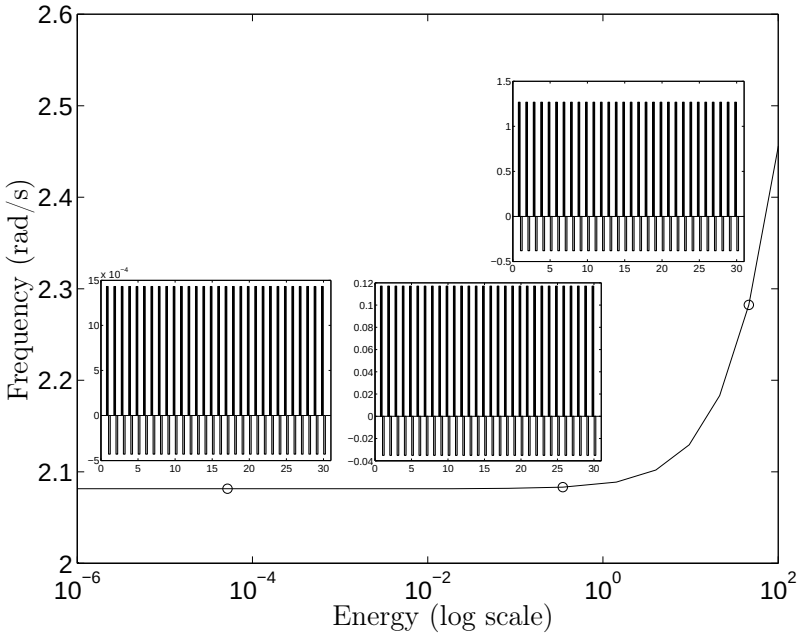

Figure 3.6: FEP of mode (1,0). NNM shapes represented by bar graphs are inset; they are given in terms of the initial displacements that realize the periodic motion (with zero initial velocities assumed). The blade and disk masses are shown in black and grey, respectively.

Nonsimilar NNMs resemble the corresponding LNMs at low energy. The structure (i.e., the number of nodal circles and diameters) is preserved, and, as for the modes of the linear system, they mostly appear in pair. Nonsimilar NNMs in this system are either weakly, moderately or strongly affected by nonlinearity for increasing energy levels:

- Figure 3.7 represents a mode of the mode pair (0,2), whose shape is almost energy-independent.
- Figure 3.8 shows that the NNM motions of mode pair (0,14) have a marked energy dependence.
- A remarkable property of the NNM motions of mode (1,14) is that the vibrational energy localizes to a limited number of sectors (4 in this case), the remaining of the system being virtually motionless (see Figure 3.9). The resulting spatial confinement of the energy causes the responses of some blades to become dangerously high and might lead to premature failure of the blades. For illustration, the time series corresponding to such an NNM motion are displayed in Figure 3.10. This localization phenomenon was also observed in linear mistuned bladed assemblies [24], but, here, it occurs even in the absence of structural disorder and direct interblade coupling. Localization is in fact the result of the frequency-energy dependence inherent to nonlinear oscillations, as mentioned in Chapter 1 and discussed in reference [155].

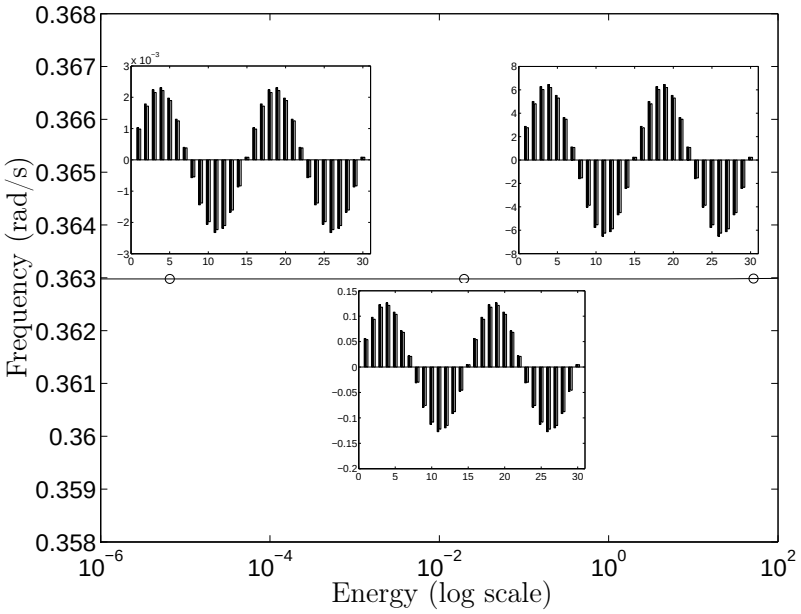

Figure 3.7: FEP of one mode of the mode pair (0,2). NNM shapes represented by bar graphs are inset; they are given in terms of the initial displacements that realize the periodic motion (with zero initial velocities assumed). The blade and disk masses are shown in black and grey, respectively.

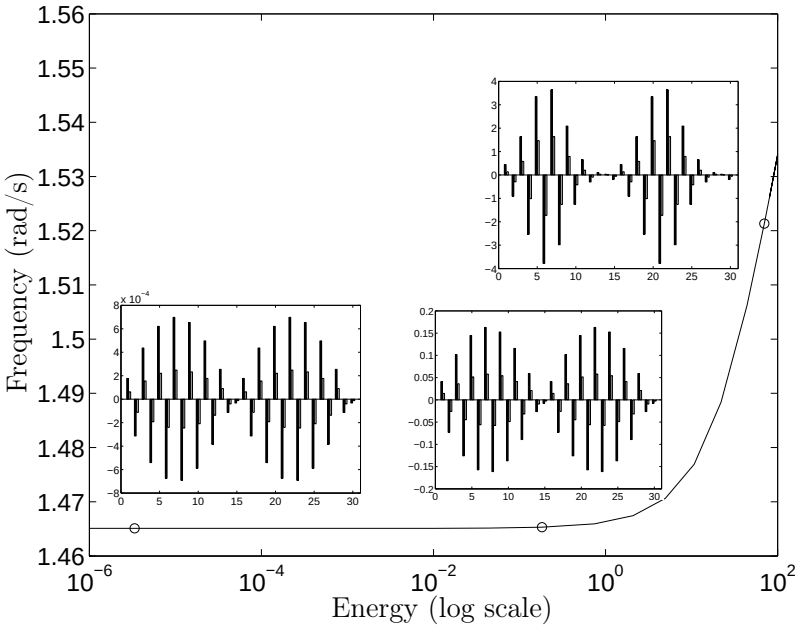

Figure 3.8: FEP of one mode of the mode pair (0,14). NNM shapes represented by bar graphs are inset; they are given in terms of the initial displacements that realize the periodic motion (with zero initial velocities assumed). The blade and disk masses are shown in black and grey, respectively.

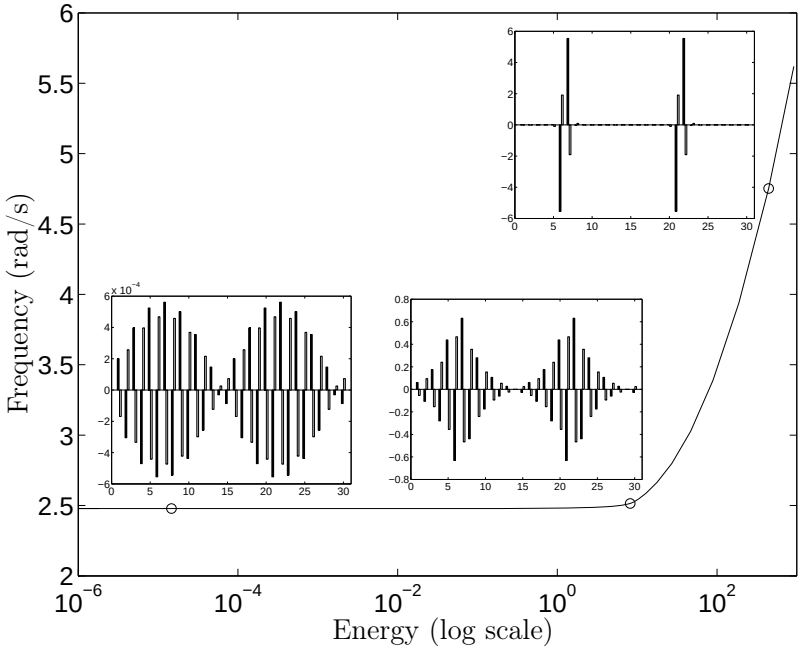

Figure 3.9: FEP of one mode of the mode pair (1,14). NNM shapes represented by bar graphs are inset; they are given in terms of the initial displacements that realize the periodic motion (with zero initial velocities assumed). The blade and disk masses are shown in black and grey, respectively.

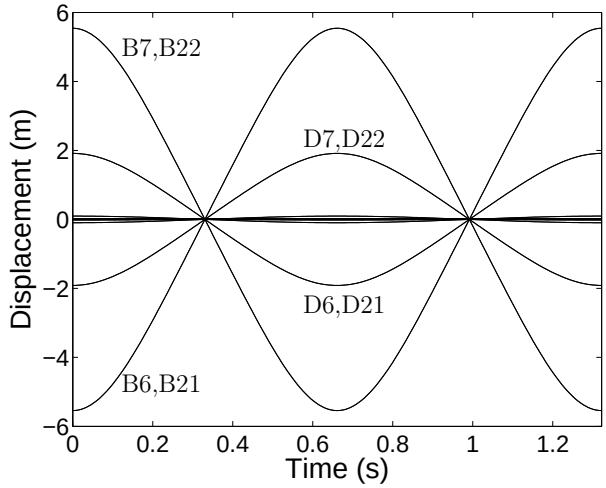

Figure 3.10: Time series corresponding to the localized NNM motion of mode (1,14) (see Figure 3.9).

All these NNM motions correspond to standing-wave motions in the sense that the system coordinates vibrate in a synchronous manner. They are represented by lines or curves in the configuration space. The phase condition used for their computation assumes that all initial velocities are zero (practical strategy, see Section 2.3.3). One therefore starts the motion from a maximum of the potential energy (see, e.g., Figure 3.10).

Modal Interaction: Internally Resonant NNMs

A first example of modal interaction is the 1:1 internal resonance between the two modes of a mode pair. This resonance scenario results in NNM motions which take the form of traveling waves and which are represented by ellipses in the configuration space. A detailed analytical study of these modes is given in reference [147]. Due to the existence of a phase difference between the coordinates, a different phase condition is considered for the NNM computation: only one initial velocity is set to zero (general strategy, see Section 2.3.3), which is compatible with a traveling-wave motion. For instance, Figure 3.11 depicts the NNM corresponding to 1:1 internal resonance between the modes of mode pair (1,3). The mode structure is preserved in the sense that this traveling-wave motion also features one nodal circle and three nodal diameters. Representative time series are shown in Figure 3.12 and clearly highlight that the motion is no longer synchronous. In this particular case, the traveling wave is propagating in the anticlockwise direction, but its companion propagating in the clockwise direction also exists. These modes have an important practical significance, because they can be excited with an appropriate engine order excitation.

Other resonance scenarios can be observed in this system through the occurrence of tongues of internally resonant NNMs, following a mechanism similar to that described in detail in Chapter 1. Unlike backbone branches, tongues are localized to a specific region of the FEP. They bifurcate from the backbone branch of a specific mode and coalesce into the backbone branch of another mode, thereby realizing an internal resonance between the two modes. For instance, Figure 3.13 depicts a 3:1 internal resonance between modes (0,6) and (1,12) in the FEP. To illustrate the resonance mechanism, the backbone of mode (1,12) is represented at the third of its characteristic frequency (this is relevant, because a periodic solution of period T is also periodic with period $3T$). This shows that a smooth transition from mode (0,6) to mode (1,12) occurs on the tongue. A further illustration is that modes M1 and M2, which are the modes right after and before the coalescence of the two NNM branches, are almost identical.

During this 3:1 internal resonance, the system vibrates along a subharmonic NNM; i.e., an NNM motion characterized by more than one dominant frequency component. On the branch of mode (0,6), the motion is characterized by one dominant frequency component, say ω. As we move along the tongue from this branch, a third harmonic progressively appears, and the system vibrates with two dominant frequency components ω and 3ω. As we progress further on the tongue, the third harmonic tends to dominate the component

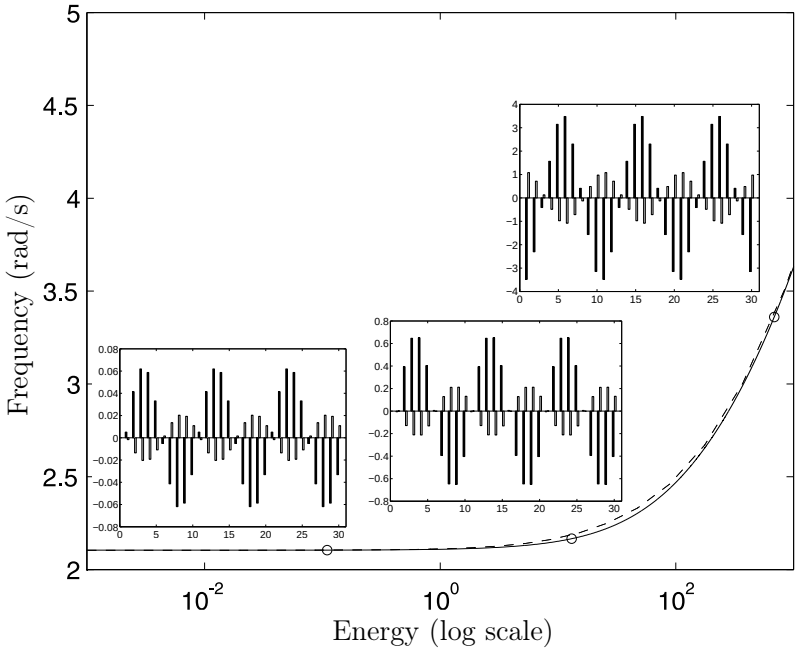

Figure 3.11: FEP of the traveling-wave NNM corresponding to 1:1 internal resonance between the modes of mode pair (1,3) (solid line). For comparison, the dashed line represents the backbone of one standing-wave NNM of the mode pair (1,3). NNM shapes represented by bar graphs are inset.

at the fundamental frequency, until this latter completely disappears. At this precise moment, a transition to mode (1,12) is realized. This transition is illustrated in Figure 3.14 using time series representative of the NNM motion at three different locations on the tongue.

As already reported in Chapter 1, modal interactions may occur without necessarily having commensurate linear natural frequencies in the underlying linear system. Indeed, the ratio of the linear natural frequencies of modes (0,6) and (1,12) is far from 3; it is equal to 2.47. However, a 3:1 internal resonance between the two modes can still be realized, because the frequency of mode (0,6) increases much less rapidly than that of mode (1,12), as shown in Figure 3.5. It turns out that a 3:1 internal resonance is not the only possible interaction between modes (0,6) and (1,12). Depending on the relative evolution of the frequencies on the backbones of these modes, other $n : m$ resonances with n and m being relatively prime integers can exist.

As a result, there exists a countable infinity of branches of internally resonant NNMs in this system, similarly to what was observed for the 2DOF system in Chapter 1. Figure 3.15 depicts the same FEP as in Figure 3.13, but the algorithm is not stopped after the tongue. Clearly, there is an intricate succession of modal interactions, each one being a different realization of an internal resonance between mode (0,6) and another mode of the system.

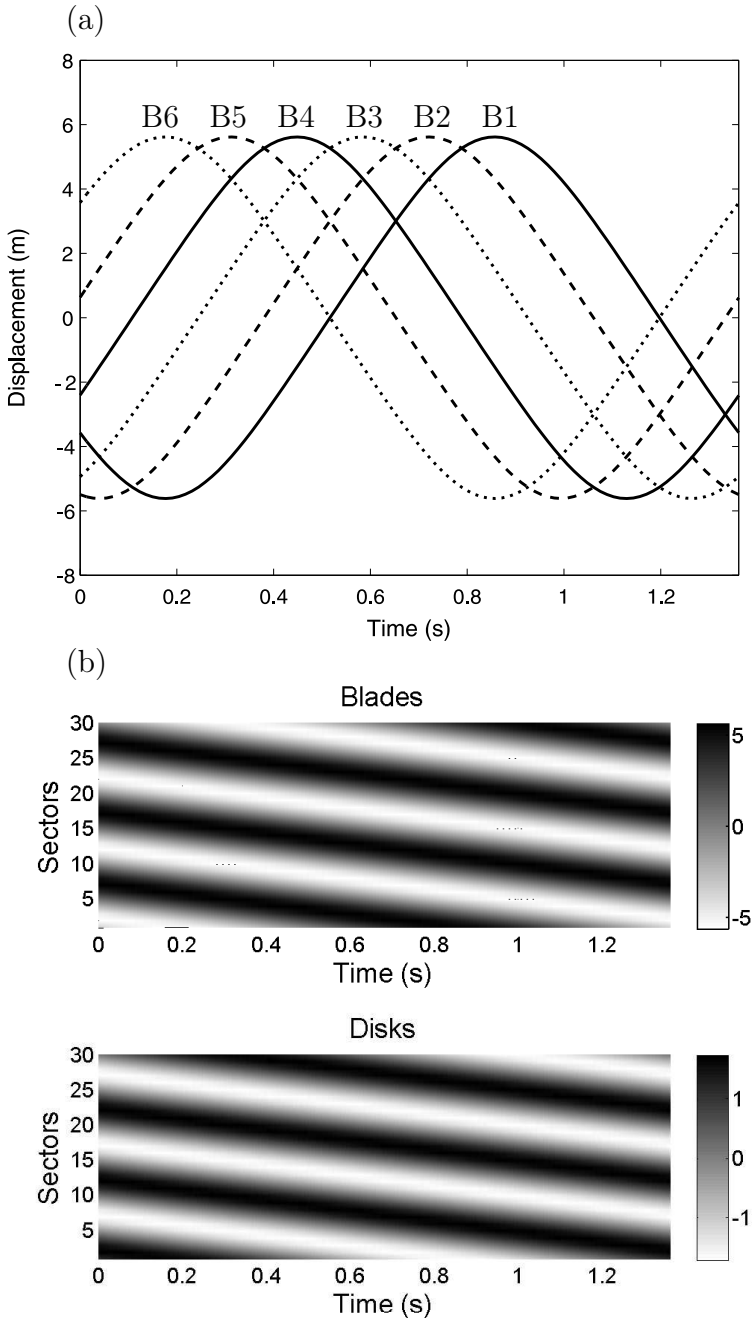

Figure 3.12: (a) Time series of the first six blades during traveling-wave NNM motion of mode pair (1,3) (see Figure 3.11); (b) contour plot.

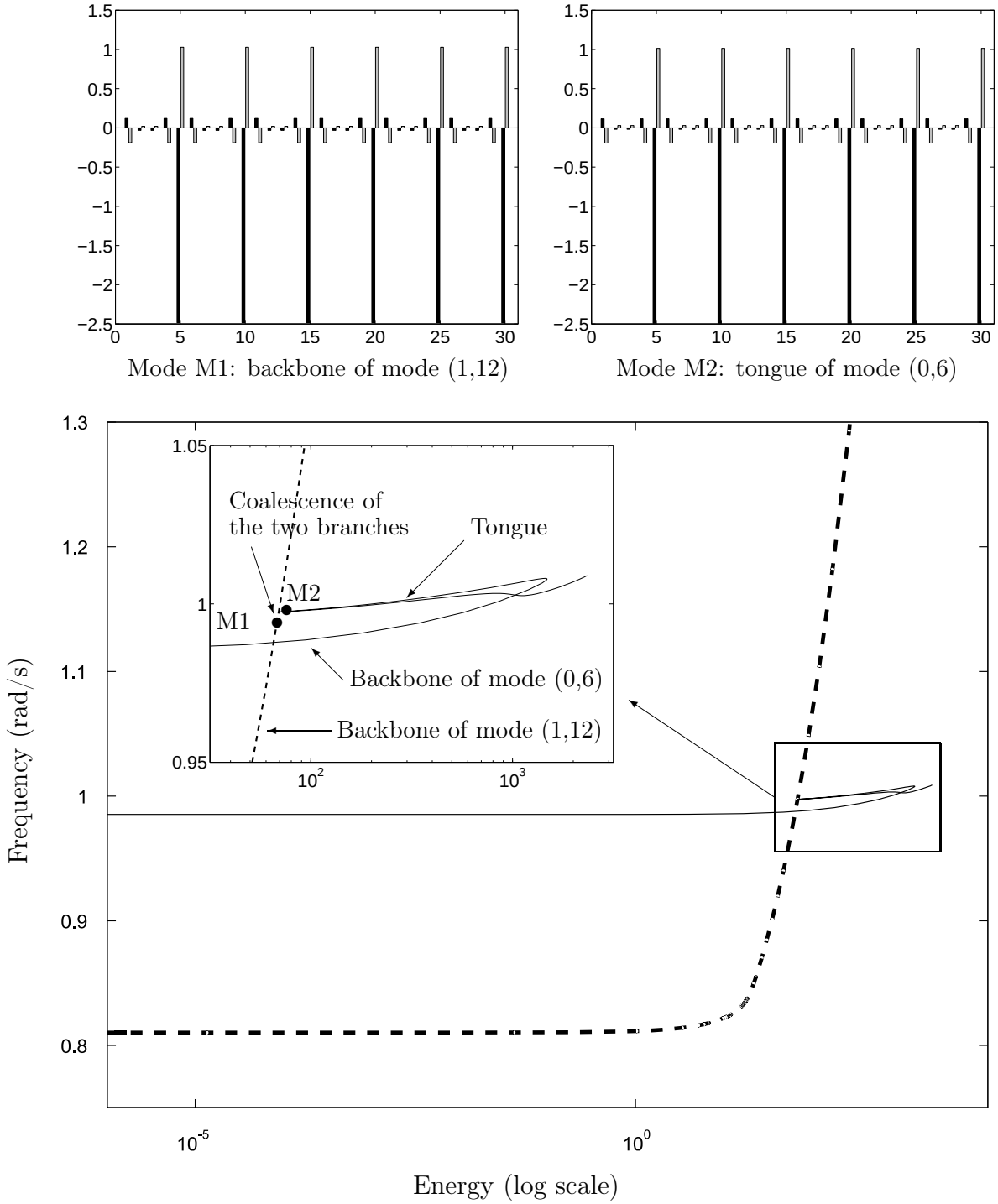

Figure 3.13: 3:1 internal resonance between modes of the mode pairs (0,6) and (1,12). The solid line corresponds to the backbone of one mode of the mode pair (0,6), which is continued by a tongue of internally resonant NNMs. The dashed line corresponds to the backbone of one mode of the mode pair (1,12) represented at the third of its dominant frequency.

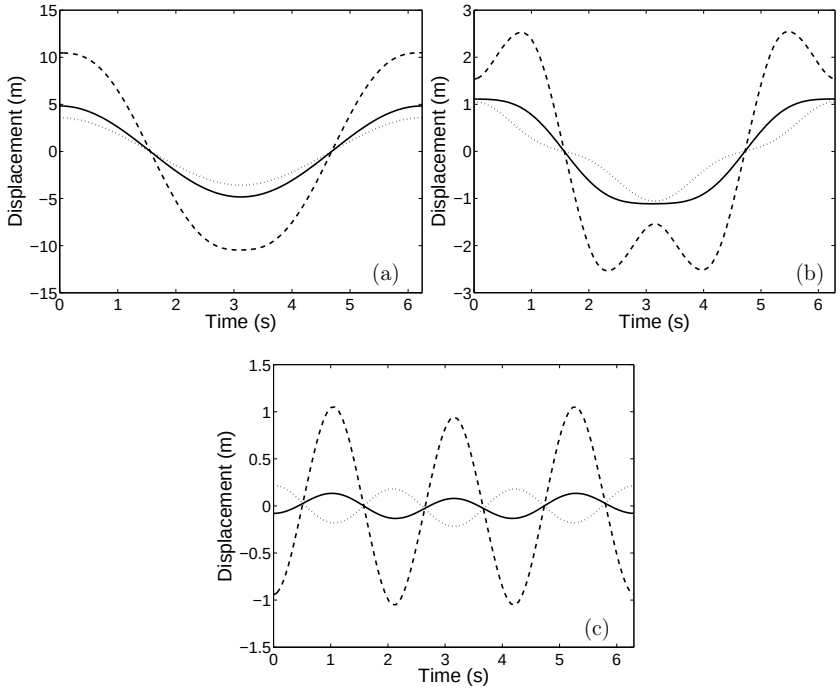

Figure 3.14: Time series corresponding to NNM motions on the tongue of 3:1 internal resonance (——: blade 1; − − −: disk 10; ·····: disk 14). (a) Beginning of the tongue (in the vicinity of the branch of mode (0,6)); (b) middle of the tongue; and (c) extremity of the tongue (in the vicinity of the branch of mode (1,12)).

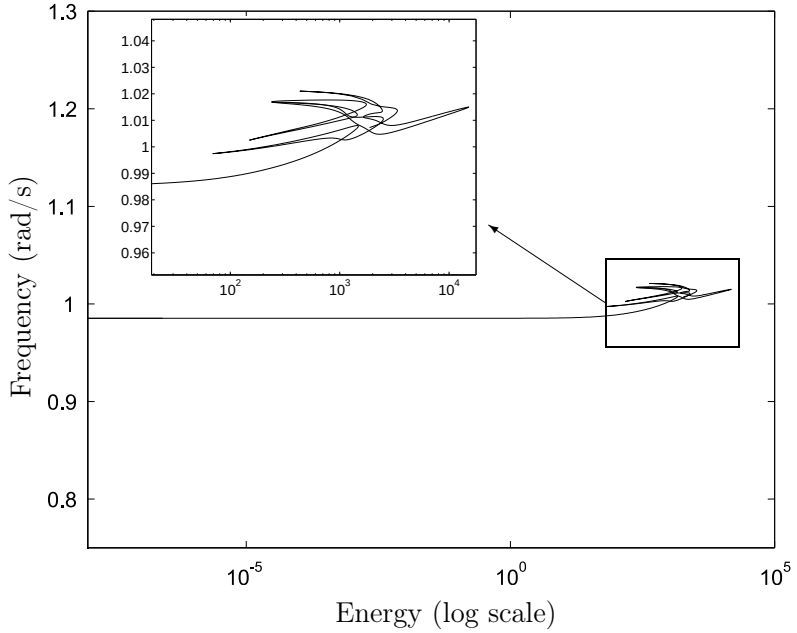

Figure 3.15: Intricate succession of modal interactions between mode (0,6) and other modes of the system.

Additional Mode Bifurcations

For linear mistuned bladed assemblies and according to the degree of detuning, double modes with identical frequencies may split into two different modes with distinct natural frequencies [37]. Due to mode bifurcations, mode splitting may still occur in nonlinear systems with cyclic symmetry. A direct consequence is that a mode pair can bifurcate into two mode pairs, and the number of NNMs exceeds the number of DOFs of the system. For illustration, the splitting of one mode of the mode pair (1,5) is depicted in Figure 3.16. Clearly, after the bifurcation, two NNM branches exist and are characterized by different oscillation frequencies and modal curves.

Other examples of mode bifurcations are shown in Figures 3.17 and 3.18 for the mode pair (1,14) and mode (1,15), respectively. Mode pair (1,14) undergoes a bifurcation during which a new NNM branch is generated. Interestingly, this branch is characterized by modes that are localized to two sectors only. Even more interesting is the bifurcation of mode (1,15), which generates mode shapes that are localized to only one sector. Depending on their stability properties, these NNMs may be excited in practice, giving rise to potentially harmful motion that must be accounted for.

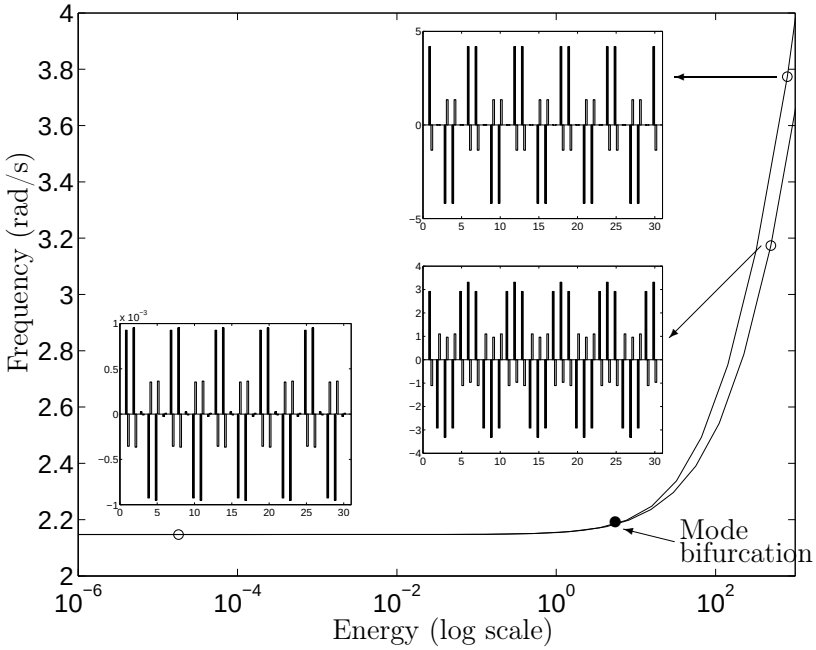

Figure 3.16: Splitting of one mode of the mode pair (1,5). NNM shapes represented by bar graphs are inset; they are given in terms of the initial displacements that realize the periodic motion (with zero initial velocities assumed). The blade and disk masses are shown in black and grey, respectively.

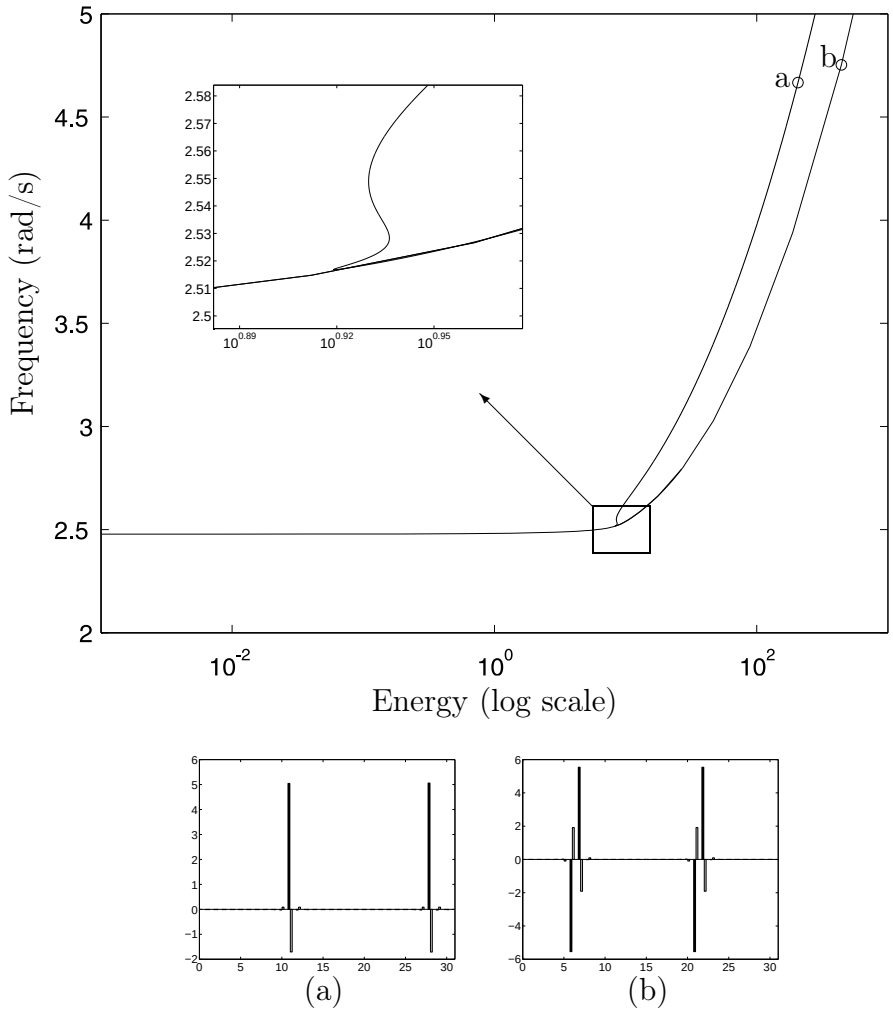

Figure 3.17: Bifurcation of the mode pair (1,14).

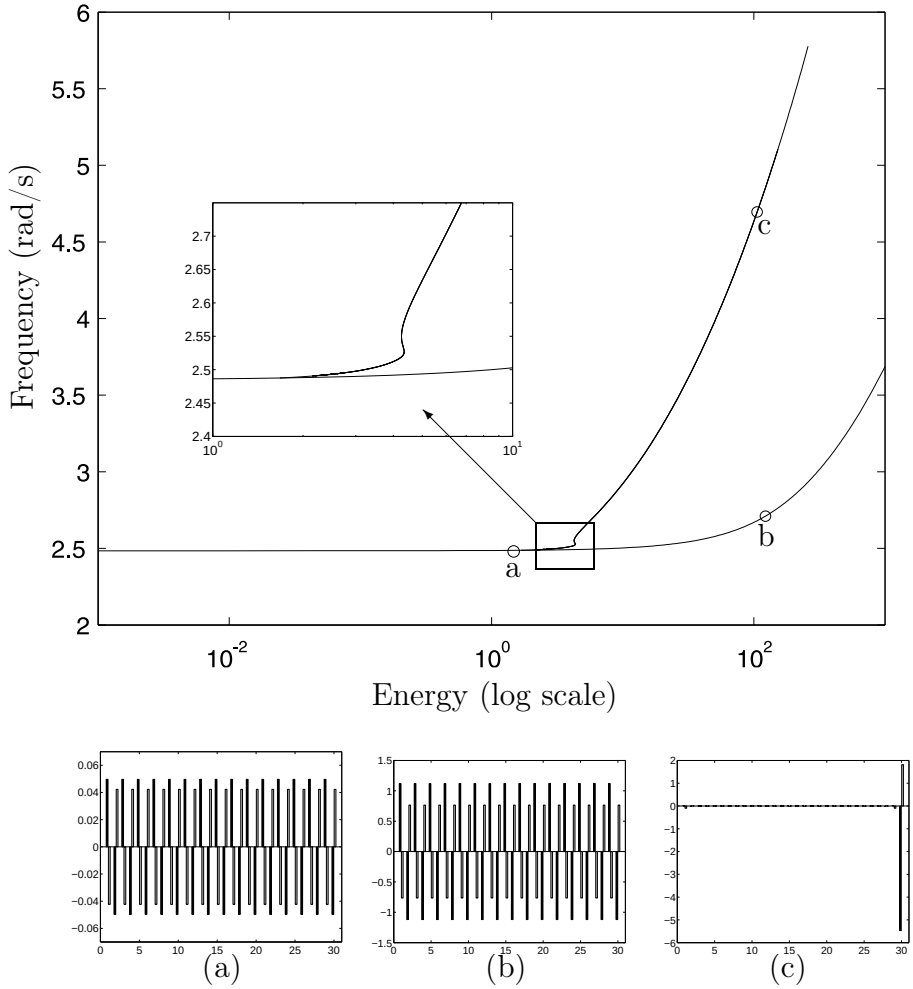

Figure 3.18: Bifurcation of mode (1,15).

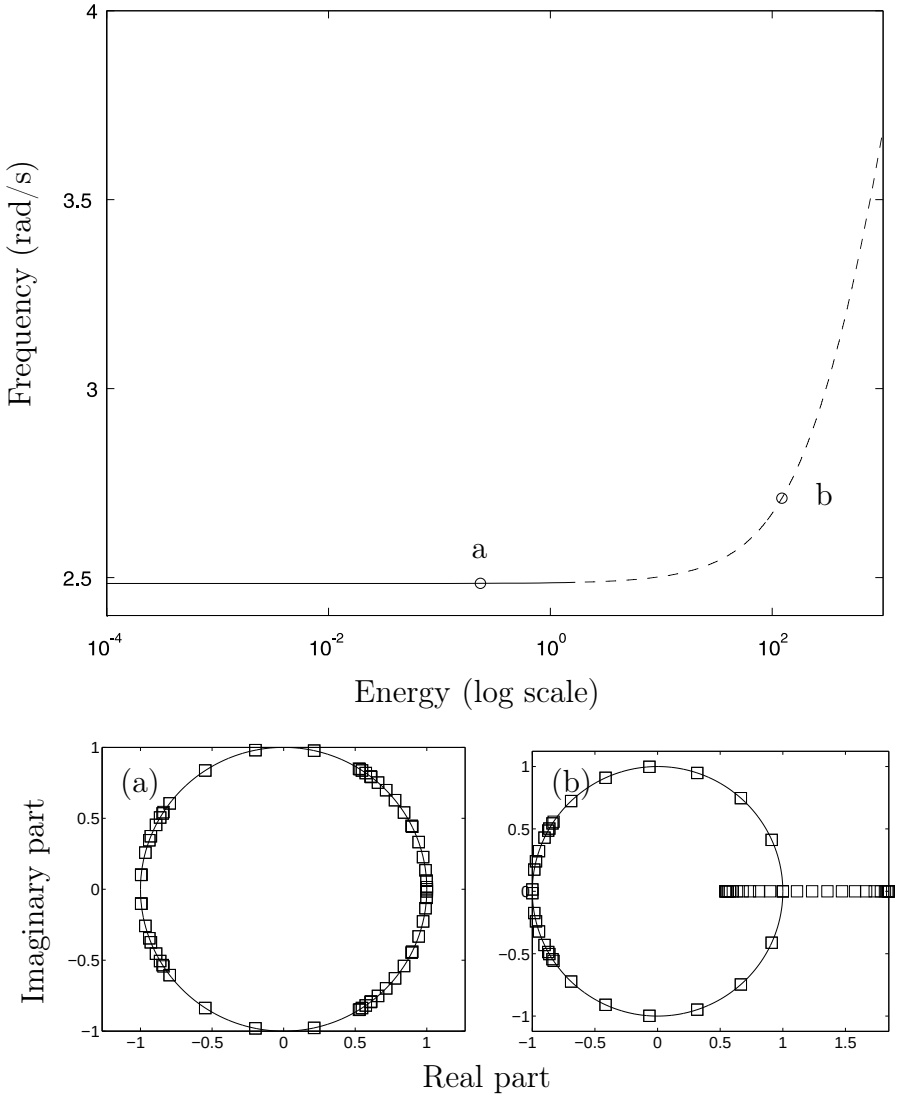

Figure 3.19: Stability analysis of mode (1,15). Top plot: FEP; a solid (dashed) line indicates stability (instability). Bottom plots: unit circle and Floquet multipliers represented by squares.

Mode Stability

Stability analysis is performed numerically through the eigenvalues of the monodromy matrix (i.e., the Floquet multipliers), which are a by-product of the proposed algorithm. For instance, Figure 3.19 shows the stability properties of mode (1,15). From very low energies to energies slightly above $1J$, the Floquet multipliers lie on the unit circle. The NNM motions are stable and, hence, physically realizable. From this latter energy, the Floquet multipliers leave the unit circle, and the NNM motions become unstable. This stability change occurs through a bifurcation, which coincides exactly with the generation of the branch of NNMs localized to one sector in Figure 3.18.

3.4 Full-Scale Aircraft

As a final example, the numerical computation of the NNMs of a complex real-world structure is addressed. This structure is the airframe of the Morane-Saulnier Paris aircraft, which is represented in Figure 3.20. This French jet aircraft was built during the 1950s and was used as a trainer and liaison aircraft. The structural configuration under consideration corresponds to the aircraft without its jet engines and standing on the ground through its three landing gears with deflated tires. For information, general characteristics are listed in Table 3.2. A specimen of this plane is present in ONERA's laboratory, and ground vibration tests exhibited nonlinear behavior in the connection between the wings and external fuel tanks located at the wing tip. As illustrated in Figure 3.21, this connection consists of bolted attachments.

3.4.1 Structural Model of the Morane-Saulnier Paris Aircraft

Finite Element Model of the Underlying Linear Structure

The linear finite element model of the full-scale aircraft, illustrated in Figure 3.22, was elaborated from drawings by ONERA [119]. The wings, vertical stabilizer, horizontal tail and fuselage are modeled by means of 2-dimensional elements such as beams and shells. The complete finite element model has more than 80000 DOFs. Three-dimensional spring elements, which take into account the structural flexibility of the tires and landing gears, are used as boundary conditions of the aircraft. At each wing tip, the fuel tank is connected with front and rear attachments (see Figure 3.21). In this linear model, these connections between the wings and the fuel tanks are modeled using beam elements. The linear model, originally created in the Nastran software, was converted and exploited in the Samcef finite element environment for this study.

The natural frequencies of the underlying linear system in the [0-50Hz] frequency range are given in Table 3.3. The first nine modes correspond to aircraft rigid-body modes: six

Figure 3.20: Morane-Saulnier Paris aircraft.

Length (m)	Wingspan (m)	Height (m)	Wing area (m^2)	Weight (kg)
10.4	10.1	2.6	18	1945

Table 3.2: Properties of the Morane-Saulnier Paris aircraft

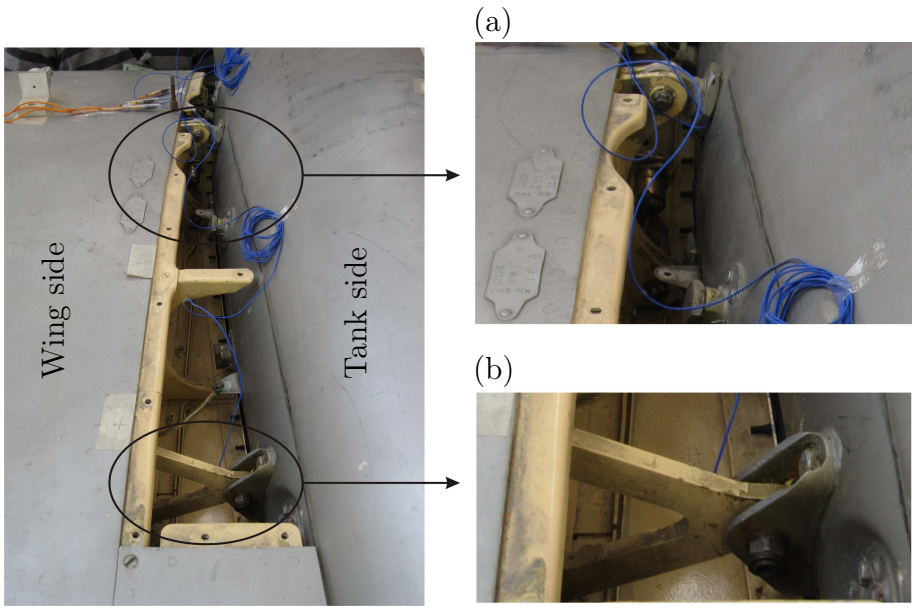

Figure 3.21: Connection between external fuel tank and wing tip (top view). Close-up of (a) front and (b) rear bolted attachments.

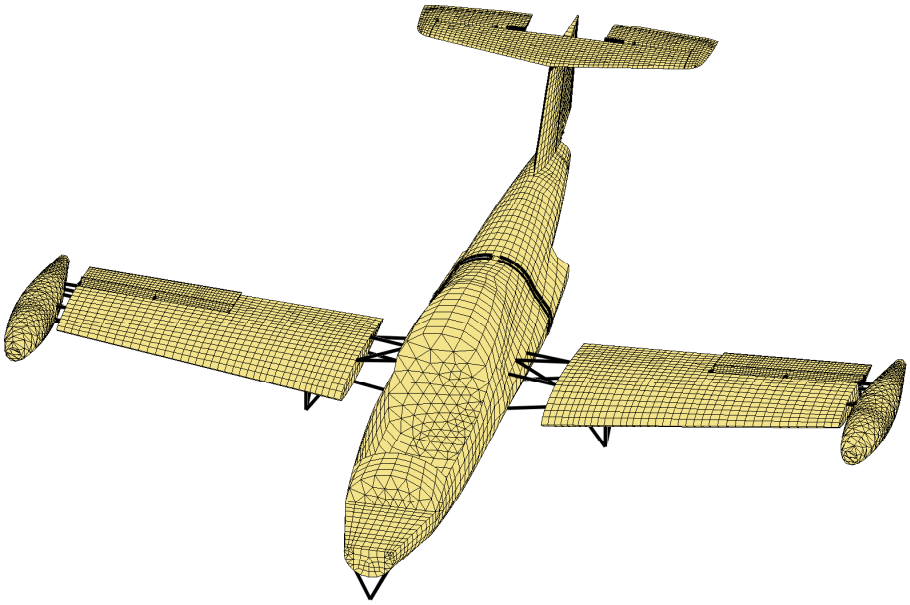

Figure 3.22: Finite element model of the Morane-Saulnier Paris aircraft.

Mode	Freq. (Hz)	Mode	Freq. (Hz)
1	0.0936	13	21.2193
2	0.7260	14	22.7619
3	0.9606	15	23.6525
4	1.2118	16	25.8667
5	1.2153	17	28.2679
6	1.7951	18	29.3309
7	2.1072	19	31.0847
8	2.5157	20	34.9151
9	3.5736	21	39.5169
10	8.1913	22	40.8516
11	9.8644	23	47.3547
12	16.1790	24	52.1404

Table 3.3: Natural frequencies of the linear finite element model of the Paris aircraft.

modes are modes of suspensions of the landing gear while the three others are associated to rigid-body motions of the control surfaces (i.e., the ailerons, elevator and rudder). The frequency range of the rigid-body modes is comprised between 0.09 and 3.57 Hz, i.e., noticeably lower than the first flexible mode located at 8.19 Hz. The modal shapes of different elastic normal modes of vibrations are depicted in Figure 3.23. Figure 3.23(a) represents the first wing bending mode. The first and second wing torsional modes are depicted in Figures 3.23(b) and 3.23(c). These two torsional modes correspond to symmetric and anti-symmetric wing motions, respectively. As shown thereafter, these modes are of particular interest in nonlinear regime since there is a significant deformation of the connections between the wings and fuel tanks. Indeed, the other modes mainly concern the aircraft tail and are consequently almost unaffected by these nonlinear connections.

Reduced-Order Model

The proposed algorithm for the numerical computation of NNMs is computationally intensive for the large-scale original model. Since the nonlinearities are spatially localized, condensation of the linear components of the model is an appealing approach for a computationally tractable and efficient calculation.

A reduced-order model of the linear finite element model is constructed using the Craig-Bampton (also called component mode synthesis) reduction technique [29, 46]. This method consists in describing the system in terms of some retained DOFs and internal vibration modes. By partitioning the complete system in terms of n_R remaining $\mathbf{x}_R$ and $n_C = n - n_R$ condensed $\mathbf{x}_C$ DOFs, the n governing equations of motion of the global finite element model are written as

$$\begin{bmatrix} \mathbf{M}_{RR} & \mathbf{M}_{RC} \\ \mathbf{M}_{CR} & \mathbf{M}_{CC} \end{bmatrix} \begin{bmatrix} \ddot{\mathbf{x}}_R \\ \ddot{\mathbf{x}}_C \end{bmatrix} + \begin{bmatrix} \mathbf{K}_{RR} & \mathbf{K}_{RC} \\ \mathbf{K}_{CR} & \mathbf{K}_{CC} \end{bmatrix} \begin{bmatrix} \mathbf{x}_R \\ \mathbf{x}_C \end{bmatrix} = \begin{bmatrix} \mathbf{g}_R \\ \mathbf{0} \end{bmatrix} \tag{3.3}$$

The Craig-Bampton method expresses the complete set of initial DOFs in terms of: (i) the remaining DOFs through the static modes (resulting from unit displacements on the remaining DOFs) and (ii) a certain number $m < n_C$ of internal vibration modes (relating to the primary structure fixed on the remaining nodes). Mathematically, the reduction is described by relation

$$\begin{bmatrix} \mathbf{x}_R \\ \mathbf{x}_C \end{bmatrix} = \begin{bmatrix} \mathbf{I} & \mathbf{0} \\ -\mathbf{K}_{CC}^{-1}\mathbf{K}_{CR} & \mathbf{\Phi}_m \end{bmatrix} \begin{bmatrix} \mathbf{x}_R \\ \mathbf{y} \end{bmatrix} = \mathbf{R} \begin{bmatrix} \mathbf{x}_R \\ \mathbf{y} \end{bmatrix} \tag{3.4}$$

which defines the $n \times (n_R + m)$ reduction matrix $\mathbf{R}$. $\mathbf{y}$ are the modal coordinates of the m internal LNMs collected in the $n_C \times m$ matrix $\mathbf{\Phi}_m = [\phi_{(1)} \dots \phi_{(m)}]$. These modes are solutions of the linear eigenvalue problem corresponding to the system fixed on the remaining nodes

$$\left(\mathbf{K}_{CC} - \omega_{(j)}^2 \mathbf{M}_{CC}\right) \phi_{(j)} = \mathbf{0} \tag{3.5}$$

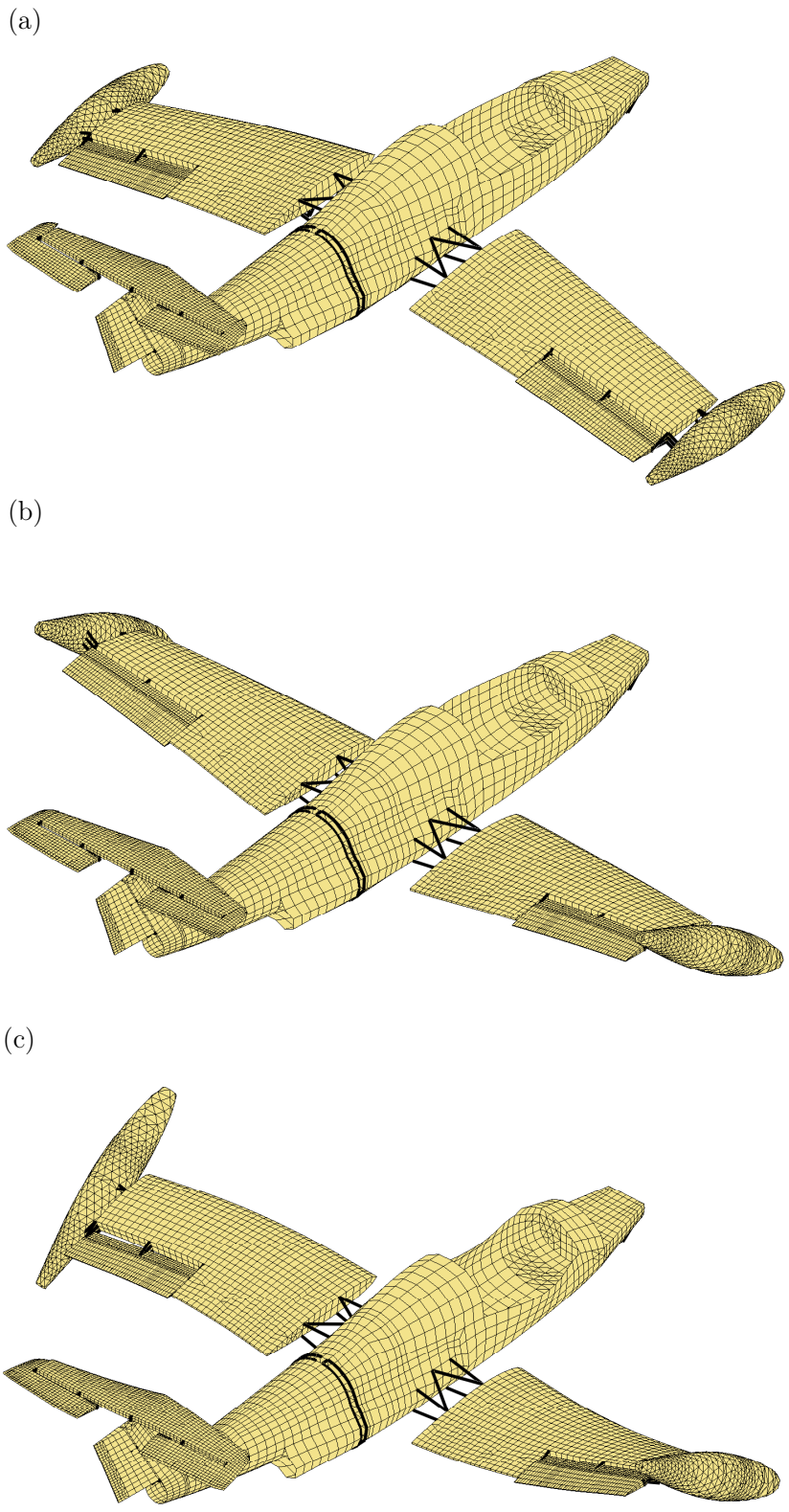

Figure 3.23: Normal modes of the linear finite element model of the Morane-Saulnier Paris aircraft. (a) First wing bending mode (8.19 Hz), (b) first (symmetric) wing torsional mode (31.08 Hz) and (b) second (anti-symmetric) wing torsional mode (34.92 Hz).

The reduced model is thus defined by the $(n_R+m)\times(n_R+m)$ reduced stiffness and mass matrices given by

$$\begin{aligned}\overline{\mathbf{M}} &= \mathbf{R}^*\mathbf{M}\mathbf{R}\\ \overline{\mathbf{K}} &= \mathbf{R}^*\mathbf{K}\mathbf{R}\end{aligned} \tag{3.6}$$

where star denotes the transpose operation. After reduction, the system configuration is expressed in terms of the reduced coordinates (i.e., the remaining DOFs and the modal coordinates). The initial DOFs of the complete model are then determined by means of the reduction matrix using relation 3.4.

In order to introduce the nonlinear behavior of the connections between the wings and the tanks, the reduced-order linear model of the aircraft is constructed by keeping one node on both sides of the attachments. For each wing, four nodes are retained: two nodes for the front attachment and two nodes for the rear attachment. In total, only eight nodes of the finite element model are kept to build the reduced model. It is completed by retaining the first 500 internal modes of vibrations. Finally, the model is thus reduced to 548 DOFs: 6 DOFs per node (3 translations and 3 rotations) and 1 DOF per internal mode. The reduction is performed using the Samcef software. The generated reduced-order model is next imported in the MATLAB environment.

Before proceeding to nonlinear analysis, the accuracy of the reduced-order linear model is assessed. To this end, the LNMs of the initial complete finite element model are compared to those predicted by the reduced model. The deviation between the mode shapes of the original model $\mathbf{x}_{(o)}$ and of the reduced model $\mathbf{x}_{(r)}$ is determined using the Modal Assurance Criterion (MAC)

$$\mathrm{MAC} = \frac{\left|\mathbf{x}_{(o)}^*\mathbf{x}_{(r)}\right|^2}{\left|\mathbf{x}_{(o)}^*\mathbf{x}_{(o)}\right|\left|\mathbf{x}_{(r)}^*\mathbf{x}_{(r)}\right|} \tag{3.7}$$

MAC values range from 0 in case of no correlation to 1 for a complete coincidence. In the [0-100Hz] range, MAC values between modes shapes are all greater than 0.999 and the maximum relative error on the natural frequencies is 0.2%. It therefore validates the excellent accuracy of the reduced linear model in this frequency range. It is worth noticing that less internal modes are sufficient to ensure such a correlation in the [0-100Hz] frequency range, which is typically the range of interest for aircrafts. However, a larger number of modes was deliberately chosen for two main reasons. On the one side, it serves to illustrate the ability of the numerical algorithm to deal with the NNM computation of higher-dimensional systems. On the other hand, due to nonlinearity, modes of higher frequencies may interact with lower modes of interest. In nonlinear regimes, internal modes of higher frequencies may then be necessary to guarantee the accuracy of the model.

Nonlinear Model

The existence of a softening nonlinear behavior was evidenced during different vibration tests conducted by ONERA. In particular, FRF measurements revealed the decrease of resonant frequencies with the level of excitation. The connections between the wings and fuel tanks were assumed to cause this observed nonlinear effect.

To confirm this hypothesis, both (front and rear) connections of each wing were instrumented and experimental measurements were carried out. Specifically, accelerometers were positioned on both (wing and tank) sides of the connections and two shakers were located at the tanks. This is illustrated in Figure 3.24 for a rear connection.

The dynamic behavior of these connections in the vertical direction is investigated using the restoring force surface (RFS) method [84]. By writing Newton's second law at the wing side of each connection, it follows

$$m_c \ddot{x}_c(t) + f_{r,c} = 0 \tag{3.8}$$

where $f_{r,c}$ is the restoring force applied to this point. The index c is related to the connection under consideration (i.e., either the rear or front attachment of the left or right wing). From Equation (3.8), the restoring force is obtained by

$$f_{r,c} = -m_c \ddot{x}_c(t) \tag{3.9}$$

Except the multiplicative mass factor m_c, the restoring force is then given by the acceleration $\ddot{x}_c(t)$. Nevertheless, this total restoring force does not consist only of the internal force related to the connection of interest, but also includes contributions from the linking forces associated to the wing elastic deformation. Provided that these latter do not play a prominent role, the measurement of the acceleration signal may still provide a qualitative insight into the nonlinear part of the restoring force in the connection between the tank and the wing.

The aircraft is excited close to the second torsional mode (see Figure 3.23(c)) using a band-limited swept sine excitation in the vicinity of its corresponding resonant frequency. In Figure 3.25, the measured acceleration at the wing side is represented in terms of the relative displacement x_{rel} and velocity $\dot{x}_{rel}$ of the connection obtained by integrating the accelerations on both sides of the attachment. It is given for the rear connections of the right and left wings. A nonlinear softening elastic effect is observed from the evolution of these estimated restoring force surfaces. In particular, the detected behavior has a piecewise characteristic. This is more clearly evidenced by the corresponding stiffness curves also depicted in Figure 3.25. Softening nonlinearity is typical of bolted connections [43, 52]. Similar nonlinear effect occurs for the front connections, but they participate much less in the considered response. Finally, the deviation between the right and left connections seems to show asymmetry of the connections.

Although purely qualitative, the RFS results therefore indicate that the tank connections present a softening stiffness in the vertical direction. As previously mentioned,

Figure 3.24: Instrumentation of the rear attachment of the right wing.

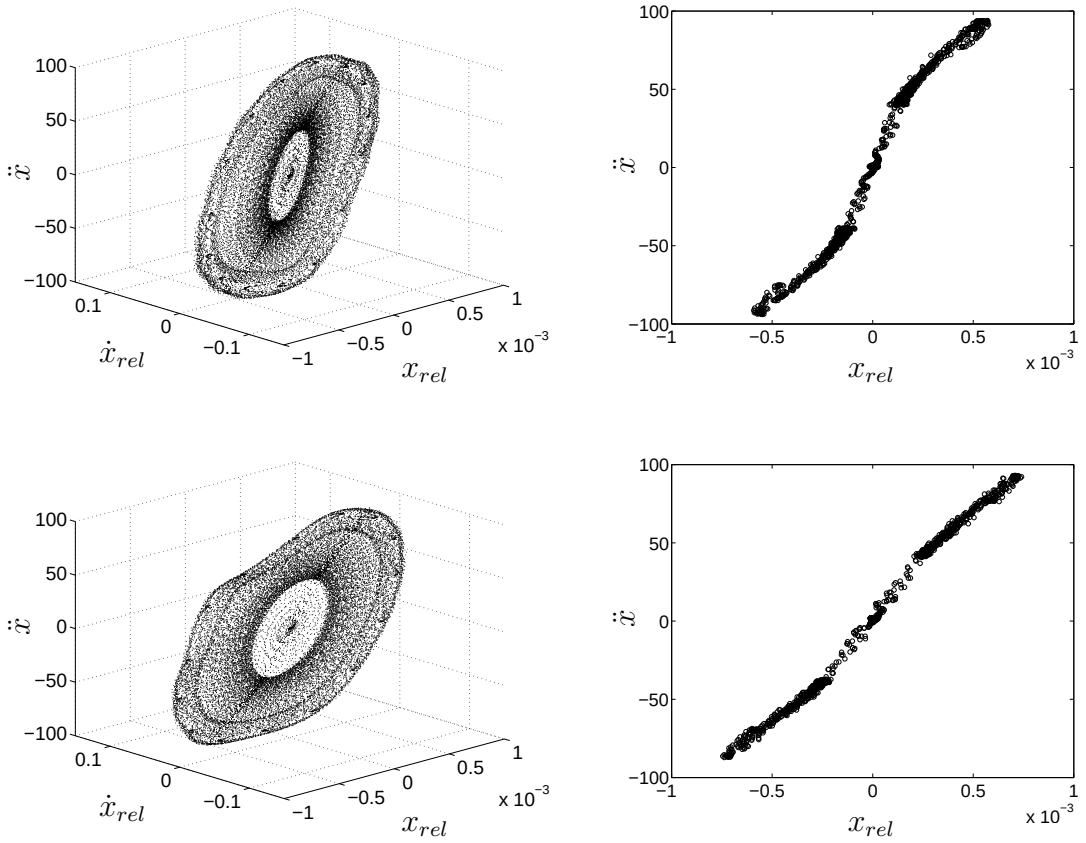

Figure 3.25: Estimated restoring force in the connections between tanks and wings. Left plots: measured acceleration (m/s^2) in terms of the relative displacement (m) and velocity (m/s). Right plots: stiffness curve given by two-dimensional section of the three-dimensional plot for zero relative velocity. Top plots: rear tank connection of the left wing. Bottom plots: rear tank connection of the right wing.

a model with piecewise characteristic could be consistent with the experimental observations. However, the NNM algorithm, in its present form, cannot handle nonsmooth nonlinearities. Alternatively, linear and negative cubic stiffness terms are one possible manner of describing the observed nonlinear behavior. Hence, the reconstructed stiffness curve is obtained by fitting to the data the mathematical model

$$f_{r,c} = kx_{rel} + k_{nl}^{-}x_{rel}^{3} \qquad (k_{nl}^{-} < 0) \tag{3.10}$$

In view of the qualitative value of this approach, we note that the objective followed here is to derive a simplified realistic model in order to illustrate the numerical computation procedure of NNMs. Accordingly, in the present study, the nonlinear behavior is modeled by adding negative cubic stiffness nonlinearities into the linear part of the connections. An indicative value of $-10^{13}\mathrm{N/m^3}$ is adopted for each connection. Finally, the nonlinear system is constructed from the reduced-order model by means of cubic springs positioned vertically between both corresponding nodes retained on either side of connections.

3.4.2 Nonlinear Modal Analysis

The numerical computation of NNMs is realized in the MATLAB environment using the nonlinear reduced-order model. In this context, this section focuses on some specific modes.

Fundamental NNMs

The modes of the aircraft can be classified into two categories, depending on whether they correspond to wing motions or not. The modes localized mainly on other structural parts (such as the vertical stabilizer, the horizontal tail or the fuselage) are almost unaffected by the nonlinear connections located at the wing tips. Only the modes involving wing deformations are perceptibly affected by nonlinearity. According to the relative motion of the fuel tanks, these modes are more or less altered for increasing energy levels.

An unaffected mode is first examined in Figure 3.26. It corresponds to the nonlinear extension of the first tail bending LNM (mode 13 in Table 3.3). In this figure, the computed backbone and related NNM motions are depicted in the FEP. The modal shapes are given in terms of the initial displacements (with zero initial velocities assumed) that realize the NNM motion. It clearly confirms that the modal shape and the oscillation frequency remain practically unchanged with the energy in the system.

Modes involving wing deformations are now investigated. The first wing bending mode (i.e., the nonlinear extension of mode 10 in Table 3.3) is illustrated in Figure 3.27. The FEP reveals that this mode is weakly affected by the nonlinearities. The frequency of the NNM motions on the backbone slightly decreases with increasing energy levels, which

results from the softening characteristic of the nonlinearity. Regarding the modal shapes, they are almost identical over the energy range and resemble the corresponding LNM. MAC value between the NNM shapes at low and high energy levels (see (a) and (b) in Figure 3.27) is 0.99.

Figure 3.28 represents the FEP of the first (symmetric) wing torsional mode (i.e., mode 19 in Table 3.3). For this mode, the relative motion of the fuel tanks is more important, which enhances the nonlinear effect of the connections. As a result, the oscillation frequency has a stronger energy dependence along the backbone branch. On the other hand, the modal shapes are still weakly altered. MAC value between the NNM shapes on the backbone at low and high energy levels (see (a) and (b) in Figure 3.28) is equal to 0.98. In addition, the FEP highlights the presence of three tongues, revealing the existence of internal resonances between this symmetric torsional mode and other modes. These observed modal interactions are discussed in the next section.

Finally, the second (anti-symmetric) wing torsional mode (i.e., mode 20 in Table 3.3) is plotted in the FEP of Figure 3.29. While the oscillation frequency is noticeably altered by nonlinearity, modal shapes are again slightly changed. Over the energy range of interest, the decrease in frequency is around 5% along the backbone branch. MAC value between the modal shapes at low and high energy levels (see (a) and (b) in Figure 3.29) is 0.97. It shows that the nonlinearities spatially localized between the wing tips and the tanks weakly influence the NNM spatial shapes. Besides the NNM backbone, one tongue is present at higher energy. For information, the computation of the backbone branch up to the tongue needs 20 min with 100 time steps over the half period (using Intel i7 920 2.67GHz processor). Due to the presence of turning points, the computation of the tongue is more expensive and demands about one hour.

Similar dynamics were observed for the higher modes and are not further described herein.

Internally Resonant NNMs

Besides the backbone branches, the previous FEPs show the presence of tongues of internally resonant NNMs, similarly to what was observed for the previously studied systems. Following the resonance scenario already detailed, these additional branches emanate from the backbone of a specific NNM and coalesce into the backbone branch of another NNM, thereby realizing an internal resonance between the two modes.

This is briefly illustrated in Figure 3.30 regarding the 3:1 tongue emanating from the backbone of the first wing torsional mode (see Figure 3.28). Modal shapes are given at three different locations on the tongue (see (a), (b) and (c) in Figure 3.30). When the energy gradually increases along the tongue, a smooth transition from the first wing torsional mode to a higher tail torsional mode occurs. Interestingly, Figure 3.30(b) shows an inherently nonlinear mode with no counterpart in the underlying linear system. It corresponds to a 3:1 internal resonance as evidenced by the evolution of the time series and

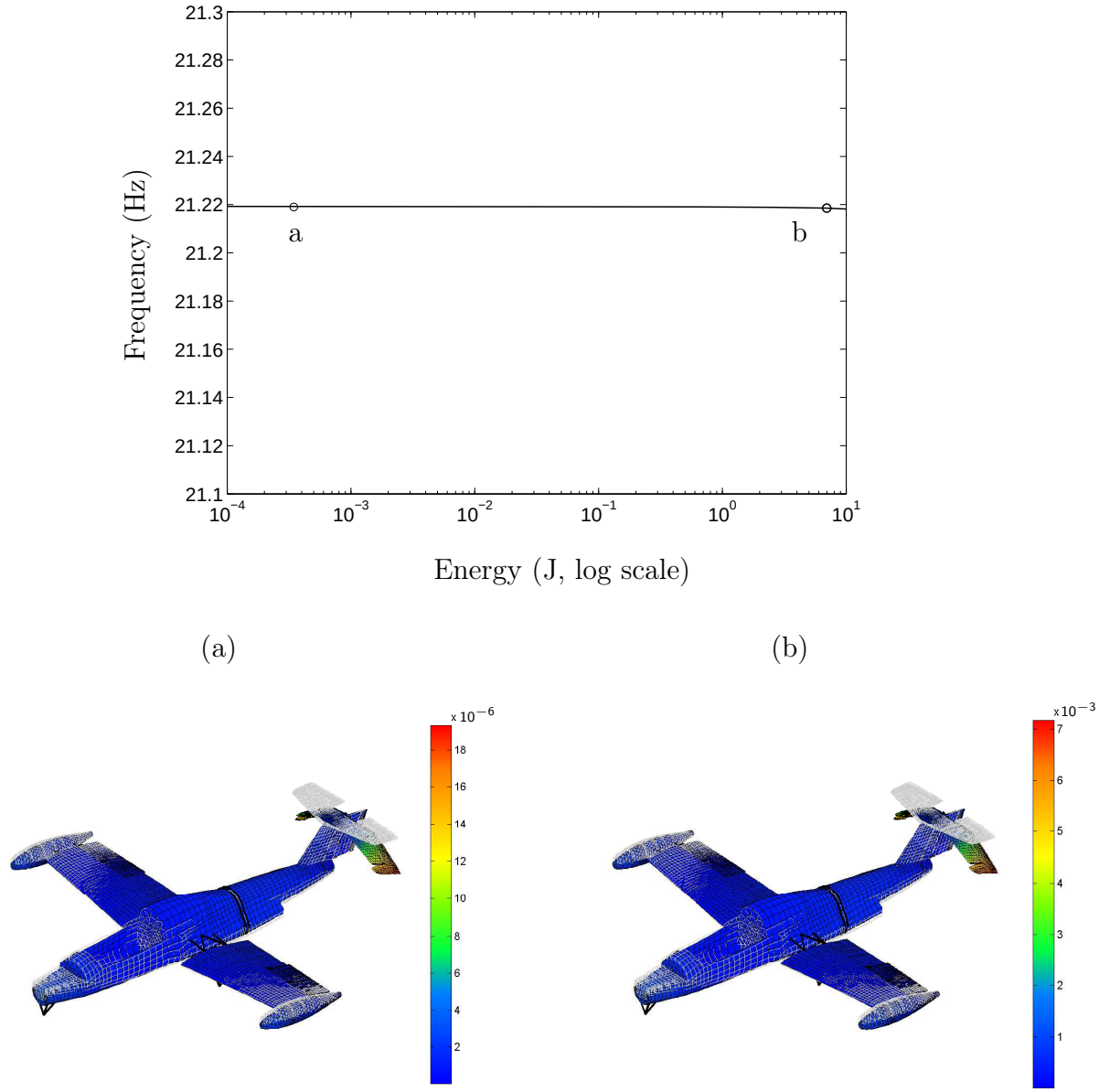

Figure 3.26: FEP of the first tail bending NNM of the Paris aircaft. NNM shapes at energy levels marked in the FEP are inset; they are given in terms of the initial displacements (m) that realize the periodic motion (with zero initial velocities assumed).

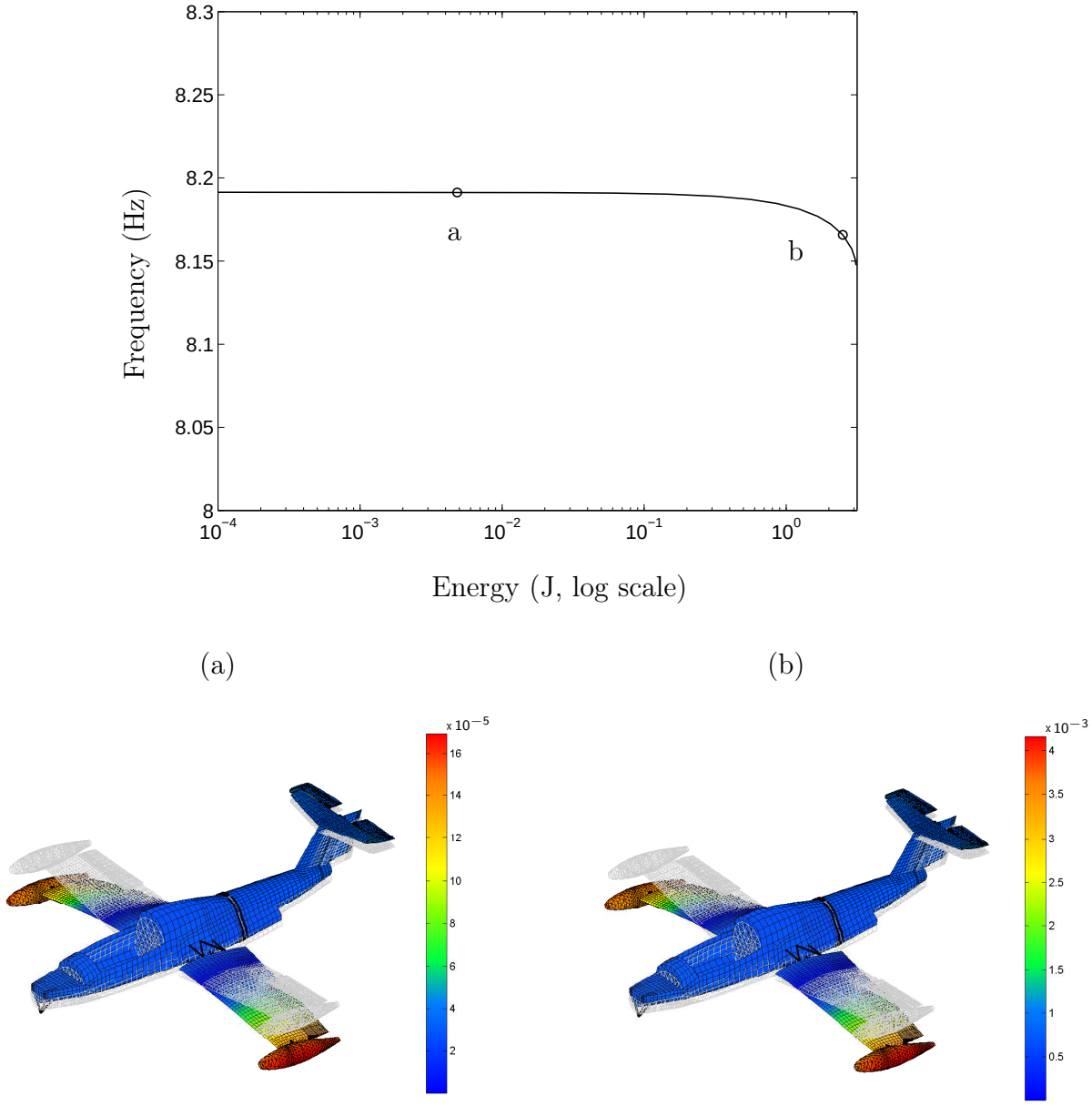

Figure 3.27: FEP of the first wing bending NNM of the Paris aircraft. NNM shapes at energy levels marked in the FEP are inset; they are given in terms of the initial displacements (m) that realize the periodic motion (with zero initial velocities assumed).

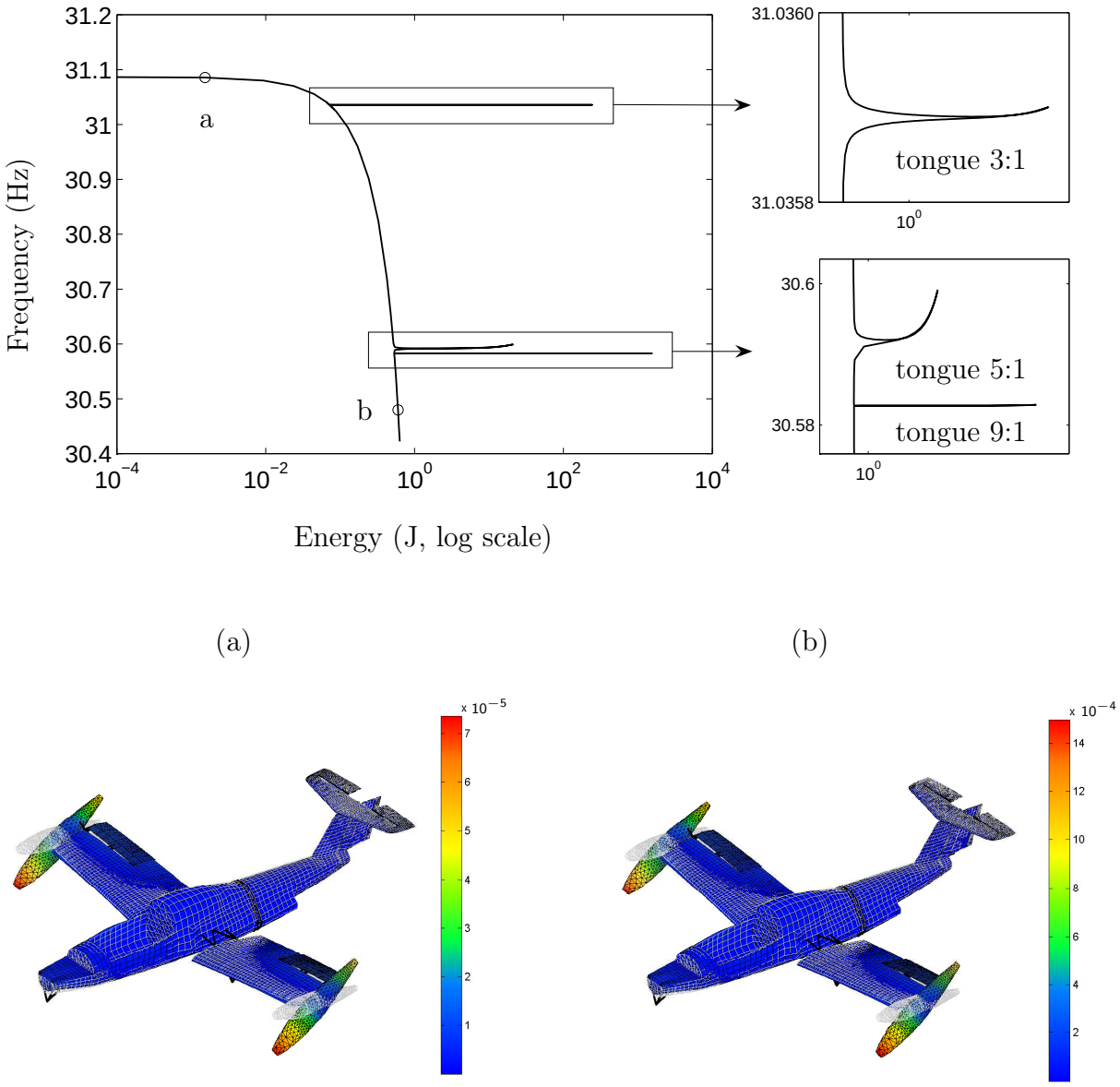

Figure 3.28: FEP of the first (symmetric) wing torsional NNM of the Paris aircraft. NNM shapes at energy levels marked in the FEP are inset; they are given in terms of the initial displacements (m) that realize the periodic motion (with zero initial velocities assumed).

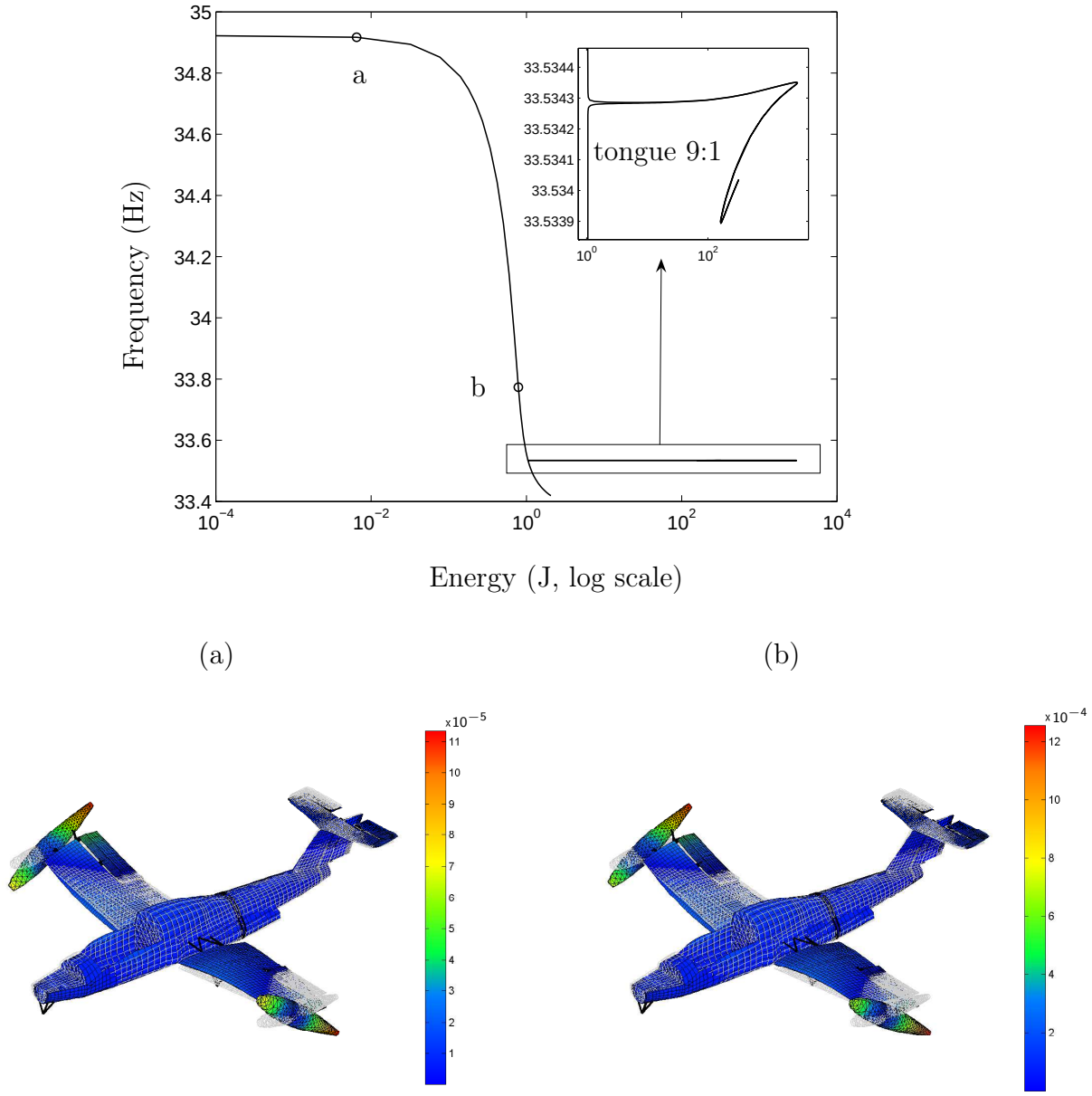

Figure 3.29: FEP of the second (anti-symmetric) wing torsional NNM of the Paris aircraft. NNM shapes at energy levels marked in the FEP are inset; they are given in terms of the initial displacements (m) that realize the periodic motion (with zero initial velocities assumed).

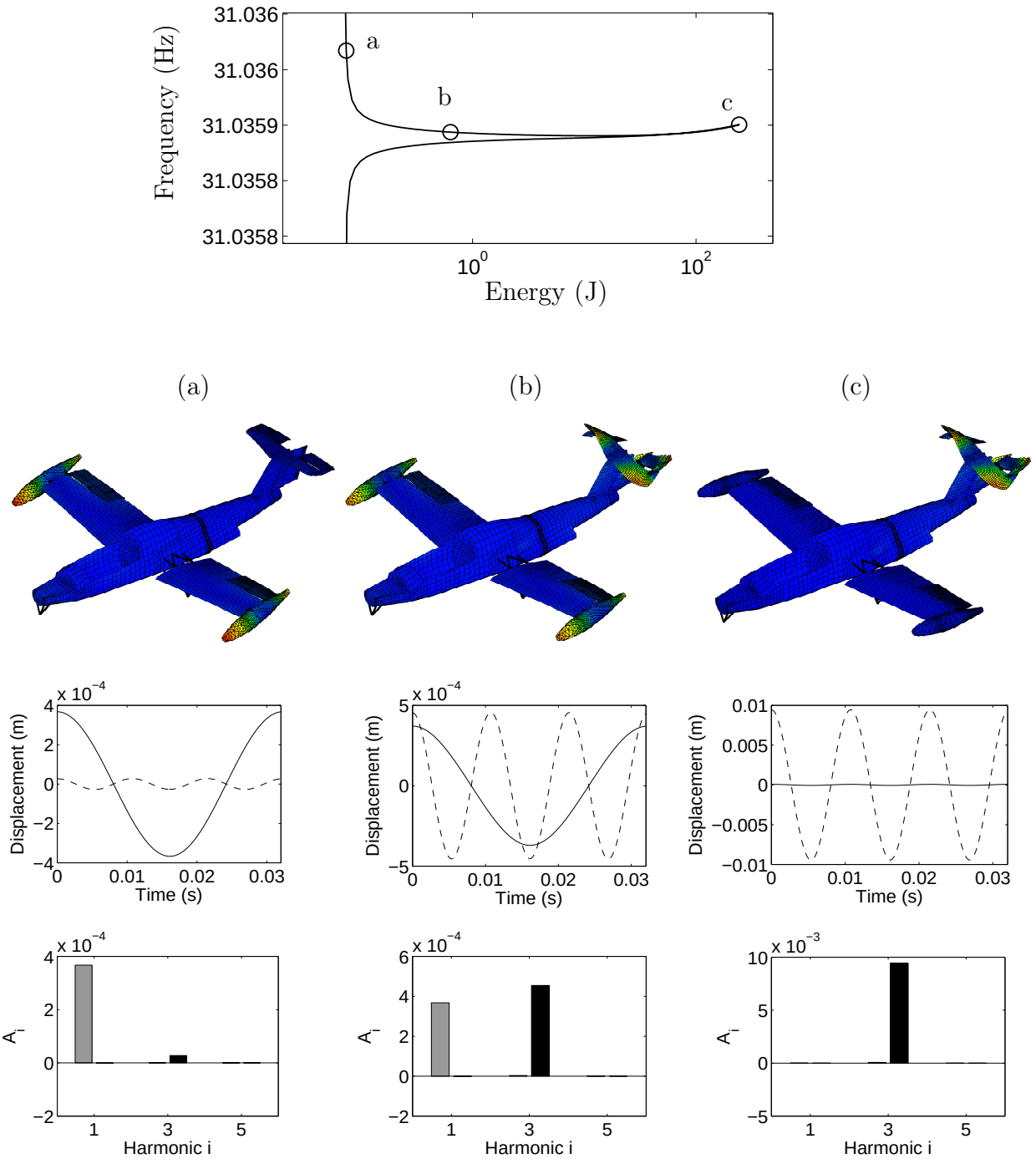

Figure 3.30: 3:1 internal resonance between the first wing torsional mode and a higher tail mode of the Paris aircraft. Top plot: close-up in the FEP of the 3:1 tongue of Figure 3.28. Bottom plots: NNM motions at (a) beginning of the tongue (in the vicinity of the backbone of the the first wing torsional mode); (b) middle of the tongue; and (c) extremity of the tongue. From top to bottom: NNM shapes; time series of the vertical displacements at the rear tip of the right tank (——) and at the right side of the horizontal tail (− − −); Fourier coefficients of both displacements (in grey and black, respectively).

the frequency content, also represented in Figure 3.30, of the periodic motions along the tongue. A third harmonic progressively appears, and the structure vibrates according to a subharmonic motion characterized by two dominant frequency components. The relative importance of the third harmonic grows along the tongue, until the mode transition is realized.

Similarly, two other tongues corresponding to 5:1 and 9:1 internal resonances between this first wing torsional mode and higher modes are observed in the FEP of Figure 3.28. Moreover, the FEP of Figure 3.29 reveals the presence of a 9:1 internal resonance between the second wing torsional mode and another higher mode of the aircraft. We note that the practical realization of these internal resonances is questionable in view of the low frequency changes, and would deserve more attention in further studies.

3.5 Concluding Remarks

A computational approach for NNM calculation was considered in this chapter for performing theoretical modal analysis of nonlinear systems of increasing complexity. The different examples revealed that the proposed numerical algorithm can investigate strongly nonlinear regimes of motion, something which is not possible using existing analytic techniques. Nonlinear phenomena with no linear counterparts, including localization and modal interactions with no commensurate linear frequencies, were also exhibited by the method. An important finding of this chapter is that the accurate computation of NNMs of real-world structural systems, such as the full-scale aircraft studied herein, is now within reach. This clearly opens up new horizons for the application of the NNM theory in practical applications.

Chapter 4

Modal Testing based on Nonlinear Normal Mode Force Appropriation

Abstract

Modal testing and analysis is well-established for linear mechanical systems. The objective of the present chapter is to progress toward an experimental modal analysis (EMA) methodology of nonlinear structures by targeting the extraction of nonlinear normal modes (NNMs) from time responses. A nonlinear extension of force appropriation techniques is developed in this study in order to isolate a single NNM during the experiments. Thanks to the invariance principle, the energy dependence of that nonlinear mode (i.e., the NNM modal curves and their frequencies of oscillation) can be extracted from the resulting free decay response using time-frequency analysis. The proposed methodology is demonstrated using two numerical examples, a 2DOF system and a planar cantilever beam with a cubic spring at its free end.

4.1 Introduction

In the virtual prototyping era, dynamic testing remains an important step of the design of engineering structures, because the accuracy of finite element predictions can be assessed [39]. In this context, experimental modal analysis (EMA) is indubitably the most popular approach and extracts the modal parameters (i.e., the mode shapes, natural frequencies and damping ratios). The popularity of EMA stems from its great generality; modal parameters can describe the behavior of a system for any input type and any range of the input.

For linear structures, the techniques available today for EMA are really quite sophisticated and advanced: eigensystem realization algorithm [58], stochastic subspace identification method [158], polyreference least-squares complex frequency-domain method [107], to name a few. Modal identification of complex industrial structures with high modal density and large modal overlap is now within reach. Unification of the theoretical development of EMA algorithms was attempted in [2, 3], which is another sign of the maturity of this research field.

As reported in [64], a large body of literature exists regarding dynamic testing and identification of nonlinear structures, but very little work addresses nonlinear phenomena during modal survey tests. Interesting contributions in this context are [10, 49, 113]. The force appropriation of nonlinear systems (FANS) method extends linear force appropriation to nonlinear structures [10]. A multi-exciter force pattern that includes higher harmonic terms is used to counteract nonlinear coupling terms, which prevent any response other than the linear normal mode (LNM) of interest. The nonlinear resonant decay (NLRD) method applies a burst of a sine wave at the undamped natural frequency of a linear mode and enables small groups of modes coupled by nonlinear forces to be excited [113]. A nonlinear curve fit in modal space is then carried out using the restoring force surface (RFS) method. Another test strategy that identifies nonlinearities in modal space using the RFS method is discussed in [49]. Alternatively, a nonlinear modal identification approach based on the single nonlinear resonant mode concept [138, 139] and on a first-order frequency-domain approximation is proposed and applied in [26, 47, 124, 125]. The forced frequency responses are expressed as a combination of a resonant nonlinear mode response and of linear contributions from the remaining modes. By a curve-fitting procedure, the amplitude-dependent nonlinear modal parameters may be identified from experimental responses close to the resonance. In a recent work [23], nonlinear modal identification is carried out by means of a linearization procedure.

In this chapter, an attempt is made to extend EMA to a practical nonlinear analog using the nonlinear normal mode (NNM) theory. Following the philosophy of force appropriation, the proposed method excites the NNMs of interest, one at a time. To this end, the phase lag quadrature criterion is generalized to nonlinear structures in order to locate single-NNM responses. Thanks to the invariance principle (i.e., if the motion is initiated on one specific NNM, the remaining NNMs remain quiescent for all time), the energy de-

pendence of the NNM modal curves and their frequencies of oscillation can be extracted directly from experimental time data.

When used in conjunction with the numerical computation of the NNMs introduced in Chapter 2 for theoretical modal analysis (TMA), the approach described herein leads to an integrated methodology for modal analysis of nonlinear vibrating structures (see Figure 1). This methodology can, for instance, be used for validating dynamic models, as is routinely carried out for aerospace structures (e.g., ground vibration testing of aircrafts [48, 106]).

The present chapter is organized as follows. In the next section, the proposed procedure for nonlinear EMA is presented. The different concepts are illustrated using a nonlinear 2DOF system. The approach is demonstrated and assessed in Section 4.3 using numerical experiments carried out on a nonlinear beam.

4.2 Experimental Modal Analysis

There are two classical linear approaches for EMA. Phase separation methods excite several modes at once using either broadband excitation (e.g., hammer impact and random excitation) or swept-sine excitation covering the frequency range of interest. Phase resonance methods excite one mode at a time using multi-point sine excitation at the corresponding natural frequency [40]. A careful selection of the shaker locations is required to induce single-mode behavior. This process is also known as normal-mode tuning or force appropriation [165].

Phase resonance methods have been used for decades, particularly in the aerospace industry (e.g., for ground vibration testing of aircrafts [30] and modal survey of satellites [31, 32]). They provide a very accurate identification of the modal parameters, but they are time-consuming. In order to reduce the testing time, phase separation methods are now used in conjunction with phase resonance methods [48, 106]; these latter are reserved for modes that need a special attention (e.g., closely spaced modes and important modes for flutter computations).

4.2.1 Proposed Methodology for NNM Identification

In the present chapter, the objective is to develop nonlinear EMA by targeting the identification of NNMs. Realizing that the general motion of a nonlinear system cannot be expressed as a superposition of NNMs, it is not clear how individual NNMs can be extracted using phase separation methods. This is why our focus is on the extension of phase resonance testing to nonlinear structures.

The present section introduces a two-step approach that extracts the NNM modal curves

and their frequencies of oscillation directly from experimental data. This method is summarized in Figure 4.1.

First, the method consists in exciting the system to induce single-NNM behavior at a specific energy level. To this end, an extension of force appropriation to nonlinear systems is developed. In particular, the phase lag of the response with respect to the applied force is used as an indicator to assess the quality of the appropriation. This first step, referred to as *NNM force appropriation*, is represented in the upper part of Figure 4.1.

The second step turns off the excitation to track the energy dependence of the NNM of interest using the free damped response resulting from the appropriated NNM motion. A schematic representation is presented in the lower part of Figure 4.1. During this *NNM free decay identification*, the frequency-energy dependence may be extracted using time-frequency analysis. More details on the two steps of the procedure are given in the next sections.

The methodology therefore consists in extracting one NNM at a time from the time series by means of this two-step procedure. In order to relate the forced and free responses of the damped system to the NNMs of the underlying conservative (i.e., undamped and unforced) system, the approach relies on three fundamental properties already discussed in Chapter 1:

1. Forced responses of nonlinear systems at resonance occur in the neighborhood of NNMs [154].
2. According to the invariance property, motions that start out in the NNM manifold remain in it for all time [129].
3. For weak to moderate damping, its effect on the transient dynamics may be considered to be purely parasitic. The damped invariant manifold can therefore be approximated by the undamped invariant manifold. The free damped dynamics closely follows the NNM of the underlying undamped system [104, 153].

From a practical viewpoint, the overall procedure for nonlinear EMA may be viewed as forced vibration testing where the appropriate force is applied as a burst excitation through several exciters for inducing single-NNM decay response. The philosophy of the resonant decay method [113] is then extended to the identification of NNMs of vibrating structures.

4.2.2 Force Appropriation

For linear EMA, the force appropriation method generates appropriate harmonic forces at different locations on the structure to isolate a single normal mode. The measurement of the single-mode response then allows to extract the corresponding modal parameters.

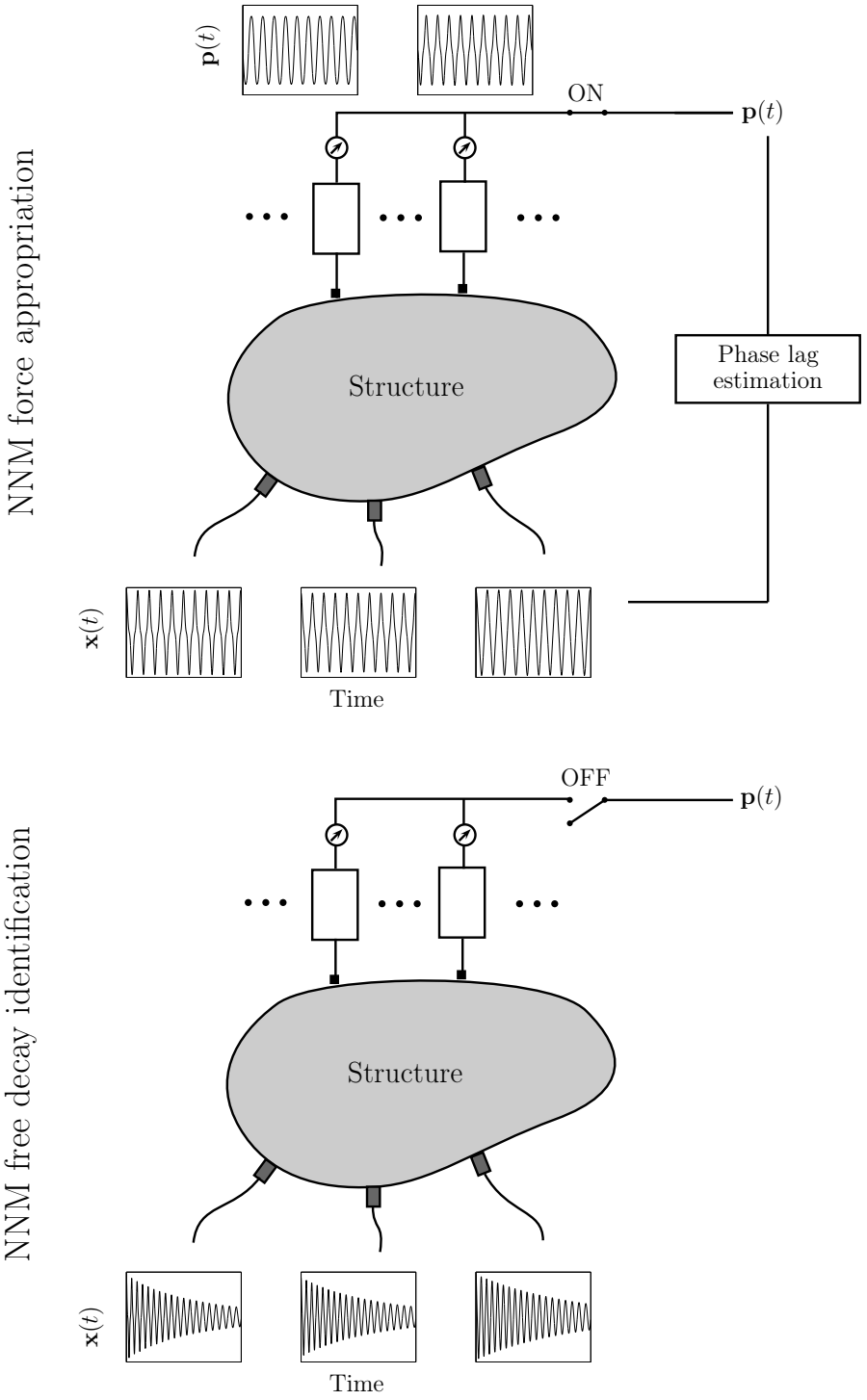

Figure 4.1: Proposed methodology for experimental modal analysis of nonlinear systems.

Force appropriation is usually performed by adapting the frequency and the amplitude distribution of the multi-point excitation. According to the phase lag quadrature criterion (also called phase resonance criterion) [40, 46], a linear damped structure vibrates according to one of the normal modes of the underlying conservative system if all degrees of freedom vibrate synchronously with a phase lag of 90° with respect to the harmonic excitation. Hence, if the phase quadrature criterion is verified during the experimental testing, a single undamped normal mode is isolated, and the natural frequency and the mode shape can be identified.

The NNM framework is used herein to extend force appropriation to nonlinear structures in order to isolate and extract a single NNM at a time. To this end, the forced response of a nonlinear structure with linear viscous damping is considered

$$\mathbf{M}\,\ddot{\mathbf{x}}(t) + \mathbf{C}\,\dot{\mathbf{x}}(t) + \mathbf{K}\,\mathbf{x}(t) + \mathbf{f}_{nl}\left\{\mathbf{x}(t)\right\} = \mathbf{p}(t) \tag{4.1}$$

where $\mathbf{p}(t)$ is the external excitation and $\mathbf{C}$ is the damping matrix. It is assumed that the nonlinear restoring force contains only stiffness nonlinearities.

In what follows, the necessary and sufficient conditions for isolating a single NNM are formulated. In this context, the excitation that induces a single NNM, termed appropriate excitation, is first examined. A generalization of the phase lag quadrature criterion to nonlinear structures is next introduced. It is important to note that when an 'NNM' is referred to in this study, it stands for the NNM of the underlying conservative (no damping and no external force) system (1.1), i.e., the undamped NNM, according to the definition in Chapter 1.

Appropriate Excitation

Extracting a given NNM motion $\mathbf{x}_{nnm}(t)$ of the underlying conservative system by means of appropriate excitation is equivalent to assume

$$\mathbf{x}(t) = \mathbf{x}_{nnm}(t) \tag{4.2}$$

in the equations of motion of the forced and damped system (4.1). It leads to

$$\mathbf{M}\,\ddot{\mathbf{x}}_{nnm}(t) + \mathbf{C}\,\dot{\mathbf{x}}_{nnm}(t) + \mathbf{K}\,\mathbf{x}_{nnm}(t) + \mathbf{f}_{nl}\left\{\mathbf{x}_{nnm}(t)\right\} = \mathbf{p}_{nnm}(t) \tag{4.3}$$

where $\mathbf{p}_{nnm}(t)$ is the corresponding appropriate excitation.

Because an undamped NNM motion $\mathbf{x}_{nnm}(t)$ is defined as a periodic solution of the underlying conservative system, it follows that

$$\mathbf{M}\,\ddot{\mathbf{x}}_{nnm}(t) + \mathbf{K}\,\mathbf{x}_{nnm}(t) + \mathbf{f}_{nl}\left\{\mathbf{x}_{nnm}(t)\right\} = \mathbf{0} \tag{4.4}$$

Substituting expression (4.4) in Equation (4.3), the excitation vector achieving a perfect appropriation (i.e., $\mathbf{x}(t)$=$\mathbf{x}_{nnm}(t)$) of the damped system (4.1) is given by

$$\mathbf{p}_{nnm}(t) = \mathbf{C}\,\dot{\mathbf{x}}_{nnm}(t) \tag{4.5}$$

As in the linear case, it expresses that the applied excitation has to compensate for the damping terms. This relationship shows that the appropriate excitation is periodic and has the same frequency components as the corresponding NNM motion (i.e., generally including multi-harmonic components).

An NNM motion is now expressed as a Fourier cosine series

$$\mathbf{x}_{nnm}(t) = \sum_{k=1}^{\infty} \mathbf{X}_k^{nnm} \cos(k\omega t). \tag{4.6}$$

where ω is the fundamental pulsation of the NNM motion and $\mathbf{X}_k$ is the amplitude vector of the kth harmonic. This type of motion is referred to as monophase NNM motion due to the fact that the displacements of all DOFs reach their extreme values simultaneously. Regarding the monophase NNM motion (4.6), the expression of the corresponding appropriate excitation is given by

$$\mathbf{p}_{nnm}(t) = -\sum_{k=1}^{\infty} \mathbf{C}\mathbf{X}_k^{nnm} k\omega \sin(k\omega t) \tag{4.7}$$

Comparing Equations (4.6) and (4.7), the excitation of a monophase NNM is thus characterized by a phase lag of 90° of each harmonic with respect to the displacement response.

For illustration, the nonlinear 2DOF system studied previously and represented in Figure 1.1 is considered. Linear viscous damping is now taken into account to model dissipative effects in the structure. The forced response of the damped system is governed by the equations of motion

$$\begin{aligned} \ddot{x}_1 + 0.03\dot{x}_1 + (2x_1 - x_2) + 0.5\,x_1^3 &= p_1 \\ \ddot{x}_2 + 0.01\dot{x}_2 + (2x_2 - x_1) &= p_2 \end{aligned} \tag{4.8}$$

which corresponds to moderate damping and where $p_1(t)$ and $p_2(t)$ represent the forces applied to this system. The NNMs of the underlying conservative system

$$\begin{aligned} \ddot{x}_1 + (2x_1 - x_2) + 0.5\,x_1^3 &= 0 \\ \ddot{x}_2 + (2x_2 - x_1) &= 0 \end{aligned} \tag{4.9}$$

have been examined in detail in Chapter 1 and are represented in the frequency-energy plot (FEP) of Figure 1.13.

Figure 4.2 shows the time series and the configuration space of an undamped in-phase NNM motion at low energy (see point (a) in Figure 4.10). This free motion of the underlying undamped system (4.9) resembles that of the in-phase LNM. The modal curve represented in the configuration space is a straight line. The appropriate excitation corresponding to this NNM motion calculated using expression (4.5) is depicted in Figure 4.3. The steady-state forced response of the damped system (4.8) under this appropriate excitation is shown in Figure 4.4. The response is in perfect agreement with the undamped and unforced NNM motion in Figure 4.2. The Fourier coefficients of the forced

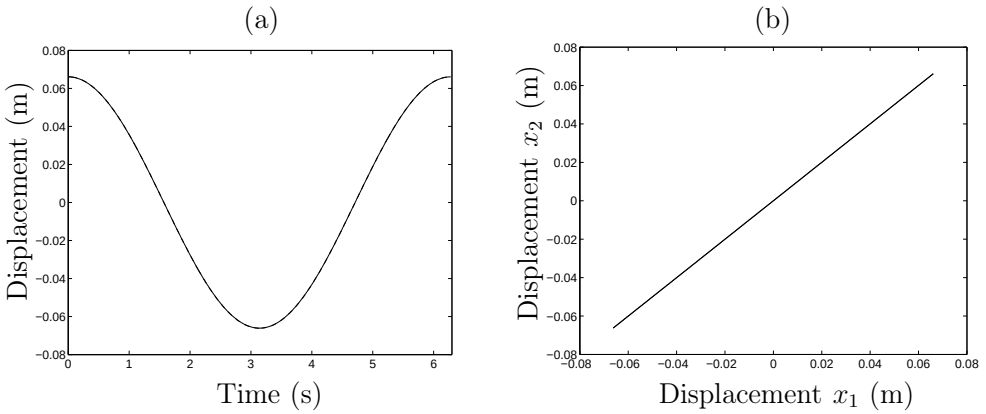

Figure 4.2: Low-energy in-phase NNM motion of the conservative 2DOF system (4.9). (a) Time series (——: $x_1(t)$; $- - -$: $x_2(t)$). (b) Modal curve in the configuration space.

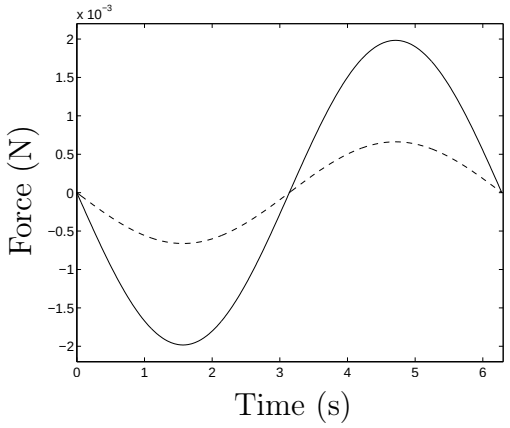

Figure 4.3: Time series of the appropriate excitation corresponding to the low-energy NNM motion in Figure 4.2 (——: $p_1(t)$; $- - -$: $p_2(t)$).

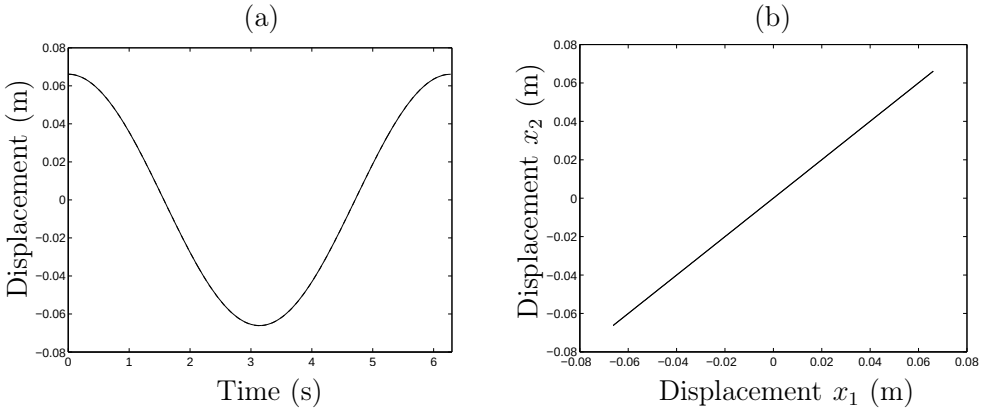

Figure 4.4: Forced response of the damped 2DOF system (4.8) to the appropriate excitation of Figure 4.3. (a) Time series (——: $x_1(t)$; $- - -$: $x_2(t)$). (b) Motion in the configuration space.

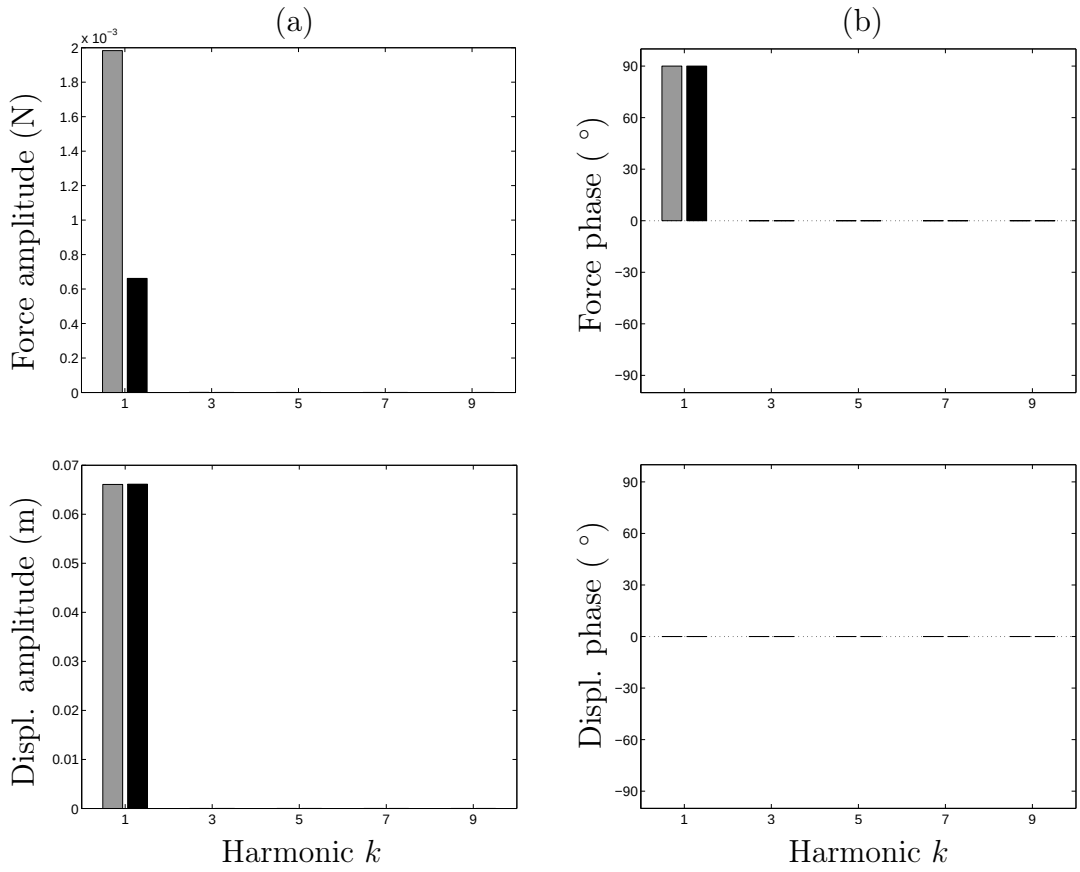

Figure 4.5: Fourier coefficients of the appropriate excitation and the corresponding forced response of the damped 2DOF system (4.8) consisting of a low-energy NNM motion ((a) amplitude; (b) phase). Top plots: appropriate excitation (grey: p_1; black p_2); bottom plots: forced response (grey: x_1; black x_2).

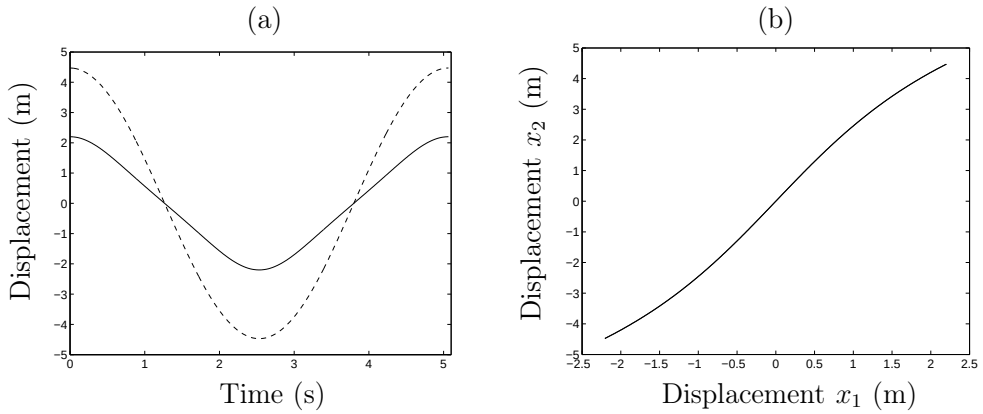

Figure 4.6: High-energy in-phase NNM motion of the conservative 2DOF system (4.9). (a) Time series (——: $x_1(t)$; $- - -$: $x_2(t)$). (b) Modal curve in the configuration space.

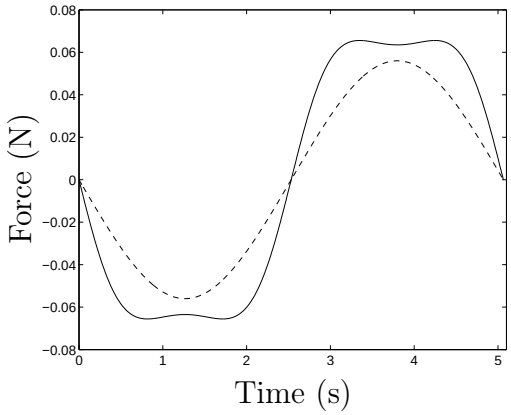

Figure 4.7: Time series of the appropriate excitation corresponding to the high-energy NNM motion in Figure 4.6 (——: $p_1(t)$; $- - -$: $p_2(t)$).

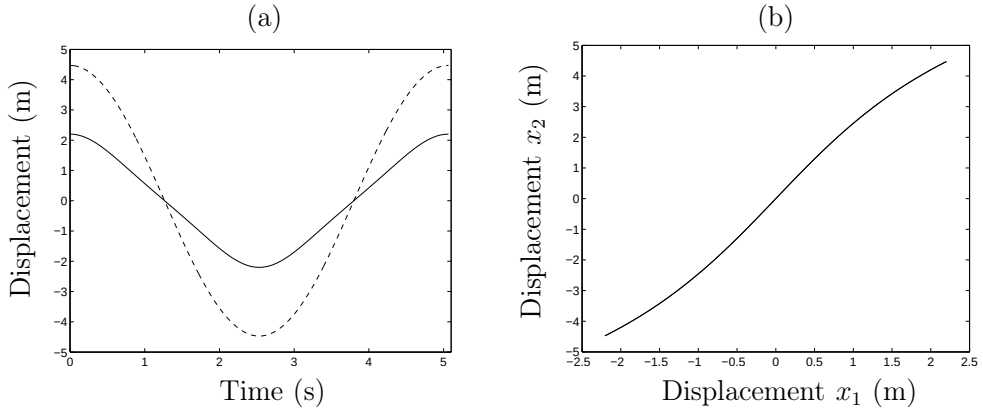

Figure 4.8: Forced response of the damped 2DOF system (4.8) to the appropriate excitation of Figure 4.7. (a) Time series (——: $x_1(t)$; $- - -$: $x_2(t)$). (b) Motion in the configuration space.

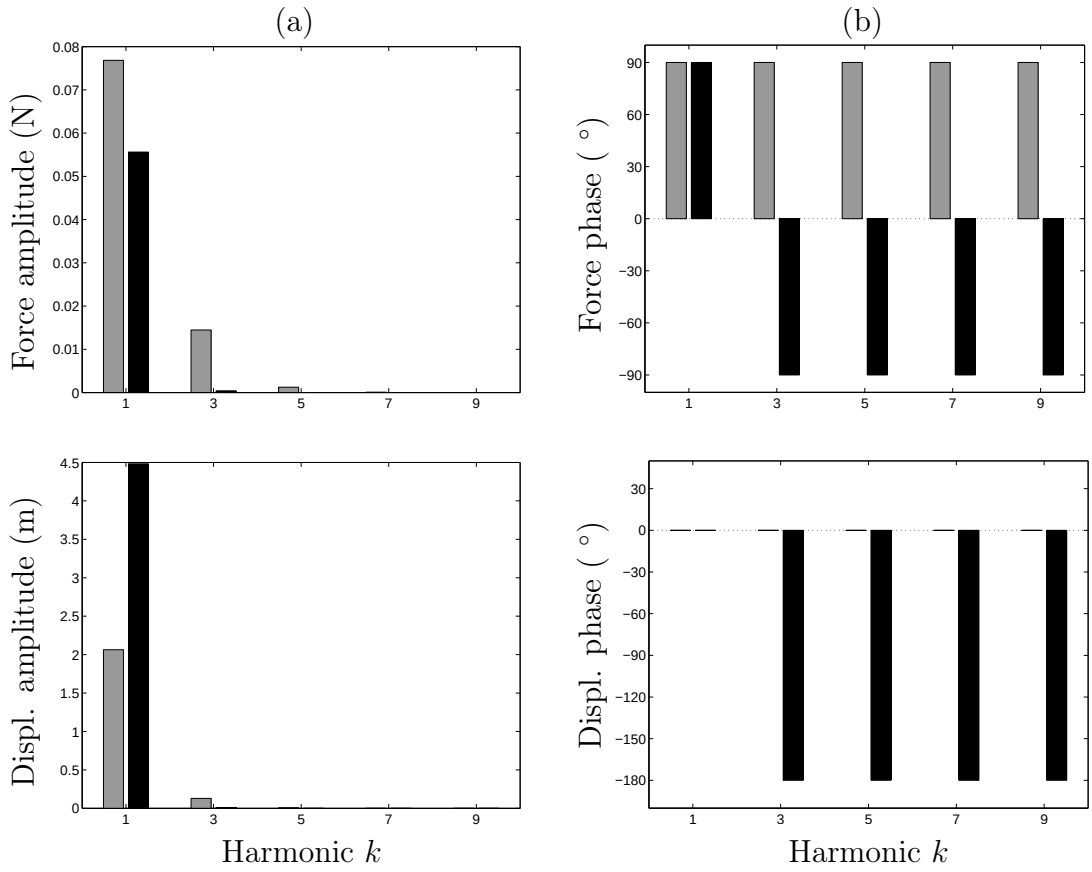

Figure 4.9: Fourier coefficients of the appropriate excitation and the corresponding forced response of the damped 2DOF system (4.8) consisting of a high-energy NNM motion ((a) amplitude; (b) phase). Top plots: appropriate excitation (grey: p_1; black p_2); bottom plots: forced response (grey: x_1; black x_2).

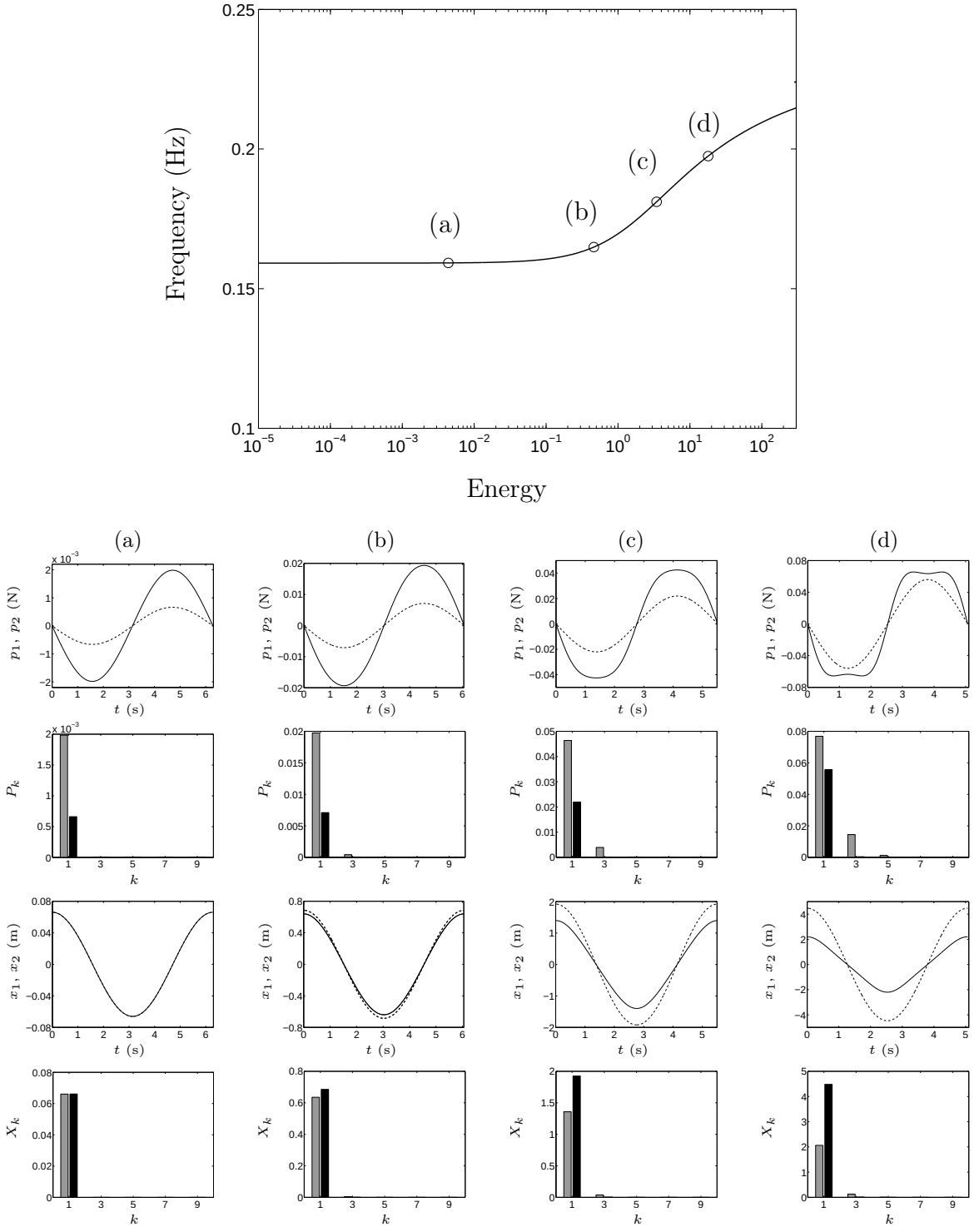

Figure 4.10: Frequency-energy dependence of the appropriate excitation for the 2DOF system (4.8). Top plot: FEP of the in-phase NNM of the underlying undamped system (4.9). Bottom plots (from top to bottom): time series of the appropriate excitation (——: $p_1(t)$; $-\,-\,-$: $p_2(t)$); Fourier coefficients of the appropriate excitation (grey: p_1; black: p_2); time series of the corresponding NNM motion (——: $x_1(t)$; $-\,-\,-$: $x_2(t)$); Fourier coefficients of the NNM motion (grey: x_1; black: x_2).

response and of the appropriate excitation are represented in Figure 4.5. There is one main harmonic component in the excitation and in the response: this fundamental frequency corresponds to the linear natural frequency of the in-phase LNM. A phase lag of 90° is observed between the excitation and the response. At this low energy level, the nonlinear terms are negligible and the results are therefore consistent with the linear theory.

Similarly, an undamped in-phase NNM motion at high energy (see point (d) in Figure 4.10) is considered. The time series and the configuration space of this NNM motion are depicted in Figure 4.6. The related appropriate excitation is illustrated in Figure 4.7. Figure 4.8 shows that the corresponding steady-state forced response of the damped system (4.8) agrees very well with the undamped NNM motion of Figure 4.6. The Fourier coefficients are presented in Figure 4.9. For this strongly nonlinear regime, multi-harmonic components are observed. In addition to the fundamental frequency, higher harmonic terms are necessary to induce exactly this high-energy NNM motion. Figure 4.9 also reveals the phase lag of 90° of each harmonic of the excitation with respect to that of the response.

One important feature of the appropriate excitation is that it is energy-dependent. In particular, it is characterized by the same frequency-energy dependence as the corresponding NNM. As evidenced in (4.5), both signals possess the same frequency components. This is illustrated for the 2DOF example in Figure 4.10 where the FEP of the in-phase NNM is depicted. The appropriate excitation and the resulting NNM motion are depicted for four different energy levels. Their Fourier coefficients are also represented. Clearly, when progressing from low to high energies, the fundamental frequency of the appropriate excitation increases, which is due to the hardening behavior of the system. In addition, multiple harmonics are necessary to induce single-NNM behavior.

Phase Lag Quadrature Criterion for NNM Force Appropriation

The previous section has demonstrated that nonlinear systems can successfully be forced according to a given NNM at a specific energy level through force appropriation. Specifically, if the applied force obeys Equation (4.5), an NNM can be isolated. Because limited knowledge of the damping matrix is available in practical applications, a direct application of Equation (4.5) is generally not possible, and one has to resort to an iterative force appropriation. In this context, an indicator highlighting that the NNM appropriation has effectively been achieved would be particularly useful. This is why the objective of the present section is to generalize the phase lag quadrature criterion (or phase resonance criterion) to nonlinear systems.

The forced response of the damped system (4.1) is examined when it vibrates according to a monophase periodic motion with a phase lag of 90° of each harmonic with respect to

the periodic excitation, i.e.,

$$\mathbf{x}(t) = \sum_{k=1}^{\infty} \mathbf{X}_k \cos(k\omega t) \tag{4.10}$$

and

$$\mathbf{p}(t) = \sum_{k=1}^{\infty} \mathbf{P}_k \sin(k\omega t) \tag{4.11}$$

As the response is even with respect to the time, the nonlinear restoring forces can be written as a cosine series

$$\mathbf{f}_{nl}(\mathbf{x}(t)) = \sum_{k=1}^{\infty} \mathbf{F}_{nl,k} \cos(k\omega t) \tag{4.12}$$

where $\mathbf{F}_{nl,k} = \mathbf{F}_{nl,k}(\mathbf{X}_r)$ is a function of the harmonic coefficients $\mathbf{X}_r$ $(r = 1, \ldots, \infty)$.

In addition, the velocity and the acceleration vectors are computed by time differentiation

$$\begin{aligned} \dot{\mathbf{x}}(t) &= -\sum_{k=1}^{\infty} k\omega \mathbf{X}_k \sin(k\omega t) \\ \ddot{\mathbf{x}}(t) &= -\sum_{k=1}^{\infty} k^2\omega^2 \mathbf{X}_k \cos(k\omega t) \end{aligned} \tag{4.13}$$

By inserting all these expressions into the equations of motion (4.1), we obtain

$$-\mathbf{M}\sum_{k=1}^{\infty} k^2\omega^2 \mathbf{X}_k \cos(k\omega t) - \mathbf{C}\sum_{k=1}^{\infty} k\omega \mathbf{X}_k \sin(k\omega t) + \mathbf{K}\sum_{k=1}^{\infty} \mathbf{X}_k \cos(k\omega t) + \sum_{k=1}^{\infty} \mathbf{F}_{nl,k} \cos(k\omega t) = \sum_{k=1}^{\infty} \mathbf{P}_k \sin(k\omega t) \tag{4.14}$$

By balancing the coefficients of respective harmonics, it follows that

$$\begin{aligned} -k^2\omega^2 \mathbf{M}\mathbf{X}_k + \mathbf{K}\mathbf{X}_k + \mathbf{F}_{nl,k}(\mathbf{X}_r) &= \mathbf{0} \\ -k\omega \mathbf{C}\mathbf{X}_k &= \mathbf{P}_k \end{aligned} \tag{4.15}$$

for $k = 1, \ldots, \infty$. So, the external force is given by

$$\begin{aligned} \mathbf{p}(t) &= \sum_{k=1}^{\infty} \mathbf{P}_k \sin(k\omega t) \\ &= -\sum_{k=1}^{\infty} k\omega \mathbf{C}\mathbf{X}_k \sin(k\omega t) \\ &= \mathbf{C}\dot{\mathbf{x}}(t) \end{aligned} \tag{4.16}$$

and the periodic response $\mathbf{x}(t)$ is a solution of the underlying conservative system (1.1). The response $\mathbf{x}(t)$ is therefore an undamped NNM motion of the system: the NNM force appropriation is realized.

In conclusion, *the phase lag quadrature criterion, valid for linear systems, can be generalized to monophase NNM motions of nonlinear structures*, where the phase lag is defined with respect to each harmonic of the monophase signals.

In other words, if the response (in terms of displacements or accelerations) across the structure is a monophase periodic motion in quadrature with the excitation, the structure vibrates according to a single NNM of the underlying conservative system. The phase lag of the generated monophase excitation with respect to the response can thus be used as an indicator of the NNM appropriation.

No direct constructive method exists to determine the appropriate excitation of a given NNM. Such an excitation has to be derived through successive approximations based on this indicator. For nonlinear structures, in addition to the spatial distribution of the multi-point excitation, the amplitude distribution of harmonic terms has also to be tuned. In fact, the frequency-energy dependence of nonlinear systems prevents the direct separation of space and time in the governing equations of motion, which may complicate the experimental realization of force appropriation from a theoretical viewpoint.

The phase resonance feature has been highlighted in the previous section. For NNM motions of the damped 2DOF system, a phase lag of 90° of the displacement response with respect to the monophase appropriate excitation has been shown (see Figures 4.3 and 4.7). The phase lag quadrature criterion is now used for estimating the quality of the NNM appropriation. The periodic forced responses of the damped 2DOF system (4.8) to a harmonic force of frequency ω and amplitude F applied to the first DOF

$$\begin{aligned} \ddot{x}_1 + 0.03\dot{x}_1 + (2x_1 - x_2) + 0.5\,x_1^3 = &\quad F\sin(\omega t) \\ \ddot{x}_2 + 0.01\dot{x}_2 + (2x_2 - x_1) = &\quad 0 \end{aligned} \tag{4.17}$$

are analyzed. An imperfect force appropriation (i.e., $p_2(t) = 0$ and purely harmonic excitation) is purposely considered to investigate the robustness of the proposed procedure.

The nonlinear frequency responses close to the resonance of the in-phase mode were computed using shooting and continuation methods and are depicted in Figure 4.11. They are given in terms of amplitude and phase lag (of the fundamental frequency component) of the displacement response for increasing forcing amplitudes. It is observed that the phase quadrature criterion is almost verified close to the forced resonance. For $F = 0.2$N, i.e., at the point marked by a square, the phase lag is equal to 90° and 91° for the first and second DOFs, respectively. Figure 4.12 represents the time series of the displacement response. Clearly, the displacement is practically monophase with a phase lag around 90° with respect to the excitation $p_1(t) = F\sin(\omega t)$.

These results also confirm that forced responses of nonlinear systems at resonance occur in the neighborhood of NNMs as already shown in Chapter 1. The backbone of the in-phase

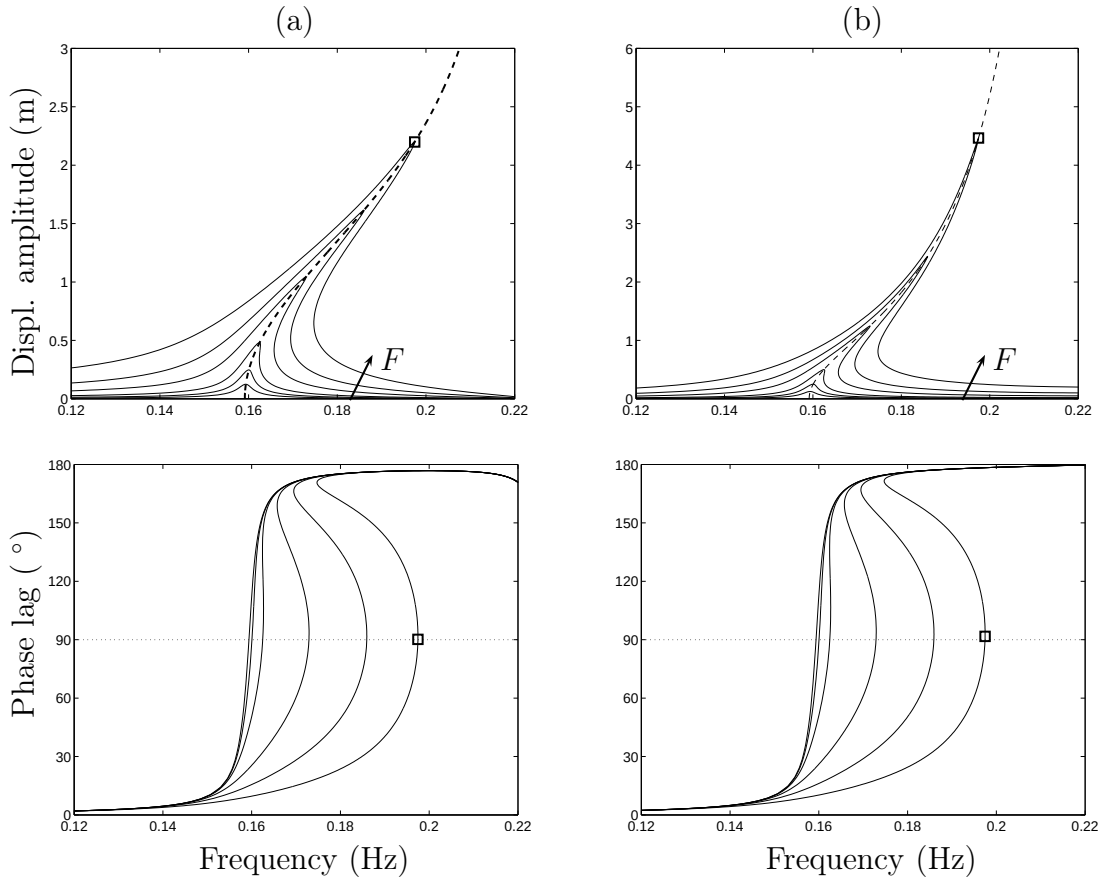

Figure 4.11: Nonlinear frequency responses of the damped 2DOF system (4.17) close to the first resonant frequency (6 different forcing amplitudes F: 0.005N, 0.01N, 0.02N, 0.05N, 0.1N, 0.2N). The dashed line is the backbone of the first undamped NNM (computed by means of the numerical algorithm). Top plots: displacement amplitude. Bottom plots: phase lag of the displacement with respect to the excitation. (a) x_1; (b) x_2.

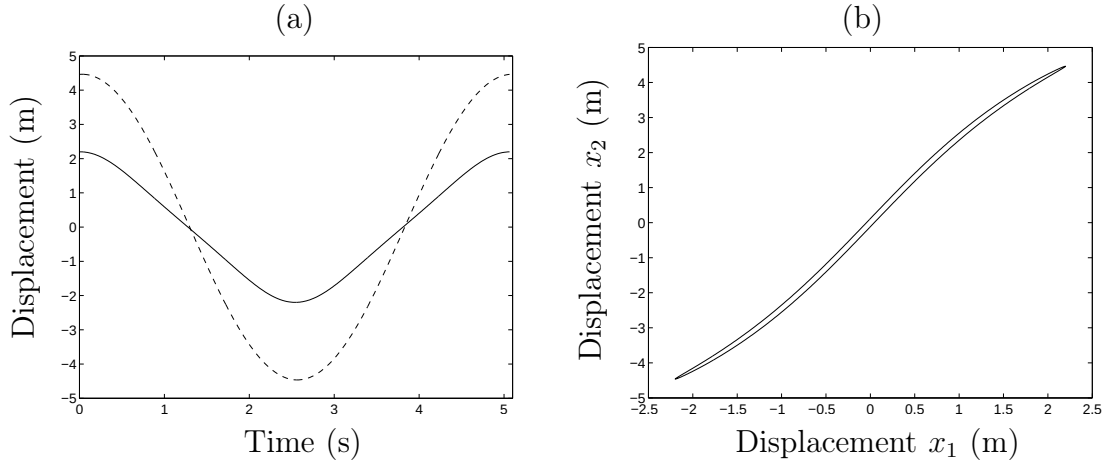

Figure 4.12: Forced response (corresponding to $F = 0.2$N and marked by a square in Figure 4.11) of the damped 2DOF system (4.17). (a) Time series (——: $x_1(t)$; − − −: $x_2(t)$). (b) Motion in the configuration space.

undamped NNM (represented in Figure 1.13) is expressed in terms of amplitude and is displayed using a dashed line in Figure 4.11. This backbone curve traces the locus of the frequency response peaks. In addition, the undamped NNM motion corresponding to the same frequency as the point marked by a square in Figure 4.11 is shown in Figure 4.6. An excellent agreement is observed between the time series of Figures 4.6 and 4.12, the mean-square error (MSE) being around 0.01%.

It is interesting that no forcing on the second DOF and no higher harmonic terms were necessary to isolate this high-energy NNM motion. This is an appealing feature for future practical realizations, at least for structures with relatively well-separated modes. A constructive procedure for inducing single-NNM behavior could be to perform successive adjustments of a stepped sine excitation until the phase lag criterion is verified. This approach is considered in Section 4.3 where the proposed methodology is demonstrated using simulated experiments of a nonlinear beam.

It is worth pointing out that the phase lag quadrature criterion, demonstrated here for linear viscous damping, still holds in case of nonlinear damping provided that the damping force $\mathbf{f}_{d,nl}$ is an odd function of the velocity only, i.e., $\mathbf{f}_{d,nl}(\dot{\mathbf{x}}) = -\mathbf{f}_{d,nl}(-\dot{\mathbf{x}})$. For monophase motion (4.10), the damping terms are indeed expressed as a sine series and therefore have to be compensated by the applied force (4.11). However, if the stiffness and damping nonlinearities are coupled (i.e., $\mathbf{f}_{nl} = \mathbf{f}_{nl}(\mathbf{x}, \dot{\mathbf{x}})$), this criterion generally disappears at the same time as the concept of NNMs of the underlying conservative system.

4.2.3 Free Decay Identification

By means of nonlinear force appropriation, the forced response of the damped system (4.1) may be restricted to a single undamped NNM at a specific energy level. In view of the frequency-energy dependence, successive appropriate excitations at different force levels have to be considered to provide a complete characterization of the NNM of interest. This may complicate the experimental realization.

The alternative strategy proposed here consists in exploiting the NNM invariance property. When a high-energy NNM motion is isolated using force appropriation, the excitation is stopped to obtain the resulting free damped response. Due to invariance, this free decay response initiated on the undamped NNM remains close to it when energy decreases. Using this procedure, the energy dependence of the NNM modal curves and the corresponding frequencies of oscillation may easily be extracted from the single-mode free damped response at each measurement location.

As mentioned above, according to invariance, the resulting free damped response closely follows the corresponding undamped NNM provided that the damping is moderate. The relation between the two responses is only phenomenological, nevertheless it enables one to interpret the damped response in terms of NNM motions of the underlying undamped system. In fact, the damped manifold corresponds to the exact invariant manifold of the

damped dynamics. However, for lightly damped structures, the latter may be approximated by the undamped NNM that can be viewed as an attractor of the free damped response. For illustration, the 2DOF system (4.8) is considered. From the appropriated in-phase undamped NNM motion of Figure 4.8, the resulting free damped response when the excitation is removed is depicted in Figure 4.13. Figure 4.14 compares the manifold corresponding to the in-phase undamped NNM with the free damped response represented in the same projection of phase space. Clearly, it confirms that the free damped response traces the NNM manifold of the underlying undamped system with very good accuracy when energy decreases.

NNM Extraction

As a result, the NNM modal curves may be extracted directly from the single-NNM free decay response. They are obtained by representing the time series in the configuration space for one oscillation around specific time instants, associated with different energy levels. It is illustrated in Figure 4.15 for the 2DOF system around four distinct instants.

To compute the oscillation frequency of NNMs, time-frequency analysis is considered. The continuous wavelet transform (CWT) is used to track the temporal evolution of the instantaneous frequencies. The oscillation frequency of the NNM may then be extracted from the time series of the free damped response. The usual representation of the transform is to plot its modulus as a function of time and frequency in a three-dimensional or contour plot. For illustration, the CWT of the free decay response of the 2DOF system represented in Figure 4.13 is shown in Figure 4.16. The instantaneous frequency decreases with time, and hence with energy, which reveals the hardening characteristic of the system.

Reconstructed FEP

When the total energy (i.e., the sum of the kinetic and potential energies) in the system can be determined, the experimental FEP can be reconstructed in a straightforward manner by substituting the instantaneous energy in the system for time: (i) the backbone expressing the frequency-energy dependence of the NNM is provided by the CWT, (ii) the obtained modal curves around different energy levels are superposed in the plot.

For the 2DOF example, the experimental FEP calculated from the time series of the free damped response is represented in Figure 4.17. It displays the experimental backbone determined through the CWT and the experimental modal curves. For comparison, the theoretical FEP of the undamped NNM computed from the equations of motion is also illustrated. Except the CWT edge effects, a perfect agreement is obtained between the two FEPs, which shows again that the undamped NNM is an attractor for the damped trajectories. In the present case, the linear modal damping ratios are 1% and 0.6%, but

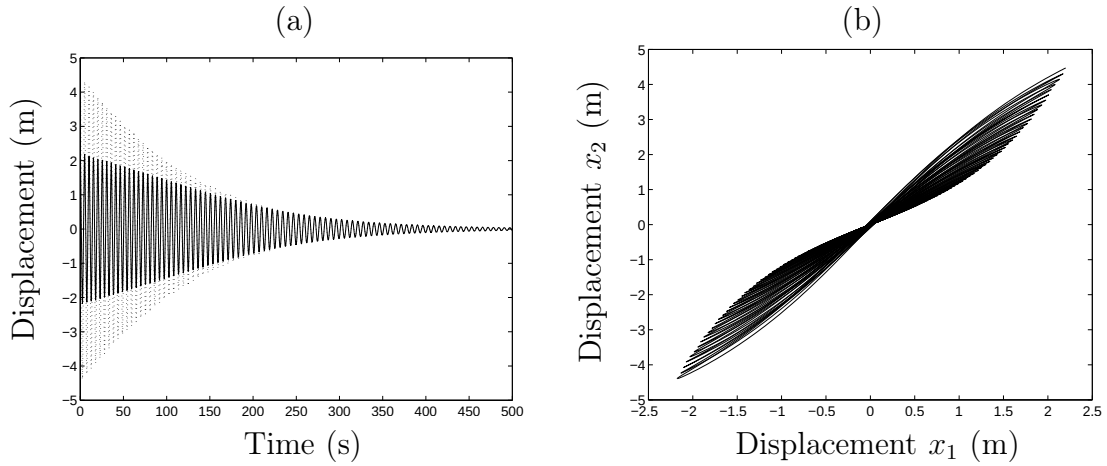

Figure 4.13: Free response of the damped 2DOF system (4.8) initiated from the in-phase NNM motion of Figure 4.8. (a) Time series (——: $x_1(t)$; − − −: $x_2(t)$). (b) Motion in the configuration space.

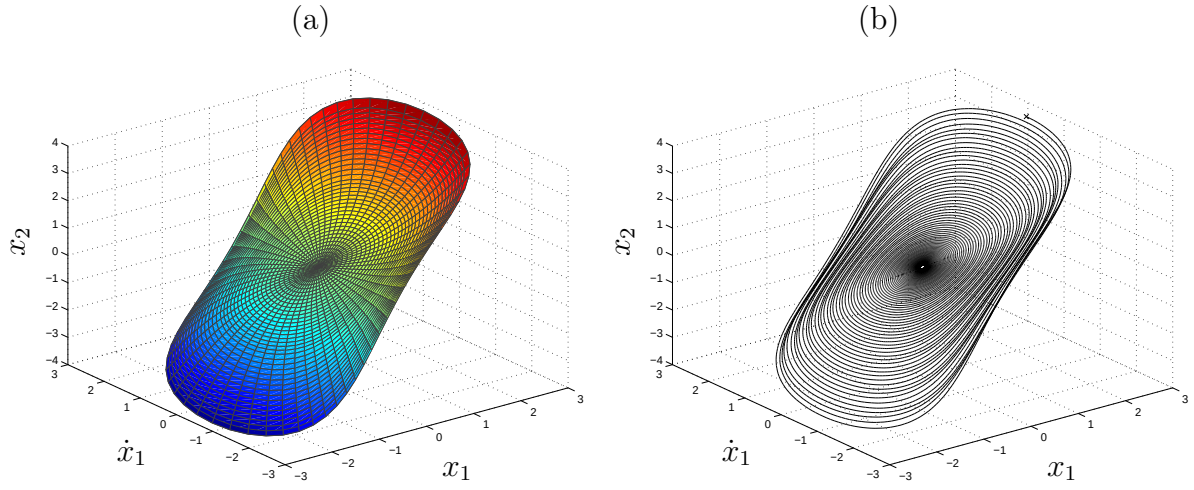

Figure 4.14: Invariant manifold of the in-phase NNM of the 2DOF system. (a) NNM manifold of the underlying undamped system (4.9). (b) Free response of the damped system (4.8).

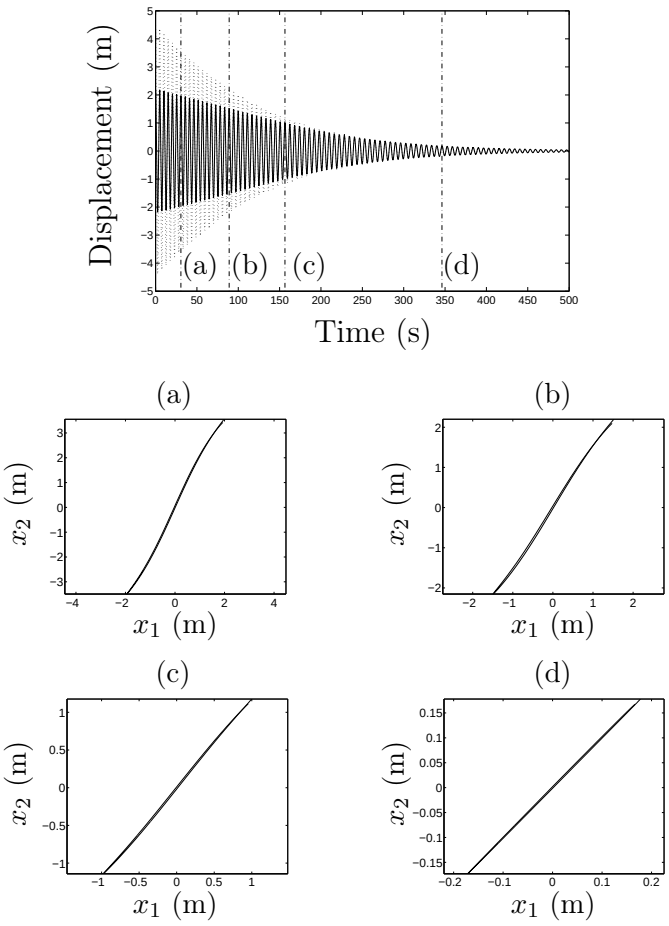

Figure 4.15: Extraction of NNM modal curves during the free decay. Top plot: time series of the resulting single-NNM free response of the damped 2DOF system (4.8). Bottom plots: NNM modal curves extracted from the time series around four time instants marked in the top plot by (a), (b), (c) and (d).

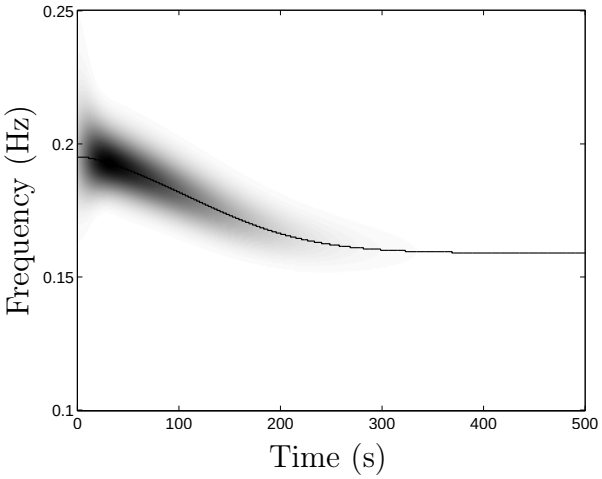

Figure 4.16: Extraction of oscillation frequencies of the NNM during the free decay. Temporal evolution of the instantaneous frequency of the single-NNM free response of the damped 2DOF system (4.8) computed using the CWT. The solid line is the ridge of the transform; i.e., the locus of the maxima at each time instant.

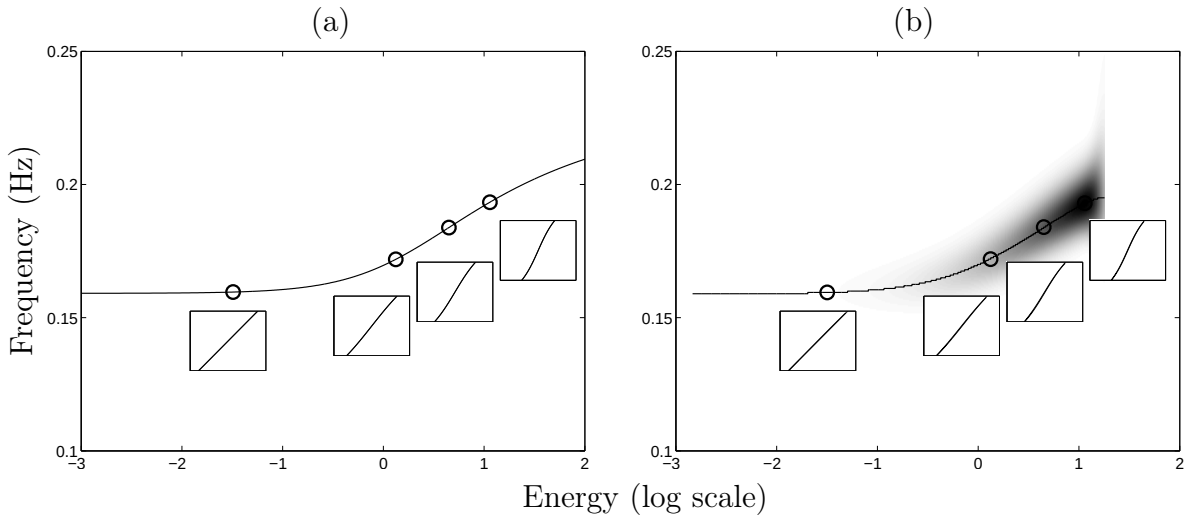

Figure 4.17: Frequency-energy plot of the in-phase NNM of the 2DOF system. (a) Theoretical FEP computed by means of the numerical algorithm from the undamped system (4.9). (b) Experimental FEP calculated directly from the time series of the free damped response of system (4.8) using the CWT. The solid line is the ridge of the transform.

we note that this result holds for higher damping ratios.

In summary, it is thus validated that the free damped dynamics can be interpreted based on the topological structure of the NNM of the underlying conservative system. As a result, one can fully reconstruct the FEP and extract the modal curves together with the oscillation frequencies of the NNM using the proposed procedure.

4.3 Numerical Experiments of a Nonlinear Beam

The proposed methodology is now demonstrated using simulated experiments of an existing nonlinear beam. This structure was used as a benchmark for nonlinear system identification during the European action COST F3 [141] and consists of a cantilever beam with geometrical nonlinearity. The finite element model considered herein is represented in Figure 4.18. The main beam is modeled with 14 beam elements and the thin part with three beam elements. An additional rotational stiffness is used to model the junction between the two beams. As shown in [63, 75], the nonlinear behavior of the thin beam can be modeled using a grounded cubic spring at the junction of the main and the thin beams. The cubic term takes the geometrical stiffening effect of the thin part into account. The geometrical and mechanical properties of the structure are listed in Tables 4.1 and 4.2.

4.3.1 Theoretical Modal Analysis

The NNMs of the underlying conservative system are computed using the numerical algorithm detailed in Chapter 2. The theoretical FEPs of the first and second NNMs are represented in Figures 4.19 and 4.20, respectively. The backbone of the plots corresponds to fundamental synchronous NNM motions. The NNM frequency undergoes a strong increase with increasing energy levels, which reveals the hardening behavior of the cubic stiffness nonlinearity. The evolution with energy of the modal shapes of the main beam, expressed in terms of displacement amplitudes, is also superposed. The FEPs highlight the presence of two other branches, termed tongues, emanating from the NNM backbone. These tongues reveal the existence of internal resonances. For instance, a 9:1 internal resonance between the first and third NNMs appears on the tongue in Figure 4.19.

4.3.2 Experimental Modal Analysis

The proposed approach for EMA is now demonstrated numerically. In this context, Newmark's numerical time integration scheme is used. Linear proportional damping is considered to model dissipative forces in the structure. The damping matrix $\mathbf{C}$ is given

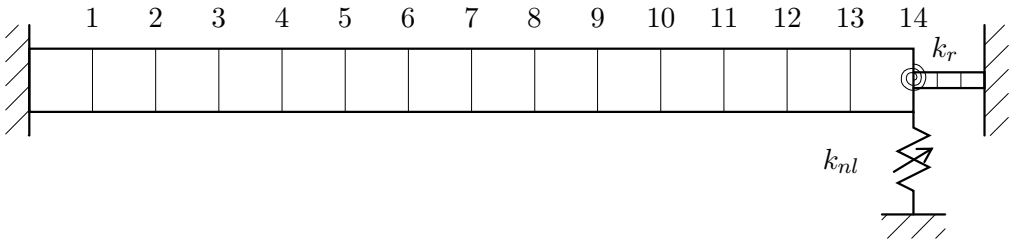

Figure 4.18: Finite element model of the nonlinear beam.

	Length (m)	Width (m)	Thickness (m)
Main beam	0.7	0.014	0.014
Thin beam part	0.04	0.014	0.0005

Table 4.1: Geometrical properties of the nonlinear beam.

Young's modulus (N/m^2)	Density (kg/m^3)	Nonlinear coeff. k_{nl} (N/m^3)
2.05×10^{11}	7800	8×10^9

Table 4.2: Mechanical properties of the nonlinear beam.

by

$$\mathbf{C} = 3\,10^{-7}\,\mathbf{K} + 5\,\mathbf{M} \tag{4.18}$$

which corresponds to moderate damping; for instance, the modal damping ratio is equal to 1.28% for the first LNM. We note that the identified modal damping ratio is much smaller for the existing beam (see Chapter 5). Nevertheless, damping is deliberately chosen larger in order to ensure the applicability of the methodology to moderately damped structures.

NNM Force Appropriation Procedure

Imperfect Force Appropriation

From a practical viewpoint, it is useful to study the quality of imperfect force appropriation consisting of a single-point mono-harmonic excitation, i.e., using a single shaker with no harmonics of the fundamental frequency. The harmonic force $p(t) = F\sin(\omega t)$ is applied to node 4 of the main beam (see Figure 4.18). The nonlinear forced frequency responses of the damped system close to the first resonance are numerically determined. They are represented in terms of displacement amplitudes for increasing forcing ampli-

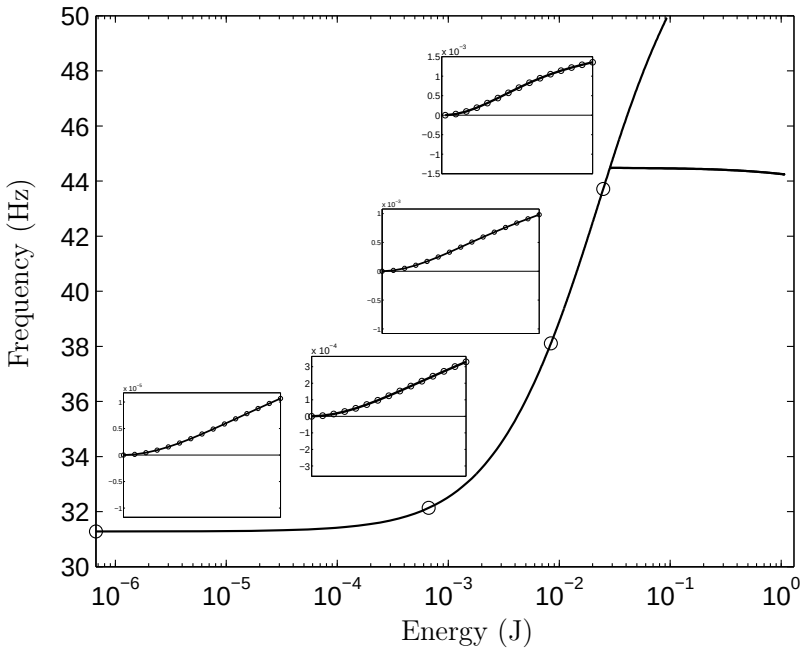

Figure 4.19: Theoretical frequency-energy plot of the first undamped NNM of the nonlinear beam computed using the numerical algorithm. The NNM shapes (displacement amplitudes of the main beam) for four energy levels are inset.

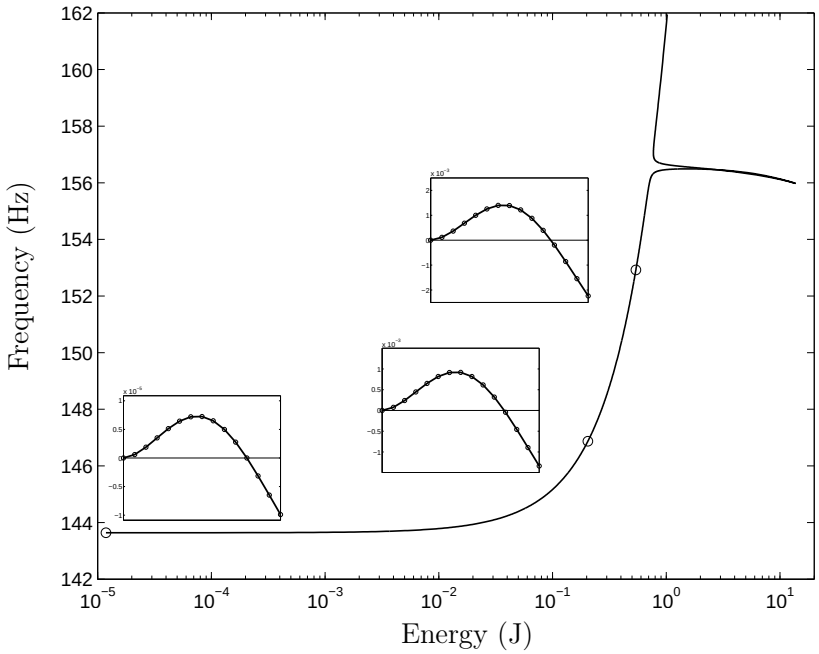

Figure 4.20: Theoretical frequency-energy plot of the second undamped NNM of the nonlinear beam computed using the numerical algorithm. The NNM shapes (displacement amplitudes of the main beam) for four energy levels are inset.

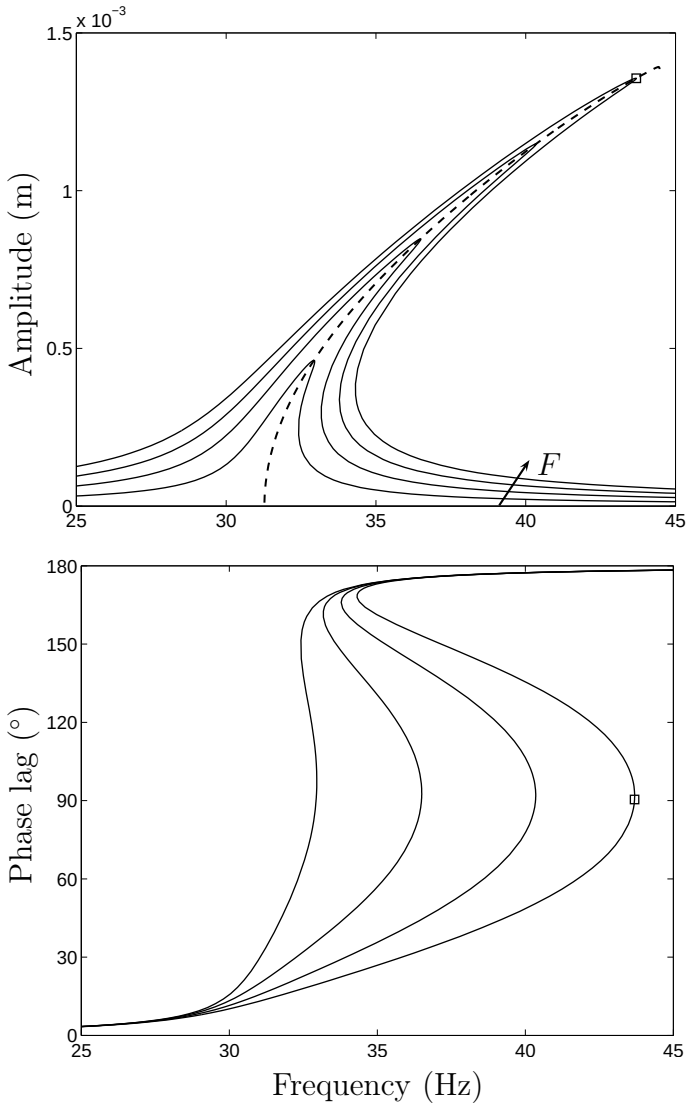

Figure 4.21: Nonlinear forced frequency responses of the damped nonlinear beam close to the first resonant frequency (4 different forcing amplitudes: 1N, 2N, 3N, 4N). The dashed line is the backbone of the first undamped NNM (computed by means of the numerical algorithm). Displacement at the tip of the main beam (node 14); top plot: amplitude, bottom: phase lag with respect to the excitation force.

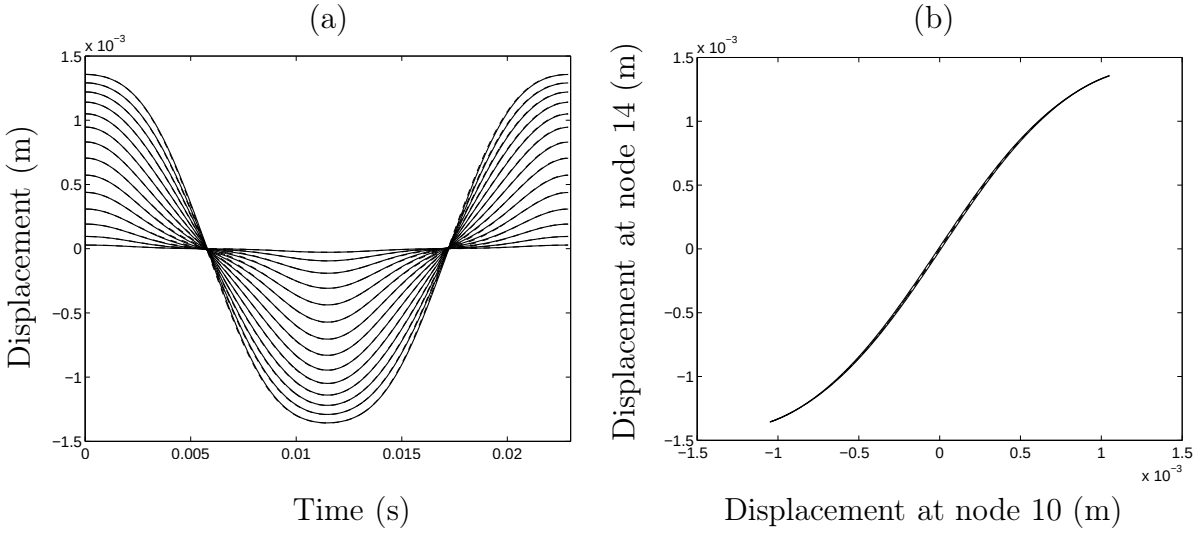

Figure 4.22: Forced response (——) of the damped nonlinear beam resulting from the imperfect force appropriation (for $F = 4$N and marked by a square in Figure 4.21) and the corresponding undamped NNM motion (− − −). (a) Time series of the displacements of the main beam. (b) Motion in the configuration space composed of the displacements at nodes 10 and 14.

tudes F in Figure 4.21. The backbone of the undamped NNM of Figure 4.19, expressed in terms of amplitude, is also superposed. Figure 4.22 shows the forced damped response close to the resonance for $F = 4$N (marked by a square in Figure 4.21) and the corresponding undamped NNM motion at the same frequency. Results similar to those of Section 4.2.2 are obtained:

- The phase lag quadrature criterion is fulfilled close to resonant frequencies.
- Forced responses at resonance occur in the neighborhood of NNMs.
- Imperfect appropriation can isolate the NNM of interest (the beam has well-separated modes).

These findings also hold for the second beam NNM.

Practical Realization of Force Appropriation

An assumption made throughout this chapter is that the forced response at resonance can be reached (i.e., no unstable, quasi-periodic and chaotic motions). Unlike the linear case, nonlinear systems possess coexisting stable solutions with their own domains of attraction. A procedure relying on stepped sine frequency response measurements is examined herein to study the practical feasibility of the force appropriation methodology for nonlinear structures. It gradually changes the frequency of the excitation $p(t) = F\sin(\omega t)$ to

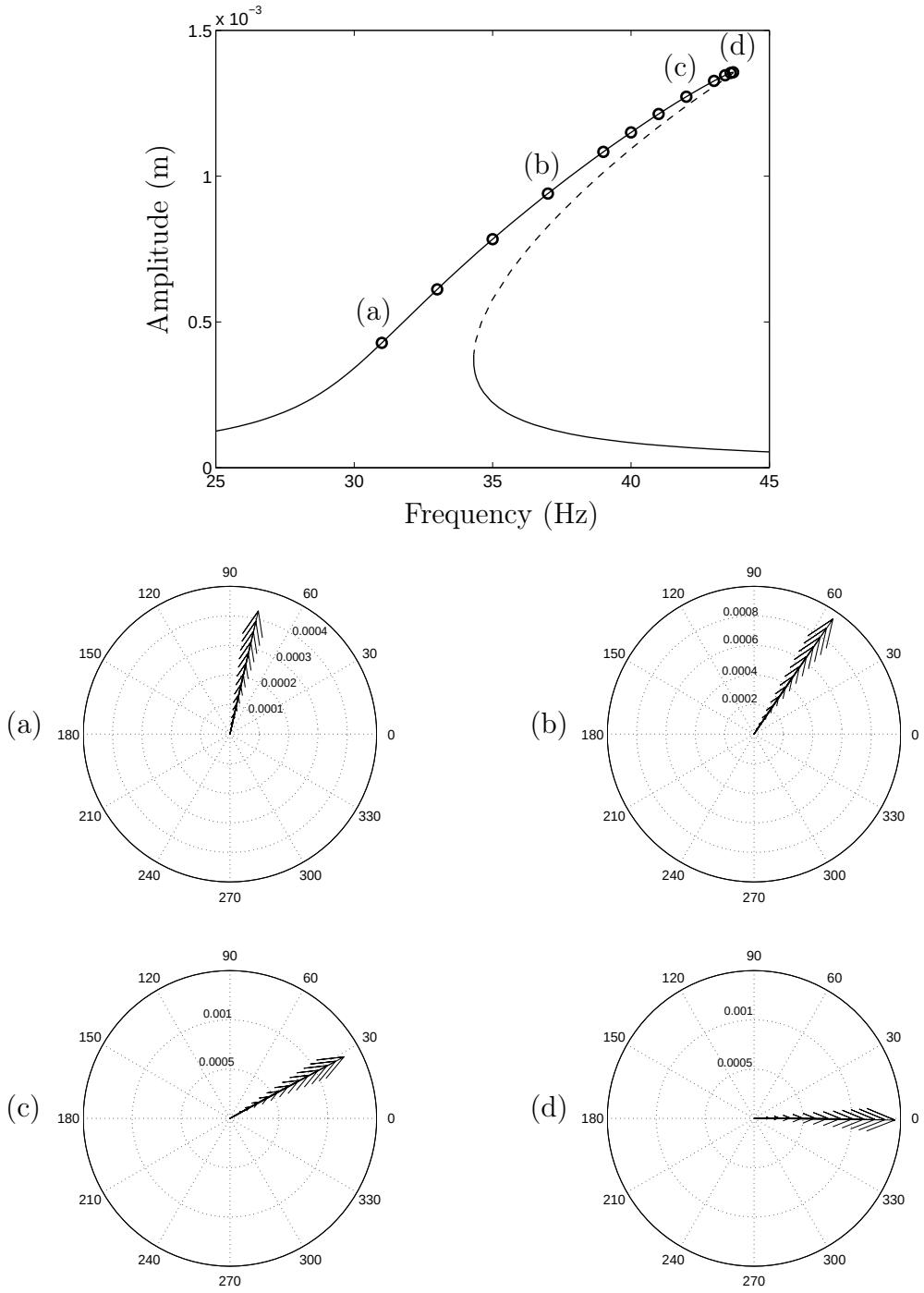

Figure 4.23: Stepped sine excitation procedure for carrying out the NNM force appropriation ($F = 4$N) of the damped nonlinear beam. Top plot: responses along the branch close to the first resonance are marked by circles. Bottom plots: phase scatter diagrams of the complex Fourier coefficients of the displacements corresponding to the fundamental frequency for the responses (a), (b), (c) and (d).

track the change of the forced frequency responses until the NNM force appropriation is achieved.

From the rest position, the structure is forced at the natural frequency of the undamped LNM. After some transients, steady-state periodic forced response is obtained. Depending on the nonlinearities, the excitation frequency is then gradually increased or decreased to approach phase resonance. The phase lag indicator is continuously monitored during this process to assess the quality of the NNM force appropriation. The process is carried out until sufficiently good approximation of the phase quadrature criterion is achieved. In view of the basins of attraction of the coexisting forced responses, this procedure needs to adapt the frequency increments carefully. While quite large increments are initially suitable, smaller changes of the excitation frequency are required near the resonance to remain on the frequency response branch of interest. This stepped excitation frequency procedure is illustrated in Figure 4.23 for a constant force amplitude F=4N. The frequency responses obtained through this sequential process are represented by circles. The evolution of the phase response is also shown for four specific frequencies: the complex Fourier coefficients of the displacement responses corresponding to the fundamental frequency are illustrated. Since the excitation force $p(t) = F\sin(\omega t)$ is characterized by a phase of 90°, the NNM force appropriation is achieved when the phase of the displacements tends to 0°. This is performed for a frequency of 43.6 Hz, which corresponds to point (d) in Figure 4.23. The imperfect appropriated response of Figure 4.22 is then reached, and the NNM is therefore isolated. The second fundamental NNM may be appropriated in the same way.

NNM Free Decay Identification

Now that an NNM vibrates in isolation, its energy dependence is determined by turning off the excitation and tracking the single-NNM free damped response. The resulting response at the main beam tip is depicted in Figure 4.24. The dynamics closely follows the corresponding undamped NNM.

The FEP determined from the numerical experiments and computed through the CWT is illustrated in Figure 4.25. The ridge of the transform provides the corresponding backbone. For comparison, the theoretical FEP computed from the conservative equations of motion is also represented. Apart from the CWT edge effects, a very good agreement is obtained between the two backbones. The relative error of the frequency is lower than 0.2% for the complete energy range.

The modal curves extracted from the time series at different energy levels (marked by circles in Figure 4.25) are displayed in Figure 4.26. The left plots represent the motions in a two-dimensional projection of the configuration space while the right plots depict the modal shapes. The theoretical undamped NNM motions are superposed using dashed lines. The theoretical modal curves and those extracted from the time series agree to the point where the motions cannot be distinguished. The MSE between the time series is consistently lower than 0.1%.

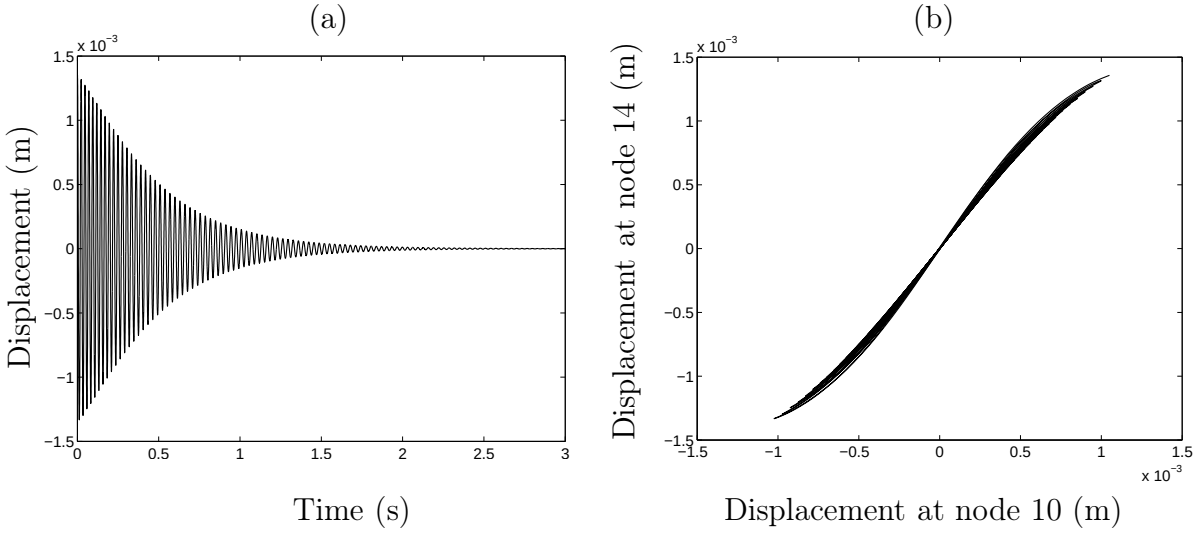

Figure 4.24: Free response of the damped nonlinear beam initiated from the imperfect appropriated forced response represented in Figure 4.22. (a) Time series of the displacement at the tip of the main beam (node 14). (b) Motion in the configuration space composed of the displacements at nodes 10 and 14.

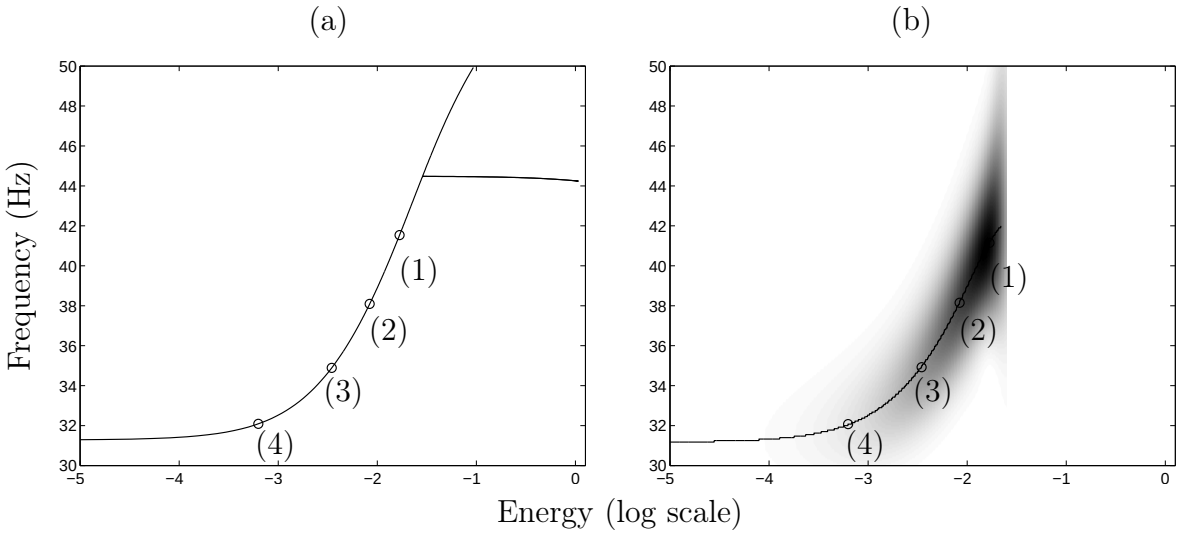

Figure 4.25: Frequency-energy plot of the first NNM of the nonlinear beam. (a) Theoretical FEP. (b) FEP calculated from the time series of the free damped response using the CWT. The solid line is the ridge of the transform.

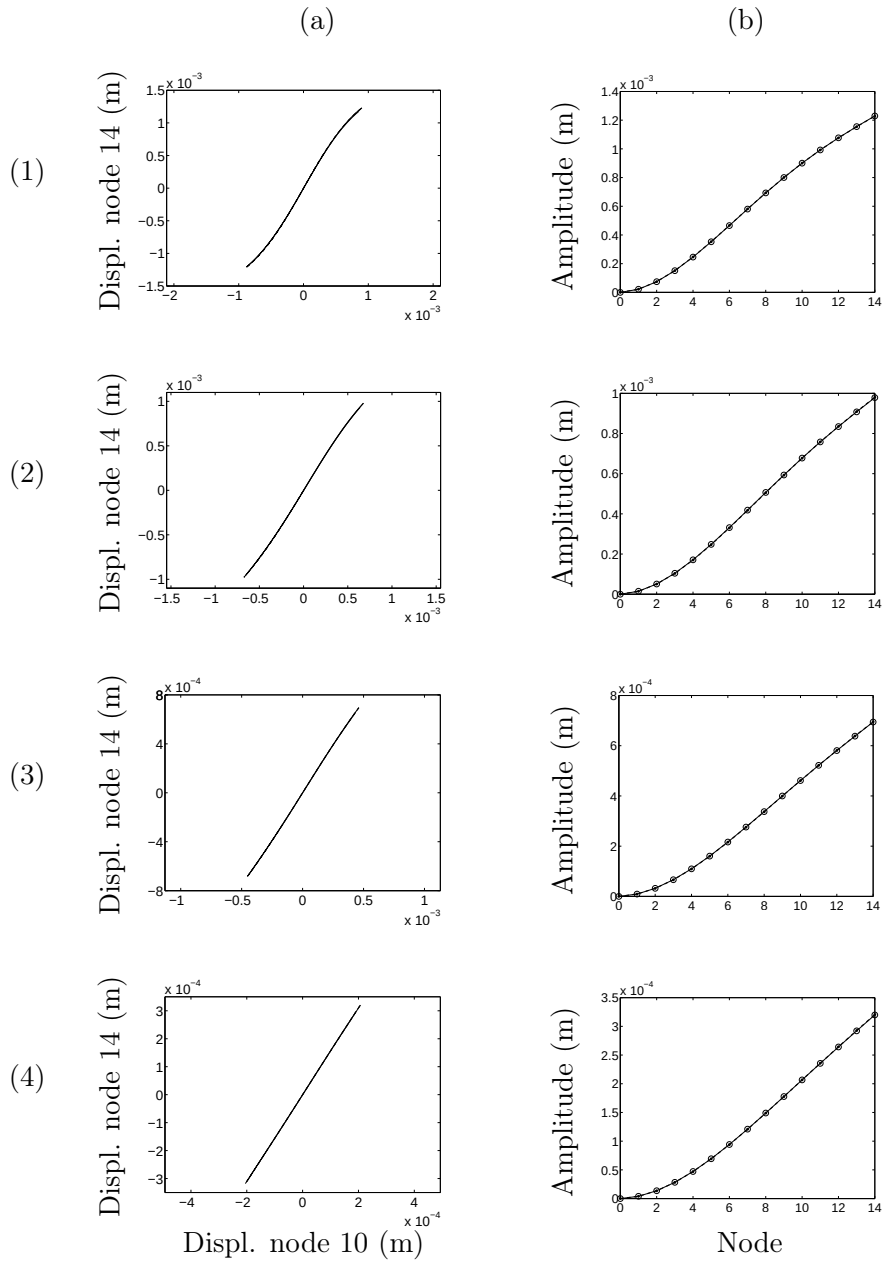

Figure 4.26: Modal curves and modal shapes of the first NNM of the nonlinear beam for decreasing energy levels marked in Figure 4.25 by circles (1), (2), (3) and (4). (a) Modal curves in the configuration space composed of the displacements at nodes 10 and 14. (b) Modal shapes composed of the displacement amplitudes of the main beam. The theoretical NNM motions are also superposed using dashed lines.

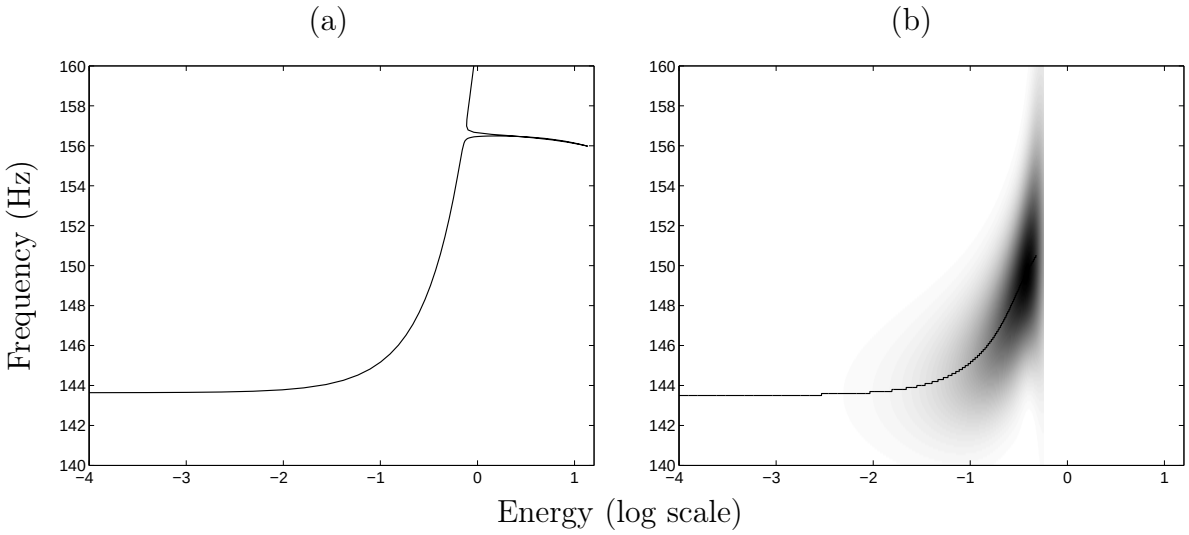

Figure 4.27: Frequency-energy plot of the second NNM of the nonlinear beam. (a) Theoretical FEP. (b) FEP calculated from the time series of the free damped response using the CWT. The solid line is the ridge of the transform.

Similar results are obtained for the second NNM. For illustration, the FEPs are depicted in Figure 4.27.

4.4 Concluding Remarks

Realizing that linear EMA is of limited usefulness for nonlinear structures, the present chapter was an attempt to develop nonlinear EMA by targeting the extraction of NNMs from time series.

Because modal superposition is no longer valid, dynamic testing of nonlinear structures is realized through a nonlinear phase resonance method, which relies on the extension of the phase lag quadrature criterion. Specifically, if the forced response across the structure is a monophase periodic motion in quadrature with the excitation, an NNM vibrates in isolation. Once the NNM appropriation is achieved, the complete frequency-energy dependence of that nonlinear mode can be identified during the free decay response using time-frequency analysis. Eventually, an experimental FEP for one specific NNM can be obtained, and the procedure can be applied for all NNMs of interest. To relate the NNMs of the underlying undamped system to those extracted from the experimental data, the procedure assumes moderately damped systems possessing elastic nonlinearities.

This two-step methodology paves the way for a practical nonlinear analog of EMA, which may be applied to strongly nonlinear systems. For instance, it can certainly be a solid basis for extending standard ground vibration testing to nonlinear aircrafts. Through the combination of EMA with TMA, finite element model updating and validation of

nonlinear structures are also within reach.

The objective of this chapter was to lay down the foundations for a rigorous experimental identification of NNMs. However, several issues still need to be addressed before the methodology can be applied to large-scale, real-life structures. Unlike LNMs, which are neutrally stable, NNMs can be stable or unstable, which may complicate their practical realization. NNMs also possess basins of attraction which may shrink or expand along the backbone branch of the FEP. Sensitivity to measurement noise and uncertainty might therefore render nonlinear force appropriation more challenging than its linear counterpart. Experimental demonstration of these results is the next logical step and is carried out in the following chapter using the existing nonlinear beam.

Chapter 5

Experimental Demonstration of Nonlinear Modal Testing

Abstract

This chapter deals with the experimental application of the methodology for nonlinear normal mode (NNM) identification introduced in Chapter 4. To demonstrate its efficacy, the methodology is applied to an experimental cantilever beam with geometrical nonlinearity. To this end, based on the phase lag quadrature criterion, an indicator function is developed to assess whether satisfactory NNM appropriation is effectively achieved.

5.1 Introduction

The present chapter is devoted to the experimental demonstration of the methodology developed in Chapter 4 for nonlinear experimental modal analysis (EMA). To this end, an experimental structure corresponding to the nonlinear beam model studied in Chapter 4 is considered, and the ability of the proposed methodology to extract its nonlinear normal modes (NNMs) from measured responses is assessed.

This chapter is organized as follows. In the next section, an indicator for NNM force appropriation is introduced. The experimental set-up considered here is presented in Section 5.3. Finally, the methodology is applied to the test structure in Section 5.4, and the NNM identification is carried out.

5.2 Indicator for NNM Force Appropriation

As shown in Chapter 4, the phase lag quadrature criterion, valid for linear systems, can be generalized to nonlinear systems (4.1). As a result, a nonlinear structure vibrates according to a single NNM of the underlying conservative system if the response (in terms of displacements or accelerations) across the structure is a monophase periodic motion with a phase lag of 90° with respect to the excitation. It expresses that the applied excitation compensates for the viscous damping forces. Specifically, the phase lag of nonlinear signals (i.e., generally including multi-harmonic components) is defined with respect to each harmonic, and the nonlinear monophase response $\mathbf{x}(t)$

$$\mathbf{x}(t) = \sum_{k=1}^{\infty} \mathbf{X}_k \cos(k\omega t) \tag{5.1}$$

is in quadrature with the excitation $\mathbf{p}(t)$ if

$$\mathbf{p}(t) = \sum_{k=1}^{\infty} \mathbf{P}_k \sin(k\omega t) \tag{5.2}$$

i.e., if the force and the response can be written as a sine and cosine series, respectively.

For linear structures, the phase resonance criterion is frequently checked by means of the mode indicator function (MIF) to evaluate the quality of modal appropriation [165]. This indicator can be extended to assess the quality of a tuned NNM motion of nonlinear systems by taking into account the different harmonic components in the measured response.

The general periodic response of nonlinear systems can be expressed as a complex Fourier series

$$\mathbf{x}(t) = \sum_{k} \mathrm{Re}\left(\mathbf{Z}_k e^{ik\omega t}\right) \tag{5.3}$$

where $\mathbf{Z}_k$ is the complex Fourier coefficient vector of the kth harmonic. Following the MIF philosophy, the quality of NNM appropriation for the kth harmonic is given by

$$\Delta_k = \frac{\mathrm{Re}\,(\mathbf{Z}_k)^* \,\mathrm{Re}\,(\mathbf{Z}_k)}{\mathbf{Z}_k^* \mathbf{Z}_k} \tag{5.4}$$

where star denotes the conjugate transpose of the vector. This scalar expression returns a value between zero and unity depending on the degree to which the kth harmonic component of the responses deviate from being in quadrature with the applied force. Assuming a sine series excitation (5.2), a value of unity indicates a perfect phase quadrature of the corresponding harmonic. The NNM appropriation may therefore be assessed by examining separately this indicator for all harmonics in the response. A global confidence indicator of NNM appropriation is introduced herein by considering the N significant harmonic components in the measured responses

$$\Delta = \frac{1}{N}\sum_{k=1}^{N} \Delta_k = \frac{1}{N}\sum_{k=1}^{N} \frac{\mathrm{Re}\,(\mathbf{Z}_k)^* \,\mathrm{Re}\,(\mathbf{Z}_k)}{\mathbf{Z}_k^* \mathbf{Z}_k} \tag{5.5}$$

This *NNM appropriation indicator* is related to the purity of the appropriated response: a value of unity indicates a perfect NNM isolation.

5.3 Experimental Set-Up

5.3.1 Description of the Experimental Fixture

Targeting the experimental application of the proposed EMA methodology, a set-up composed of a cantilever beam with a thin beam at its end is considered throughout this chapter. This experimental structure is represented in Figure 5.1, and the related geometrical and mechanical properties are listed in Table 5.1. The nonlinear behavior comes from the geometrical stiffening effect of the thin beam. This benchmark is similar to the structure used during the European action COST F3 [141] for nonlinear system identification and corresponds to the nonlinear beam model studied in Chapter 4. In particular, its nonlinear behavior was identified and modeled in [63, 75].

In order to avoid the effect of gravity, the thin beam is positioned vertically with its neutral axis parallel to ground, and the structure is excited in a horizontal plane by means of an electrodynamic shaker (Figures 5.1 and 5.2). The structural response is measured using seven accelerometers which span the main beam regularly, and a displacement sensor (laser vibrometer) is located at the end of the beam, i.e., at position 7. The exciter is connected to the structure by means of a rod at the end of which a force transducer is mounted. As a result, the phase lag of the forced responses with respect to the measured applied excitation may be determined during testing.

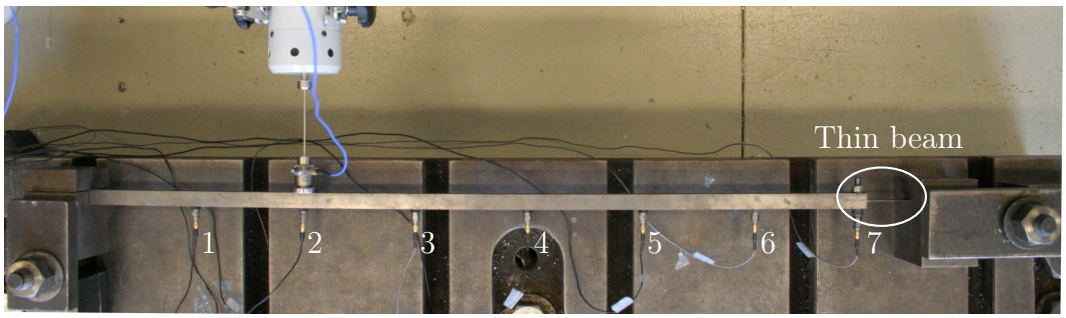

Figure 5.1: Experimental set-up (top view)

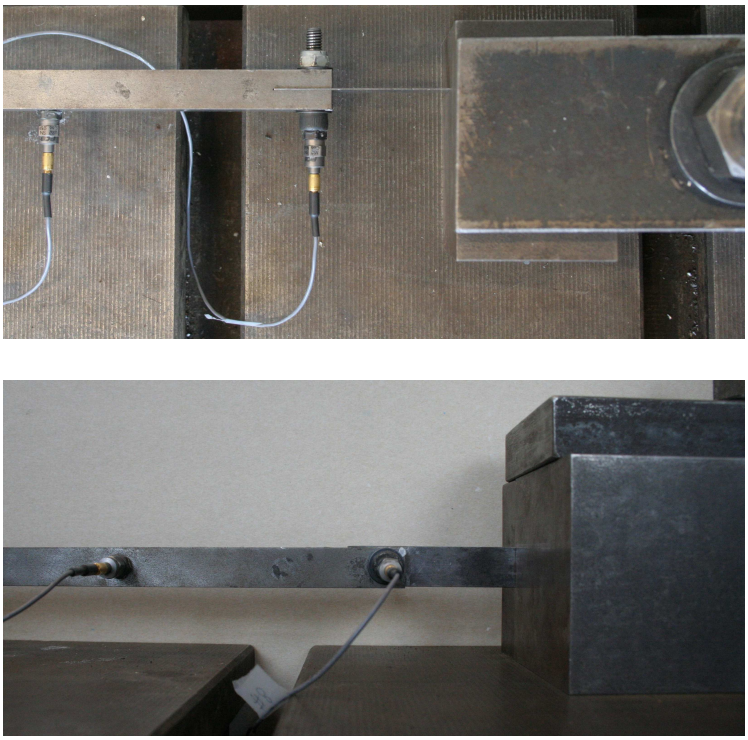

Figure 5.2: Close-up of the thin beam of the experimental set-up. Top plot: top view. Bottom plot: front view.

	Length (m)	Width (m)	Thickness (m)	Material
Main beam	0.7	0.014	0.014	Steel
Thin beam part	0.04	0.014	0.0005	Steel

Table 5.1: Geometrical and mechanical properties of the nonlinear beam.

5.3.2 Preliminary Experimental Characterization

Prior to nonlinear modal analysis, a preliminary analysis consisting in the experimental investigation of the dynamics of the test structure is performed. This first step is necessary to characterize the nonlinear behavior of the structure in order to apply the methodology for NNM extraction.

Nonlinear Characterization

To highlight its nonlinear behavior, the structure is forced by means of the shaker at position 2 (see Figure 5.1) using white-noise excitation band-limited in the 0-500 Hz range. Figure 5.3 shows two FRFs measured at low and high force levels. At low excitation level, the test structure responds linearly while the large deflection of the thin beam at high level induces geometrically nonlinear effects. As shown in Figure 5.3, distortions appear in the FRF at high excitation level which significantly differs from the FRF measured at low level. It is confirmed by the close-up where the resonant frequencies clearly increases with the forcing amplitude, which reveals the hardening characteristic of the geometrical nonlinearity. The first mode is the most affected by the nonlinear effect over the energy range of interest. The FRF close to the second mode is moderately altered while the third mode is practically unaffected by the nonlinearity.

Modal Analysis of the Underlying Linear Structure

Traditional modal analysis of the test structure considered as linear may therefore be carried out at very low level of excitation. The identification of modal parameters of the underlying linear structure then provides valuable insight into the structure for the extraction of NNMs at higher energy levels (i.e., in the nonlinear range of motion). In particular, the preliminary knowledge of linear natural frequencies allows to initiate the stepped sine procedure for NNM force appropriation. In addition, the linear modal shapes may be useful to determine suitable shaker locations.

To this end, hammer impact testing is performed at low excitation level on the test structure alone, i.e., without the presence of the exciter system. This prevents possible perturbations of the original test structure due to the presence of the exciter (i.e., shaker-structure interactions). The linear modal properties are estimated using Ibrahim time domain method [54], which is a phase separation approach commonly used for linear modal analysis. The three linear normal modes (LNMs) obtained in the 0-500 Hz range are given in Figure 5.4. The associated linear modal damping ratios are lower than 0.1%, which highlights the weak damping of the structure.

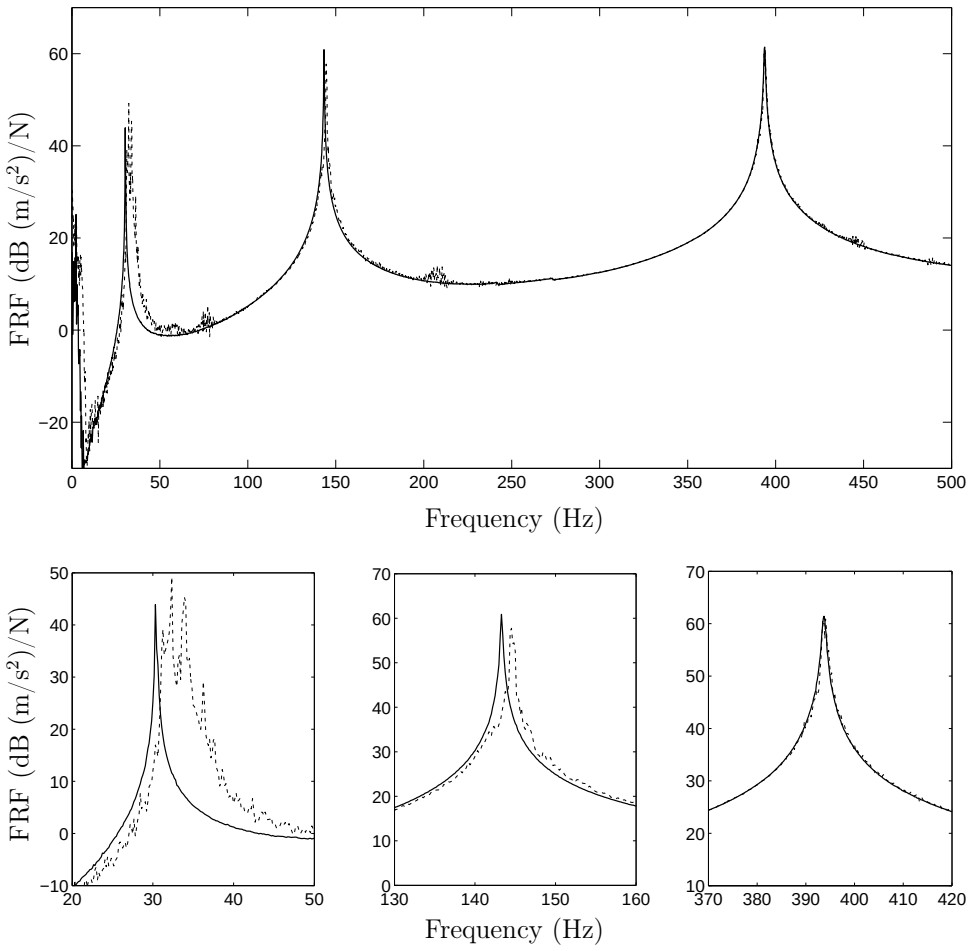

Figure 5.3: Measured FRFs of the experimental set-up using white-noise excitation (shaker at position 2). ——: low excitation level (0.7 N r.m.s.); − − − high excitation level (9 N r.m.s.). Top plot: magnitude of measured FRFs at position 7. Bottom plot: close-up around resonant frequencies.

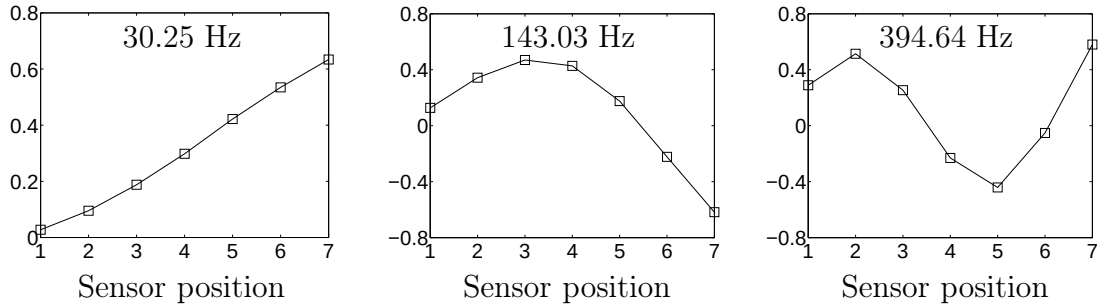

Figure 5.4: Linear normal modes of the test structure identified at low excitation level in the $0 - 500$ Hz range. From left to right: first, second and third normal modes.

5.4 Experimental Demonstration of NNM Identification

In the present section, the experimental extraction of NNMs of the test structure is considered using the two-step methodology detailed in Chapter 4. As evidenced in this chapter, the use of a single shaker may be suitable for NNM appropriation of such a structure with well-separated modes. This imperfect force appropriation approach combined with a stepped sine excitation procedure is considered herein, and it is shown that the NNMs of the test structure are isolated satisfactorily.

5.4.1 Extraction of the First NNM

NNM Force Appropriation using Stepped Sine Excitation

To minimize shaker-structure interaction, the shaker is placed near the clamped end of the main beam. For the first mode, the exciter is located at position 2 (see Figure 5.1). The generated force is a single-sine (i.e., mono-harmonic) excitation of tunable frequency.

Based on the knowledge of the underlying linear properties, the stepped sine excitation procedure may be initiated using the natural frequency of the LNM as excitation frequency. In view of the hardening nonlinear behavior observed previously, it is gradually increased to follow the forced response branch of interest until resonance. At each step, if the excitation frequency increment leads to a sudden change in the measured responses (i.e., discontinuity in the amplitude and phase of the motion) indicating a jump to another coexisting stable solution, the procedure is then restarted, and the last increment is decreased to remain on the initial branch of forced responses. This procedure is stopped when sufficiently good NNM appropriation is achieved. To this end, the indicator introduced previously is continuously monitored during the process.

It is worth noticing that the shaker amplification does not operate at constant current source, but the generated voltage is rather fixed during the experiments. As a result, the amplitude and phase of the actual force introduced by the exciter may fluctuate during the stepped sine procedure. It is of little importance since the applied force is measured during experimental testing, which enables to determine the phase lag between the responses and the excitation, this latter being relevant herein.

The measured steady-state forced responses are illustrated in Figure 5.5. The maximum amplitude of the displacement at the main beam tip is depicted as a function of the excitation frequency. The fundamental complex Fourier coefficients (i.e., corresponding to the forcing frequency) of the measured acceleration responses along the structure are also given in phase scatter diagrams. Initially, quite large increments of the excitation frequency are suitable. Close to resonance, smaller variations are required to remain on

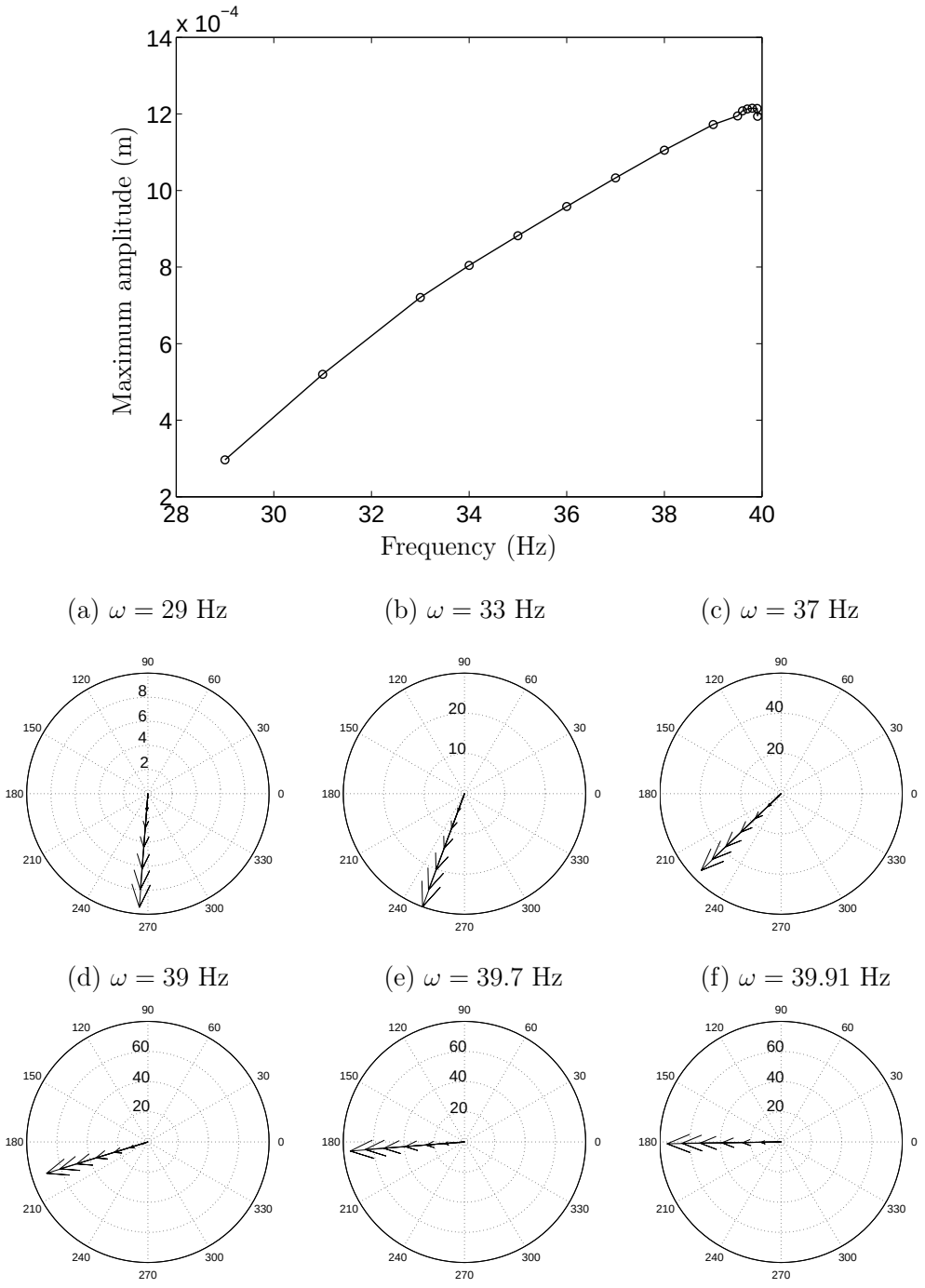

Figure 5.5: Force appropriation of the first NNM of the test structure through experimental stepped sine excitation procedure. Top plot: Measured steady-state periodic forced responses (marked by circles) given in terms of the maximum amplitude of the displacement at the main beam tip (i.e., at position 7) as a function of the excitation frequency. Bottom plots: phase scatter diagrams of the fundamental complex Fourier coefficients of the measured accelerations (m/s^2) across the beam (i.e., positions from 1 to 7) at different excitation frequencies.

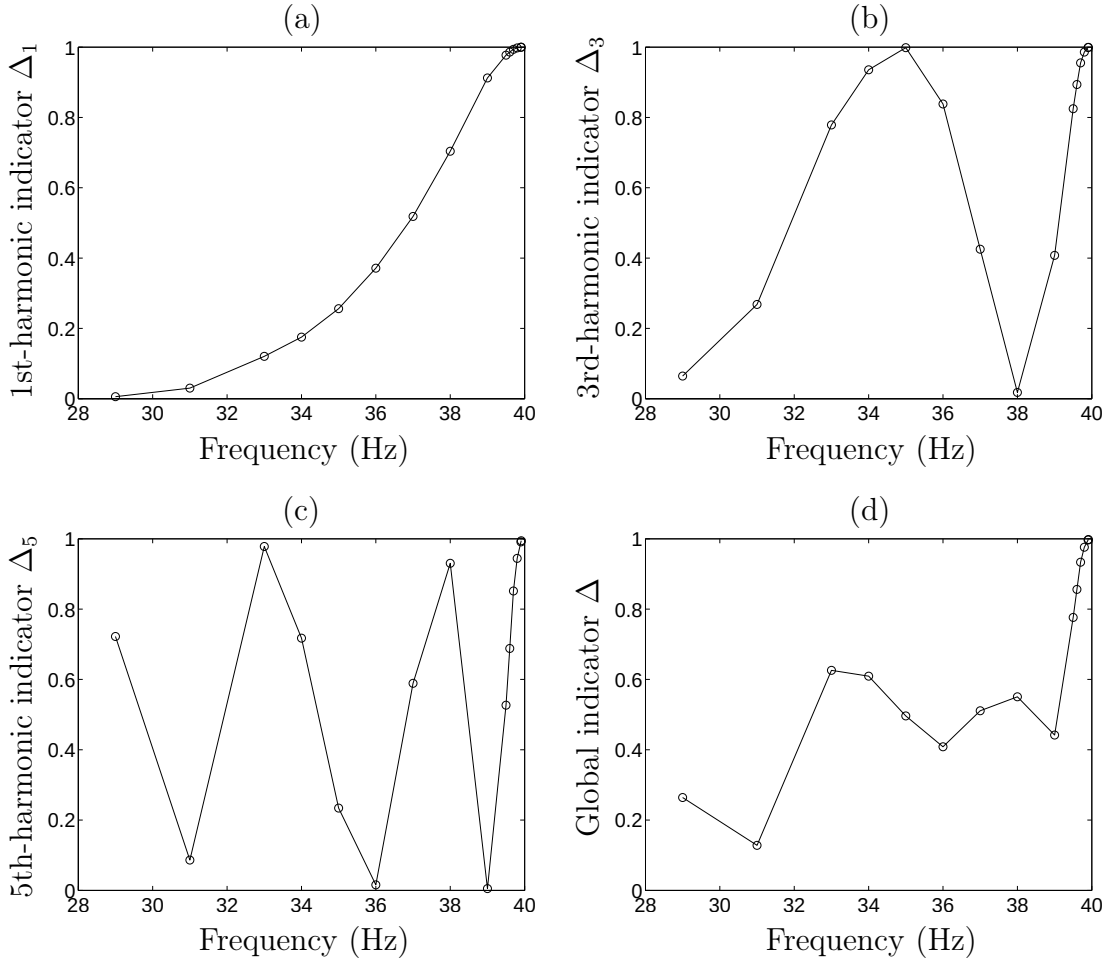

Figure 5.6: Evolution of the NNM force appropriation indicator for the first NNM of the test structure with respect to the excitation frequency. Indicator for (a) the fundamental frequency, (b) the 3rd-harmonic, (c) the 5th-harmonic components, and (d) global NNM appropriation indicator.

the frequency response branch of interest. It confirms the numerical results reported in Chapter 4. For constant force amplitude, another branch of stable periodic motions coexists near the resonance, and the basin of attraction of the initial forced responses gets smaller as the frequency increases. From a practical viewpoint, the NNM appropriation is then realizable by carefully changing the frequency of the generated excitation. For instance, increments of 0.1 Hz are finally necessary during the stepped sine procedure to prevent jump phenomenon.

The scatter plots display the evolution of the phase of the forced responses with respect to the sine excitation which is along the vertical axis (purely imaginary excitation). The motion across the structure is synchronous, and the phase lag changes with the excitation frequency to come close to 90°. It is confirmed by the evolution of the NNM appropria-

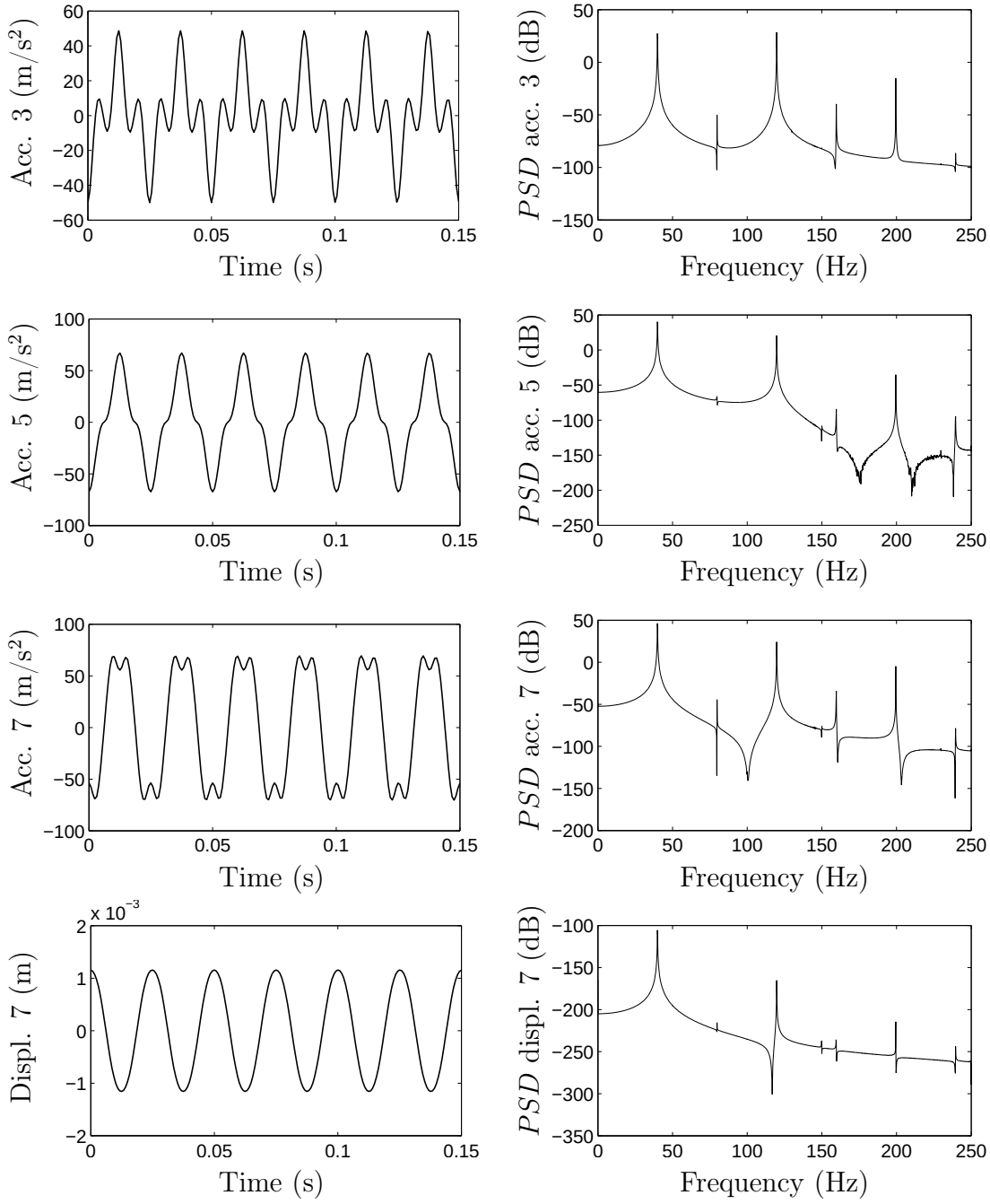

Figure 5.7: Appropriated forced response of the first NNM of the test structure ($\omega = 39.91$ Hz). Left plots: measured time series. Right plots: power spectral density. From top to bottom: accelerations at position 3, position 5, position 7 and displacement at the tip of the beam, i.e., at position 7.

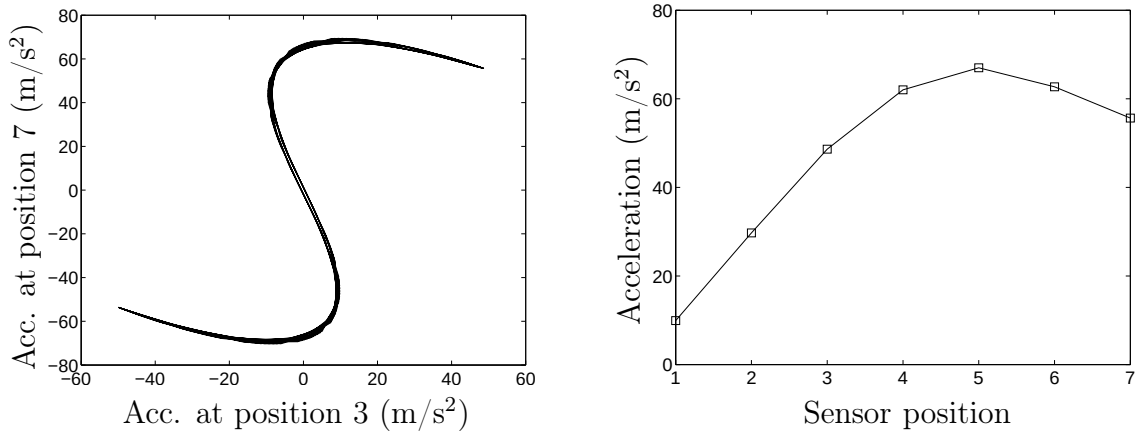

Figure 5.8: Appropriated forced response of the first NNM of the test structure ($\omega = 39.91$ Hz). Left plot: Modal curve in a two-dimensional projection of the configuration space in terms of measured accelerations. Right plot: Modal shape composed of the amplitudes of the measured accelerations along the main beam.

tion indicator depicted in Figure 5.6 which tends to 1. The proposed indicator, calculated from the measured accelerations across the structure, is initially evaluated for each of the significant harmonics included in the responses (i.e., for the fundamental, third and fifth harmonics). The global NNM purity indicator combining all these harmonics is also displayed in this figure. Only odd harmonics are considered herein, even harmonic components of the responses being negligible (see Figure 5.7). In particular, the evolution observed for the fundamental frequency indicator is in agreement with the change noticed by the scatter diagrams. On the other hand, multiple quadratures of the harmonic components occur prior to the one of the fundamental frequency terms. It is evidenced by the existence of several unit values of the indicator for the harmonics of the fundamental frequency, which explains that the evolution of the global NNM indicator is not a monotonically increasing function. Eventually, the forced response obtained for the final excitation frequency of 39.91 Hz corresponds to a value of the indicator very close to 1 for all harmonics. The global NNM appropriation indicator is thus equal to 0.99. This very satisfactory value reveals that the structure practically vibrates synchronously in quadrature with the harmonic excitation. For each measured response along the beam, a phase lag of 89° is actually observed for each harmonic.

As a result, the first undamped NNM is experimentally isolated at a specific energy level. The measured time series of the resulting forced response are represented in Figure 5.7. The displacement at the main beam end is about 1.2 mm. The nonlinearity is then activated, and harmonic components of the excitation frequency appear in the response as clearly noticed by the power spectral density (PSD) shown in Figure 5.7. The NNM modal curve, expressing the motion in a two-dimensional projection of the configuration space, is given in Figure 5.8 in terms of accelerations. This figure also represents the

NNM modal shape composed of the maximum amplitudes of the accelerations for all measurement locations along the structure. The modal shape is a snapshot of the NNM motion at a specific time instant corresponding to the maximum response amplitude.

NNM Free Decay Identification

Now that the structure vibrates according to the first NNM at a specific energy level, the exciter amplifier is turned off to initiate NNM free decay. The resulting response is illustrated in Figure 5.9 where the time series of the measured displacement at the beam end is depicted. The dashed line corresponds to the time instant when the shaker is stopped, i.e., the boundary between the steady-state forced response (NNM force appropriation step) and the free damped motion (NNM free decay step). In addition, Figure 5.10 shows the measured response in a two-dimensional projection of the configuration space in terms of accelerations.

In practice, the applied excitation does not immediately drop to zero at the turn-off instant. Nevertheless, the excitation rapidly reduces and can be assumed as negligible. It confirms that the influence of the presence of the exciter on the free decay of the initial test structure may be viewed as moderate. Finally, in view of the weak damping of the structure and thanks to the invariance principle, the induced free damped response is expected to follow the first undamped NNM when energy decreases with time.

The continuous wavelet transform (CWT) is computed to track the frequency content of the measured single-NNM free decay response. For illustration, the time-frequency dependence given by the CWT of the displacement at the beam tip is represented in Figure 5.11. The temporal evolution of the instantaneous fundamental frequency is determined from the maximum ridge of the transform. The frequency-energy dependence of the first NNM is then extracted from the measured time series. This dependence can be clearly highlighted by substituting the response amplitude for time. The identified frequency as a function of the amplitude (envelope) of the displacement at the end of the main beam is illustrated in Figure 5.12. In Section 5.5.3, the total energy present in the system is estimated, and the experimental frequency-energy plot (FEP) is fully reconstructed from these measured data.

The modal curves of the first NNM are directly extracted from the measured time series around specific time instants, related to different energy levels. The first NNM at five distinct response levels corresponding to the squares in Figure 5.12 is displayed in Figure 5.13. This plot presents the identified modal curves and the associated modal shapes.

Figures 5.12 and 5.13 clearly reveal that the first NNM and its oscillation frequency are strongly affected by nonlinearity for increasing energy levels. The frequency increases with the energy level which confirms the hardening characteristic of the structure. The NNM motions have also a marked energy dependence. At high energy, the modal curves distinctly deviate from a straight line, which reveals the higher harmonic contents (mostly

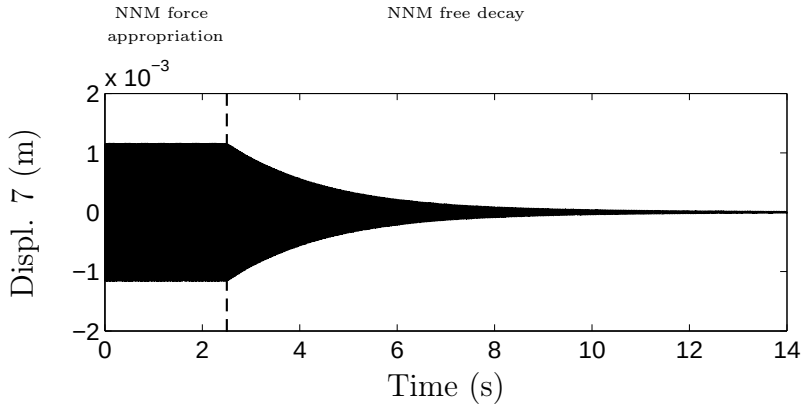

Figure 5.9: Free decay identification of the first NNM of the test structure. Measured free response initiated from the appropriated forced response (ω = 39.91 Hz). Time series of the displacement at the tip of the beam, i.e., at position 7. The dashed line corresponds to the turn-off time instant of the shaker, i.e., the boundary between NNM force appropriation and NNM free decay.

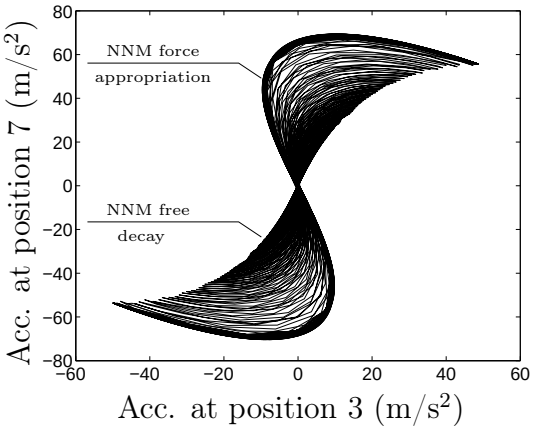

Figure 5.10: Measured free decay of the first NNM of the test structure initiated from the appropriated forced response (ω = 39.91 Hz) in a two-dimensional projection of the configuration space in terms of accelerations.

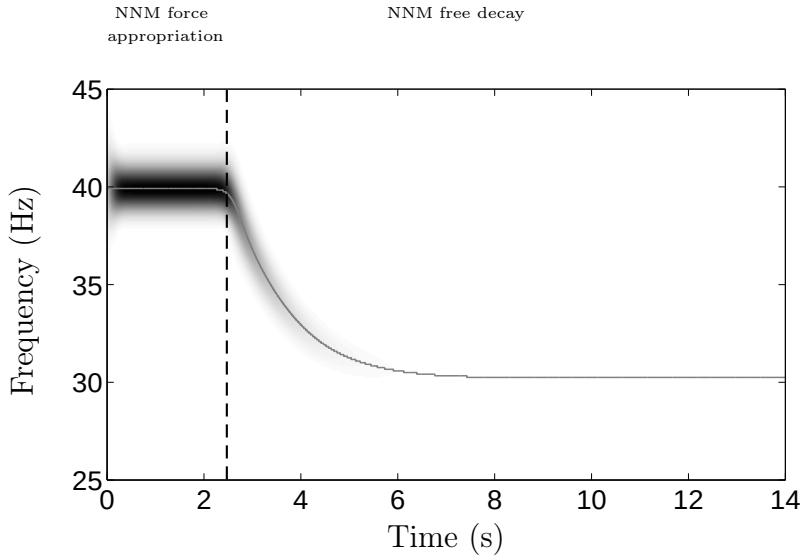

Figure 5.11: Wavelet transform of the measured free decay of the first NNM of the test structure initiated from the appropriated forced response (ω = 39.91 Hz). Temporal evolution of the instantaneous frequency of the displacement at the tip of the beam, i.e., at position 7. The solid line corresponds to the maximum ridge of the transform.

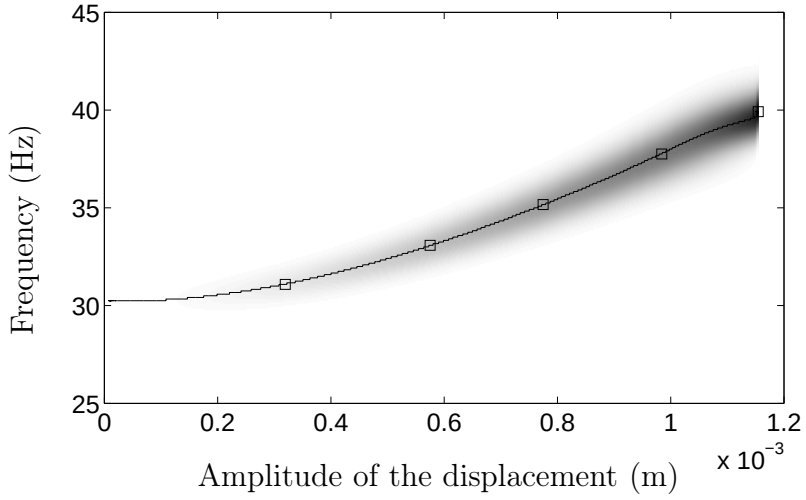

Figure 5.12: Frequency of the first NNM of the test structure, identified from the measured free decay using the CWT, as a function of the amplitude displacement at the main beam tip (i.e., at position 7). The solid line corresponds to the maximum ridge of the transform.

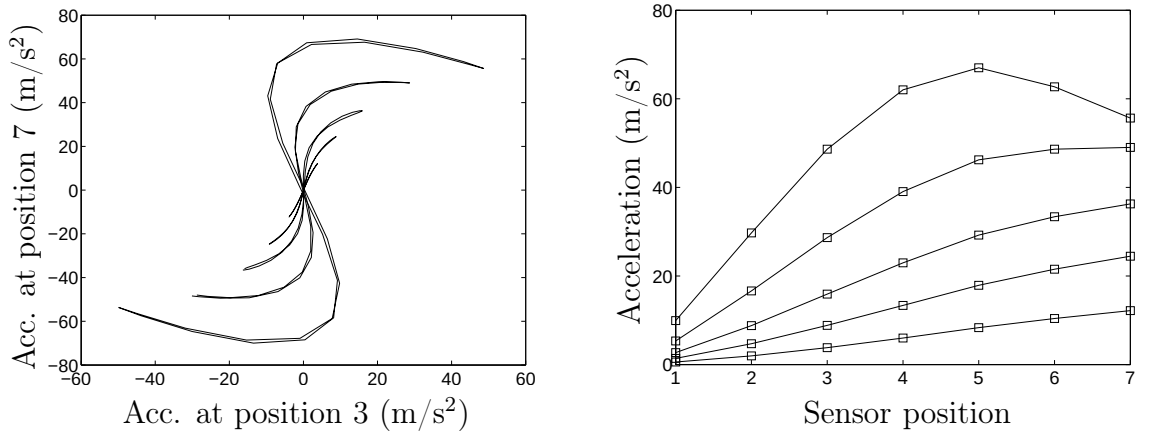

Figure 5.13: First NNM of the test structure extracted from the measured free decay at five different energy levels marked by squares in Figure 5.12. Left plot: modal curves in a two-dimensional projection of the configuration space in terms of measured accelerations. Right plot: modal shapes composed of the amplitudes of the measured accelerations along the main beam.

the third harmonic) in the response. It is particularly pronounced given that the motion is represented in terms of accelerations. The modal shape is also altered as shown in Figure 5.13. At low energy, the NNM thus comes close to the first LNM identified previously. In particular, the modal curve tends to a straight line in the configuration space and the NNM frequency corresponds to the natural frequency of the first linear mode.

5.4.2 Extraction of the Second NNM

NNM Force Appropriation using Stepped Sine Excitation

In view of its deformation shape, the second mode is more sensitive to the presence of the exciter device in proximity to its antinode of vibration, which was also evidenced by experimental investigations. The shaker is consequently positioned closer to the clamped end of the main beam (namely at location 1) for the extraction of the second NNM.

Similarly, the NNM force appropriation of the second mode is carried out using stepped sine excitation. Starting from the natural frequency of the second linear mode, the excitation frequency is next gradually increased. In Figure 5.14, the measured steady-state periodic responses resulting from this forced vibration testing are represented by means of the displacement at the tip of the main beam. The fundamental frequency components of the forced frequency responses are also given in scatter plots. The corresponding evolution of the NNM appropriation indicator is illustrated in Figure 5.15. Similar results as for the force appropriation of the first NNM are observed. Regarding the practical

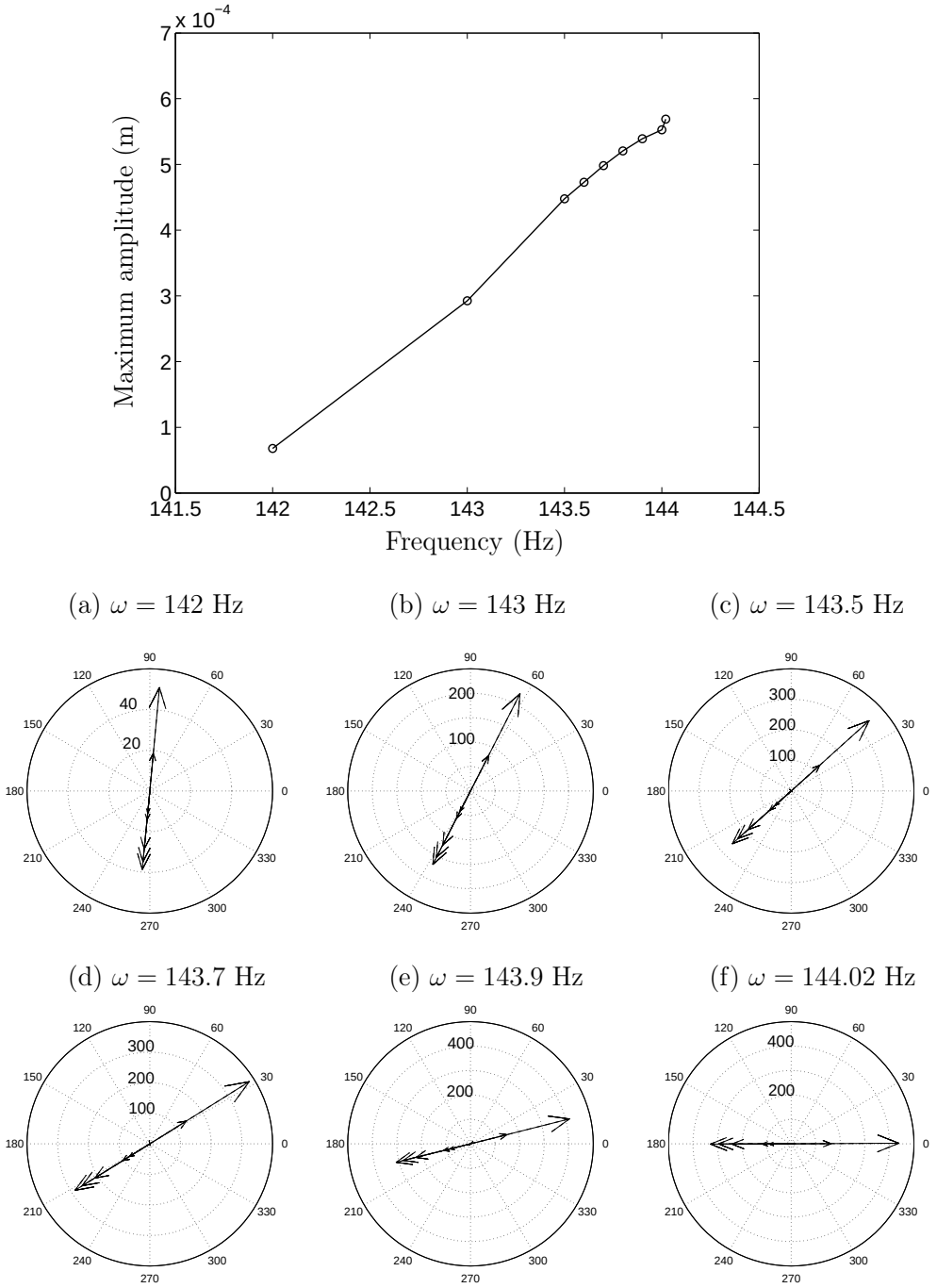

Figure 5.14: Force appropriation of the second NNM of the test structure through experimental stepped sine excitation procedure. Top plot: Measured steady-state periodic forced responses (marked by circles) given in terms of the maximum amplitude of the displacement at the main beam tip (i.e., at position 7) as a function of the excitation frequency. Bottom plots: phase scatter diagrams of the fundamental complex Fourier coefficients of the measured accelerations (m/s^2) across the beam (i.e., positions from 1 to 7) at different excitation frequencies.

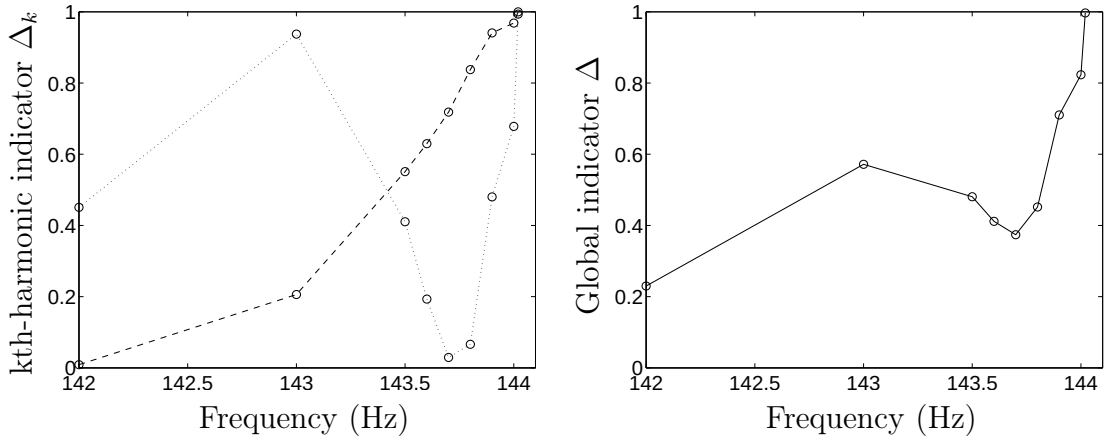

Figure 5.15: Evolution of the NNM force appropriation indicator for the second NNM of the test structure with respect to the excitation frequency. Left plot: indicator for the fundamental frequency ($- - -$) and 3rd-harmonic components ($\cdots\cdots$). Right plot: global NNM appropriation indicator.

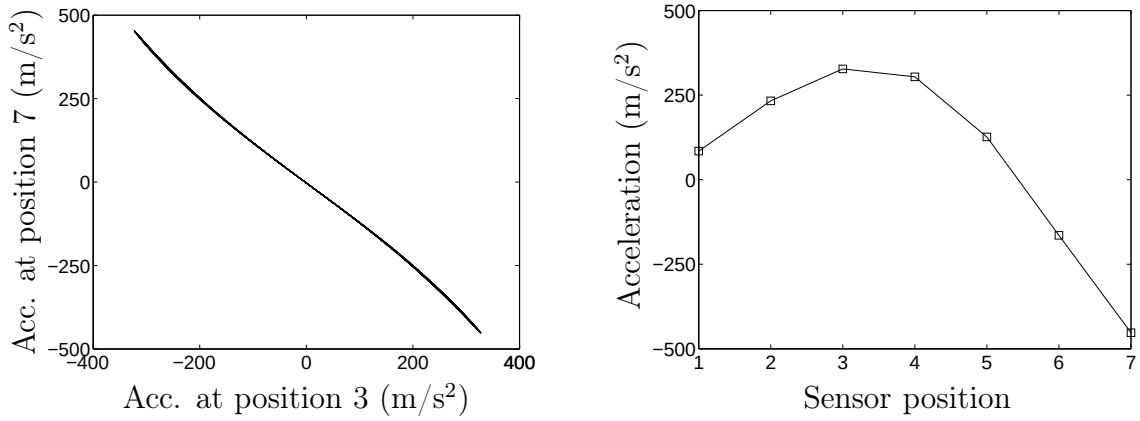

Figure 5.16: Appropriated forced response of the second NNM of the test structure ($\omega =$ 144.02 Hz). Left plot: Modal curve in a two-dimensional projection of the configuration space in terms of measured accelerations. Right plot: Modal shape composed of the amplitudes of the measured accelerations along the main beam.

realization, the frequency of the excitation must nevertheless be adapted more carefully, which indicates narrower domain of attraction of the forced responses close to the second resonance. The NNM force appropriation is then performed for an excitation frequency of 144.02 Hz that corresponds to a global NNM indicator of 0.99. At each measurement location, the phase lag of the responses with respect to the excitation is 89° for all harmonics. Accordingly, the second NNM practically vibrates in isolation. The measured modal curve and modal shape are displayed in Figure 5.16.

From the considered location of the shaker, the magnitude of the induced response of the test structure is limited by the maximum force that can be generated by the exciter. For this higher-frequency mode, the displacement at the beam tip reached during NNM force appropriation is around 0.6 mm. However, as shown in Section 5.5.3, the corresponding energy level is of the same order of magnitude than for the appropriation of the first NNM. So, for this energy level, the second mode seems to be moderately affected by nonlinearity. The oscillation frequency of the NNM motion is slightly altered in comparison with the natural frequency of the second linear mode: the frequency increases by only 1 Hz due to the hardening effect of the geometrical nonlinearity. In addition, the NNM modal shape does barely differ from the corresponding linear mode. The modal curve is practically a straight line in the configuration space, which illustrates that the higher harmonic components in the motion are insignificant.

NNM Free Decay Identification

As for the first NNM, the excitation is stopped by turning off the amplifier. Hence, the measurement of the free damped response enables to identify the energy dependence of the second NNM. Figure 5.17 shows the oscillation frequency identified from the time series using the CWT as a function of the displacement at the main beam end. The modal curves and the corresponding modal shapes extracted for five different energy levels (marked by squares in Figure 5.17) are depicted in Figure 5.18.

It clearly illustrates the weak energy-dependence observed for the second NNM. The frequency and modal curves are slightly affected by nonlinearity over the energy range under consideration.

As previously evidenced by the FRF measurements at low and high levels, the third mode is almost unaffected by the nonlinearity for the considered energy range. Accordingly, the experimental extraction of the third NNM was not investigated herein.

The validation of these experimental results by means of a finite element model of the structure is achieved in the next section.

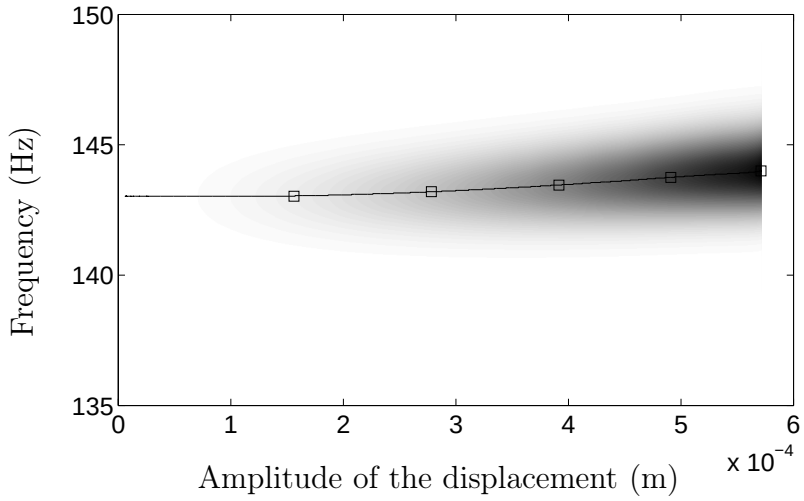

Figure 5.17: Frequency of the second NNM of the test structure, identified from the measured free decay using the CWT, as a function of the amplitude displacement at the main beam tip (i.e., at position 7). The solid line corresponds to the maximum ridge of the transform.

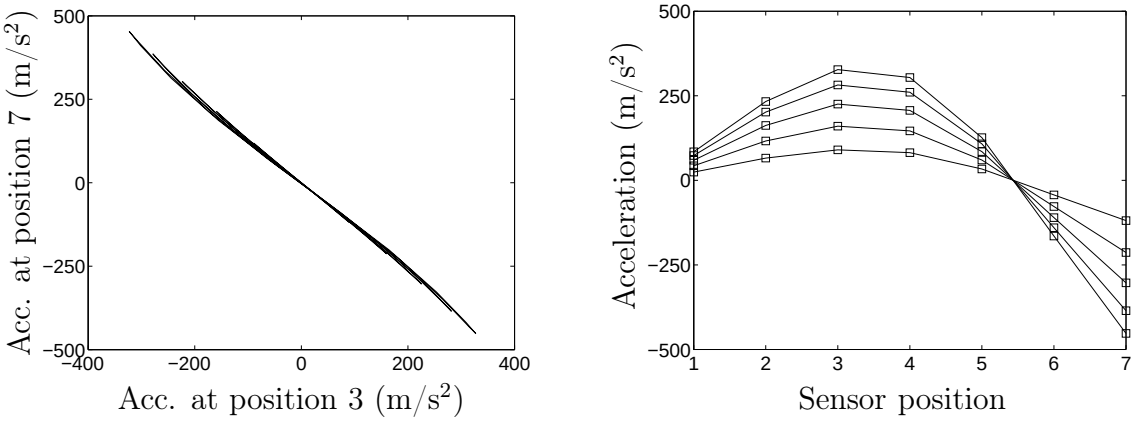

Figure 5.18: Second NNM of the test structure extracted from the measured free decay at five different energy levels marked by squares in Figure 5.17. Left plot: modal curves in a two-dimensional projection of the configuration space in terms of measured accelerations. Right plot: modal shapes composed of the amplitudes of the measured accelerations along the main beam.

5.5 Validation of NNM Identification

As mentioned previously, the proposed methodology for nonlinear EMA lies on moderate damping assumption, in which case the NNMs identified from experimental responses can be related to the NNMs of the underlying conservative system. In this section, a conservative finite element model of the test structure is considered. Theoretical modal analysis (TMA) of the structure is carried out using the numerical algorithm developed for NNM computation in Chapter 2. The computed theoretical NNMs may therefore be compared with the NNMs experimentally extracted. From a practical viewpoint, the procedure combining TMA and EMA may be used in the context of model validation of nonlinear structures. In this study, it is performed to assess the ability of the proposed methodology to extract the NNMs from experimental measurements. To this end, a reliable finite element model of the structure is independently identified.

5.5.1 Mathematical Model of the Test Structure

The undamped model of the nonlinear test structure is obtained based on a finite element approach. The governing equations of motion are then

$$\mathbf{M}\,\ddot{\mathbf{x}}(t) + \mathbf{K}\,\mathbf{x}(t) + \mathbf{f}_{nl}\left\{\mathbf{x}(t)\right\} = \mathbf{0} \tag{5.6}$$

The underlying linear system (i.e., the mass and stiffness matrices $\mathbf{M}$ and $\mathbf{K}$) is identified through the linear modal analysis performed at low energy level. The nonlinear behavior (i.e., the nonlinear restoring force $\mathbf{f}_{nl}$) is introduced in the model by resorting to a nonlinear system identification method. It is worth pointing out that the finite element model considered here corresponds to the system studied in Chapter 4 in which the parameters are now updated from experimental data.

Finite Element Model of the Underlying Linear Structure

The finite element model of the test structure is illustrated in Figure 5.19. As in Chapter 4, the main and thin beams are modeled using 14 and 3 two-dimensional Euler-Bernoulli beam elements, respectively. An additional linear rotational stiffness is used to model the junction between the two beams. Based on the linear modal parameters extracted in Section 5.3.2, the updating of the model provides an estimation of the rotational stiffness term at the junction.

Nonlinearity Identification

As performed in [63], the conditioned reverse path method is applied to identify the nonlinear behavior of the test structure. To this end, the structure is forced using white-

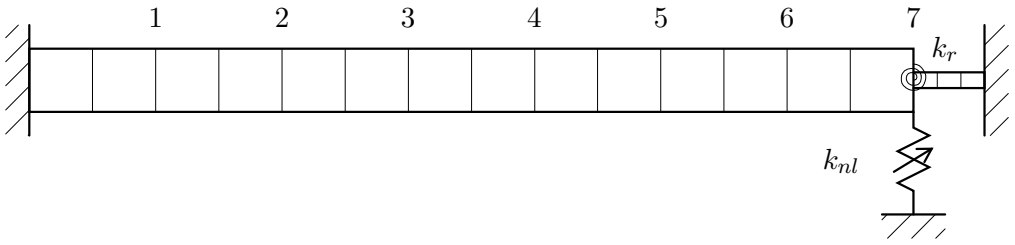

Figure 5.19: Finite element model of the test structure.

noise excitation band-limited in the 0-500 Hz range. It shows that the nonlinear behavior of the thin beam can be modeled using a grounded cubic spring at the junction of the main and thin beams:

$$f(x) = k_{nl}|x|^3 \text{sign}(x) \tag{5.7}$$

This cubic term takes the geometrical stiffening effect of the thin part into account. The estimated value of the nonlinear coefficient k_{nl} is 8.5×10^9 N/m^3.

5.5.2 Comparison between Experimental and Theoretical NNMs

The undamped NNMs of the finite element model of the structure are computed using the numerical algorithm introduced in Chapter 2. In this section, these theoretical NNMs are compared to the NNMs extracted from the experimental measurements.

For the first NNM, the dependence of its frequency on the displacement at the main beam tip is plotted in Figure 5.20. The experimental evolution was identified previously from the ridge of the CWT of the free decay. The frequency of the theoretical NNM closely matches the experimental one with a relative error lower than 1.25%. This error reaches its maximum value shortly after stopping the exciter. It could result from the imperfect realization of the free decay phase because of the presence of the exciter. Due to the existing coupling between the shaker and the structure, the applied excitation is not initially negligible which may lead to a parasitic deviation from the actual single-NNM free decay. In other words, the test structure of interest might be altered by interacting with the shaker system during the free decay step. However, this observed difference remains fully satisfactory and is rapidly reduced as evidenced in Figure 5.20.

The experimental modal curves and modal shapes of this first NNM at five different energy levels (marked by squares in Figure 5.20) are depicted in Figure 5.21. The left plots represent the modal curves in a two-dimensional projection of the configuration space while the right plots depict the modal shapes of the main beam. For comparison, the theoretical NNM at the same amplitude levels (marked by circles in Figure 5.20) is also superimposed. From this figure, it is observed that the first NNM of the finite element model is in good agreement with the experimental one for the complete energy range of

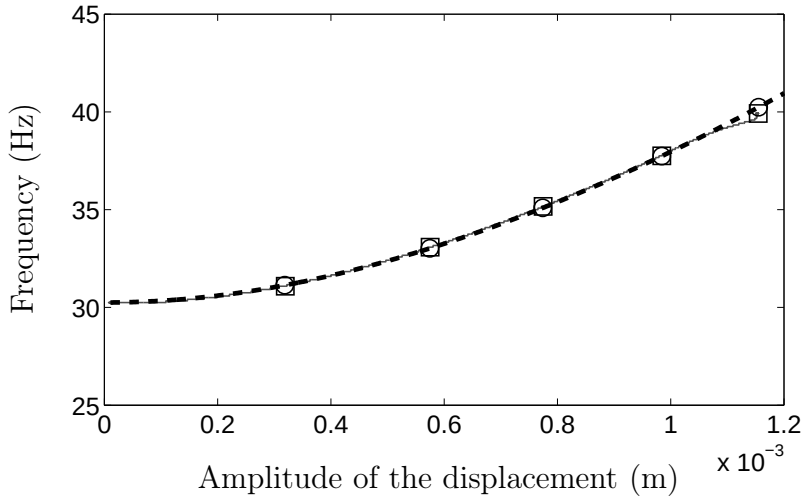

Figure 5.20: Frequency of the first NNM of the nonlinear beam. —□—: experimental frequency identified from the measured free decay of the test structure using the CWT; – – ○ – –: theoretical frequency computed from the finite element model of the structure. The frequency is given as a function of the amplitude (envelope) displacement at the tip of the main beam, i.e., at position 7.

interest.

Figure 5.22 shows the comparison between the experimental and theoretical frequencies of the second NNM. For this weakly energy-dependent NNM, the observed deviation is insignificant. Indeed, the maximum relative error is about 0.3% and corresponds to the initial difference in frequency resulting from the linear model updating, i.e., the error between the second normal mode of the updated underlying linear system and the experimental one extracted at low energy.

The modal curves and modal shapes of this second NNM for the five amplitude levels (marked in Figure 5.22) are compared in Figure 5.23. It shows that the experimental and theoretical NNM match very well for all considered energy levels.

In conclusion, these results confirm that the proposed methodology is capable of reliably extracting the energy dependence of NNMs of the test structure from experimental measurements. Both a strongly and a weakly energy-dependent NNM have been identified.

5.5.3 Reconstructed Frequency-Energy Plot

Because a FEP facilitates the interpretation of the dynamics, it is convenient to reconstruct this plot from the experimental results. To this end, it is necessary to determine the total energy (i.e., the sum of the kinetic and potential energies) present in the structure from the experimental measurements.

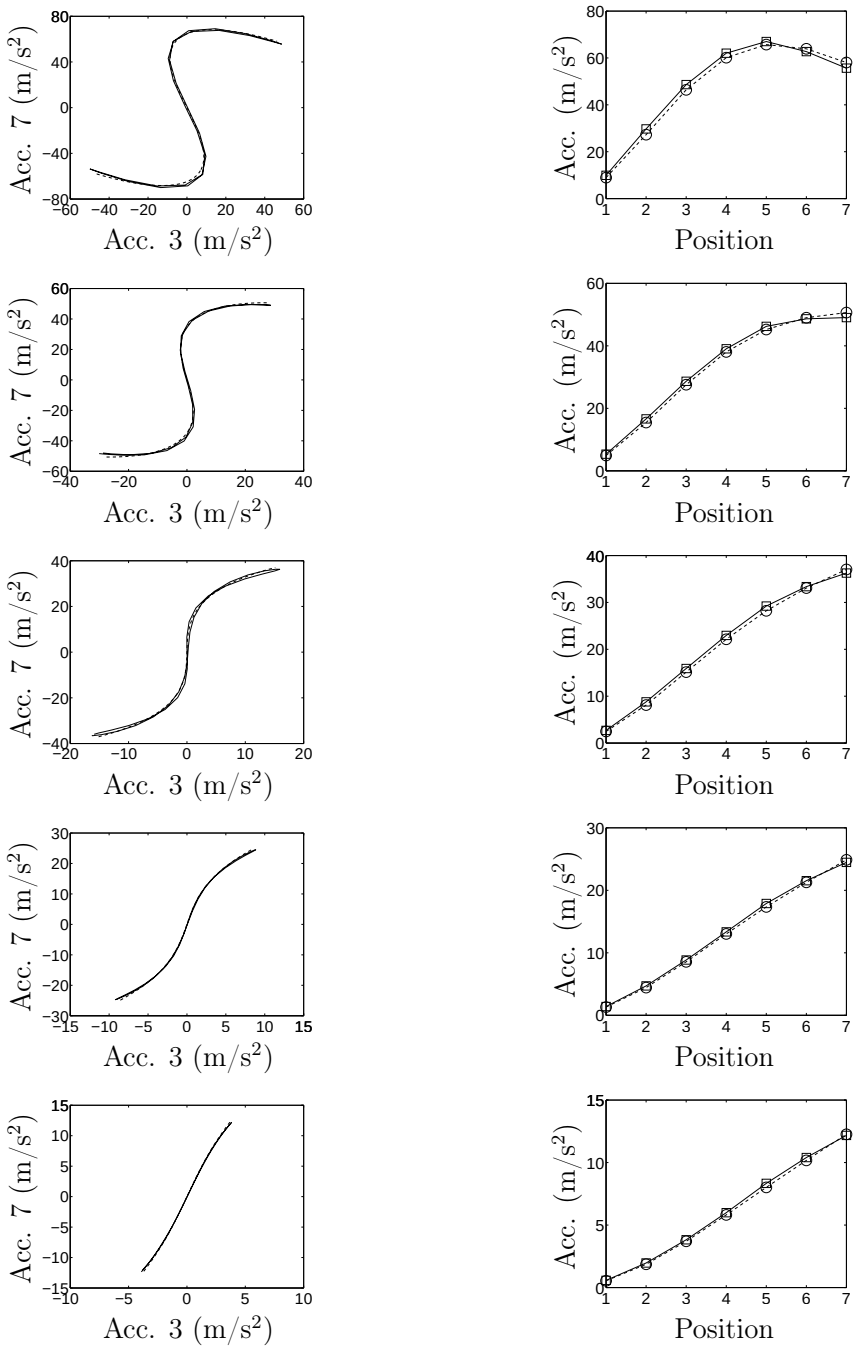

Figure 5.21: First NNM of the nonlinear beam. —□—: experimental NNM identified from the free decay of the test structure; − − ∘ − −: theoretical NNM computed from the finite element model of the structure. Left plots: modal curves in the configuration space composed of the accelerations at locations 3 and 7. Right plots: modal shapes composed of the amplitudes of the accelerations across the main beam. From top to bottom: NNM for decreasing energy levels marked in Figure 5.20.

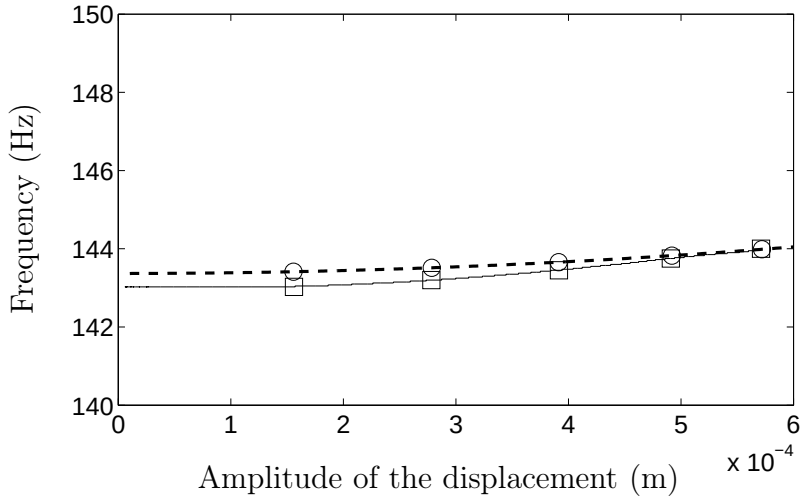

Figure 5.22: Frequency of the second NNM of the nonlinear beam. —□—: experimental frequency identified from the measured free decay of the test structure using the CWT; – – ∘ – –: theoretical frequency computed from the finite element model of the structure. The frequency is given as a function of the amplitude (envelope) displacement at the tip of the main beam, i.e., at position 7.

Considering system (5.6), the expressions for the kinetic and potential energies are provided by

$$\mathcal{T} = \frac{1}{2}\dot{\mathbf{x}}^*\mathbf{M}\dot{\mathbf{x}} \tag{5.8}$$

and

$$\mathcal{V} = \frac{1}{2}\mathbf{x}^*\mathbf{K}\mathbf{x} + \mathcal{V}_{nl}(\mathbf{x}) \tag{5.9}$$

respectively, where star denotes the transpose operation. In addition to the linear contribution, the potential energy is composed of the nonlinear term $\mathcal{V}_{nl}(\mathbf{x})$, which represents the strain energy associated to the stiffness nonlinearities. The energy in the system, which is time dependent, may thus be estimated from the time response of the structure through the finite element model. Nevertheless, the response is only available at the measurement locations considered during the experiments.

Following the philosophy of model reduction techniques [46], the total energy can be expressed in terms of measured responses only. The equations of motions (5.6) of the conservative structural model can be partitioned as

$$\begin{bmatrix} \mathbf{M}_{RR} & \mathbf{M}_{RC} \\ \mathbf{M}_{CR} & \mathbf{M}_{CC} \end{bmatrix} \begin{bmatrix} \ddot{\mathbf{x}}_R \\ \ddot{\mathbf{x}}_C \end{bmatrix} + \begin{bmatrix} \mathbf{K}_{RR} & \mathbf{K}_{RC} \\ \mathbf{K}_{CR} & \mathbf{K}_{CC} \end{bmatrix} \begin{bmatrix} \mathbf{x}_R \\ \mathbf{x}_C \end{bmatrix} + \begin{bmatrix} \mathbf{f}_{R,nl}(\mathbf{x}_R) \\ \mathbf{0} \end{bmatrix} = \begin{bmatrix} \mathbf{0} \\ \mathbf{0} \end{bmatrix} \tag{5.10}$$

where $\mathbf{x}_R$ and $\mathbf{x}_C$ are the vectors of the remaining and condensed DOFs, respectively. Keeping the nonlinear DOFs in the remaining coordinates, the equations of motion associated to the condensed DOFs are linear as evidenced by Equation (5.10) in which the

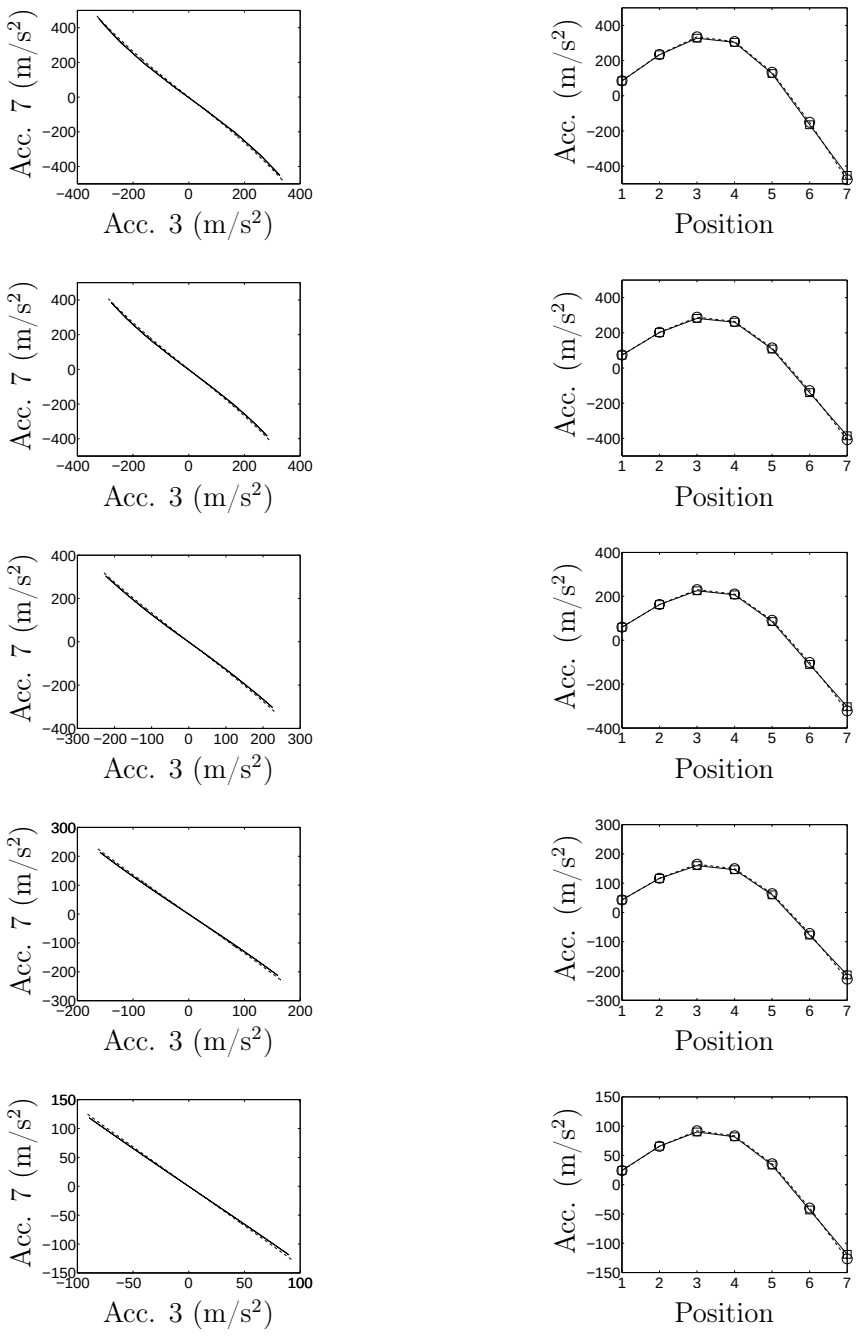

Figure 5.23: Second NNM of the nonlinear beam. —□—: experimental NNM identified from the free decay of the test structure; – – ○ – –: theoretical NNM computed from the finite element model of the structure. Left plots: modal curves in the configuration space composed of the accelerations at locations 3 and 7. Right plots: modal shapes composed of the amplitudes of the accelerations across the main beam. From top to bottom: NNM for decreasing energy levels marked in Figure 5.22.

condensed part of the nonlinear restoring force $\mathbf{f}_{C,nl}$ is zero. The finite element model can then be reduced using linear static condensation, commonly known as Guyan reduction method. This static condensation technique consists in neglecting the dynamic part of the condensed coordinates $\mathbf{x}_C$ and thence expressing the global DOFs in terms of the remaining ones as follows

$$\mathbf{x} = \begin{bmatrix} \mathbf{x}_R \\ \mathbf{x}_C \end{bmatrix} = \mathbf{R}\mathbf{x}_R \tag{5.11}$$

where $\mathbf{R}$ is the static reduction matrix given by

$$\mathbf{R} = \begin{bmatrix} \mathbf{I} \\ -\mathbf{K}_{CC}^{-1}\mathbf{K}_{CR} \end{bmatrix} \tag{5.12}$$

The reduced kinetic and potential energies are thus expressed as

$$\mathcal{T} = \frac{1}{2}\dot{\mathbf{x}}_R^*\overline{\mathbf{M}}\dot{\mathbf{x}}_R \tag{5.13}$$

$$\mathcal{V} = \frac{1}{2}\mathbf{x}_R^*\overline{\mathbf{K}}\mathbf{x}_R + \mathcal{V}_{nl}(\mathbf{x}_R) \tag{5.14}$$

with the $n_R \times n_R$ reduced structural matrices

$$\begin{aligned} \overline{\mathbf{M}} &= \mathbf{R}^*\mathbf{M}\mathbf{R} \\ \overline{\mathbf{K}} &= \mathbf{R}^*\mathbf{K}\mathbf{R} \end{aligned} \tag{5.15}$$

The expression for the nonlinear deformation energy $\mathcal{V}_{nl}$ is unchanged since it initially depends only on the nonlinear DOFs which belongs to the remaining coordinates.

In order to estimate the energy from the available measurements, the remaining DOFs chosen here are the nodal coordinates corresponding to the measurement locations across the structure. Hence, an estimation of the total energy can be determined using expressions (5.13) and (5.14). Obviously, the quality of this estimation depends on the number and positions of measured responses.

Targeting a general approach, the total energy is estimated by evaluating the kinetic energy at the time instants when the displacements pass through zero, i.e., when the potential energy vanishes. Since the kinetic energy depends only on the parameters of the underlying linear system, this prevents from resorting to the nonlinear parameters which are generally unknown a priori in practice. On the other hand, prior to nonlinear modal testing, the underlying linear model can be identified by means of traditional linear modal analysis performed at low energy level (i.e., when the geometrical nonlinearity is not activated). Furthermore, the mass properties are generally better assessed and subject to less uncertainty than the stiffness properties. A good approximation of the model mass matrix could even be built based only on the geometrical and mechanical properties of the experimental set-up. The resulting estimation of the energy, determined from the experimental measurements and the reduced mass matrix, is referred to as the reconstructed energy of the system.

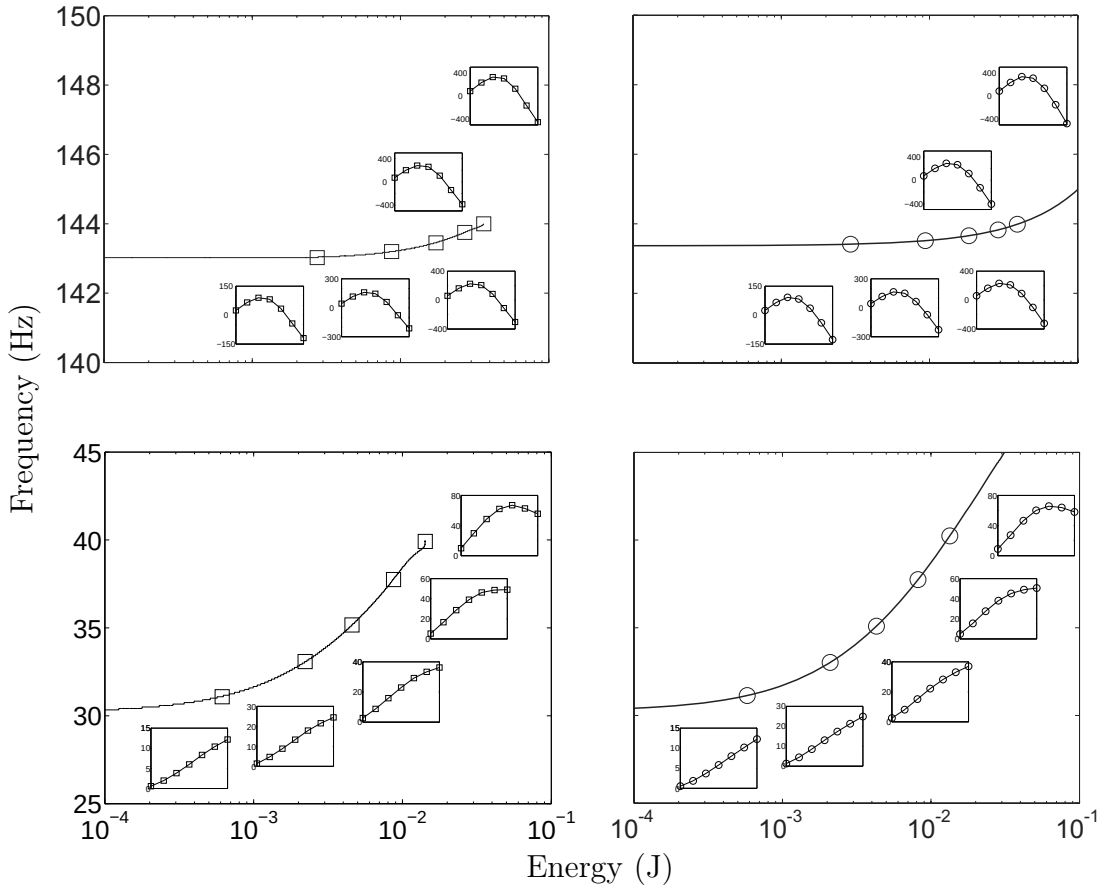

Figure 5.24: Frequency-energy plot of the NNMs of the nonlinear beam. Left plot: experimental FEP reconstructed from the NNM identification results using the modal testing methodology. Right plot: theoretical FEP computed from the finite element model of the structure. The modal shapes composed of the amplitudes of the accelerations (m/s^2) across the main beam are inset.

For the considered test structure, the established finite element model is condensed by keeping the translational DOFs at the positions of the seven accelerometers which span the main beam. Based on this structural model, the displacement of the main beam end is the only nonlinear DOF and is then kept in the reduction. Since the evaluation of the kinetic energy requires the velocities, the time responses measured in terms of acceleration are numerically integrated and filtered.

The instantaneous energy in the system during the NNM free decay is evaluated from the experimental measurements. The experimental FEP is reconstructed through the CWT by substituting the estimated instantaneous energy for time. The maximum ridge of the transform therefore provides the experimental backbone of the NNM expressing its frequency-energy dependence. The reconstructed experimental FEP of the first and second NNMs is depicted in Figure 5.24. The experimental modal shapes extracted pre-

viously for different energy levels are also superimposed in the plot. For comparison, the theoretical FEP numerically computed from the finite element model is also displayed in this figure. This figure confirms the good agreement between the theoretical and experimental NNMs.

Finally, the quality of the energy estimation can be assessed from the finite element model. It is observed that the reduced energy is very close to the actual energy present in the system. For the first two NNMs, the theoretical FEPs given in terms of the actual energy or the reduced energy cannot be distinguished. It confirms that the reconstructed energy gives an excellent quantitative insight into the total energy in the structure.

5.6 Concluding Remarks

This chapter dealt with the experimental demonstration of the nonlinear phase resonance methodology proposed in Chapter 4 for EMA of nonlinear vibrating structures. To this end, a set-up composed of a nonlinear beam with geometrical nonlinearity was considered. Based on the nonlinear extension of the phase quadrature criterion, an indicator was introduced for assessing the quality of NNM force appropriation. The experimental realization of NNM force appropriation was completed by means of a stepped sine procedure using a single exciter at a single frequency. Eventually, the energy dependence of NNM was properly identified from the measured single-NNM free decay response, which indicates the robustness of the procedure.

Finally, this chapter experimentally validated the main assumption of the methodology: the nonlinear dynamics of a moderately damped structure can be related to the NNMs of the underlying conservative system. As a result, these experimental findings support the approach followed throughout the present dissertation which consists in performing nonlinear modal analysis based on the topological structure of the NNMs of the underlying undamped system.

Conclusions

Because linear modal analysis fails dramatically in the presence of nonlinear dynamical phenomena, the development of a practical nonlinear analog of theoretical and experimental modal analysis (TMA and EMA) is the objective of this doctoral dissertation. To this end, an adequate framework for modal analysis of nonlinear vibrating structures, which includes the computation of nonlinear normal modes (NNMs) from finite element models and their identification from experimental data, was introduced.

Targeting a useful, yet understandable by the practicing engineer, analysis of nonlinear structural dynamics, several key aspects were reported and highlighted in Chapter 1 by means of different examples. First, an appropriate NNM definition, in which an NNM motion is defined as a (non-necessarily synchronous) periodic motion of the nonlinear conservative system, was proposed to extend Rosenberg's approach. Following this extended definition, NNMs can handle dynamical phenomena with no counterpart in linear theory (e.g., frequency-energy dependence, modal interactions, mode bifurcations, instability) in a rigorous manner, yet they have a clear conceptual relation to the classical linear normal modes (LNMs). Secondly, a suitable graphical depiction of NNMs, termed a frequency-energy plot (FEP), was introduced to facilitate their interpretation and exploitation. Finally, in view of its ability to track the frequency-energy dependence inherent to nonlinear systems, time-frequency analysis using the wavelet transform was shown to be the ideal companion to NNMs for modal analysis. Thanks to this tool, the damped dynamics can be related to the different branches of NNM motions in the FEP.

To address the limitations of existing analytic techniques for NNM computation, an important contribution of this thesis is to resort to numerical methods. Interestingly enough, shooting algorithms have not received much attention from the NNM community whereas they offer an exact computation of these modes, even in strongly nonlinear regimes of motion. When advantageously combined with continuation methods, we showed in Chapter 2 that they hold promise for an effective computation of NNMs. Because such algorithms are known to be computationally intensive, a particular effort was devoted to progress toward a practical NNM computation tool that can deal with large-scale structures. In particular, a significant improvement was to resort to sensitivity analysis for the computation of the monodromy matrix to reduce the computational burden.

The ability of the numerical algorithm was demonstrated in Chapter 3 using different non-

linear structures, namely an essentially nonlinear 2DOF system, a bladed disk assembly and a full-scale aircraft. The NNMs were computed accurately with a reasonable computational burden. Some complex nonlinear phenomena, including modal interactions with no commensurate linear frequencies and mode localization in periodic structures with cyclic symmetry, were also highlighted. One significant result is that the algorithm has the potential to deal with complex real-world structures, such as the full-scale aircraft studied herein.

To make NNMs a viable tool, this doctoral dissertation also laid down the foundations for their identification from experimental data. This topic has clearly been disregarded in the literature and is another important contribution of the thesis. Based on a nonlinear extension of phase resonance testing (also known as force appropriation), the methodology developed in Chapter 4 consists in exciting the structure using stepped sine excitation to isolate a single NNM. To propose a robust identification procedure, two important properties of NNMs were exploited. First, similarly to linear theory, forced resonances in nonlinear systems occur in the direct neighborhoods of NNMs. In this context, the phase lag quadrature criterion was generalized to nonlinear structures. To our knowledge, it is the first time that a nonlinear analog of this criterion is introduced to locate single-NNM motions. Second, the invariance principle, valid for linear systems, extends to nonlinear systems and states that, if the motion is initiated on one specific mode, the remaining modes remain quiescent for all time. As a result, we showed that the frequency-energy dependence of the NNM can be identified from the free damped dynamics using time-frequency analysis. The procedure was illustrated by means of numerical experiments using a 2DOF system and a nonlinear beam.

Finally, the experimental demonstration of NNM identification was addressed in Chapter 5 using a cantilever beam possessing geometrical nonlinearity. Based on the phase lag quadrature criterion, a mode indicator function was developed to assess whether a satisfactory isolation of NNMs was effectively achieved. This information is crucial when targeting practical applications. One important result of this research work is that the NNMs were successfully extracted from measured responses, which indicates the practical feasibility of the methodology. In addition, this experimental study confirms that the nonlinear dynamics of a moderately damped structure can be related to NNMs of the underlying conservative system, an assumption considered throughout this dissertation.

Directions for Future Work

The results presented herein clearly show promise to progress toward practical modal analysis of nonlinear vibrating structures. Nevertheless, there is still much work to be done to provide a broadly applicable framework, effective for large-scale, complex real-world structures. The following discussion presents some aspects that might drive its development in the years to come.

Theoretical modal analysis. Further research should be carried out to develop a robust NNM computation tool capable of dealing with a variety of large-scale structures:

- Due to mode bifurcations, supernumerary NNMs with no linear counterparts (i.e., those that are not the direct extension of the LNMs) may exist. Therefore, the development of a robust and automatic branch switching strategy would be a meaningful advancement for facilitating their computation [126].
- The procedure for NNM computation relies on numerical simulations, which may be computationally intensive for large-scale finite element models. It was shown that sensitivity analysis is an effective alternative to reduce the computational burden. Future research should continue in this direction to optimize the algorithm. For instance, an automatic time step control, which selects the most appropriate time step in view of the current dynamics, should be investigated to speed up the computations.
- All the structures considered in this thesis possessed spatially localized and smooth nonlinearities. In particular, the studied nonlinearities were restricted to polynomial stiffness terms. One interesting contribution would thus be to address more complicated nonlinear behaviors, such as structures with distributed nonlinearities (e.g., geometrical nonlinearity) and nonsmooth nonlinearities (e.g., clearance nonlinearity). Even though particular effort is still required, our computational approach has certainly the potential to deal with such systems. For example, nonsmooth behavior generally demands special treatment [74].

Experimental modal analysis. Further investigations need to be carried out to assess the efficiency of the NNM identification in case of large-scale industrial structures:

- Because nonlinear systems undergo bifurcations, modal interactions and shrinking basins of attraction, the practical realization of nonlinear force appropriation is more challenging than its linear counterpart. In this context, validation of the methodology was performed using an experimental structure. However, it consists of an academic benchmark and the next logical step should be to consider more complex structures, e.g., structures possessing close modes or spatially distributed nonlinearities. To this end, the development of a more general constructive procedure for NNM force appropriation, resorting to several shakers with harmonics of the fundamental frequency, is of particular interest to ensure the robustness of the proposed methodology. In addition, to address changing basins of attraction, the experimental continuation of periodic orbits, as proposed in [131], is particularly attractive and should be investigated in detail.
- The experimental methodology assumes that the damped dynamics can be interpreted based on the NNMs of the underlying conservative system in the presence of weak to moderate viscous damping. This issue deserves more attention and should

be investigated more thoroughly. For instance, large damping may modify the type of nonlinear behavior (e.g., hardening or softening) that is observed [142]. When targeting practical applications, a rigorous criterion indicating the validity of the methodology would be a crucial contribution. The effect of the damping could be examined by computing the damped NNMs as discussed below.

Nonlinear damping. Due to the lack of knowledge of damping mechanisms, its modeling is known to be challenging. In this context, the framework developed in this thesis for modal analysis is based on conservative systems and only addresses stiffness nonlinearities. An ambitious contribution would thus be to extend theoretical and experimental methods for properly accounting for nonlinear damping (e.g., dry friction). To this end, an meaningful approach is to resort to the invariant manifold theory in order to consider the calculation of damped NNMs [127–130].

Finite element model updating. The methods introduced in this manuscript for TMA and EMA could jointly be used to propose a new finite element model validation technique of nonlinear systems. For this purpose, the potential exploitation of this integrated approach for model identification and updating of nonlinear structures is yet to be studied in detail.

Ground vibration testing. One important aerospace application that should benefit from nonlinear modal analysis is aircraft ground vibration testing (GVT). GVTs are carried out on aircraft prototypes and provide critical data for flutter analysis. Identification of an accurate model during GVTs could allow the effects of nonlinearity on flutter to be explored by calculation prior to the flight test programme. Specifically, the methodology proposed for nonlinear modal identification may be directly and fully integrated into the strategy currently followed for standard GVT of aircrafts. Indeed, besides traditional linear modal analysis performed using phase separation methods, it is still common nowadays to resort to classical force appropriation for some particular modes (e.g., closely spaced modes and important modes for flutter computations) [48]. Similarly, in case of modes affected by nonlinearity, the nonlinear phase resonance approach introduced for NNM identification could therefore be realized, which should extend the existing strategy to nonlinear structures.

Appendix A

Newmark's Time Integration Scheme

Newmark's time integration method [46] is briefly reviewed here. It is applied to numerically solve:

- The original initial value problem defined by the governing equations of motion

$$\mathbf{M}\,\ddot{\mathbf{x}}(t) + \mathbf{K}\,\mathbf{x}(t) + \mathbf{f}_{nl}\left\{\mathbf{x}(t)\right\} = \mathbf{0} \tag{A.1}$$

  with the initial conditions $\mathbf{z}_0 = \begin{bmatrix} \mathbf{x}(0) \\ \dot{\mathbf{x}}(0) \end{bmatrix} = \begin{bmatrix} \mathbf{x}_0 \\ \dot{\mathbf{x}}_0 \end{bmatrix}$.

- The associated sensitivity problem given by

$$\mathbf{M}\,\frac{d^2}{dt^2}\left[\frac{\partial \mathbf{x}(t)}{\partial \mathbf{z}_0}\right] + \mathbf{K}\,\left[\frac{\partial \mathbf{x}(t)}{\partial \mathbf{z}_0}\right] + \left.\frac{\partial \mathbf{f}_{nl}\left\{\mathbf{x}\right\}}{\partial \mathbf{x}}\right|_{\mathbf{x}(t)}\left[\frac{\partial \mathbf{x}(t)}{\partial \mathbf{z}_0}\right] = \mathbf{0} \tag{A.2}$$

  with $\begin{bmatrix} \frac{\partial \mathbf{x}(0)}{\partial \mathbf{z}_0} \\ \frac{\partial \dot{\mathbf{x}}(0)}{\partial \mathbf{z}_0} \end{bmatrix} = \mathbf{I}$.

A.1 Equations of Motion

Let us rewrite the equations of motion as a relationship in terms of the displacement $\mathbf{x}(t)$

$$\mathbf{r}(\mathbf{x}) = \mathbf{M}\,\ddot{\mathbf{x}}(t) + \mathbf{K}\,\mathbf{x}(t) + \mathbf{f}_{nl}\left\{\mathbf{x}(t)\right\} = \mathbf{0} \tag{A.3}$$

where $\mathbf{r}$ is the residual vector.

From time t to $t+h$, Newmark's integration formulae are obtained from a Taylor series expansion of the displacements and velocities with respect to the time step h

$$\begin{cases} \dot{\mathbf{x}}_{t+h} = \dot{\mathbf{x}}_t + (1-\gamma)h\ddot{\mathbf{x}}_t + \gamma h\ddot{\mathbf{x}}_{t+h} \\ \mathbf{x}_{t+h} = \mathbf{x}_t + h\dot{\mathbf{x}}_t + h^2(\frac{1}{2}-\beta)\ddot{\mathbf{x}}_t + h^2\beta\ddot{\mathbf{x}}_{t+h} \end{cases} \tag{A.4}$$

where γ and β are integration constants. These equations can be rewritten as

$$\begin{cases} \dot{\mathbf{x}}_{t+h} = \dot{\mathbf{x}}^*_{t+h} + \gamma h \ddot{\mathbf{x}}_{t+h} \\ \mathbf{x}_{t+h} = \mathbf{x}^*_{t+h} + h^2 \beta \ddot{\mathbf{x}}_{t+h} \end{cases} \tag{A.5}$$

where the predictions correspond to $\ddot{\mathbf{x}}_{t+h} = \mathbf{0}$ and depend only on the previously time step t

$$\dot{\mathbf{x}}^*_{t+h} = \dot{\mathbf{x}}_t + (1-\gamma) h \ddot{\mathbf{x}}_t \tag{A.6}$$

$$\mathbf{x}^*_{t+h} = \mathbf{x}_t + h\dot{\mathbf{x}}_t + h^2 (\frac{1}{2} - \beta) \ddot{\mathbf{x}}_t \tag{A.7}$$

Newmark's time integration relationships may be expressed in terms of $\mathbf{x}_{t+h}$ only in the following way

$$\begin{cases} \ddot{\mathbf{x}}_{t+h} = \frac{1}{\beta h^2} (\mathbf{x}_{t+h} - \mathbf{x}^*_{t+h}) \\ \dot{\mathbf{x}}_{t+h} = \dot{\mathbf{x}}^*_{t+h} + \frac{\gamma}{\beta h} (\mathbf{x}_{t+h} - \mathbf{x}^*_{t+h}) \end{cases} \tag{A.8}$$

By substituting (A.8) into (A.3), the residual equation is expressed in terms of $\mathbf{x}_{t+h}$ only

$$\mathbf{r}(\mathbf{x}_{t+h}) = \mathbf{0} \tag{A.9}$$

A Newton-Raphson procedure is used for solving this set of nonlinear equations in an iterative manner

$$\mathbf{r}(\mathbf{x}^k_{t+h}) + \mathbf{S}(\mathbf{x}^k_{t+h})(\mathbf{x}^{k+1}_{t+h} - \mathbf{x}^k_{t+h}) = \mathbf{0} \tag{A.10}$$

where subscript k denotes iteration step. The iteration matrix

$$\mathbf{S}(\mathbf{x}^k_{t+h}) = \left[\frac{d\mathbf{r}}{d\mathbf{x}} \right]_{\mathbf{x}^k_{t+h}} \tag{A.11}$$

is given by

$$\mathbf{S}(\mathbf{x}) = \frac{1}{\beta h^2} \mathbf{M} + \mathbf{K} + \frac{\mathbf{f}_{nl}\{\mathbf{x}\}}{\partial \mathbf{x}} \tag{A.12}$$

The displacement, velocity and acceleration approximations are then corrected

$$\mathbf{x}^{k+1}_{t+h} = \mathbf{x}^k_{t+h} + \Delta \mathbf{x}^k_{t+h} \tag{A.13}$$

$$\dot{\mathbf{x}}^{k+1}_{t+h} = \dot{\mathbf{x}}^k_{t+h} + \Delta \dot{\mathbf{x}}^k_{t+h} \tag{A.14}$$

$$\ddot{\mathbf{x}}^{k+1}_{t+h} = \ddot{\mathbf{x}}^k_{t+h} + \Delta \ddot{\mathbf{x}}^k_{t+h} \tag{A.15}$$

where the displacement corrections are determined by solving

$$\mathbf{S}(\mathbf{x}^k_{t+h}) \Delta \mathbf{x}^k_{t+h} = -\mathbf{r}(\mathbf{x}^k_{t+h}) \tag{A.16}$$

and with

$$\Delta\dot{\mathbf{x}}^k_{t+h} = \frac{\gamma}{\beta h}\Delta\mathbf{x}^k_{t+h} \tag{A.17}$$

$$\Delta\ddot{\mathbf{x}}^k_{t+h} = \frac{1}{\beta h^2}\Delta\mathbf{x}^k_{t+h} \tag{A.18}$$

For nonlinear systems, Newmark's time iteration scheme therefore contains, at each time step t, an Newton-Raphson iterative process which is carried out until the residual value of the equations of motion is lower than a prescribed accuracy threshold.

A.2 Sensitivity Equations

At the time step end of integration of (A.1), the sensitivity matrix $\left[\frac{\partial \mathbf{x}}{\partial \mathbf{z}_0}\right]$ is obtained by solving (A.2). Using Newmark's time integration scheme, $\left[\frac{\partial \ddot{\mathbf{x}}}{\partial \mathbf{z}_0}\right]$ and $\left[\frac{\partial \dot{\mathbf{x}}}{\partial \mathbf{z}_0}\right]$ at time $t+h$ are written as

$$\left[\frac{\partial \ddot{\mathbf{x}}}{\partial \mathbf{z}_0}\right]_{t+h} = \frac{1}{\beta h^2}\left(\left[\frac{\partial \mathbf{x}}{\partial \mathbf{z}_0}\right]_{t+h} - \left[\frac{\partial \mathbf{x}}{\partial \mathbf{z}_0}\right]^*_{t+h}\right) \tag{A.19}$$

$$\left[\frac{\partial \dot{\mathbf{x}}}{\partial \mathbf{z}_0}\right]_{t+h} = \left[\frac{\partial \dot{\mathbf{x}}}{\partial \mathbf{z}_0}\right]^*_{t+h} + \frac{\gamma}{\beta h}\left(\left[\frac{\partial \mathbf{x}}{\partial \mathbf{z}_0}\right]_{t+h} - \left[\frac{\partial \mathbf{x}}{\partial \mathbf{z}_0}\right]^*_{t+h}\right) \tag{A.20}$$

with the predictions given by

$$\left[\frac{\partial \dot{\mathbf{x}}}{\partial \mathbf{z}_0}\right]^*_{t+h} = \left[\frac{\partial \dot{\mathbf{x}}}{\partial \mathbf{z}_0}\right]_t + (1-\gamma)h\left[\frac{\partial \ddot{\mathbf{x}}}{\partial \mathbf{z}_0}\right]_t \tag{A.21}$$

$$\left[\frac{\partial \mathbf{x}}{\partial \mathbf{z}_0}\right]^*_{t+h} = \left[\frac{\partial \mathbf{x}}{\partial \mathbf{z}_0}\right]_t + h\left[\frac{\partial \dot{\mathbf{x}}}{\partial \mathbf{z}_0}\right]_t + h^2(\frac{1}{2}-\beta)\left[\frac{\partial \ddot{\mathbf{x}}}{\partial \mathbf{z}_0}\right]_t \tag{A.22}$$

By substituting (A.19) in the linear equations (A.2), the sensitivity matrix at time $t+h$ is determined by solving

$$\left[\frac{1}{\beta h^2}\mathbf{M} + \mathbf{K} + \frac{\partial \mathbf{f}_{nl}\left\{\mathbf{x}_{t+h}\right\}}{\partial \mathbf{x}}\right]\left[\frac{\partial \mathbf{x}}{\partial \mathbf{z}_0}\right]_{t+h} = \frac{1}{\beta h^2}\mathbf{M}\left[\frac{\partial \mathbf{x}}{\partial \mathbf{z}_0}\right]^*_{t+h} \tag{A.23}$$

Equations (A.19), (A.20) and (A.23) are then used to integrate the sensitivity problem. Since Equations (A.2) are linear, only one single iteration is needed. Interestingly, the left hand side of Equation (A.23) corresponds to the iteration matrix of the original problem.

By marching in time, the current motion and its sensitivity with respect to initial conditions are therefore obtained at any time t using Newmark's time integration.

Bibliography

[1] G.S. Agnes and D.J. Inman. Performance of nonlinear vibration absorbers for multi-degrees-of-freedom systems using nonlinear normal modes. *Nonlinear Dynamics*, 25:275–292, 2001.

[2] R.J. Allemang and D.L. Brown. A unified matrix polynomial approach to modal identification. *Journal of Sound and Vibration*, 211:301–322, 1998.

[3] R.J. Allemang and A.W. Phillips. The unified matrix polynomial approach to understanding modal parameter estimation: An update. In *Proceedings of the International Seminar on Modal Analysis (ISMA)*, Leuven, Belgium, 2004.

[4] E.L. Allgower and K. Georg. *Introduction to Numerical Continuation Methods*. Classics in applied mathematics. SIAM, Philadelphia, 2003.

[5] M. Amabili and C. Touzé. Reduced-order models for nonlinear vibrations of fluid-filled circular cylindrical shells: Comparison of POD and asymptotic nonlinear normal modes methods. *Journal of Fluids and Structures*, 23:885–903, 2007.

[6] P. Apiwattanalunggarn, S. Shaw, and C. Pierre. Component mode synthesis using nonlinear normal modes. *Nonlinear Dynamics*, 41:17–46, 2005.

[7] P. Argoul and T.P. Le. Continuous wavelet transform for modal identification using free decay response. *Journal of Sound and Vibration*, 277:73–100, 2004.

[8] R. Arquier. *Une méthode de calcul des modes de vibrations non-linéaires de structures*. PhD thesis, Université de la Méditerrané, Marseille, 2007.

[9] R. Arquier, S. Bellizzi, R. Bouc, and B. Cochelin. Two methods for the computation of nonlinear modes of vibrating systems at large amplitudes. *Computers & Structures*, 84:1565–1576, 2006.

[10] P.A. Atkins, J.R. Wright, and K. Worden. An extension of force appropriation to the identification of non-linear multi-degree of freedom systems. *Journal of Sound and Vibration*, 237:23–43, 2000.

[11] J. Aubrecht and A.F. Vakakis. Localized and non-localized nonlinear normal modes in a multi-span beam with geometric nonlinearities. *Journal of Vibration and Acoustics*, 118:533–542, 1996.

[12] S. Bellizzi and R. Bouc. A new formulation for the existence and calculation of nonlinear normal modes. *Journal of Sound and Vibration*, 287:545–569, 2005.

[13] S. Bellizzi and R. Bouc. An amplitude-phase formulation for nonlinear modes and limit cycles through invariant manifolds. *Journal of Sound and Vibration*, 300:896–915, 2007.

[14] R. Benamar, M.M.K. Bennouna, and R.G. White. The effects of large vibration amplitudes on the mode shapes and natural frequencies of thin elastic structures, part I: Simply supported and clamped-clamped beams. *Journal of Sound and Vibration*, 149:179–195, 1991.

[15] G. Benini, J.E. Cooper, and J.R. Wright. Quantification of aircraft non-linearities from flight flutter test data. In *Proceedings of the International Seminar on Modal Analysis (ISMA)*, Leuven, Belgium, 2004.

[16] N. Boivin, C. Pierre, and S.W. Shaw. Non-linear modal analysis of structural systems featuring internal resonances. *Journal of Sound and Vibration*, 182:336–341, 1995.

[17] N. Boivin, C. Pierre, and S.W. Shaw. Non-linear normal modes, invariance, and modal dynamics approximations of non-linear systems. *Nonlinear Dynamics*, 8:315–346, 1995.

[18] O. Brüls and P. Eberhard. Sensitivity analysis for dynamic mechanical systems with finite rotations. *International Journal for Numerical Methods in Engineering*, 1:1–29, 2006.

[19] T.D. Burton. Numerical calculation of nonlinear normal modes in structural systems. *Nonlinear Dynamics*, 49:425–441, 2007.

[20] T.D. Burton and M.N. Hamdan. On the calculation of non-linear normal modes in continuous systems. *Journal of Sound and Vibration*, 197:117–130, 1996.

[21] E.A. Butcher and R. Lu. Order reduction of structural dynamic systems with static piecewise linear nonlinearities. *Nonlinear Dynamics*, 49:375–399, 2007.

[22] K. Carney, I. Yunis, K. Smith, and C.Y. Peng. Nonlinear dynamic behavior in the Cassini spacecraft modal survey. In *Proceedings of the International Modal Analysis Conference (IMAC)*, Orlando, USA, 1997.

[23] A. Carrella and D.J. Ewins. Identifying and quantifying structural nonlinearities in engineering applications from measured frequency response functions. *Mechanical Systems and Signal Processing*, In Press, 2010.

[24] M.P. Castanier and C. Pierre. Modeling and analysis of mistuned bladed disk vibration: status and emerging directions. *Journal of Propulsion and Power*, 22:384–396, 2006.

[25] T.K. Caughey, A.F. Vakakis, and J.M. Sivo. Analytical study of similar normal modes and their bifurcations in a class of strongly nonlinear systems. *International Journal of Non-Linear Mechanics*, 25:521–533, 1990.

[26] Y.H. Chong and M. Imregun. Development and application of a nonlinear modal analysis technique for MDOF systems. *Journal of Vibration and Control*, 7:167–179, 2001.

[27] B. Cochelin, N. Damil, and M. Potier-Ferry. Asymptotic numerical methods and Padé approximants for nonlinear elastic structures. *International Journal for Numerical Methods in Engineering*, 37:1187–1213, 1994.

[28] B. Cochelin and C. Vergez. A high order purely frequency-based harmonic balance formulation for continuation of periodic solutions. *Journal of Sound and Vibration*, 324:243–262, 2009.

[29] R. Craig and M. Bampton. Coupling of substructures for dynamic analysis. *AIAA Journal*, 6:1313–1319, 1968.

[30] M. Degener. Ground vibration testing for validation of large aircraft structural dynamics. In *Proceedings of the International Forum on Aeroelasticity and Structural Dynamics*, Manchester, UK, 1995.

[31] M. Degener. Experiences in large satellite modal survey testing. In *Proceedings of the European Conference on Spacecraft Structures, Materials and Mechanical Testing — ESA SP-428*, pages 659–664, Braunschweig, Germany, 1998.

[32] M. Degener, J. Gschwilm, S.P. Lopriore, R.S. Capitanio, V.E. Hill, and P.W. Johnston. Vibration tests for dynamic verification and qualification of the PPF/ENVISAT-1 satellite. In *Proceedings of the 3rd International Symposium on Environmental Testing for Space Programmes — ESA SP-408*, pages 83–90, Noordwijk, The Netherlands, 1997.

[33] A.J. Dick, B. Balachandran, and C.D. Mote. Nonlinear vibration modes in microresonator arrays. In *Proceedings of the SPIE, Smart Structures and Materials: Modeling, Signal Processing, and Control*, volume 6166, pages 206–217, San Diego, 2006.

[34] S.W. Doebling, C.R. Farrar, M.B. Prime, and D.W. Shevitz. Damage identification and health monitoring of structural and mechanical systems from changes in their vibration characteristics: a literature review. Technical report, Los Alamos National Laboratory Report, 1996.

[35] E.J. Doedel. AUTO, software for continuation and bifurcation problems in ordinary differential equations, http://indy.cs.concordia.ca/auto/. 2007.

[36] E.J. Doedel, R.C. Paffenroth, H.B. Keller, D.J. Dichmann, J. Galan Vioque, and A. Vanderbauwhede. Computation of periodic solutions of conservative systems with application to the 3-body problem. *International Journal of Bifurcations and Chaos*, 13:1353–1381, 2003.

[37] D.J. Ewins. Structural dynamics characteristics of bladed assemblies. In *Lecture Series 1992-06 on Vibration and Rotor Dynamics*. Von Karman Institute for Fluid Dynamics, 1992.

[38] D.J. Ewins. *Modal Testing: Theory, Practice and Application*. Research Studies Press Ltd., Hertfordshire, 2nd edition, 2000.

[39] D.J. Ewins. A future for experimental structural dynamics. In *Proceedings of the International Seminar on Modal Analysis (ISMA)*, Leuven, Belgium, 2006.

[40] B. Fraeijs de Veubeke. A variational approach to pure mode excitation using characteristic phase lag theory. *AGARD Report*, 39, 1956.

[41] M.I. Friswell and J.E. Mottershead. *Finite Element Model Updating in Structural Dynamics*. Kluwer Academic Publishers, London, 1995.

[42] L. Garibaldi, M. Ruzzene, A. Fasana, and B. Piombo. Identification of non-linear damping mechanisms using the wavelet transform. *Mecanique Industrielle et Materiaux*, 51:92–94, 1998.

[43] L. Gaul and J. Lenz. Nonlinear dynamics of structures assembled by bolted joints. *Acta Mechanica*, 125:169–181, 1997.

[44] O.V. Gendelman. Bifurcations of nonlinear normal modes of linear oscillator with strongly nonlinear damped attachment. *Nonlinear Dynamics*, 37:115–128, 2004.

[45] O.V. Gendelman, L.I. Manevitch, A.F. Vakakis, and R. McCloskey. Energy pumping in nonlinear mechanical oscillators: Part I - dynamics of the underlying hamiltonian systems. *Journal of Applied Mechanics*, 68:34–41, 2001.

[46] M. Géradin and D. Rixen. *Mechanical Vibrations, Theory and Application to Structural Dynamics*. Wiley, Chichester, 1994.

[47] C. Gibert. Fitting measured frequency response using non-linear modes. *Mechanical Systems and Signal Processing*, 17:211–218, 2003.

[48] D. Göge, M. Böswald, U. Füllekrug, and P. Lubrina. Ground vibration testing of large aircraft — state-of-the-art and future perspectives. In *Proceedings of the 25th International Modal Analysis Conference (IMAC)*, Orlando, 2007.

[49] D. Göge, U. Fullekrug, M. Sinapius, M. Link, and L. Gaul. Advanced test strategy for identification and characterization of nonlinearities of aerospace structures. *AIAA Journal*, 43:974–986, 2005.

[50] W. Govaerts, Y.A. Kuznetsov, and A. Dhooge. Numerical continuation of bifurcations of limit cycles in MATLAB. *SIAM Journal on Scientific Computing*, 27:231–252, 2005.

[51] J. Guckenheimer and P. Holmes. *Nonlinear Oscillations, Dynamical Systems and Bifurcation of Vector Fields*. Springer–Verlag, New York, 1983.

[52] C.J. Hartwigsen, Y. Song, D.M. McFarland, L.A. Bergman, and A.F. Vakakis. Experimental study of non-linear effects in a typical shear lap joint configuration. *Journal of Sound and Vibration*, 277:327–351, 2004.

[53] M. Haterbouch and R. Benamar. Geometrically nonlinear free vibrations of simply supported isotropic thin circular plates. *Journal of Sound and Vibration*, 280:903–924, 2005.

[54] S.R. Ibrahim and E.C. Mikulcik. A time domain modal vibration test technique. *The Shock and Vibration Bulletin*, 43:21–37, 1973.

[55] L. Jézéquel and C.H. Lamarque. Analysis of nonlinear dynamic systems by the normal form theory. *Journal of Sound and Vibration*, 149:429–459, 1991.

[56] D. Jiang, C. Pierre, and S.W. Shaw. Large-amplitude non-linear normal modes of piecewise linear systems. *Journal of Sound and Vibration*, 272:869–891, 2004.

[57] D. Jiang, C. Pierre, and S.W. Shaw. The construction of non-linear normal modes for systems with internal resonance. *International Journal of Non-Linear Mechanics*, 40:729–746, 2005.

[58] J.S. Juang and R.S. Pappa. An eigensystem realization algorithm for modal parameter identification and model reduction. *AIAA Journal of Guidance, Control and Dynamics*, 12:620–627, 1985.

[59] H.B. Keller. *Numerical Solution of Two-Point Boundary Value Problems*. SIAM, Philadelphia, 1976.

[60] H.B. Keller. *Numerical Methods in Bifurcation Problems*. Springer–Verlag, Berlin, 1987.

[61] G. Kerschen, J.J. Kowtko, D.M. McFarland, L.A. Bergman, and A.F. Vakakis. Theoretical and experimental study of multimodal targeted energy transfer in a system of coupled oscillators. *Nonlinear Dynamics*, 47:285–309, 2007.

[62] G. Kerschen, Y. S. Lee, A.F. Vakakis, D.M. McFarland, and L.A. Bergman. Irreversible passive energy transfer in coupled oscillators with essential nonlinearity. *SIAM Journal on Applied Mathematics*, 66:648–679, 2006.

[63] G. Kerschen, V. Lenaerts, and J.C. Golinval. Identification of a continuous structure with a geometrical non-linearity. Part I: Conditioned reverse path method. *Journal of Sound and Vibration*, 262:889–906, 2003.

[64] G. Kerschen, K. Worden, A.F. Vakakis, and J.C. Golinval. Past, present and future of nonlinear system identification in structural dynamics. *Mechanical Systems and Signal Processing*, 20:505–592, 2006.

[65] M.E. King and A.F. Vakakis. An energy-based formulation for computing nonlinear normal modes in undamped continuous systems. *Journal of Vibration and Acoustics*, 116:332–340, 1994.

[66] M.E. King and A.F. Vakakis. An energy-based approach to computing resonant nonlinear normal modes. *Journal of Applied Mechanics*, 63:810–819, 1995.

[67] W. Lacarbonara and R. Camillacci. Nonlinear normal modes of structural systems via asymptotic approach. *International Journal of Solids and Structures*, 41:5565–5594, 2004.

[68] W. Lacarbonara, A. Paolone, and F. Vestroni. Non-linear modal properties of non-shallow cables. *International Journal of Non-Linear Mechanics*, 42:542–554, 2007.

[69] W. Lacarbonara and G. Rega. Resonant non-linear normal modes, part II: activation/orthogonality conditions for shallow structural systems. *International Journal of Non-Linear Mechanics*, 38:873–887, 2003.

[70] W. Lacarbonara, G. Rega, and A.H. Nayfeh. Resonant non-linear normal modes, part I: analytical treatment for structural one-dimensional systems. *International Journal of Non-Linear Mechanics*, 38:851–872, 2003.

[71] D. Laxalde and F. Thouverez. Complex non-linear modal analysis for mechanical systems: Application to turbomachinery bladings with friction interfaces. *Journal of Sound and Vibration*, 322:1009–1025, 2009.

[72] Y.S. Lee, G. Kerschen, A.F. Vakakis, P.N. Panagopoulos, L.A. Bergman, and D.M. McFarland. Complicated dynamics of a linear oscillator with a light, essentially nonlinear attachment. *Physica D*, 204:41–69, 2005.

[73] Y.S. Lee, A.F. Vakakis, L.A. Bergman, D.M. McFarland, and G. Kerschen. Suppression of aeroelastic instability by means of broadband passive TET: Part I, theory. *AIAA Journal*, 45:693–711, 2007.

[74] R.I. Leine and H. Nijmeijer. *Dynamics and Bifurcations of Non-Smooth Mechanical Systems*. Springer–Verlag, Berlin, 2004.

[75] V. Lenaerts, G. Kerschen, and J.C. Golinval. Identification of a continuous structure with a geometrical non-linearity. Part II: Proper orthogonal decomposition. *Journal of Sound and Vibration*, 262:907–919, 2003.

[76] S. Lenci and G. Rega. Dimension reduction of homoclinic orbits of buckled beams via the non-linear normal modes technique. *International Journal of Non-Linear Mechanics*, 42:515–528, 2007.

[77] R. Lewandowski. Application of the Ritz method to the analysis of non-linear free vibrations of beams. *Journal of Sound and Vibration*, 114:91–101, 1987.

[78] R. Lewandowski. Computational formulation for periodic vibration of geometrically nonlinear structures, part I: theoretical background. *International Journal of Solids and Structures*, 34:1925–1947, 1997.

[79] R. Lewandowski. Computational formulation for periodic vibration of geometrically nonlinear structures, part II: numerical strategy and examples. *International Journal of Solids and Structures*, 34:1949–1964, 1997.

[80] X. Li, J.C. Ji, and C.H. Hansen. Non-linear normal modes and their bifurcation of a two DOF system with quadratic and cubic non-linearity. *International Journal of Non-Linear Mechanics*, 41:1028–1038, 2006.

[81] A. Lyapunov. *The General Problem of the Stability of Motion*. Princeton University Press., Princeton, New Jersey, 1947.

[82] S. Mallat. *A Wavelet Tour of Signal Processing*. Academic Press, London, 2nd edition, 1999.

[83] L.I. Manevitch and Y.V. Mikhlin. On periodic solutions close to rectilinear normal vibration modes. *Journal of Applied Mathematics and Mechanics (PMM)*, 36:1051–1058, 1972.

[84] S.F. Masri and T.K. Caughey. A nonparametric identification technique for nonlinear dynamic problems. *Journal of Applied Mechanics*, 46:433–447, 1979.

[85] C.E.N. Mazzilli and O.G.P. Baracho Neto. Evaluation of non-linear normal modes for finite-element models. *Computers & Structures*, 80:957–965, 2002.

[86] C.E.N. Mazzilli, M.E.S. Soares, and O.G.P. Baracho Neto. Non-linear normal modes of a simply supported beam: continuous system and finite-element models. *Computers & Structures*, 82:2683–2691, 2004.

[87] N. Mihajlović. *Torsional and Lateral Vibrations in Flexible Rotor Systems with Friction*. PhD thesis, Eindhoven University of Technology, 2005.

[88] Y.V. Mikhlin. Normal vibrations of a general class of conservative oscillators. *Nonlinear Dynamics*, 11:1–15, 1996.

[89] F.J. Munoz-Almaraz, E. Freire, J. Galán, E.J. Doedel, and A. Vanderbauwhede. Continuation of periodic orbits in conservative and hamiltonian systems. *Physica D*, 181:1–38, 2003.

[90] A.I. Musienko and L.I. Manevitch. Short wavelength dynamics of the system of nonlinear oscillators coupled by stretched weightless beam. *Chaos, Solitons & Fractals*, 26:107–116, 2005.

[91] A.H. Nayfeh. On direct methods for constructing nonlinear normal modes of continuous systems. *Journal of Vibration and Control*, 1:389–430, 1995.

[92] A.H. Nayfeh. *Nonlinear Interactions: Analytical, Computational and Experimental Methods*. Wiley-Interscience, New York, 2000.

[93] A.H. Nayfeh and B. Balachandran. *Applied Nonlinear Dynamics. Analytical, Computational, and Experimental Methods*. Wiley-Interscience, Chichester, 1995.

[94] A.H. Nayfeh, C.M. Chin, and S.A. Nayfeh. On nonlinear normal modes of systems with internal resonance. *Journal of Vibration and Acoustics*, 118:340–345, 1996.

[95] A.H. Nayfeh and D.T. Mook. *Nonlinear Oscillations*. Wiley–Interscience, New York, 1979.

[96] A.H. Nayfeh and S.A. Nayfeh. On nonlinear modes of continuous systems. *Journal of Vibration and Acoustics*, 116:129–136, 1994.

[97] A.H. Nayfeh and S.A. Nayfeh. Nonlinear normal modes of a continuous system with quadratic nonlinearities. *Journal of Vibration and Acoustics*, 117:199–205, 1995.

[98] N. Okuizumi and M.C. Natori. Nonlinear vibrations of a satellite truss structure with gaps. In *Proceedings of the 45th AIAA Structures, Structural Dynamics & Materials Conference*, Palm Springs, USA, 2004.

[99] S. Oueini, C.M. Chin, and A.H. Nayfeh. Dynamics of a cubic nonlinear vibration absorber. *Nonlinear Dynamics*, 20:283–295, 1999.

[100] C. Padmanabhan and R. Singh. Analysis of periodically excited nonlinear systems by a parametric continuation technique. *Journal of Sound and Vibration*, 184:35–58, 1995.

[101] C.H. Pak. *Nonlinear Normal Mode Dynamics for Two-Degree-of-Freedom Systems*. Inha University Press, Seoul, 1999.

[102] C.H. Pak. On the coupling of non-linear normal modes. *International Journal of Non-Linear Mechanics*, 41:716–725, 2006.

[103] C.H. Pak. Synge's concept of stability applied to non-linear normal modes. *International Journal of Non-Linear Mechanics*, 41:657–664, 2006.

[104] P. Panagopoulos, F. Georgiades, S. Tsakirtzis, A.F. Vakakis, and L.A. Bergman. Multi-scaled analysis of the damped dynamics of an elastic rod with an essentially nonlinear end attachment. *International Journal of Solids and Structures*, 44:6256–6278, 2007.

[105] T.S. Parker and L.O. Chua. *Practical Numerical Algorithms for Chaotic Systems*. Springer–Verlag, New York, 1989.

[106] B. Peeters, W. Hendricx, J. Debille, and H. Climent. Modern solutions for ground vibration testing of large aircraft. *Sound & Vibration*, 43:8–15, 2009.

[107] B. Peeters, H. Van Der Auweraer, and P. Guillaume. The polymax frequency domain method: a new standard for modal parameter estimation. *Shock and Vibration*, 11:395–409, 2004.

[108] F. Pérignon. *Vibration forcées de structures minces, élastiques, non-linéaires*. PhD thesis, Université de la Méditerrané, Marseille, 2004.

[109] E. Pesheck. *Reduced-Order Modelling of Nonlinear Structural Systems using Nonlinear Normal Modes and Invariant Manifolds*. PhD thesis, University of Michigan, Ann Arbor, 2000.

[110] E. Pesheck, C. Pierre, and S.W. Shaw. Accurate reduced-order models for a simple rotor blade model using nonlinear normal modes. *Mathematical and Computer Modelling*, 33:1085–1097, 2001.

[111] E. Pesheck, C. Pierre, and S.W. Shaw. A new Galerkin-based approach for accurate non-linear normal modes through invariant manifolds. *Journal of Sound and Vibration*, 249:971–993, 2002.

[112] C. Pierre, D. Jiang, and S.W. Shaw. Nonlinear normal modes and their application in structural dynamics. *Mathematical Problems in Engineering*, 10847:1–15, 2006.

[113] M.F. Platten, J.R. Wright, G. Dimitriadis, and J.E. Cooper. Identification of multi-degree of freedom non-linear systems using an extended modal space model. *Mechanical Systems and Signal Processing*, 23:8–29, 2009.

[114] M.I. Qaisi. Non-linear normal modes of a continuous system. *Journal of Sound and Vibration*, 209:561–569, 1998.

[115] R. Rand. A higher-order approximation for nonlinear normal modes in two-degree-of-freedom systems. *International Journal of Non-Linear Mechanics*, 6:545–547, 1971.

[116] R. Rand. Nonlinear normal modes in two-degree-of-freedom systems. *Journal of Applied Mechanics*, 38:561–573, 1971.

[117] R. Rand. A direct method for nonlinear normal modes. *International Journal of Non-Linear Mechanics*, 9:363–368, 1974.

[118] G. Recktenwald and R. Rand. Stability of strongly nonlinear normal modes. *Communications in Nonlinear Science and Numerical Simulation*, 12:1128–1132, 2007.

[119] A. Remy. Training period report at ONERA, Updating of the finite element model of the MS 760 Paris aircraft. Technical report, Institut Polytechnique des Sciences Avancées, Paris, 2006.

[120] P. Ribeiro. Non-linear forced vibrations of thin/thick beams and plates by the finite element and shooting methods. *Computers & Structures*, 82:1413–1423, 2004.

[121] R.M. Rosenberg. Normal modes of nonlinear dual-mode systems. *Journal of Applied Mechanics*, 27:263–268, 1960.

[122] R.M. Rosenberg. The normal modes of nonlinear n-degree-of-freedom systems. *Journal of Applied Mechanics*, 30:7–14, 1962.

[123] R.M. Rosenberg. On nonlinear vibrations of systems with many degrees of freedom. *Advances in Applied Mechanics*, 9:155–242, 1966.

[124] S. Setio, H.D. Setio, and L. Jézéquel. A method of non-linear modal identification from frequency response tests. *Journal of Sound and Vibration*, 158:497–515, 1992.

[125] S. Setio, H.D. Setio, and L. Jézéquel. Modal analysis of nonlinear multi-degree-of-freedom structures. *The International Journal of Analytical and Experimental Modal Analysis*, 7:75–93, 1992.

[126] R. Seydel. *Practical Bifurcation and Stability Analysis. From Equilibrium to Chaos.* Springer-Verlag, New York, 2nd edition, 1994.

[127] S.W. Shaw and C. Pierre. Nonlinear normal modes and invariant manifolds. *Journal of Sound and Vibration*, 150:170–173, 1991.

[128] S.W. Shaw and C. Pierre. On nonlinear normal modes. In *ASME Winter Annual Meeting*, 1992.

[129] S.W. Shaw and C. Pierre. Normal modes for nonlinear vibratory systems. *Journal of Sound and Vibration*, 164:85–124, 1993.

[130] S.W. Shaw and C. Pierre. Normal modes of vibration for nonlinear continuous systems. *Journal of Sound and Vibration*, 169:319–347, 1994.

[131] J. Sieber, A. Gonzalez-Buelga, S.A. Neild, D.J. Wagg, and B. Krauskopf. Experimental continuation of periodic orbits through a fold. *Physical Review Letters*, 100:244101 1–4, 2008.

[132] S.C. Sinha, S. Redkar, and E.A. Butcher. Order reduction of nonlinear systems with time periodic coefficients using invariant manifolds. *Journal of Sound and Vibration*, 284:985–1002, 2005.

[133] J.C. Slater. A numerical method for determining nonlinear normal modes. *Nonlinear Dynamics*, 10:19–30, 1996.

[134] M.E.S. Soares and C.E.N. Mazzilli. Nonlinear normal modes of planar frames discretised by the finite element method. *Computers & Structures*, 77:485–493, 2000.

[135] N. Srinil and G. Rega. Two-to-one resonant multi-modal dynamics of horizontal/inclined cables. Part II: Internal resonance activation, reduced-order models and nonlinear normal modes. *Nonlinear Dynamics*, 48:253–274, 2007.

[136] W.J. Staszewski. Identification of non-linear systems using multi-scale ridges and skeletons of the wavelet transform. *Journal of Sound and Vibration*, 214:639–658, 1998.

[137] P. Sundararajan and S.T. Noah. An algorithm for response and stability of large order non-linear systems — application to rotor systems. *Journal of Sound and Vibration*, 4:695–723, 1998.

[138] W. Szemplinska-Stupnicka. The modified single mode method in the investigations of the resonant vibrations of non-linear systems. *Journal of Sound and Vibration*, 63:475–489, 1979.

[139] W. Szemplinska-Stupnicka. Non-linear normal modes and the generalized Ritz method in the problems of vibrations of non-linear elastic continuous systems. *International Journal of Non-Linear Mechanics*, 18:149–165, 1983.

[140] W. Szemplinska-Stupnicka. *The Behavior of Nonlinear Vibrating Systems — Volume II: Advanced Concepts and Application to Multi-degree-of-freedom Systems*. Kluwer Academic Publishers, Dordrecht, 1990.

[141] F. Thouverez. Presentation of the ECL benchmark. *Mechanical Systems and Signal Processing*, 17:195–202, 2003.

[142] C. Touzé and M. Amabili. Nonlinear normal modes for damped geometrically nonlinear systems: Application to reduced-order modelling of harmonically forced structures. *Journal of Sound and Vibration*, 298:958–981, 2006.

[143] C. Touzé, M. Amabili, and O. Thomas. Reduced-order models for large-amplitude vibrations of shells including in-plane inertia. *Computer Methods in Applied Mechanics and Engineering*, 197:2030–2045, 2008.

[144] C. Touzé, O. Thomas, and A. Chaigne. Hardening/softening behaviour in non-linear oscillations of structural systems using non-linear normal modes. *Journal of Sound and Vibration*, 273:77–101, 2004.

[145] C. Touzé, O. Thomas, and A. Huberdeau. Asymptotic non-linear normal modes for large-amplitude vibrations of continuous structures. *Computers & Structures*, 82:2671–2682, 2004.

[146] A.F. Vakakis. *Analysis and Identification of Linear and Nonlinear Normal Modes in Vibrating Systems*. PhD thesis, California Institute of Technology, 1990.

[147] A.F. Vakakis. Dynamics of a nonlinear periodic structure with cyclic symmetry. *Acta Mechanica*, 95:197–226, 1992.

[148] A.F. Vakakis. Non-similar normal oscillations in a strongly non-linear discrete system. *Journal of Sound and Vibration*, 159:341–361, 1992.

[149] A.F. Vakakis. Non-linear normal modes and their applications in vibration theory: an overview. *Mechanical Systems and Signal Processing*, 11:3–22, 1997.

[150] A.F. Vakakis. Inducing passive nonlinear energy sinks in vibrating systems. *Journal of Vibration and Acoustics*, 123:324–332, 2001.

[151] A.F. Vakakis and C. Cetinkaya. Mode localization in a class of multidegree-of-freedom nonlinear systems with cyclic symmetry. *SIAM Journal on Applied Mathematics*, 53:265–282, 1993.

[152] A.F. Vakakis and O. V. Gendelman. Energy pumping in nonlinear mechanical oscillators: Part II - resonance capture. *Journal of Sound and Vibration*, 68:42–48, 2001.

[153] A.F. Vakakis, O.V. Gendelman, L.A. Bergman, D.M. McFarland, G. Kerschen, and Y.S. Lee. *Nonlinear Targeted Energy Transfer in Mechanical and Structural Systems*. Springer, Dordrecht, 2009.

[154] A.F. Vakakis, L.I. Manevitch, Y.V. Mikhlin, V.N. Pilipchuk, and A.A. Zevin. *Normal Modes and Localization in Nonlinear Systems*. Wiley, New York, 1996.

[155] A.F. Vakakis, T. Nayfeh, and M.E. King. A multiple-scales analysis of nonlinear, localized modes in a cyclic periodic system. *Journal of Applied Mechanics*, 60:388–397, 1993.

[156] A.F. Vakakis and R.H. Rand. Normal modes and global dynamics of a 2-degree-of-freedom non-linear system; part I: low energies. *International Journal of Non-Linear Mechanics*, 27:861–874, 1992.

[157] A.F. Vakakis and R.H. Rand. Normal modes and global dynamics of a 2-degree-of-freedom non-linear system; part II: high energies. *International Journal of Non-Linear Mechanics*, 27:875–888, 1992.

[158] P. Van Overschee and B.L.R. De Moor. *Subspace Identification for Linear Systems: Theory, Implementation, Applications*. Kluwer Academic Publishers, Dordrecht, 1996.

[159] R. Viguié. *Tuning Methodology of Nonlinear Vibration Absorbers Coupled to Nonlinear Mechanical Systems*. PhD thesis, University of Liège, 2010.

[160] R. Viguié, M. Peeters, G. Kerschen, and J.C. Golinval. Energy transfer and dissipation in a Duffing oscillator coupled to a nonlinear attachment. *Journal of Computational and Nonlinear Dynamics*, 4:041012 1–13, 2009.

[161] C.V. Serra Villa, J.J. Sinou, and F. Thouverez. The invariant manifold approach applied to nonlinear dynamics of a rotor-bearing system. *European Journal of Mechanics A/Solids*, 24:676–689, 2005.

[162] F.X. Wang and A.K. Bajaj. Nonlinear normal modes in multi-mode models of an inertially coupled elastic structure. *Nonlinear Dynamics*, 47:25–47, 2007.

[163] F.X. Wang, A.K. Bajaj, and K. Kamiya. Nonlinear normal modes and their bifurcations for an inertially coupled nonlinear conservative system. *Nonlinear Dynamics*, 42:233–265, 2005.

[164] Y. Wang, D.M. McFarland, A.F. Vakakis, and L.A. Bergman. Seismic base isolation by nonlinear mode localization. *Archive of Applied Mechanics*, 74:387–414, 2005.

[165] J.R. Wright, J.E. Cooper, and M.J. Desforges. Normal-mode force appropriation — theory and application. *Mechanical Systems and Signal Processing*, 13:217–240, 1999.

[166] W.C. Xie, H.P. Lee, and S.P. Lim. Nonlinear dynamic analysis of MEMS switches by nonlinear modal analysis. *Nonlinear Dynamics*, 31:243–256, 2003.

[167] H. Yabuno and A.H. Nayfeh. Nonlinear normal modes of a parametrically excited cantilever beam. *Nonlinear Dynamics*, 25:65–77, 2001.

List of Journal Publications

1. G. Kerschen, M. Peeters, J.C. Golinval, and A.F. Vakakis. Nonlinear normal modes, Part I: A useful framework for the structural dynamicist. *Mechanical Systems and Signal Processing*, 23:170-194, 2009.

2. M. Peeters, R. Viguié, G. Kerschen, and J.C. Golinval. Nonlinear normal modes, Part II: Toward a practical computation using numerical continuation techniques. *Mechanical Systems and Signal Processing*, 23:195-216, 2009.

3. R. Viguié, M. Peeters, G. Kerschen, and J.C. Golinval. Energy transfer and dissipation in a Duffing oscillator coupled to a nonlinear attachment. *Journal of Computational and Nonlinear Dynamics*, 4:041012 1-13, 2009.

4. F. Georgiades, M. Peeters, G. Kerschen, J.C. Golinval, and M. Ruzzene. Modal analysis of nonlinear periodic structure with cyclic symmetry. *AIAA Journal*, 47:1014-1025, 2009.

5. M. Peeters, G. Kerschen, and J.C. Golinval. Dynamic testing of nonlinear vibrating structures using nonlinear normal modes. *Journal of Sound and Vibration*, 330:486-509, 2010.

6. K.R. Jayaprakash, Y. Starosvetsky, A.F. Vakakis, M. Peeters, and G. Kerschen. Nonlinear normal modes and band zones in granular chains with no pre-compression. *Nonlinear Dynamics*, In Press.

7. M. Peeters, G. Kerschen, and J.C. Golinval. Modal testing of nonlinear vibrating structures based on nonlinear normal modes: Experimental demonstration. *Mechanical Systems and Signal Processing*, In Press.

8. M. Peeters, G. Kerschen, J.C. Golinval, C. Stéphan, and P. Lubrina. Nonlinear normal modes of a full-scale aircraft. *AIAA Journal*, In Preparation.